A Novel Multi-Scale Domain Overlapping CFD/STH Coupling Methodology for Multi-Dimensional Flows Relevant to Nuclear Applications

by

Timothy P. Grunloh

A dissertation submitted in partial fulfillment
of the requirements for the degree of
Doctor of Philosophy
(Nuclear Engineering and Radiological Sciences)
in the University of Michigan
2016

Doctoral Committee:

Associate Professor Annalisa Manera, Chair
Professor Thomas J. Downar
Associate Professor Krzysztof J. Fidkowski
Assistant Professor Eric Johnsen
Professor Edward W. Larsen
Assistant Research Scientist Victor E. Petrov

Dedication

To my wife, Audrey

To Paul & June, Jim & Brenda, Lynn & Aaron, Melissa & Rob, Lindsey, Ramona, Adeline, Ava, and any yet to come

Without your support, none of this would have been possible

Table of Contents

List of Figures

List of Tables

List of Appendices

List of Acronyms

ATWS – Anticipated Transient without SCRAM

BC – Boundary Conditions

BWR – Boiling Water Reactor

CFD – Computational Fluid Dynamics

IDO – Inertial Domain Overlapping

LES – Large Eddy Simulation

LOCA – Loss of Coolant Accident

LSQ – Least Squares

MSLB – Main Steam Line Beak

NI – Non-Inertial

NPP – Nuclear Power Plant

PARCS – The Purdue Advanced Reactor Core Simulator

PTS – Pressurized Thermal Shock

PWR – Pressurized Water Reactor

RANS – Reynolds-Averaged Navier-Stokes

RPV – Reactor Pressure Vessel

SBLOCA – Small Break Loss of Coolant Accident

SETS – Stability-Enhancing Two-Step

SIDO – Stabilized Inertial Domain Overlapping

SIMPLE – Semi-Implicit Method for Pressure Linked Equations

STH – System Thermal Hydraulics

TRACE – TRAC/RELAP Advanced Computational Engine

VMF – Velocity-Matching Face

Abstract

The objective of this dissertation is to develop a 3-D domain-overlapping coupling method that leverages the superior flow field resolution of the Computational Fluid Dynamics (CFD) code STAR-CCM+ and the fast execution of the System Thermal Hydraulic (STH) code TRACE to efficiently and accurately model thermal hydraulic transport properties in nuclear power plants under complex conditions of regulatory and economic importance. The primary contribution is the novel Stabilized Inertial Domain Overlapping (SIDO) coupling method, which allows for on-the-fly correction of TRACE solutions for local pressures and velocity profiles inside multi-dimensional regions based on the results of the CFD simulation. The method is found to outperform the more frequently-used domain decomposition coupling methods.

An STH code such as TRACE is designed to simulate large, diverse component networks, requiring simplifications to the fluid flow equations for reasonable execution times. Empirical correlations are therefore required for many sub-grid processes. The coarse grids used by TRACE diminish sensitivity to small scale geometric details such as Reactor Pressure Vessel (RPV) internals. A CFD code such as STAR-CCM+ uses much finer computational meshes that are sensitive to the geometric details of reactor internals. In turbulent flows, it is infeasible to fully resolve the flow solution, but the correlations used to model turbulence are at a low level. The CFD code can therefore resolve smaller scale flow processes.

The development of a 3-D coupling method was carried out with the intention of improving predictive capabilities of transport properties in the downcomer and lower plenum regions of an RPV in reactor safety calculations. These regions are responsible for the multi-dimensional mixing effects that determine the distribution at the core inlet of quantities with reactivity implications, such as fluid temperature and dissolved neutron absorber concentration.

Chapter 1. Introduction

1-1 Motivation

1-1.1 Nuclear Energy Background

Heavy energy use has become a hallmark of advanced societies around the world. Through transportation, communication, and entertainment, people in developed countries consume enormous amounts of energy. Economic growth in countries like China, India, and Brazil holds the potential to lift billions from poverty in the next few decades. While this is unquestionably a great achievement of humankind, it will result in unprecedented global energy demand. In 2013 approximately 11% of global energy production was realized through nuclear sources, a fraction that rises to 18% in member countries of The Organisation for Economic Co-operation and Development (OECD) [1].

Mounting concerns about environmental pollutants, especially greenhouse gases, are consistently drawing mainstream attention. In 2015, world leaders negotiated the Paris Agreement that called for legally-enforced strict limits on global carbon emission [2]. As governments enact policies to reduce atmospheric carbon dioxide emissions, nuclear energy, which emits virtually none of the gas, will be a candidate for increased allocation in the global energy portfolio [1]. Other popular alternatives like solar and wind power are extremely attractive in a supplemental capacity but are troublesome for base load, due to intermittent availability.

The highly radioactive waste produced through nuclear power generation is solid material with a small volume compared to the waste produced by fossil fuel consumption. While extremely dangerous, nuclear spent fuel can be dealt with in a number of ways due to the manageable volume, although the specific long term plan has yet to be determined in some countries. Nuclear energy is also potentially favorable from the standpoints of fuel economics and geopolitical stability. Known geologic sources of uranium have increased by 25% or more over the past decade, with deposits of recoverable uranium existing in a diverse set of worldwide locations such as Australia, Kazakhstan, Namibia, and Canada [3]. Widespread access to nuclear fuel works to limit the political instabilities that develop around more geographically segregated resources, such as oil.

Incidents like the oil crisis of 1973 showed that a select few countries held a disproportionate amount of control over a crucially important sector of global economics, shocking governments and their constituencies into a fear of foreign energy dependence. Global energy use is expected to increase rapidly in the foreseeable future as emerging economies continue their rapid

industrial and economic development. Furthermore, the fuel cost of nuclear is dramatically less than that of fossil fuel energy sources. For comparison, the reported cost of delivered fuel for Duke Energy over the years 2012-2014 is shown in Table 1-1. Coupled to the increasingly finite nature of fossil fuel reserves, nuclear energy appears likely to play a large role in the future global energy portfolio [4]. Despite recent setbacks to the industry, the number of reactors currently under construction has reached a 25 year high with 72 reactors globally under construction as of 2014 [1].

Table 1-1. Duke Energy reported fuel costs. [5]

	cost of fuel per kilowatt-hour generated [cents]		
	2014	**2013**	**2012**
Coal	3.54	3.67	3.55
Nuclear	0.65	0.66	0.62
Gas/Oil	4.7	4.18	4.03

A snapshot of the global reactor fleet is given in Table 1-2. A large fraction of the world's nuclear power plants are so-called Light Water Reactors (LWRs) using water as the operating fluid. LWRs are further classified as Boiling Water Reactors (BWRs) and Pressurized Water Reactors (PWRs). Both of these types of reactors use ordinary water as coolant and moderator and enriched uranium dioxide as fuel. These are also the only types of reactors used to generate commercial power in the United States. A brief introductions to these types of plants is given in §1-1.2.

Table 1-2. Global Commercial Nuclear Reactors [6]

Reactor Type	Number	GWe	Coolant	Moderator
PWR	273	253	H_20	H_20
BWR	81	76	H_20	H_20
CANDU	48	24	D_20	D_20
GCR	15	8	CO_2	graphite
Light Water Graphite Reactor	15	10.2	H_20	graphite
FBR	2	0.6	liquid Na	none
total	434	371.8		

The regulatory environment for nuclear power generation is an increasingly important consideration, especially in the wake of the Fukushima Daiichi accident, which quite dramatically exhibited the need for an independent and effective regulatory body [1]. Regulators require power providers to demonstrate that reactors will behave safely under certain sets of adverse operating conditions. Often this is demonstrated by performing experiments, which can

be very expensive, as well as through modeling practices. In order to compensate for uncertainty in experiments and simulations, a safety margin is factored into design and operation. This safety margin generally exists at the expense of nuclear power plant (NPP) operating efficiency [7]. The use of higher-fidelity computational methods can more accurately predict reactor performance than current industry standards, but at a higher computational cost. Therefore, it is desirable to develop efficient approaches to employ state-of-the-art simulation methods to reduce uncertainty in safety margin estimation.

Nuclear reactor designs continue to evolve to more innovative iterations with sophisticated coolants. Indeed, many of the cutting edge Generation IV reactor concepts utilize coolants with non-unity Prandtl numbers [8], the effects of which remain an open question [9]. Regulatory concerns will demand an accurate understanding of the behavior of these new systems, which can be aided through advanced Computational Fluid Dynamics (CFD) models. In fact, researchers have already completed significant work towards the validation of CFD methods for NGNP reactor designs [10], [11]. Simulations of liquid metal cooled reactors have also been performed [12].

1-1.2 Nuclear Reactor Fundamentals

As observed in Table 1-2, most of the power-generating reactors in the world are operated in the thermal neutron energy spectrum with water cooling and moderation, the type of reactor targeted by the work in this thesis. A brief introduction to the operation of such reactors is given in this section, followed by a brief overview of how they are modeled in §1-1.3.

A schematic of a 2-loop PWR system is shown in Fig. 1-1, referring to the two independent closed circuits through which coolant flows. Each loop includes a distinct reactor coolant pump and steam generator. A pressurizer is additionally included on one loop to maintain system pressure. Control rods are inserted into the core from the top. Cool water enters the reactor pressure vessel (RPV), travels down through a downcomer region into the RPV lower plenum, and flows upward through the core region where active nuclear fuel is located. In the core, the coolant is heated up by about 30 K. The hot fluid exits the RPV and enters the steam generators (one for each loop), where it transfers heat to the secondary fluid of the steam generator before returning to the RPV. Nuclear fuel is composed of tens of thousands of fuel pins with a diameter of about a centimeter that are approximately $3.6m$ tall. Water flows between all the pins, providing cooling and moderation functions. BWR plants are quite similar, except they have no steam generators, the control rods are inserted from the bottom, and water boils in the core.

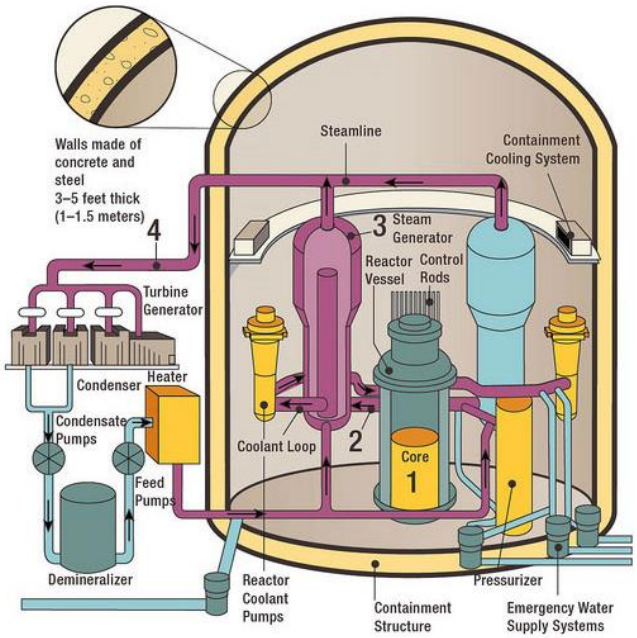

Fig. 1-1. Schematic of typical PWR plant. Source: NRC [13]

Aside from the heat source, nuclear power plants are quite similar to other power sources. In general, the major power sources are used to produce high pressure, high temperature steam [14] which is used to spin a turbine that is attached to a generator where the mechanical energy of the turbine blades is converted into electrical energy following Faraday's law. The nuclear power source, however, is different from conventional sources in important ways. For instance, due to the radioactivity of the core, a substantial amount of heat (~7% of full power) is still produced once the neutron chain reaction is halted. Although the amount of decay heat produced by irradiated fuel decreases with time, cooling is required for many days to maintain fuel integrity and avoid the release of radioactive isotopes.

The energy in fission reactors is released when a neutron enters the nucleus of certain types of large atoms, usually uranium or plutonium, creating a highly excited isotope that almost immediately fractures into smaller fragments. As the fragments come to a stop in the surrounding fuel matrix, their kinetic energy is deposited, raising the temperature of the fuel. Several neutrons are also produced by the fission of the large nucleus. When, on average, exactly 1 of these neutrons goes on to create a further fission, a steady-state nuclear chain reaction is sustained.

Neutrons born from fission are generally very high energy and travel at high velocities. Due to quantum mechanical effects, they are much less likely to interact with nuclear fuel when moving so quickly. Reactors can be classified by the energy spectrum of the neutrons in the core. In "fast" reactors, neutrons are not slowed down, and the core is designed to minimize neutron energy loss. In "thermal" reactors, the core is designed to slow down neutrons as quickly as possible. PWRs and BWRs operate in the thermal energy range.

Neutrons are most effectively slowed down through collisions with objects of similar size. For instance a billiard ball can come to a total stop after hitting another billiard ball, but a ping pong ball will bounce off a bowling ball at essentially the same speed it had before the collision. A hydrogen nucleus is a proton, which is approximately the same size as a neutron. The hydrogen content of water therefore provides, through neutron-proton collisions, a slowing down function to the neutrons in the reactor, referred to as neutron moderation.

The water in LWRs also serves as a coolant. Heat deposited in the fuel matrix by fission products is transferred to the surface of a fuel pin by conduction. From there the heat is transferred by convection to the water that is pumped through the reactor. In a BWR this water is allowed to boil and the steam is routed directly to turbines. In a PWR, the system pressure suppresses boiling, and heat is transferred through a heat exchanger (i.e. steam generator) from the primary coolant to a secondary coolant loop where boiling is allowed.

The fact that coolant also serves as a moderator is a designed safety feature. As water heats up, it becomes less dense. Lower density water means that there is less hydrogen between fuel pins, and the neutrons are not as effectively slowed down, decreasing the number of fissions occurring in the fuel. This feedback mechanism works to keep a reactor at an even power level during normal operation. During accidents in which the coolant inventory is diminished, the lack of moderator will serve to shut down the core.

1-1.3 Nuclear Power Plant Simulations and Safety Analysis

Over the years a diverse set of sophisticated computational tools have been developed to accurately predict the response of NPPs to a wide range of postulated events, so that designs can be improved, safety margins can be estimated, and mitigation strategies can be developed. Fluid dynamics and heat transfer play a central role in the simulation of the behavior of a NPP, and considerable efforts have been dedicated over the years to the development of so-called best-estimate system thermal-hydraulic (STH) codes. In STH codes, a NPP is modeled as an interconnected network of one-dimensional and zero-dimensional components (pipes, valves, pumps, etc.). Examples of such codes include RELAP5 [15] and TRACE [16] developed by US NRC, ATHLET developed by GRS in Germany [17], CATHARE developed by CEA in France [12], and MARS developed in Korea [18]. These computational tools are validated against a series of so-called separate effect tests, integral effect tests, and plant data, and are routinely used to perform safety analyses of NPPs as well as to investigate the behavior NPPs during operational transients.

While fluid dynamics is the subject of this thesis, neutronics is also of extremely high importance in NPP modeling, since it is needed to determine the power response of the reactor core. Neutron transport physics can be modeled with a stochastic approach in which the specific trajectories of a large number of neutrons throughout a core are calculated with pseudo-random numbers and tabulated to perform statistical analyses. Software packages like MCNPX [19] are based on this approach. Additionally, a deterministic approach can be taken that solves neutron transport of

diffusion equations based on discretization approaches. Software packages like PARCS [20] and MPACT [21] employ this approach.

Results from STH codes such as TRACE are accepted by government regulators only if the physical conditions are within ranges for which the code has been validated. System codes traditionally rely on a large number of 1-D correlations built on experiments. The applicability and accuracy of these correlations is well understood. When 3-D effects play an important role in the NPP system, the constitutive relations and simplifying assumptions upon which STH codes are based become invalid. Specifically, best-estimate system codes are unable to correctly capture circulating flow patterns in large open regions, such as inlet plena, which, for example, are important in boron dilution scenarios, main steam line break events, pressurized thermal shock transients, and accident scenarios involving passive safety systems.

In an attempt to address the limitations of STH when modeling flow conditions where three-dimensional effects are dominant, CFD analyses has been increasingly used over the past decades in safety analysis calculations. Currently, CFD methods are meant only to complement analytic fluid theory and fluid experiment, not to replace them. As a matter of fact, no CFD tool has been yet licensed by US NRC (or other foreign nuclear regulatory authority) for safety analyses. Just as with STH codes, results from CFD simulations are of limited use in the absence of proper experimental validation, especially when turbulence is involved [22]. However, recent years have seen remarkable maturation of CFD methods, particularly in the case of single phase flows in complex geometries. A significant amount of work towards the application of CFD methods to complex geometries relevant to nuclear engineering has been performed in recent years [23] [24] [25] [26]. As the set of experimental validation data grows, the applicability of CFD widens accordingly. Indeed, situations in which the flow in a primary reactor component is irreducibly three-dimensional, such as in case of natural circulation, mixing, and stratification have been identified as requiring the use of CFD methods to correctly model [7].

In recent years, Computational Fluid Dynamics (CFD) methods have been increasingly applied to the simulation of single phase flow in complex geometries relevant to nuclear engineering. To name just a few, Höhne et al. [25] simulated the mixing of de-borated slugs of water through the downcomer and lower plenum of a PWR RPV and validated the CFD model against experiments conducted at the ROCOM facility, Lee et al. [27] studied the effect of PWR internals on core inlet flow, and Jeong et al. [23] simulated the flow field in the downcomer and lower plenum of a PWR, explicitly accounting for reactor internals. The enduring trend of increasing availability of computational resources continues to add larger, higher resolution models to the class of tractable problems. Just recently, within the DOE Energy Hub Consortium for Advanced Simulation of Light Water Reactors (CASL), Westinghouse has developed a billion cell CFD model of a PWR RPV including all internals. Furthermore, researchers such as Merzari and Ninokata [28] and Prill and Class [29] have explored the use of Proper Orthogonal Decomposition (POD) to develop Reduced Order Models (ROM) for NPPs, potentially reducing the runtime computational burden significantly. Therefore, the coupling of CFD (or CFD-like

ROMs) codes with best-estimate STH codes is a worthwhile endeavor, particularly in view of current industry inclinations towards power uprates, with the consequent reduction of safety margins, mandating a compensating increase in the fidelity of predictive models to satisfy safety regulations.

1-2 Current State of CFD/STH Coupling Research

In the previous section, certain situations in which STH codes are unreliable were identified as being within the realm of CFD simulations. As such, researchers have developed many CFD/STH coupling methods to leverage the accuracy of CFD against the fast runtimes of STH. Primarily, two spatial coupling approaches are described in the literature, referred to as domain decomposition and domain overlapping. In the former, the system to be modeled is divided into discrete domains: one group simulated using the system code and the remaining domains simulated within the CFD code, connected through data exchange at the domain interfaces. In the domain overlapping approach, the entire system is computed within the system code, with selected regions further simulated within the CFD code as well. In this case, the CFD solution is used to correct the solution of the system code in the overlapped domain. Both methods are shown schematically in Fig. 1-2.

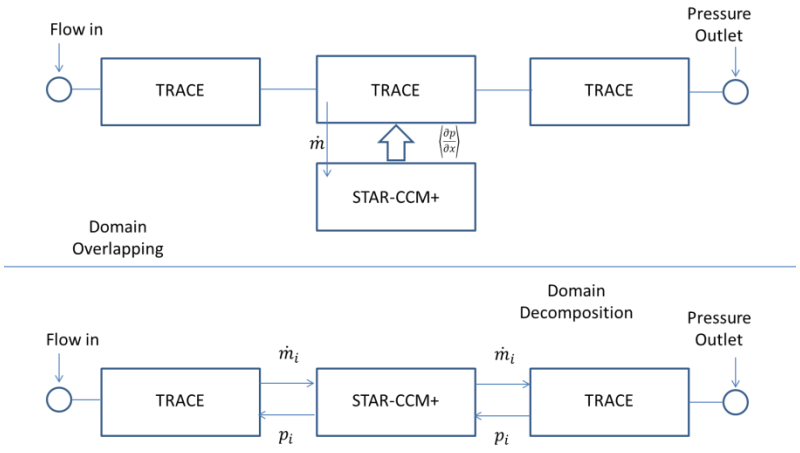

Fig. 1-2. Schematic diagram of sample coupling configurations. (TOP) Domain overlapping coupling. (BOTTOM) Domain decomposition coupling.

The first coupling efforts for nuclear applications reported in the literature were from Aumiller et al. [30] and Gibeling and Mahaffy [31], both works based on domain decomposition approaches. In recent years, several additional efforts have been focused on similar approaches. Anderson et al. [32] analyzed the Very High Temperature Reactor (VHTR). Bertolotto et al. [33] performed single phase mixing studies. Papukchiev et al. [34] coupled ATHLET and ANSYS CFX and applied it to a Pressurized Thermal Shock Transient [35]. Watanabe et al. [36] studied steam generator instability during station blackout conditions. Li et al. [37] coupled FLUENT and RELAP5 to study the Edwards-O'Brien blowdown problem as well as multi-loop flow through a 3D region. In some cases [30] [33] [34] [35], semi-implicit numerical coupling schemes are also

described, aimed at relaxing the requirements on the integration time steps posed by explicit time-stepping methods, at the expense of increased computational costs. Additionally, implicit or semi-implicit methods generally require more data storage and stronger manipulation of each code's execution due to the need for time step backups.

Researchers have also employed domain overlapping methods targeted at various phenomena. Fanning and Thomas [38] used a CFD solution to correct the energy equation and the gravitational pressure term computed by the system code SAS4A/SASSYS-1 [39] for the simulation of sodium-cooled reactors. Jeltsov et al. [40] used a CFD solution to correct the system code energy equation through the implementation of a "virtual heater". Baviere et al. [41] [42] used a CFD solution to correct both momentum and enthalpy equations using iterative controls. In this case, a source/sink term in the momentum equation of the system code CATHARE is iteratively adjusted within a given time step until the overall pressure drop across the overlapped component is identical to the CFD solution.

Another coupling approach is to modify the closure coefficients used by the system code, taking advantage of pre-existing functionality. Cadinu and Kudinov [43] employed such a method, but did not explicitly account for inertial effects on the pressure gradient, limiting the applicability of the method to steady state. The question therefore arises of how to use the CFD solution to correct the solution of the system code on-the-fly when inertial pressure effects are not negligible, without the need of additional iterations within the system code. We address this by deconstructing the pressure gradient to account for inertial effects and calculate a transient-compatible closure relation for the system code from on-demand CFD data. The coupling presented in this dissertation focuses on correcting the TRACE momentum equation.

Comparisons among coupled CFD/STH simulations based on overlapping and domain decomposition approaches have been reported in the literature. Papukchiev et al. [44] compared coupled approaches to simulations of the TALL-3D experiment and Bandini et al. [11] assessed several coupling implementations based on their application to Generation IV reactor concepts. However, because different coupled codes were used (RELAP5/STAR-CCM+, ATHLET/ANSYS CFX, CATHARE/TRIO-U), these comparisons cannot be used to draw generalized conclusions on the performance of a given coupling scheme versus another. Consequently, some of the work in this dissertation undertakes a systematic comparison of domain overlapping and domain decomposition methods to assess their relative performance. The results show that the novel domain overlapping method proposed here is able to successfully correct the solution of the system code TRACE based on the solution of the CFD code STAR-CCM+. In addition, it is found that for the cases tested, the proposed domain overlapping method exhibits superior stability and temporal convergence characteristics as compared to a domain decomposition implementation.

1-3 Objectives and Original Contributions

The objective of work presented in this dissertation is to develop a 3-D domain overlapping coupling method that leverages the superior flow field resolution of STAR-CCM+ and the fast execution of TRACE to efficiently and accurately model NPPs under complex conditions of regulatory, economic, and safety importance.

An STH code such as TRACE is designed to simulate large networks of diverse components, requiring simplifications to the governing equations of fluid flow, such as large integration volumes and neglect of intra-fluid shear forces, for reasonable execution times. Such formulations require heavy use of empirical correlations for many sub-grid processes, such as heat transfer, viscous effects, and form losses. Additionally, the coarse grid used by TRACE precludes it from sensitivity to small scale geometric details, such as those resulting from structures internal to RPVs.

A CFD code like STAR-CCM+, on the other hand, uses much finer computational meshes than TRACE. In turbulent flows, it is generally infeasible to fully resolve the flow solution, but the correlations used to model turbulence are at a significantly lower level than the correlations used in TRACE. As a result, the CFD code can resolve more aspects of processes, such as heat transfer, viscous effects, and form losses. Additionally, CFD meshes are fine enough to incorporate the effects of the geometric details of reactor internals.

Based on these considerations, the development of a 3-D coupling method was carried out with the intention of improving predictive capabilities of transport properties in the downcomer and lower plenum regions of an RPV in reactor safety calculations. These regions are responsible for the multi-dimensional mixing effects that determine the distribution at the core inlet of quantities with reactivity implications like fluid temperature and dissolved neutron absorber concentration. Potential applications of the STH/CFD coupled tool also include integral small modular reactors and LWR Gen-III+ with passive systems, where the behavior of the plant in accident conditions is dominated by heat transfer and convective motions in large water pools.

In order to successfully couple a 3-D CFD region to a TRACE RPV, the total pressure drop across the coupled component must be corrected to avoid unduly disrupting other aspects of the NPP simulation, such as coolant pumps. Additionally, it is necessary to reproduce the CFD velocity field across the core inlet. The two primary objectives of the presented coupling method are therefore the reproduction in TRACE of global CFD pressure drops and CFD velocity profiles at a specific plane.

The primary original contribution of this thesis is the development of a novel Stabilized Inertial Domain Overlapping (SIDO) coupling method. This method allows for on-the-fly correction of TRACE solutions for local pressures and velocity profiles inside multi-dimensional regions based on the results of the CFD simulation. The SIDO method developed in this dissertation was

found to outperform the more frequently-used domain decomposition coupling methods, especially in transient simulations.

Additional contributions include:

- The development of a 1-D domain overlapping coupling method that laid the foundations of using inertia-corrected friction factors to adjust the STH momentum equation.
- A systematic comparison of domain overlapping and domain decomposition coupling methods applied to identical systems.
- The development of a velocity-matching approach for calculating CFD-like velocity fields in STH codes.
- The development of the Inertial Domain Overlapping (IDO) 3-D coupling method, the predecessor to the more advanced SIDO method. This was the first extension of the 1-D domain overlapping coupling method to 3-D systems and involved locally correcting pressure and velocity fields.
- The development of stabilizing factors that improve the behavior of the IDO method in challenging transients, defining the SIDO method.
- A comparison of coupling methods in the simulation of 3-D reactor-like flows that show the ability of the SIDO method to stably simulate transients in complex configurations using explicit time stepping. Domain decomposition coupling was found to be unstable in these conditions.

1-4 Structure of Thesis

In Chapter 2, STAR-CCM+ and TRACE results for the transport of passive and active scalars in 3D components are compared to highlight the deficiency of STH codes such as TRACE in predicting mixing in large open volumes, where 3-D fluid dynamics effects play a significant role. Domain decomposition and domain overlapping coupling methods are discussed in Chapter 2 and Chapter 4, respectively. For both methods, the theoretical foundations are first discussed, following by 1-D verification test cases. A systematic comparison of the two methods is presented in Chapter 5, with special emphasis on stability and convergence characteristics. In Chapter 6 the coupling theoretical framework specific to multi-dimensional geometries is developed. In Chapter 7, 3-D domain overlapping coupling methods are verified in both Cartesian and cylindrical configurations with a diverse range of transients. In Chapter 8 the coupled simulation of reactor-representative geometries in closed loop configurations is detailed. Finally, in Chapter 9, the conclusions of the dissertation work are presented along with recommendations for future work, directed at both improving the SIDO method and at advanced applications for the method.

1-5 Software Used

1-5.1 STAR-CCM+

The multiphysics code STAR-CCM+ developed by CD-Adapco is used in this work for its CFD functionalities. In the cases presented here, STAR-CCM+ solves the incompressible Navier-Stokes momentum conservation equations, subject to certain modeling approximations alongside a mass conservation equation. Since the majority of flows of relevance in nuclear power plants exhibit turbulent behavior, the turbulence modeling features of STAR-CCM+ are employed [45].

Using two-equation models, such as k-ϵ or k-ω, to simulate turbulence leads to a system of 6 coupled partial differential equations. STAR-CCM+ solves these equations by discretizing a designated flow region into many small, but finite volumes. Thus, the system of PDEs becomes a system of algebraic equations. More details on turbulence modeling can be found in Appendix B.

The computational mesh can be provided or generated through the meshing pipeline within STAR-CCM+. As a point of reference, a "small" CFD model will often be on the order of 10^5 mesh cells, while a "large" CFD model can be 3-4 orders of magnitude larger. Further, the temporal discretization can often require time steps on the order of $1\,ms$ or less. CFD models can therefore be computationally expensive and are only applied when the importance of flow field resolution outweighs the importance of fast execution times. For instance, the flow through much of the piping in a NPP can usually be sufficiently resolved in system codes with significantly coarser meshes and larger time steps by using friction factor correlations [46].

1-5.2 TRACE

The TRAC/RELAP Advanced Computational Engine (TRACE) is a best-estimate reactor systems simulation tool developed by the U.S. NRC for the purposes of analyzing the steady state and transient behavior of light water reactors subject to neutronic and thermal hydraulic influences [16]. System codes such as TRACE excel at the simulation of the complex networks of hydraulic, thermal, and nuclear components that constitute a nuclear power plant. Due to the large scope of system codes, the necessity of reasonable execution times mandates a coarse approach to discretization.

In system codes, nuclear power plants are broken into idealized components, such as pumps, pipes, vessels, cores, separators, and pressurizers. The partial differential equations governing the hydraulic models are averaged over fairly large volumes within each component, resulting in systems of algebraic equations whose solutions provides data such as cell-averaged pressures for each volume. Closure models are used for a wide range of physics, including frictional pressure drops, heat transfer between fluid and walls, as well as heat, mass, and energy transfer at the liquid/vapor interface.

1-5.3 Janus

TRACE and STAR-CCM+ are coupled through Janus, a set of software tools developed at the University of Michigan to complete the work presented in this dissertation. While STAR-CCM+ is closed source, it is equipped with a powerful Java interface that allows for control of the code. Scripts written for this interface are the primary drivers of coupled simulations. TRACE, written in Fortran, is compiled as a shared object and run via the Java Native Access (JNA) library. Further, custom Java-Fortran interfaces specific to the data structures used in STAR-CCM+ and TRACE were developed to allow for efficient data transfer directly through memory. More details on the implementation of Janus can be found in Appendix D.

Chapter 2. Modeling of Scalar Mixing and Transport

2-1 Introduction

Coupling efforts in the nuclear power industry are in general motivated by the idea that STH codes are unable to reliably capture 3-D mixing phenomena, such as recirculation zones and turbulent diffusion. The method developed in this dissertation is based on the development of a novel efficient coupling scheme between STH codes and CFD codes, to be used for the modeling of open mixing in which 3-D effects play a dominant role. The coupling corrects the STH solution on-the-fly using the more accurate CFD solution, such that the overall pressure drop across the 3D region and the mass flow-rates through the inlets and outlets of the region computed by the STH code match the CFD solution. The coupling scheme developed in this dissertation is focused on the correction of the STH momentum equation. Future developments will extend to the energy and other scalar transport equations (e.g. boron concentration) as well.

NPPs are complex systems governed by several physical principles. As discussed in §1-1, the properties of the coolant field can have serious consequences on the performance and safety of the reactor core. For instance, the power generated by a thermal reactor core depends heavily on the temperature of the fluid. Cold fluids with higher densities lead to more neutron moderation and hence higher power generation, unless controlled by the injection of a neutron absorber (either through injection of borated water or through the insertion of control rods). A commonly analyzed scenario in which single-phase mixing in open regions is important is the Main Steam Line Break (MSLB) transient, where the fast depressurization of one of the steam generators leads to an asymmetric fluid temperature at the core inlet. Other scenarios of interest involve single-phase mixing of water with different concentration of a neutron absorber. In Boiling Water Reactors (BWRs), injected borated water is used as an alternative way to shut down the reactor when the insertion of control rod fails, during so-called Anticipated Transients Without Scram (ATWS). In Pressurized Water Reactors (PWRs) the neutron population during nominal operation is controlled by dissolution of a neutron absorber (B^{10}) in the coolant. During accident scenarios such as small-break loss of coolant accidents (SBLOCA), a plug of deborated water can form in one of the main recirculation loops, causing a reactivity insertion (i.e. a power increase) when the deborated plug reaches the core. This scenario is known as a boron-dilution accident.

MSLB, ATWS and boron dilution scenarios are all cases in which the specific transport behavior of localized fluid properties in the open downcomer and lower plenum regions of a reactor pressure vessel has a strong impact on reactor safety. As design basis accidents (DBAs), operators must demonstrate that a plant can withstand the consequences of these incidents with

acceptable safety margins. Uncertainty, both from physical sources and the numerical simulation, increases the required margins, usually at the cost of reactor economics. By reducing the uncertainty in the numerical solutions to these problems, utilities can operate reactors more cost effectively without increasing the risk of undesirable consequences to the plant and to the public. With the new reactor design trends toward increased deployment of passive safety systems and integral configurations (i.e. LWR Gen-III+ and Small Modular Reactors), there is a growing need for efficient coupled CFD/STH codes.

2-1.1 MSLB Postulated Accident

In the late 1990s, an international benchmark was organized by OECD/NEA to study the effects of the transient core behavior following the rupture of a main steam line [47]. The transient was chosen because of the unique challenges it presented, such as the strong nature of the coupling between neutronics and core thermal hydraulics. Further, the assumption of a stuck-out control rod and the presence of asymmetric cooling resulted in a strong multi-dimensionality of the problem. The utilization of point kinetics models, in which the 3-D effects of neutron transport are neglected, resulted in a return-to-power for the reactor, which was not found when more advanced spatial kinetics models were employed.

In defining a MSLB transient, it is postulated that a double-ended rupture of one steam line upstream of the main steam isolation valve occurs at full power conditions. Fluid loss in the secondary side of the affected steam generator will result in a significant decrease in the pressure of the secondary side, lowering the saturation pressure, further resulting in significantly increased heat transfer from the primary side to the secondary side in the affected loop. The colder primary coolant inventory will translate into a reactivity insertion into the core. Because only one cooling loop is affected, the MSLB transient is highly asymmetric. This transient has been the subject of much attention in the industry [48] [49] [50].

2-1.2 ATWS Postulated Accident

Boiling water reactors (BWRs) use a nuclear heat source to directly boil water in the RPV. As a result, BWR designs generally include steam separator equipment in the top part of the pressure vessel, requiring that control rods be inserted from the bottom of the core. In contract, pressurized water reactors (PWR) are designed with control rods above the core, supported by an electromagnet that is automatically de-energized when power is cut. In this case, gravity provides a passive safety system. Because BWRs do not benefit from this level of reliability, operators must consider the possibility that some occurrence will cut power to the reactor and the control rod insertion, or SCRAM, will fail. In an ATWS, it is postulated that an initiating event (typically the inadvertent closure of the main steam isolation valves) is followed by failure of control rod insertions.

During ATWS, operators rely on neutron absorbers dissolved in the reactor coolant for shutdown margin. The injected fluid (typically borated water) can be significantly denser than the primary

fluid [51]. Depending on prevailing flow conditions, the injected fluid can stratify in the lower plenum, transport directly to the core inlet, or some combination of the two. The specific behavior of the injected neutron absorbers can have strong implications on core power control.

2-1.3 Boron dilution accident scenario

A typical boron dilution accident in PWRs starts with a SBLOCA, which results in disruption of circulation in the primary circuit. In this case, reflux condensation in the U-tubes of the steam generators might occur, with accumulation of deborated condensate in the lower plenum of the steam generators and in the loop seals upstream of the main recirculation pumps. When circulation in the primary loop is re-established, plugs of deborated water can reach the reactor core, with a consequent reactivity insertion.

2-2 Passive Scalar Transport

The transients described in the previous section all involve transport and mixing of a scalar (i.e. boron concentration in the coolant or coolant temperature) in the open regions of the RPV upstream of the core inlet. In the following sections, the differences in local transport properties between CFD codes like STAR-CCM+ and STH codes like TRACE are analyzed by simulating an asymmetric injection of a scalar field into a mixing domain designed to reproduce flow phenomena typical of nuclear reactors. Standalone solutions from STAR-CCM+ and TRACE are compared in order to characterize the effects captured by each. Differences among the CFD and STH solutions are considered alongside the formulation of governing transport equations for each code. The purpose of the work presented here is to motivate the development of CFD/STH coupling by illustrating situations in which simplifications typical of STH codes affect the transport properties of the flow, and by considering the potential ramifications of these effects.

A geometry designed to simulate flow conditions found in RPVs was employed to test the transport properties of the two codes. The geometry, shown in Figure 2-1, features two inlets and two outlets, to mimic a two-loop reactor configuration. Similar to a PWR RPV, the flow enters the annular downcomer formed by the RPV external wall and the core barrel, then travels downward into the lower plenum, where it changes direction to flow upward through the core region and eventually out of the RPV at the same elevation as the inlet. More details can be found in Appendix A.

Visualization of the computed passive scalar field can provide a qualitative description of the path of a specific fluid volume including the effects of viscous diffusion, turbulent diffusion, and convective mixing. The field can also provide a quantitative description of mixing by comparing initial scalar concentrations to the values downstream in the flow domain. The mixing properties of the flow are analyzed through the distribution of the scalar at important locations in the domain over time. A defining characteristic of passive scalars refer is that they do not interact with the flow. Neutron absorbers such as orthoboric acid are sometimes modeled in this way. In some cases, the solution containing the neutron absorber is at a lower temperature compared to

the primary flow field and therefore at a lower density. If the density difference is substantial, the passive scalar approach here may be insufficient. Such an example is treated in §2-3.

2-2.1 TRACE Scalar Transport

In addition to the mass, momentum, and energy conservation equations, TRACE is also equipped to solve a convection equation for liquid solute transport [16]. The equation governing any quantity C advecting through a single phase flow domain without affecting the flow is given in Eq. 2-1, as implemented in TRACE:

$$\frac{\partial}{\partial t}(\rho C) + \nabla \cdot (\rho C \mathbf{v}) = s_C, \qquad 2\text{-}1$$

where s_C is a source or sink of the quantity C. For the analysis presented here s_C is taken as zero except at the boundaries, consistent with the addition of orthoboric to reactor coolant for neutron population control. The solubility model employed by TRACE for orthoboric acid is based on a linear correlation between the concentration and the liquid temperature, given by Eq. 2-2 [52]:

$$S(T) = \begin{cases} 0.0635 \dfrac{kg\ solute}{kg\ water}, & T < 303K, \\ 0.0635 \dfrac{kg\ solute}{kg\ water} + 0.2125 \dfrac{kg\ solute}{kg\ water \cdot K}(T - 303K), \\ 0.276 \dfrac{kg\ solute}{kg\ water \cdot K}, & T > 373K. \end{cases} \qquad 2\text{-}2$$

When the solute concentration exceeds the solubility limit in TRACE, the excess solute is plated out on the surrounding structures. In this section, only scalar transport is considered. The concentrations considered are well below the solubility limits of Eq. 2-2, and so the effects of plated-out boron will not be analyzed. Additionally, no quantitative analysis of the effects of dissolved solute on a reactor core will be undertaken. The geometry considered was designed to be hydrodynamically representative of a nuclear power plant, but the core region is left entirely empty of nuclear fuel for simplicity.

2-2.2 STAR-CCM+ Scalar Transport

CFD codes like STAR-CCM+ generally include models for passive scalar transport. This functionality is useful for applications such as visualizing the flow field, calculating residence time, or modeling the transport of a dilute neutrally buoyant solute through a flow field. The finite volume transport equation for a scalar function C in STAR-CCM+ is given by Eq. 2-3 [45]:

$$\frac{\partial}{\partial t}\iiint_V \rho C dV + \oiint_A \rho C \mathbf{v} \cdot d\mathbf{A} = \oiint_A \left[\left(\frac{\mu}{\sigma} + \frac{\mu_t}{\sigma_t}\right)\nabla C\right] \cdot d\mathbf{A} + \iiint_V S_C\, dV, \qquad 2\text{-}3$$

where σ is the molecular Schmidt number, σ_t is the turbulent Schmidt number, μ is the dynamic viscosity, μ_t is the turbulent viscosity, and S_C is a source term, taken to be zero. A striking difference between Eq. 2-2 and 2-3 is the presence of a diffusion term in the latter equation. The ability of STAR-CCM+ to model both molecular and turbulent diffusion potentially provides a strong advantage over TRACE in scalar transport, when such diffusion processes are non-negligible, such as during accident conditions characterized by low flow rates or strong scalar gradients in the lower plenum. In order to more fully describe the effects of diffusion, the case without molecular or turbulent diffusion is also performed with a passive scalar field governed by Eq. 2-4:

$$\frac{\partial}{\partial t}\iiint_V \rho C dV + \oiint_A \rho C \mathbf{v} \cdot d\mathbf{A} = 0. \qquad 2\text{-}4$$

The CFD formulation of scalar transport neglecting diffusion looks very similar to the TRACE transport equation (Eq. 2-1). Key differences, however, exist in how the codes handle geometry. The presence of simplified internals in the lower plenum would be expected to noticeably affect the scalar field. TRACE sees the obstruction only through the fraction of fluid volume that is available for flow (Table A-3) and through user-defined form loss coefficients, while STAR-CCM+ is sensitive to the geometric details of the obstruction. In the comparison between TRACE and STAR-CCM+ presented in the next sections of this chapter, STAR-CCM+ simulations have been performed with and without the effect of diffusion, in order to isolate the effect that geometry and diffusion have on the scalar transport and mixing.

2-2.3 Standalone Comparison

The time-dependent scalar variable of Eq. 2-5 was applied to inlet 1 (as indicated in Fig. 2-1) of both STAR-CCM+ and TRACE for analysis of how each code transports the scalar. We examine the transport of the scalar in two cases where the flow rates at both inlets are set to the same value, either $3.0 kg/s$ or $7.0 kg/s$:

$$C(t) = \begin{cases} 0.0, & t < 1.0s, \\ C_{max}, & 1.0s \le t \le 2.0s, \\ 0.0, & t > 2.0s, \end{cases} \qquad 2\text{-}5$$

where $C(t)$ is the inlet value of the scalar field and C_{max} is taken as 0.005. The transport of the scalar is analyzed by considering the concentration through the downcomer inlet ring and the core inlet, shown in Fig. 2-1. These regions provide insight into what happens as a scalar enters the downcomer annulus where complex flow is present. The concentration across the core inlet provides understanding as to the mixing throughout the entire downcomer and inlet plenum region, including the effects of the flow obstruction. The downcomer and core inlets are both broken into 4 equal azimuthal divisions, referred to here as quadrants. Inlet 1 is centered on the 3rd quadrant, or Q3, while Inlet 2 is centered on Q1.

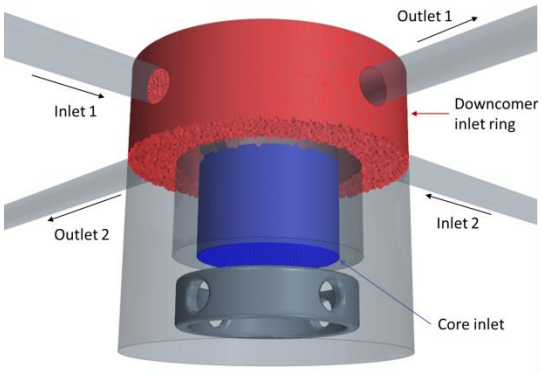

Fig. 2-1. Regions of interest for scalar transport highlighted on the dual loop geometry.

Volume-averaged scalar concentrations are shown across the downcomer inlet ring in Fig. 2-2 for a low flow test case with a flow rate of $\dot{m}_{in} = 3.0\ kg/s$ applied to both inlets. Compared to STAR-CCM+, TRACE under-predicts mixing, showing a higher concentration in the cell immediately adjacent to the inlet from which the scalar is injected (Q3) and a lower concentration in all other cells.

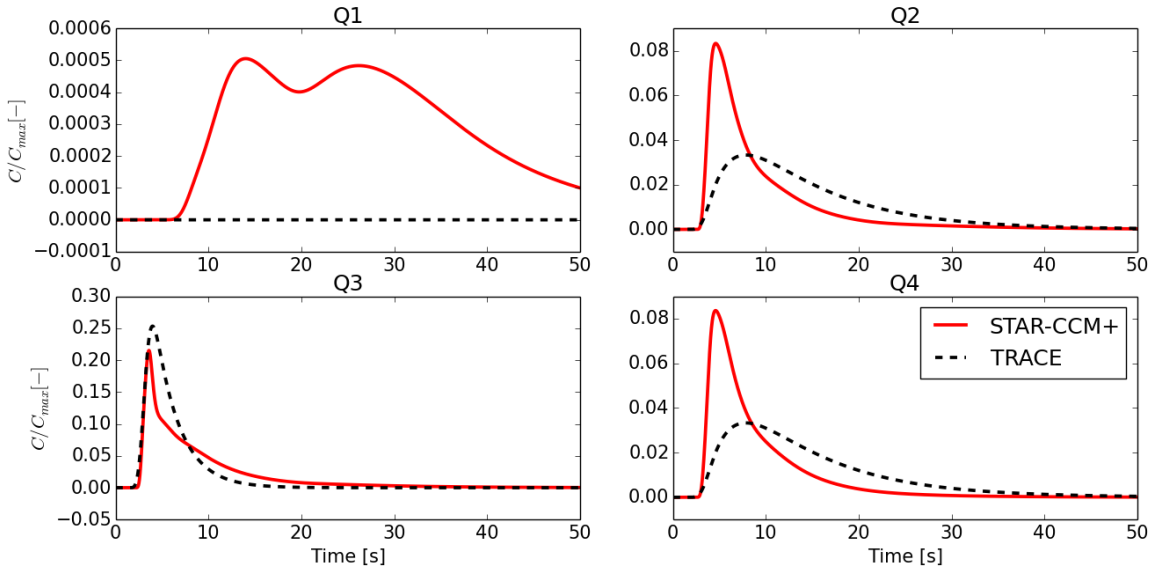

Fig. 2-2. Scalar concentrations predicted across the downcomer inlet. Calculated with a symmetric mass flow rate configuration of $3.0\ kg/s \times 3.0\ kg/s$.

The scalar concentration across the core inlet, shown in Fig. 2-3, exhibits similar behavior. TRACE over-predicts the concentration in the Q3 quadrant. Additionally, TRACE predicts no scalar concentration in Q1, even though an appreciable value is predicted by STAR-CCM+.

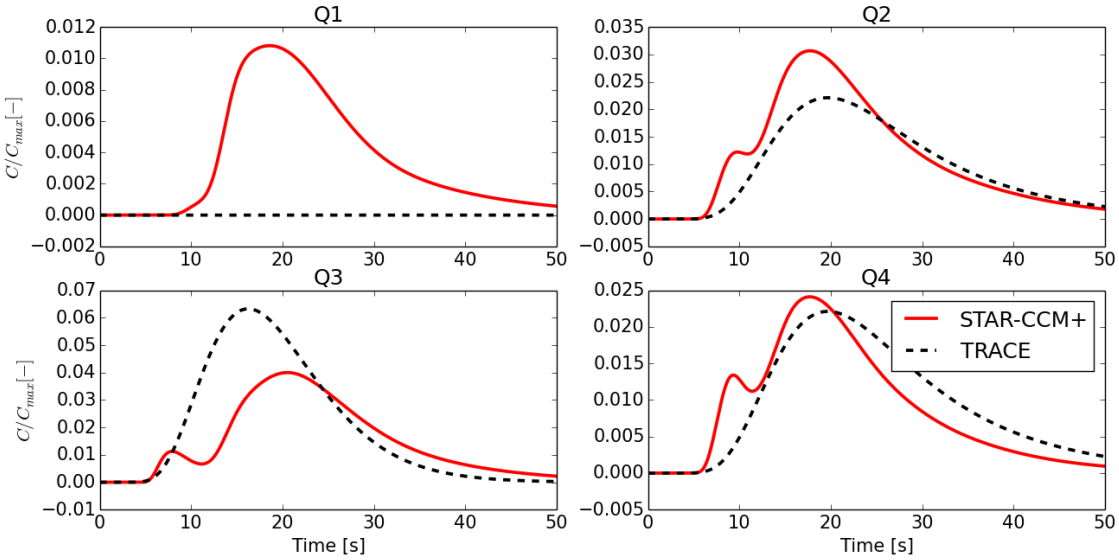

Fig. 2-3. Scalar concentrations predicted across the core inlet. Calculated with $\Delta t = 0.01s$ and a symmetric mass flow rate configuration of $3.0\ kg/s \times 3.0\ kg/s$.

The scalar concentration across the downcomer inlet ring is shown in Fig. 2-4 for a higher flow symmetric case in which both inlets were held at a flow rate of $\dot{m}_{in} = 7.0\ kg/s$. As would be expected at the higher flow rate, the pulses are considerably thinner than in the previous case. TRACE again over-predicts the scalar value in Q3 and under-predicts the value in Q2 and Q4.

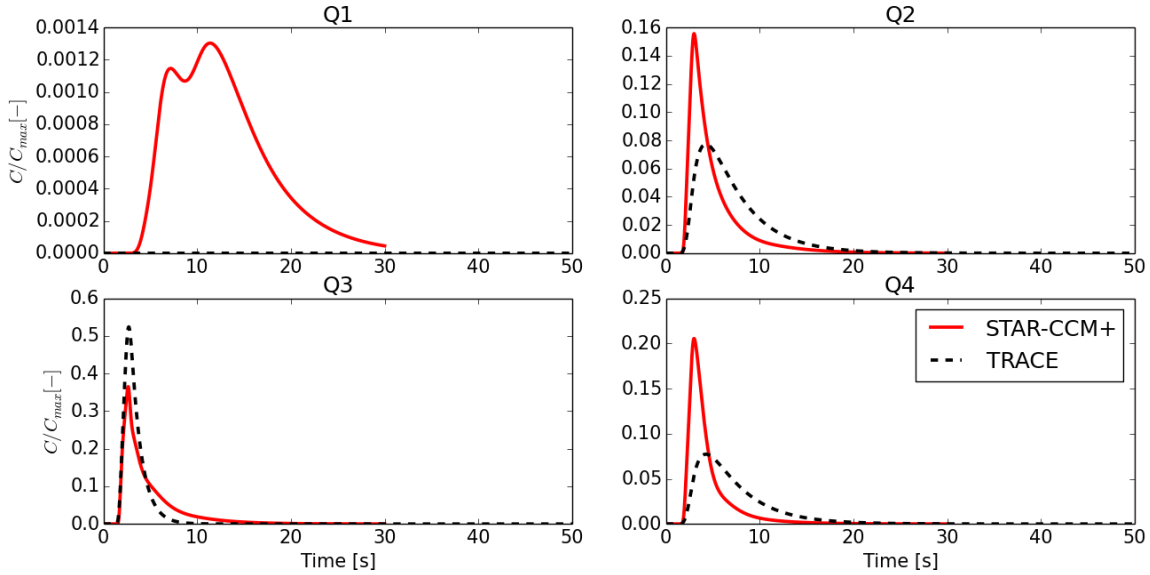

Fig. 2-4. Scalar concentrations predicted across the downcomer inlet. Calculated with $\Delta t = 0.01s$ and a symmetric mass flow rate configuration of $7.0\ kg/s \times 7.0\ kg/s$.

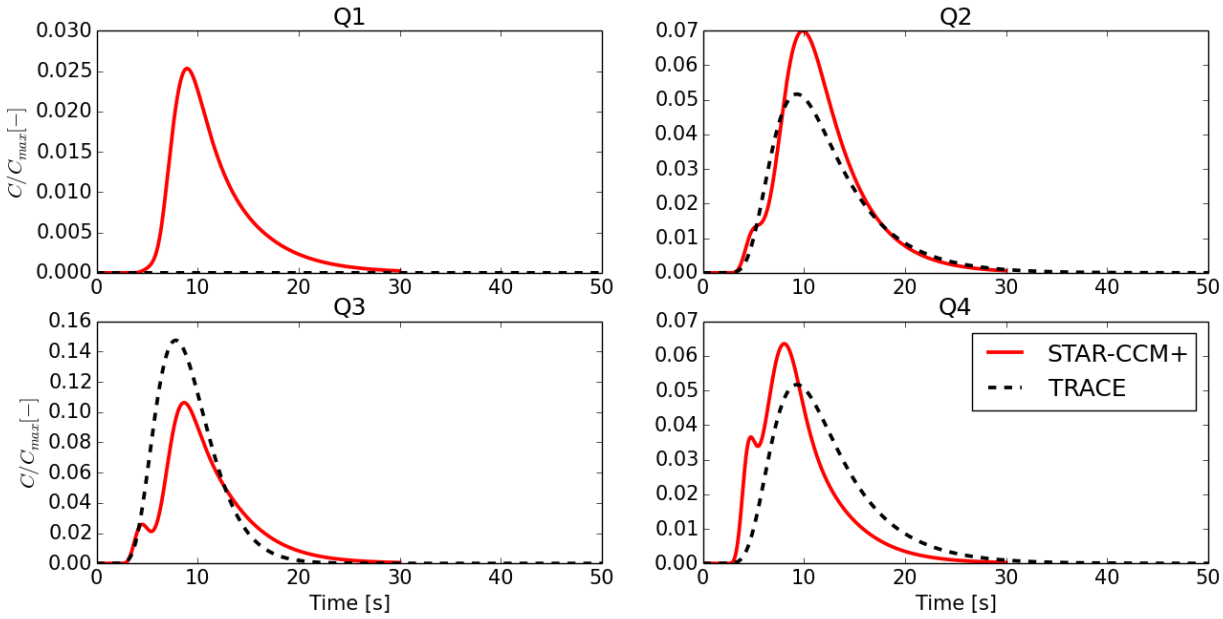

Fig. 2-5. Scalar concentrations predicted across the core inlet. Calculated with $\Delta t = 0.01s$ and a symmetric mass flow rate configuration of $7.0\ kg/s \times 7.0\ kg/s$.

The scalar concentration across the downcomer inlet ring is shown in Fig. 2-5 for the higher flow rate. Once again, TRACE predicts no scalar concentration in at the core inlet in Q1, over-predicts the concentration in Q3 (closest to the loop where the scalar was injected), and under-predicts the concentrations in the cells directly adjacent, Q2 and Q4, similar to the behavior observed in the lower flow case.

One particularly noteworthy feature of the previous figures is a double-peak occurring for the CFD-calculated data. This occurs because the scalar concentration plume is broken into smaller plumes by the obstruction in the lower plenum. One plume bypasses the obstruction by flow above it. The remainder of the scalar is pushed downward, delaying its entrance into the core region. As the first plume begins to subside, the second plume passes through, resulting in the observed shapes of the scalar concentration functions. Importantly, the TRACE model was unable to predict such behavior.

2-2.4 STAR-CCM+ Flow Field

The nature of scalar transport throughout the domain as calculated by STAR-CCM+ can be understood upon consideration of Fig. 2-6. The top left shows the scalar plug enter the flow domain. Upon impacting the inner wall of the downcomer region, a large portion of the scalar moves in the azimuthal direction, while a somewhat smaller portion moves downward. The top right shows the scalar concentration after the majority of the scalar slug has entered the downcomer. Only a small amount of the scalar is transported down directly toward the core inlet. At this time, the first traces of scalar are reaching the lower plenum, consistent with the data shown in Fig. 2-5. The bottom left shows the flow domain at $t = 3.55s$. At this time the scalar

concentration field is beginning to approach the core inlet from multiple directions. Additionally, the scalar approaching from side directions penetrates further into the downcomer, strongly interacting with the lower plenum internals.

Finally, the bottom right shows the scalar concentration field at $t = 6.75s$. Here the interaction of the scalar field with the lower plenum obstruction is made clear. The specific path of the flow in this region can have strong implications for the state of the fluid entering the core region. The lower plenum of a true reactor is strongly obstructed by structural components and flow-shaping devices.

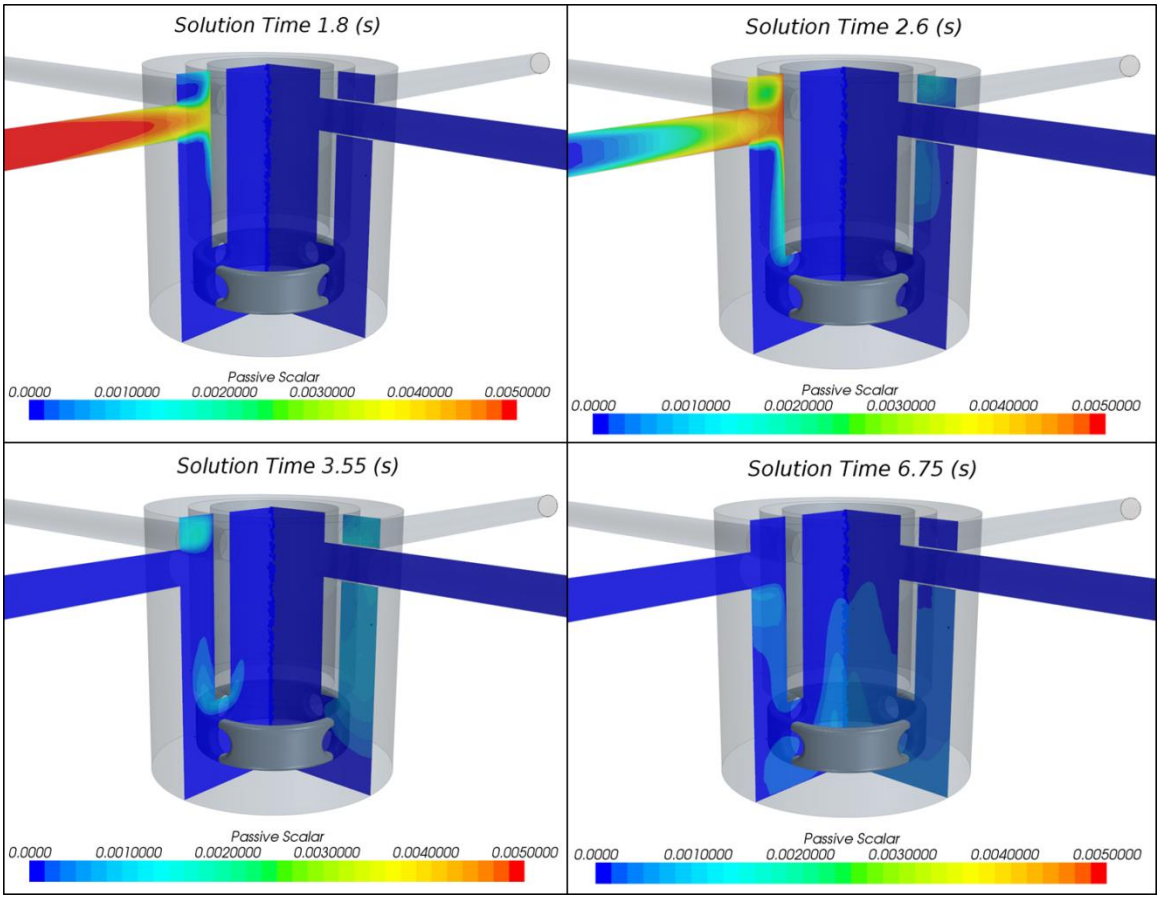

Fig. 2-6. STAR-CCM+ scalar concentrations throughout domain at selected times. Calculated with $\Delta t = 0.01s$ and a symmetric mass flow rate configuration of $7.0\ kg/s \times 7.0\ kg/s$.

2-2.5 Effect of Diffusion

In order to quantify the effects of diffusion, passive scalar transport was simulated with Eq. 2-3 (STAR-CCM+) and Eq. 2-4 (CCM+ w/o diff.) and plotted in the following figures. Fig. 2-7 compares the scalar concentration at the downcomer inlet. At this location, the difference between the two simulations is minimal as convection is the dominating influence near the inlet.

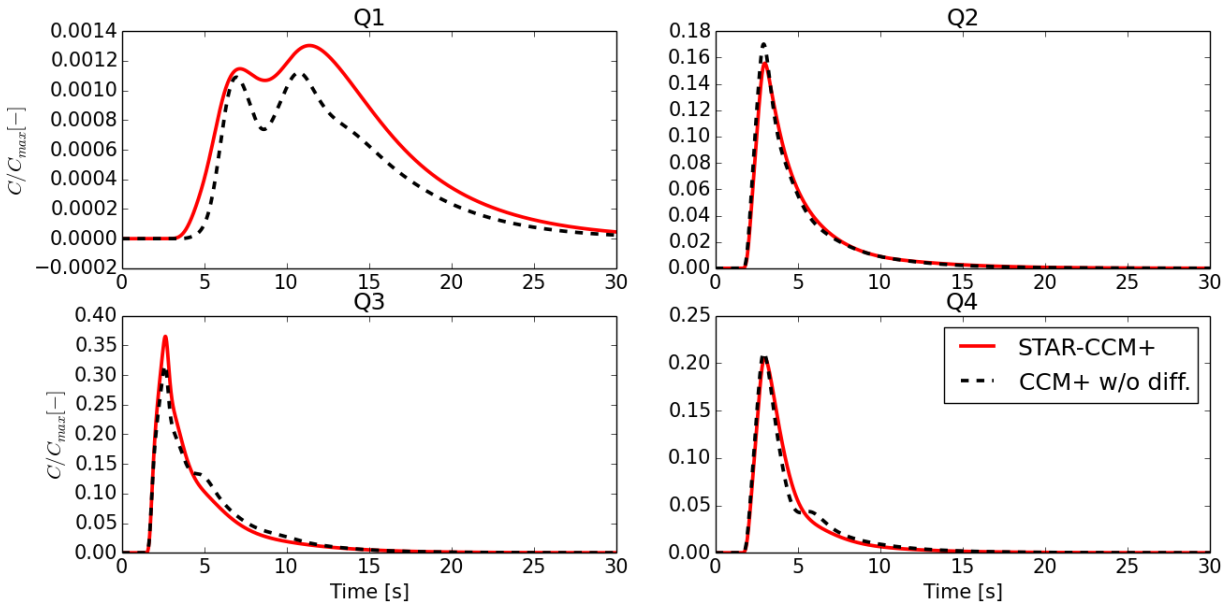

Fig. 2-7. Scalar concentrations predicted across the downcomer inlet. Calculated without a diffusion term with $\Delta t = 0.01s$ and a symmetric mass flow rate configuration of $7.0\ kg/s \times 7.0\ kg/s$.

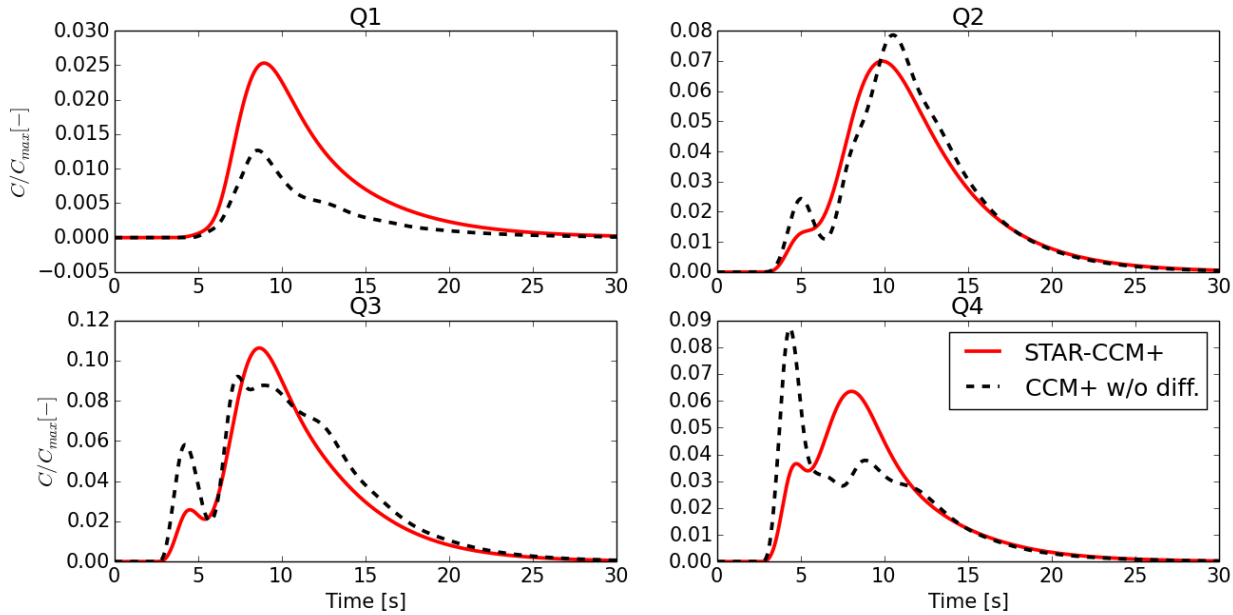

Fig. 2-8. Scalar concentrations predicted across the core inlet. Calculated without a diffusion term with $\Delta t = 0.01s$ and a symmetric mass flow rate configuration of $7.0\ kg/s \times 7.0\ kg/s$.

Fig. 2-8 compares the scalar concentration at the core inlet. At this location, diffusion clearly has a substantial effect on scalar transport. The concentrations in Q1 and Q4 appear to be the most

strongly affected by scalar diffusion. The smoothing effect of the diffusion term is also apparent in these results. The double-peaking behavior, however, is still apparent, indicating its source as a convective phenomenon.

2-3 Cold Fluid Transport

The transport of passive scalar fields, such as boron concentration, is important for reactor analysis. However, some important scalar fields such as temperature do interact directly with the flow. In particular, the relationship between fluid temperature and fluid density is quite important when appreciable elevation differences are a factor. In accidents such as the MSLB that result in asymmetric cooling, the coolant temperature field can have a strong effect on not only the velocity field, but also on the neutronic behavior of the core. When denser fluid flows through the core of a thermal spectrum reactor, neutron moderation and therefore power generation are increased. Correctly capturing the fluid temperature inside a reactor core is a high priority and requires accurate calculation of 3-D mixing phenomena. It is therefore necessary to consider active scalars like temperature in addition to passive scalars like neutron poisons in order to accommodate a wider range of transient scenarios.

2-3.1 Heat Transport Formulation

STAR-CCM+ and TRACE both calculate temperature fields by solving an energy conservation equation. The specific formulations, however, are quite different due to the scales of the computational mesh. As will be demonstrated in this section, the CFD code only relies on model coefficients for the effects of turbulence, while TRACE relies quite heavily on correlations.

2-3.1.1 STAR-CCM+ Energy Equation

In STAR-CCM+, the user has the choice of solving the energy equations in terms of either temperature or enthalpy [45]. Enthalpy formulations are generally intended for flows in which combustion occurs, since enthalpy tends to vary more smoothly than temperature in reaction zones. Since we are not presently considering such flows, a temperature formulation is employed. The total energy equation employed by STAR-CCM+ is given in Eq. 2-6:

$$\frac{d}{dt}\iiint_V \rho E dV + \oiint_A \rho H \mathbf{v}\cdot d\mathbf{A} = -\oiint_A \dot{\mathbf{q}}''\cdot d\mathbf{A} + \oiint_A \bar{\bar{\mathbf{T}}}\cdot d\mathbf{A} + \iiint_V \mathbf{f}\cdot\mathbf{v} dV, \qquad 2\text{-}6$$

where the total energy is $E = H - p/\rho$, the enthalpy is $H = h + \mathbf{v}\cdot\mathbf{v}/2$, $h = C_p T$, and $\mathbf{f}$ represents body forces. The heat flux vector $\dot{\mathbf{q}}''$ is given by Eq. 2-7:

$$\dot{\mathbf{q}}'' = -\left(k + \frac{\mu_t C_p}{\sigma_t}\right)\nabla T. \qquad 2\text{-}7$$

Here k is the thermal conductivity, μ_t is the turbulent viscosity, C_p is the specific heat and σ_t is the turbulent Prandtl number.

2-3.1.2 TRACE Energy Equation

The energy equation for a fluid in TRACE is given by Eq. 2-8 [16]:

$$\frac{\partial}{\partial t}(\rho e) + \nabla \cdot (\rho e \mathbf{v}) + p\nabla \cdot \mathbf{v} = q_{wl} + q_{dl}, \qquad 2\text{-}8$$

where q_{wl} is the heat transfer rate per unit volume from the wall to the liquid, and q_{dl} is the power per unit volume deposited directly into the fluid. The wall heat transfer coefficient used to calculate q_{wl} is taken as the maximum of the coefficients for laminar flow (h_{lam}), turbulent forced convection (h_{turb}), and natural convection (h_{NC}):

$$h_{wl} = \max\{h_{lam}, h_{turb}, h_{NC}\}. \qquad 2\text{-}9$$

In all cases, the heat transfer coefficients are calculated from Nusselt numbers based on correlation. For pipe flow, the laminar Nusselt number is a well-known analytical result:

$$Nu_{lam} = \frac{h_{lam} D_h}{k} = 4.36. \qquad 2\text{-}10$$

For the turbulent Nusselt number, TRACE uses the Gnielinski correlation [53], given by Eq. 2-11:

$$Nu_{turb} = \frac{h_{turb} D_h}{k} = \frac{0.5f(Re - 1000)Pr}{1 + 12.7(0.5f)^{0.5}(Pr^{2/3} - 1)}, \qquad 2\text{-}11$$

where the friction factor f is evaluated using Filonenko's smooth tube formula [54], shown in Eq. 2-12:

$$f = [1.58 \cdot \ln(Re) - 3.28]^{-2}. \qquad 2\text{-}12$$

TRACE calculates the Nusselt number for natural convection with Eq. 2-13:

$$Nu_{NC} = \frac{h_{NC} D_h}{k} = \max\left\{0.1 \cdot (Gr \cdot Pr)^{\frac{1}{3}}, 0.59 \cdot (Gr \cdot Pr)^{\frac{1}{4}}\right\}, \qquad 2\text{-}13$$

where Gr is the Grashof number that provides a measure of the ratio of buoyancy to viscous forces. Heat transfer in TRACE, and STH codes in general, relies heavily on empirical correlations that can introduce significant amounts of uncertainty, especially if they are applied to situations significantly different from the experimental conditions from which they were derived.

2-3.2 Standalone Comparison

The temperature transport properties of STAR-CCM+ and TRACE are investigated by injection of a slug of cold water into the flow domain. The temperature of the flow entering through Inlet 1 is given by Eq. 2-14, while the temperature at Inlet 2 is maintained at $T_2 = 330K$:

$$T_1(t) = \begin{cases} 330K, & t < 1.0s, \\ 310K, & 1.0s \leq t \leq 2.0s, \\ 330K, & t > 2.0s. \end{cases} \qquad 2\text{-}14$$

The temperature variable can be non-dimensionalized as shown in Eq. 2-15, allowing comparison with the C/C_{max} variable used for passive scalar transport. Because mixing properties were quite similar to those observed in the passive scalar section, only cells in the Q3 quadrants are considered to avoid undue redundancy:

$$\Theta(\mathrm{T}) = \frac{330K - T}{330K - 310K} = \frac{330K - T}{20K}. \qquad 2\text{-}15$$

The normalized temperature through the Q3 cell of the downcomer inlet is shown in Fig. 2-9. At this location, TRACE significantly over-predicts the maximum value of Θ. TRACE also predicts a much faster pulse that CFD. These results are consistent with an under-prediction of mixing in the flow field calculated by the STH code.

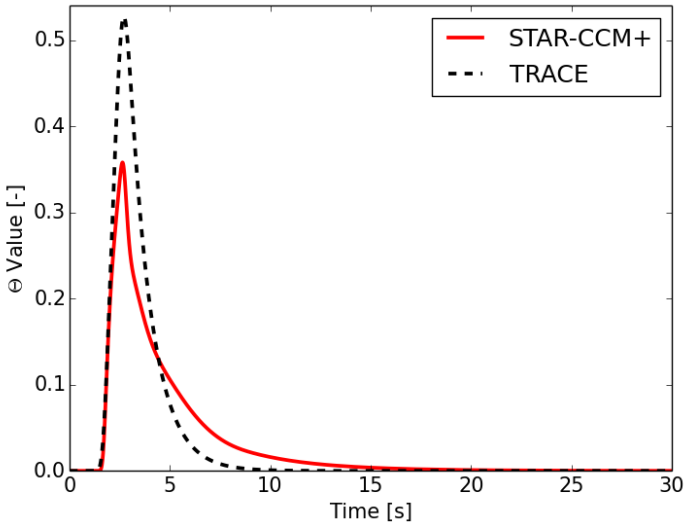

Fig. 2-9. Normalized temperature predicted in the Q3 cell of downcomer inlet. Calculated with $\Delta t = 0.01s$ and a symmetric mass flow rate configuration of $7.0\ kg/s \times 7.0\ kg/s$.

The normalized temperature through the Q3 cell of the core inlet is shown in Fig. 2-10. TRACE's inability to capture the effects of scalar interaction with the lower plenum obstruction is again apparent in the difference in structure of the Θ pulses. Specifically a double-peaked

shape is apparently for the CFD result, but not for the STH result. The STAR-CCM+ function also indicates a longer residence time in the core region owing to recirculation effects that TRACE is unable to capture.

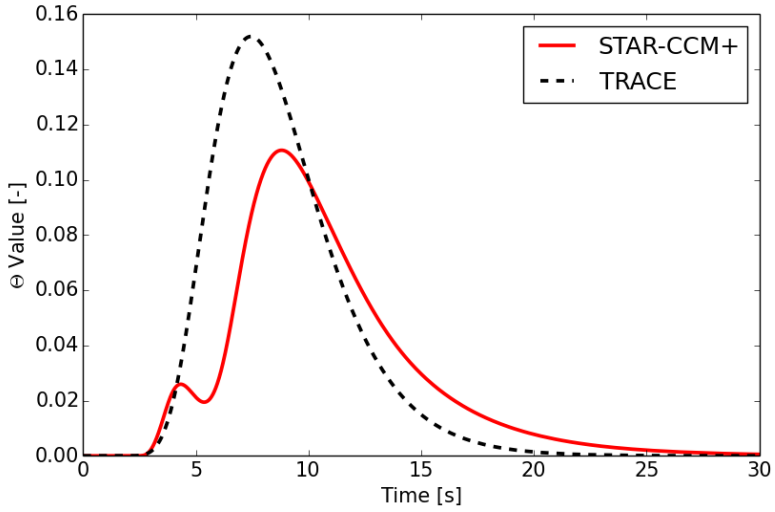

Fig. 2-10. Comparison of active scalar field in the Q3 cell of the core inlet plane. Calculated with $\Delta t = 0.01 s$ and a symmetric mass flow rate configuration of $7.0\ kg/s \times 7.0\ kg/s$.

2-3.3 STAR-CCM+ Temperature Field

Similar to §2-2.4, the temperature field is examined at several snapshots during the cold fluid injection transient. The top left of the figure shows the flow field as the cold fluid slug begins to impact the inner wall of the downcomer annulus. The colder fluid primarily flows around the annulus and then downward as it meets the stream from the opposite inlet. Some of the fluid also travels downward directly toward the inlet plenum. The top right shows the flow field near the end of the cold fluid insertion. At this point, the colder fluid is contained in the top part of the downcomer. The portion of the impacting cold fluid that travels downward has begun to reach the inlet plenum.

The bottom left of the figure shows the flow field at a time when a significant amount of colder fluid has appeared on the plane perpendicular to the axis of the inlet pipes. The source of the initial peak in Θ is also visible here. Finally, the bottom right of the figure shows the flow field with a large amount of cool fluid in the lower plenum and core region. The fluid is clearly interacting with the flow obstruction, directing some fluid downward and causing the second peak observed in the previous section.

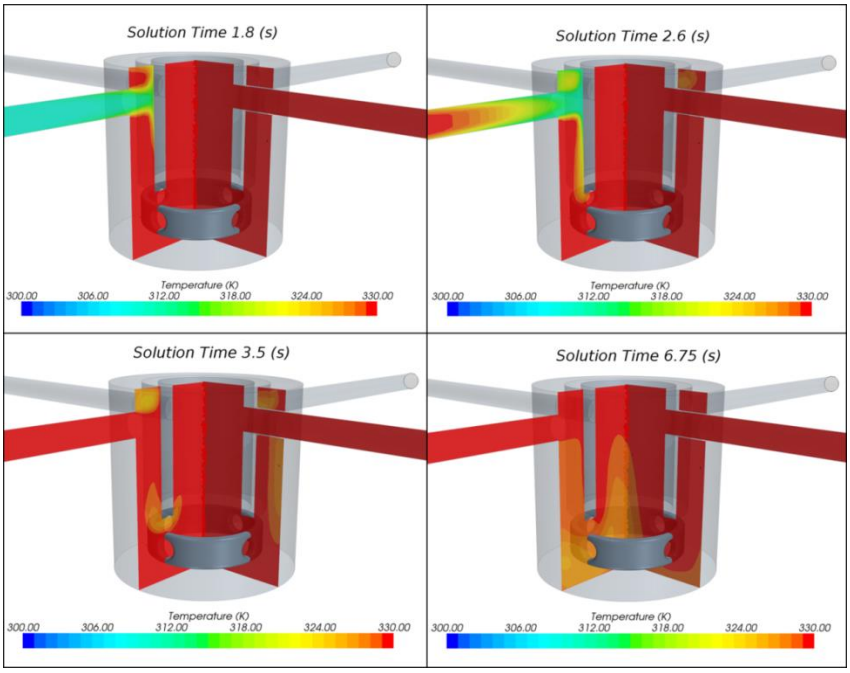

Fig. 2-11. STAR-CCM+ temperature fields throughout domain at selected times. Calculated with $\Delta t = 0.01s$ and a symmetric mass flow rate configuration of $7.0\ kg/s \times 7.0\ kg/s$.

2-4 Scalar Field Comparison

The temperature and passive scalar fields are shown side-by-side at $t = 6.75s$ in Fig. 2-12. An accumulation of lower temperature fluid in the lower plenum is clearly evident in the left side of the figure. Evidently, the action of the gravitational body force on the denser fluid is non-negligible for this test case.

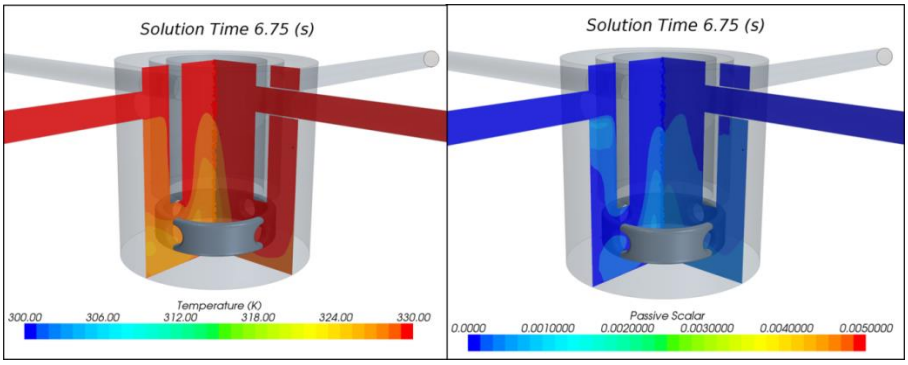

Fig. 2-12. Comparison of active (LEFT) and passive (RIGHT) scalar fields as calculated with STAR-CCM+.

Fig. 2-13 shows the passive scalar concentration and normalized temperature in the Q3 cell of the downcomer inlet through the transient for both STAR-CCM+ and TRACE. Very little difference is observed between the two because convection forces dominate at this location.

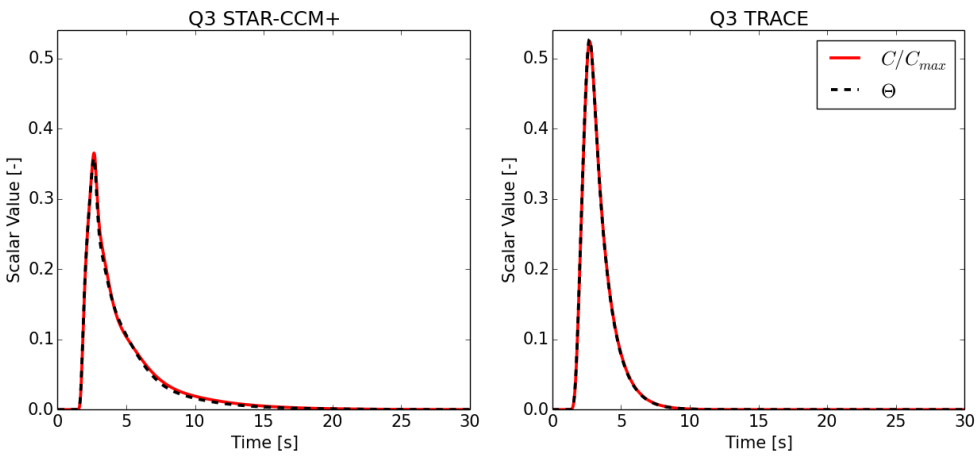

Fig. 2-13. Quantitative comparison of passive and active scalars in Q3 cell of the downcomer inlet (LEFT) STAR-CCM+. (RIGHT) TRACE. Calculated with $\Delta t = 0.01s$ and a symmetric mass flow rate configuration of $7.0\ kg/s \times 7.0\ kg/s$.

Fig. 2-14 shows the passive scalar concentration and normalized temperature in the Q3 cell of the core inlet. Both STAR-CCM+ and TRACE predict a somewhat higher peak for the normalized temperature, because gravity acts to accelerate the heavier fluid downward towards the inlet plenum and then the core.

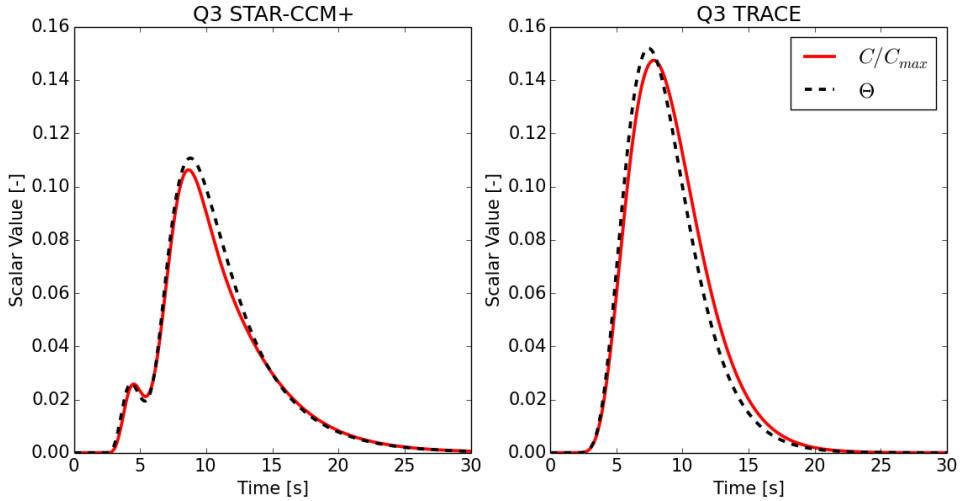

Fig. 2-14. Quantitative comparison of passive and active scalars in Q3 cell of the core inlet (LEFT) STAR-CCM+. (RIGHT) TRACE. Calculated with $\Delta t = 0.01s$ and a symmetric mass flow rate configuration of $7.0\ kg/s \times 7.0\ kg/s$.

2-5 Conclusions and implication on safety analyses

In this chapter, the transport of scalar quantities through a simplified RPV geometry has been analyzed. Both transport of a neutron poison, such as boron, and the transport of a colder water injection were simulated.

Since boron does not strongly interact with the flow, passive scalar transport can be used to predict the boron distribution in a flow. However, if the injected fluid is of a lower temperature than the coolant, buoyant effects can cause significant interaction with the bulk flow. First a passive scalar plug transporting through the region was simulated. For a dual loop RPV simulant, it was found that TRACE and STAR-CCM+ predict similar transport properties with some significant differences. TRACE is unable to predict fine scale interaction of the scalar with reactor internals, which can have significant consequences on boron distribution throughout the core. TRACE is additionally tends to under-predict mixing.

The transport of an active scalar, temperature, was also studied. The temperature field interacts with the flow by changing density and inducing buoyant effects in a gravitational field. This type of scenario is important for cases in which fluid of asymmetric temperature is injected into the lower plenum, such as the MSLB transient. The TRACE formulation for the heat equation was shown to strongly rely on a large number of correlations, while the STAR-CCM+ formulation was more robustly based on first principles. Similarly to the passive scalar case, TRACE was generally found to under-predict mixing and to be unable to predict the interaction of the field with the flow obstruction in the lower plenum.

In both cases analyzed (boron transport and injection of cold water), it has been shown that in typical RPV geometries, STH codes such as TRACE have a strong tendency to under-estimate mixing. This is due to inability of the STH code to take into account both 3-D geometrical effects, as well as the impact that turbulent fluctuations in the flow have on diffusion and therefore mixing of a passive scalar. The implications on safety analysis and economics of nuclear power plant are important. Because TRACE under-predicts mixing, in case of boron dilution, this will result in an under-estimation of the local boron concentration at the core inlet. In the MSLB transient, TRACE will considerably under-predict the coolant temperature at the inlet of one of the core sector.

In both cases, TRACE will yield a significant over-prediction of the reactivity insertion in the reactor core, and therefore will result in conservative safety analyses. Unnecessary conservatism in reactor safety analyses due to inaccurate simulations tools has a direct impact on reactor economics, as these might result in excessive limits on the reactor nominal power and other operational conditions. Therefore, the combination of STH codes with CFD to reduce conservatism in safety analyses is of considerable interest.

Chapter 3. Domain Decomposition Implementation and Verification

In this chapter, the domain decomposition coupling method is introduced and its performance is evaluated with a series of test cases. As mentioned in Chapter 1, domain decomposition is the most widely used coupling technique reported in the literature because of its simple and straightforward implementation. Throughout this work, the domain decomposition method is used as a reference point from which the performance of domain overlapping methods, the primary subject of this thesis, can be evaluated. The test cases analyzed in the current chapter are much simpler than typical NPP applications and are designed to isolate specific flow phenomena, thereby providing ideal conditions for verification and initial insight into the numerical behavior of the coupling methods. This chapter begins by describing an approach to domain decomposition coupling, focusing on one-dimensional systems, although the methods described are essentially identical to those used for higher dimensional cases. A suite of verification cases is then described with results illustrating the use of the so-called "surface interfaces" implement the domain decomposition.

3-1 Domain Decomposition Approach

In the domain decomposition approach, a system to be modeled (e.g. a nuclear power plant) is divided into two (or more) discrete domains, each simulated either within the system code or within the CFD code. Coupling is realized through data transfer at the boundaries of the region(s) assigned to the system code and those assigned to the CFD code. A schematic of the domain decomposition coupling strategy is shown in Fig. 3-1. A domain decomposition interface, also referred to as a "surface interface", can connect a TRACE break component (pressure boundary condition) to a STAR-CCM+ inlet boundary, usually a mass flow inlet, (Fig. 3-1 left), or a TRACE fill component (mass flow or velocity boundary condition) to a STAR-CCM+ pressure outlet boundary (Fig. 3-1 right). In the case of the former, the pressure calculated at the inlet of the CFD region is passed to the cell center of the break component and the flow rate in the break is passed to the CFD inlet. In the latter case, the pressure at the center of the cell nearest the interface is passed to the CFD outlet boundary while the flow rate through the CFD outlet is passed to the fill component.

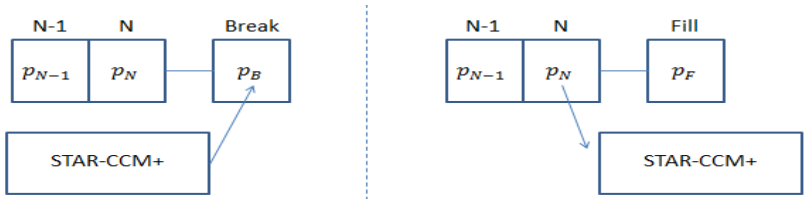

Fig. 3-1. Schematic diagram of data exchange between boundaries of TRACE and STAR-CCM+ for domain decomposition coupling

STH codes like TRACE often employ a staggered grid arrangement with scalar quantities like pressure and temperature defined in the center of control volumes (CVs) and have the physical meaning of averages over the CV. Vector quantities like velocity are defined at the boundaries of the CV. In such cases, interpolation is necessary to calculate the velocity at the center of a CV or the pressure at the CV boundary. The Janus interface developed within the current dissertation uses a surface pressure computed by the CFD code to modify the pressure in the system code coupled node, a practice that can introduce some error depending on the length of the break component. While this error is often negligible in practice, some STH codes extrapolate thermodynamic variables to the CV edge. Additionally node lengths and form loss coefficients can be adjusted to meet requirements. The primary benefit of domain decomposition coupling lies in the simplicity of its implementation and theoretical framework. In the next sections, the performance of the domain decomposition coupling is analyzed through a series of steady state and transient test cases.

3-2 Straight Pipe Verification Test Case

An isolated straight isothermal pipe with locally defined boundary conditions, the simplest physical case useful for verifying coupling methods, was designed to test the domain decomposition method. Depending on boundary conditions, flow is driven by either an imposed mass flow rate or an imposed pressure drop. The coupling is also tested under diverse spatial configurations generated by varying the domain partition between the STH and the CFD code.

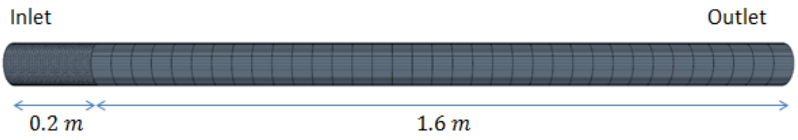

Fig. 3-2. Sample STAR-CCM+ mesh of 1.8 meter long pipe (radius = 0.05 m). A finer mesh is used for the first 0.2 meters with extruded layers making up the remainder of the pipe.

The specific geometry employed, shown in Fig. 3-2, is a straight pipe with length $L = 1.8\,m$ with a circular cross section of radius $r = 0.05\,m$. While STH codes like TRACE only need a cross-section averaged velocity for the boundary condition, a CFD code needs a velocity profile instead. When a uniform velocity profile is applied at the inlet of a channel, stronger velocity gradients near the inlet result, whereas streamwise gradients vanish as the flow develops along

the pipe. If a fully developed velocity profile is applied at the inlet of a channel, this profile will propagate unchanged along the pipe axis. All the CFD pipes in the section employ flat inlet profiles.

In order to correctly model the development of the velocity profile along the pipe axis in case c), the first $0.2\,m$ of the CFD computational domain is relatively finely meshed, while the remainder of the pipe is meshed coarsely in the axial direction (see Fig. 3-2).

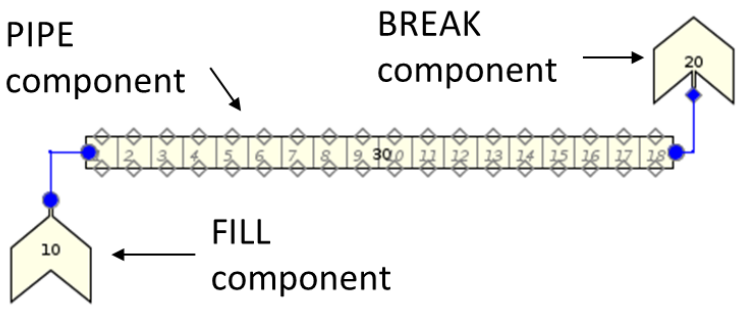

Fig. 3-3. Sample TRACE model of 1.8m pipe with imposed inlet velocity (Fill component) and outlet pressure boundary conditions (Break component).

The TRACE model of the 1.8m pipe, shown in Fig. 3-3, consists of 18 cells of equal length (i.e. $\Delta z = 0.1\,m$) long and the full $1.8\,m$ pipe is composed of 18 cells. A case with imposed inlet velocity and outlet pressure boundary conditions is first examined, followed by one with imposed inlet and outlet pressures as boundary conditions.

3-3 Imposed Mass Flow Rate

In the first set of verification cases, a mass flow boundary condition is placed at the inlet of the pipe and a pressure boundary condition is the outlet. In this configuration, the flow throughout the system is entirely driven by the mass flow boundary condition. For comparison, three standalone simulations of the entire system were calculated using a) the STH code TRACE, b) the CFD code STAR-CCM+ using uniform inlet profiles, and c) STAR-CCM+ using fully developed inlet profiles.

Fig. 3-4 shows pressure drops calculated across the straight pipe in case (a) to (c) for different inlet mass flow-rates. Both flat and fully developed profiles were used at the inlet for the CFD software. Since the TRACE formulation is based on the assumption of fully developed flow, the TRACE stand-alone results agree well with the results obtained with STAR-CCM+ when a fully developed velocity-profile is imposed at the inlet. As expected, a higher pressure drop is produced by the CFD code when a uniform inlet velocity profile is imposed.

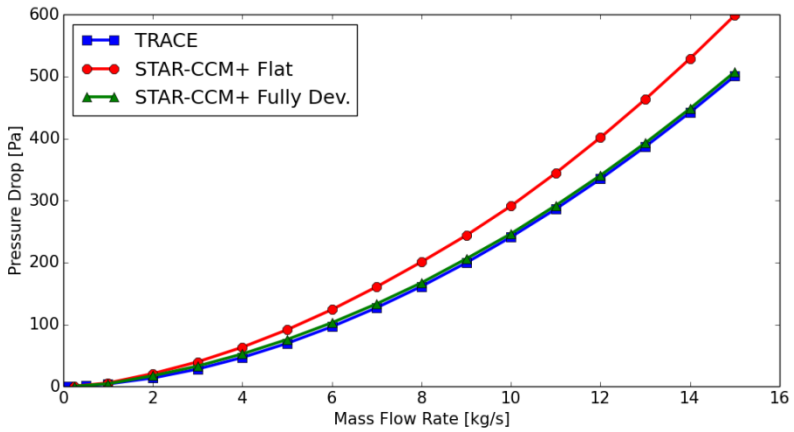

Fig. 3-4. Standalone relationships between mass flow rate and pressure drop as calculated by standalone TRACE with fully developed flow and STAR-CCM+ with both undeveloped and fully developed flow.

Because of the staggered grid arrangement in TRACE, the pressure across the STH pipe domain corresponds in reality to the pressure difference between the center of the inlet fill and outlet break components. Since pressures are not defined at cell edges in TRACE, these quantities must be interpolated in order to compare consistently with the CFD results.

3-3.1 Domain decomposition coupling results – ST mode

The configuration of the coupled run using domain decomposition coupling is depicted in Fig. 3-5. The first half of the pipe is modeled in STAR-CCM+, while the second half is modeled using TRACE. This configuration is referred to as "ST", shorthand for STAR-CCM+/TRACE, indicating that the CFD code is upstream of the STH component. The two regions are connected by a surface interface that passes the CFD outlet mass flow rate to a fill component in TRACE. In the reverse direction, the pressure at the cell center adjacent to the fill component is passed to the CFD outlet as a low-order estimate of the interface pressure. A uniform velocity profile is imposed at the inlet of the CFD domain.

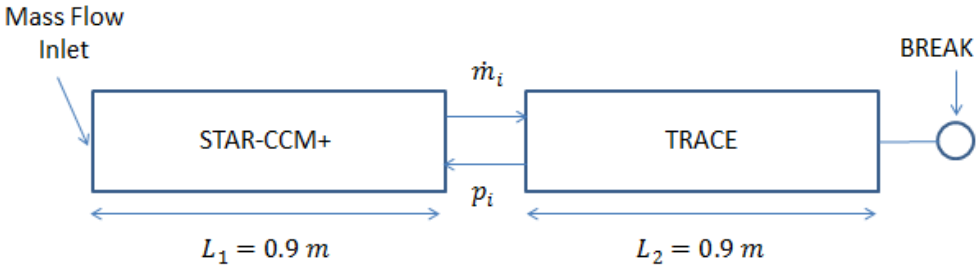

Fig. 3-5. Schematic diagram of domain decomposition test case for imposed mass flow rate in ST configuration.

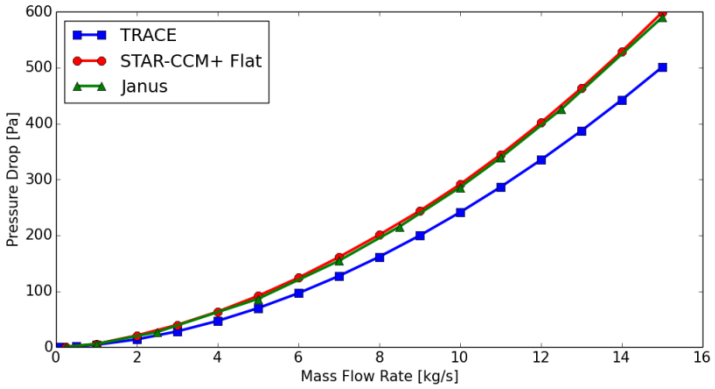

Fig. 3-6. Steady state results for domain decomposition coupling test case compared to standalone reference values.

Results for this test case are shown in Fig. 3-6, where it is noted that the Janus (coupled TRACE/STAR-CCM+) results closely follow the STAR-CCM+ standalone results. This is because most of the additional pressure losses that make up the difference between stand-alone TRACE and STAR-CCM+ predictions are incurred as the flow progresses through the first half of the pipe where the velocity profile develops. However, Janus does tend to under-predict the pressure drop slightly because the length of the CFD component is not sufficient to entirely capture the effects of the developing flow.

Table 3-1. State of each program for each iteration during a coupled simulation.

	STAR-CCM+		TRACE	
Iteration	p_{in}	$\dot{m}$	p_{in}	$\dot{m}$
0	$\Delta p_{CFD}(\dot{m}_{CFD,0}) + p^{out}_{CFD,0}$	$\dot{m}_{CFD,0}$	$\Delta p_{TRC}(\dot{m}_{TRC,0}) + p^{out}_{TRC,0}$	$\dot{m}_{TRC,0}$
1	$\Delta p_{CFD}(\dot{m}_{CFD,0}) + \Delta p_{TRC}(\dot{m}_{TRC,0}) + p^{out}_{TRC,0}$	$\dot{m}_{CFD,0}$	$\Delta p_{TRC}(\dot{m}_{CFD,0}) + p^{out}_{TRC,0}$	$\dot{m}_{CFD,0}$
2	$\Delta p_{CFD}(\dot{m}_{CFD,0}) + \Delta p_{TRC}(\dot{m}_{CFD,0}) + p^{out}_{TRC,0}$	$\dot{m}_{CFD,0}$	$\Delta p_{TRC}(\dot{m}_{CFD,0}) + p^{out}_{TRC,0}$	$\dot{m}_{CFD,0}$

Due to the simplicity of this case, coupled simulations exhibited very favorable stability and convergence characteristics. The details of the coupled simulation are laid out in Table 3-1 where $\Delta p_{TRC}(\dot{m})$ is the pressure drop across the TRACE component induced by a mass flow rate of $\dot{m}$, $\Delta p_{CFD}(\dot{m})$, is the same quantity for STAR-CCM+, $\dot{m}_{CFD,0}/p^{out}_{CFD,0}$ are the mass flow/outlet pressure initial conditions for STAR-CCM+, and $\dot{m}_{TRC,0}/p^{out}_{TRC,0}$ are the same for TRACE. Before any data transfer, at the 0^{th} iteration, both codes are simply initialized with their initial conditions. At the next iteration, the pressure at the inlet of TRACE is passed to STAR-CCM+ and the CFD flow rate is passed to TRACE. At this point the mass flow rate though the system converged, but STAR-CCM+ does not yet have the correct interface pressure. On the 2nd iteration, the CFD segment has the correct interface pressure and the system is fully converged.

3-3.2 Domain decomposition coupling results - TS mode

An imposed mass flow rate coupled case can be performed with TRACE on the upstream side, with the configuration shown in Fig. 3-7. This configuration is referred to as “TS” indicating that the STH code is upstream of the CFD component. The two regions are connected by a surface interface that passes the TRACE outlet mass flow rate to a mass flow inlet boundary in STAR-CCM+. In the reverse direction, the pressure at the surface of the CFD region is passed to a break component that is directly adjacent to the TRACE pipe.

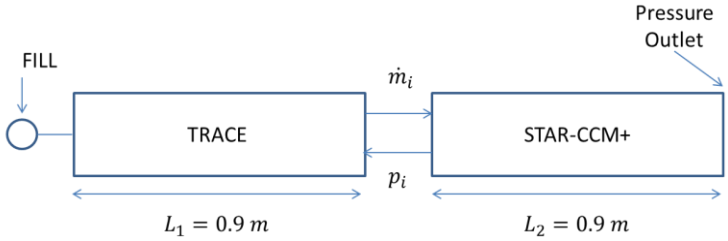

Fig. 3-7. Schematic diagram of pipe with imposed mass flow rate broken into two sections for coupling.

Steady state pressure drops for the TS case are shown in Fig. 3-8 alongside standalone TRACE and STAR-CCM+ data. The coupled results closely match the CFD results with some error resulting from the length of the CFD pipe not fully capturing developing flow effects. This case converges in the same way as was described for the previous system in Table 3-1, with TRACE and STAR-CCM+ switched.

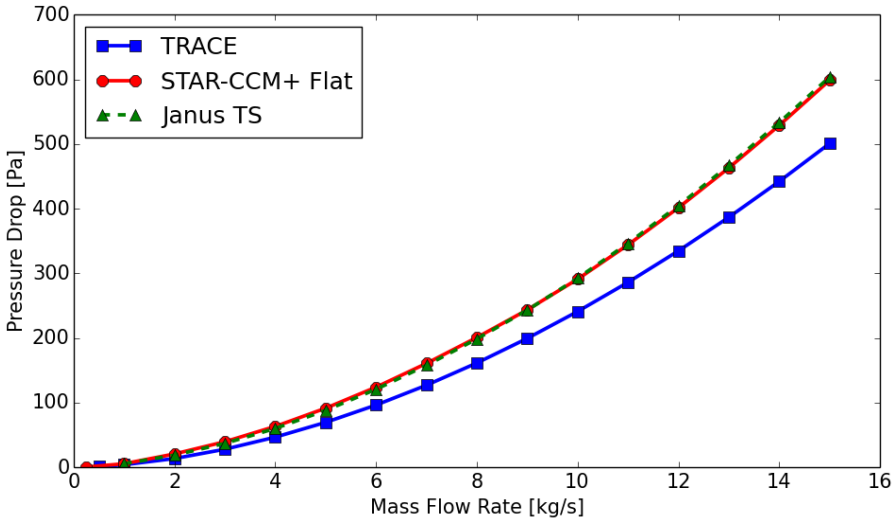

Fig. 3-8. Pressure drop comparison for TS coupling case.

The configuration depicted in Figure 2-7 was then used for a transient scenario. In this case, a transient inlet mass flow rate was applied to the inlet of the pipe:

$$\dot{m}_{in} = \begin{cases} 5.0\frac{kg}{s}, & t < 10.0s, \\ 5.0\frac{kg}{s} + (t - 10.0s)\frac{kg}{s^2}, & 10.0s \leq t \leq 15.0s, \\ 10.0\frac{kg}{s}, & t > 15.0s. \end{cases} \quad 3\text{-}1$$

The resulting pressure drops shown in Fig. 3-9. The pressure drop computed by TRACE standalone under-predicts the reference pressure drop computed by STAR-CCM+ due to the assumption of fully developed flow at the basis of the TRACE formulation. Aside from very near $t = 10s$ and $t = 15s$, the coupled curve matches the STAR-CCM+ results quite well. Small differences are again available because the length of the CFD pipe is not sufficient to capture all effects of developing flow. The error at $t = 10s$ and $t = 15s$ results from the domain decomposition method prevents boundary data communication throughout the entire domain inside a single coupled iteration, causing a delay effect.

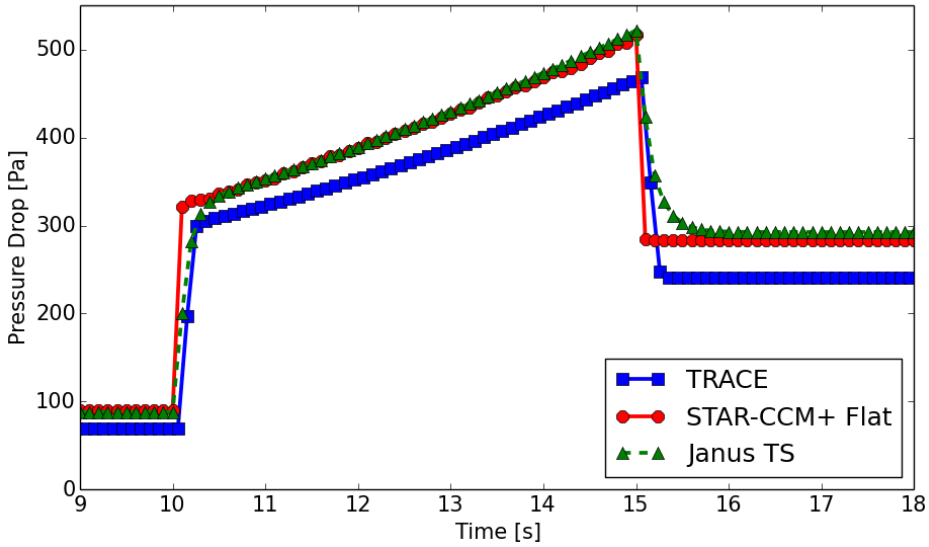

Fig. 3-9. Transient results for domain decomposition coupling test case compared to standalone reference values. Calculated with $\Delta t = 0.1s$.

3-3.3 Domain decomposition coupling results – TST mode

The pipe test case with imposed mass flow rate is next simulated using the coupling configuration depicted in Fig. 3-10, where the CFD domain interfaces with two separate STH domains. This configuration is denoted "TST" and uses two surface interfaces to couple the three segments. From left to right, the first interface passes the mass flow rate from a TRACE break component to a mass flow inlet in STAR-CCM+. The second interface passes the mass flow rate from the STAR-CCM+ outlet to the fill component attached to the final TRACE segment. A mass flow rate BC is applied to the inlet of the first TRACE pipe segment, while a pressure BC is imposed to the outlet of the second TRACE pipe segment.

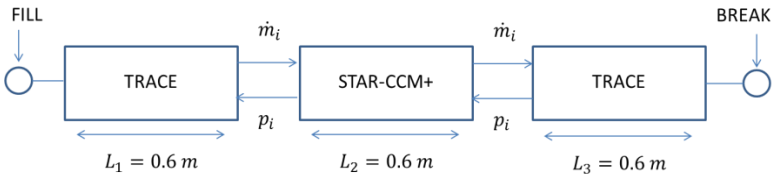

Fig. 3-10. Schematic diagram of pipe with imposed mass flow rate broken into three sections for domain decomposition coupling.

Steady state pressure drops for the TST case are shown in Fig. 3-11 alongside standalone TRACE and STAR-CCM+ data. Convergence for this case proceeds similarly to that described in Table 3-1, but the presence of an additional segment further delays the mass flow communication to the rightmost component of Fig. 3-10 and the subsequent interface pressure to the leftmost component. The overall pressure drop across the entire pipe domain computed by the TST coupling is slightly lower than the STAR-CCM+ stand-alone results because a smaller segment of the pipe is modeled by the CFD code and is insufficient to fully capture developing flow effects.

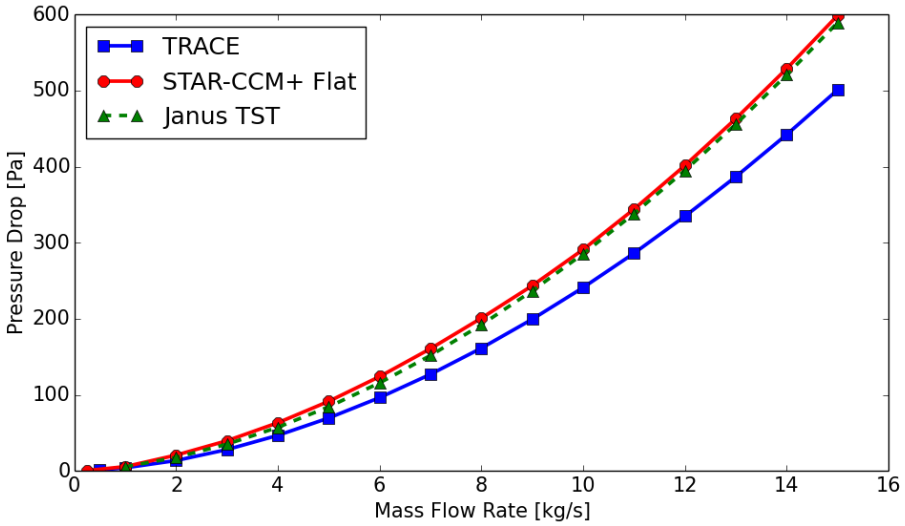

Fig. 3-11. Pressure drop comparison for TST coupling case.

For a transient test case, the inlet mass flow rate of Eq. **Error! Reference source not found.** was pplied to the inlet of the pipe, and the resulting pressure drops are shown in Fig. 3-12. Similar to the steady state results reported in Fig 2-11, the pressure drop predicted by TRACE is lower than the STAR-CCM+ standalone results.

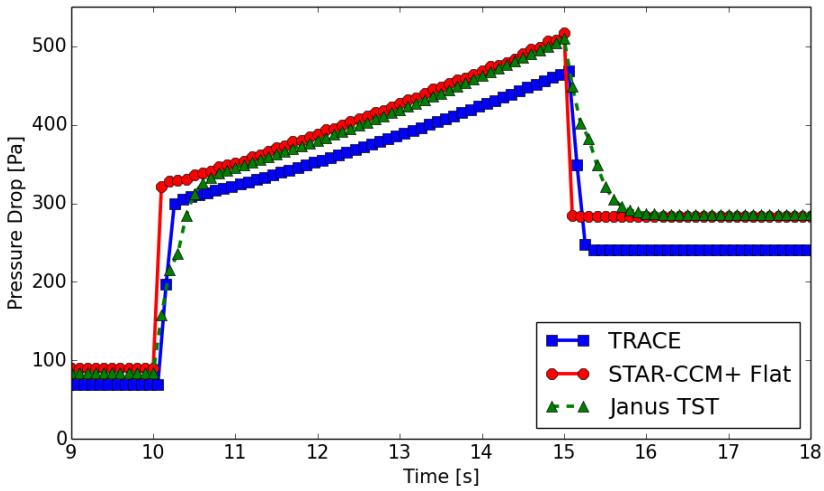

Fig. 3-12. Transient results for domain decomposition coupling test case compared to standalone reference values. Calculated with $\Delta t = 0.1s$.

3-4 Imposed Pressure Drop

For a second set of verification cases, a reference pressure boundary condition p_{out} is imposed at the pipe outlet and an inlet pressure $p_{in} > p_{out}$ is imposed at the pipe inlet. In this configuration, the flow-rate in the pipe is the result of the imposed pressure gradient. Unlike in §3-3, the pressure drop calculated by each code affects the flow rate, and therefore more coupling iterations are expected to be necessary to achieve convergence of the coupled solution. Once again, uniform velocity and turbulence profiles are used at the STAR-CCM+ inlet. A STAR-CCM+ pipe with flat velocity and imposed pressure drop is not a well-posed problem, due to the formulation of the "Pressure Outlet" BC, and transient results for such a case were not calculated. A discussion transient performance of the following simulation is deferred until §3-4.3.

3-4.1 Domain decomposition coupling results – TS mode

The TS configuration for the imposed pressure drop test case is shown in Fig. 3-13. An inlet pressure boundary condition is specified with a TRACE break component, while an outlet pressure boundary condition is specified with a pressure outlet boundary in STAR-CCM+. The results obtained with the coupled code Janus are again compared to standalone TRACE and STAR-CCM+ results, reported in Fig. 3-14.

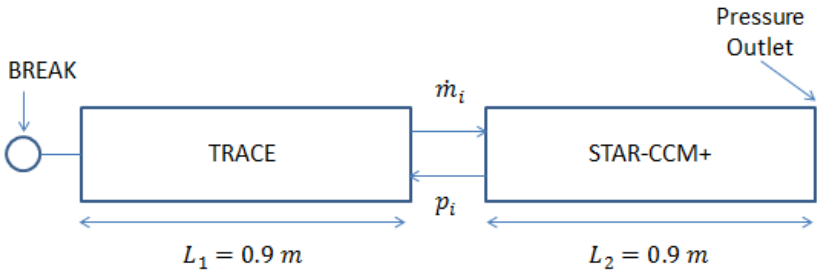

Fig. 3-13. Schematic diagram of pipe with imposed pressure drop broken into two sections for coupling.

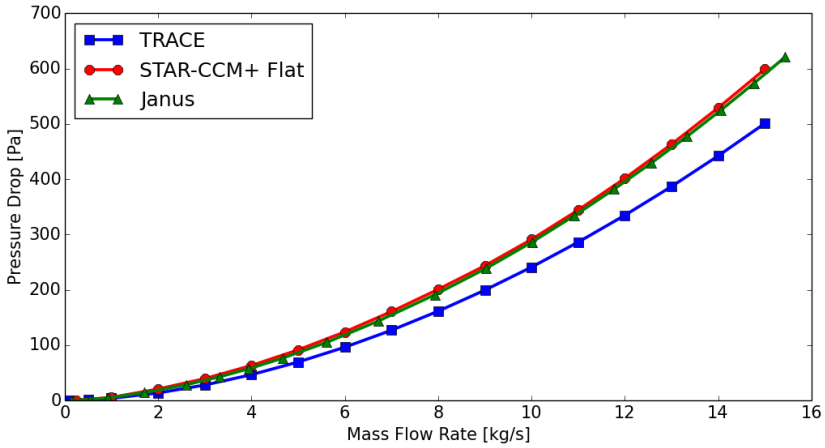

Fig. 3-14. Pressure drop vs. mass flow rate through a 1.8m pipe as calculated with TRACE, STAR-CCM+, and a domain decomposition coupling method.

The results are consistent with what was obtained for the imposed mass flow-rate test case. However, convergence required significantly more iteration steps. Under-relaxation was necessary to obtain converged solutions. Specifically, Eq. 3-2 is applied to data being transferred between the two codes to assist convergence.

$$q_{passed} = urf \times q_{new} + (1 - urf) \times q_{old}. \qquad 3\text{-}2$$

where q is the variable being passed, either mass flow rate or pressure, and urf is the under-relaxation factor, $0 < urf \leq 1.0$. Data passed during a sample coupled simulation are shown in Fig. 3-15. The top figure shows the mass flow rate passed from TRACE to STAR-CCM+, while the bottom figure shows the interface pressure passed from STAR-CCM+ to TRACE. The case with an under-relaxation factor of 0.8 shows significant oscillations in both quantities. Optimal convergence appears to require considerable under-relaxation between 0.2 and 0.5.

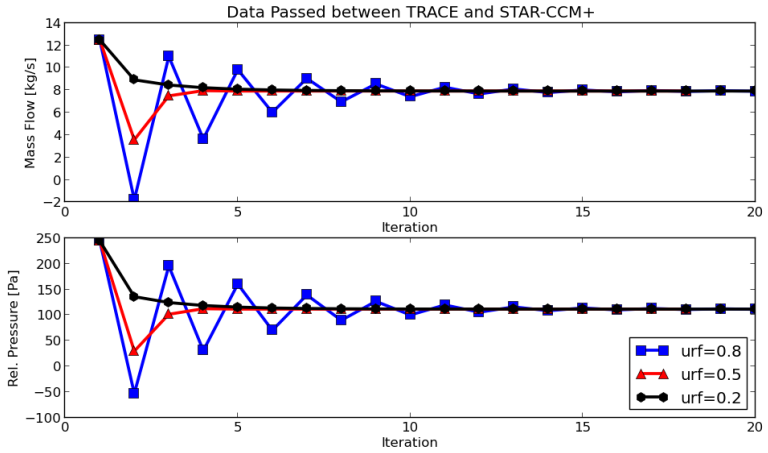

Fig. 3-15. Data passed during domain decomposition coupled simulation. (TOP) mass flow rate passed from TRACE to STAR-CCM+. (BOTTOM) interface pressure passed from STAR-CCM+ to TRACE.

3-4.2 Domain decomposition coupling results – TST mode

The imposed pressure drop test case is next calculated with the TST coupling configuration illustrated in Fig. 3-16.

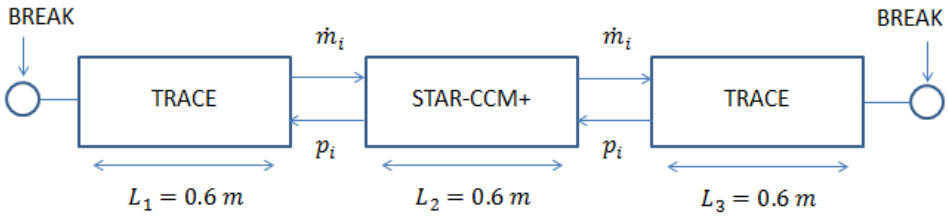

Fig. 3-16. Schematic diagram of coupling scheme using two surface interfaces for a single pipe.

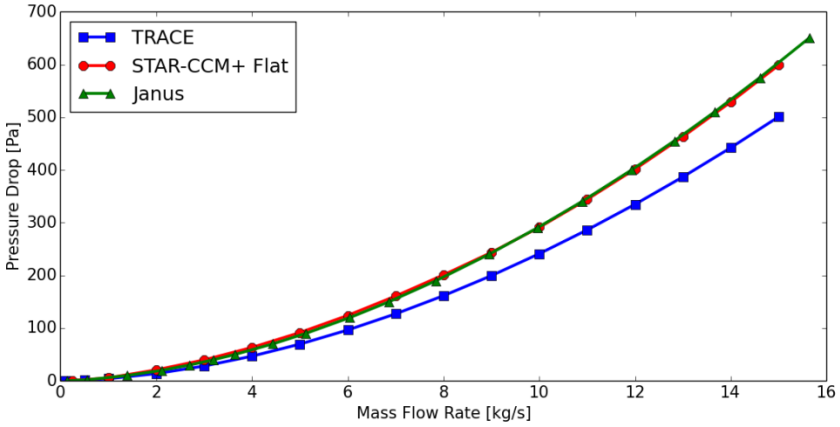

Fig. 3-17. Steady state results for the relationship between pressure drop and mass flow rate for the case of a pipe simulated with three separate segments.

Results from this test case are plotted alongside standalone data in Fig. 3-17. Once more, the coupled data overlay the STAR-CCM+ data quite well. The presence of two mutually dependent interfaces slows convergence significantly and under-relaxation was again needed to achieve a converged solution. An under-relaxation factor (Eq. 3-2) was applied to the data passed from TRACE to STAR-CCM+.

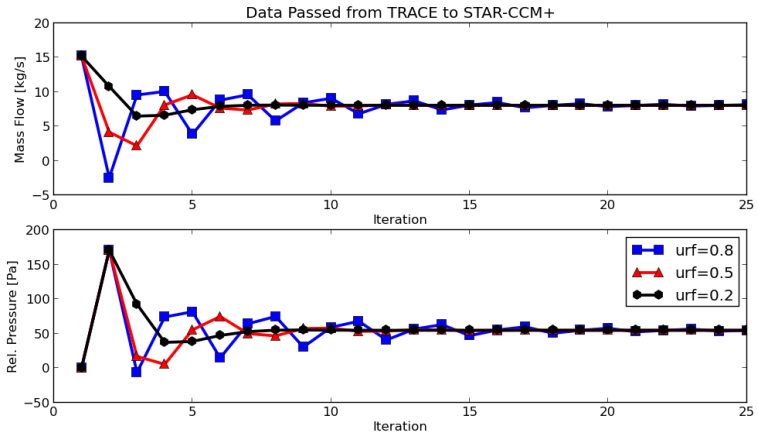

Fig. 3-18. Record of data passed through Janus over the course of steady state iteration as calculated with three selected under-relaxation factors.

Fig. 3-18 shows the progress of coupled iteration for three under-relaxation factors. Once again, significant under-relaxation is required to achieve convergence. The coupled case with $urf = 0.2$ calculated the converged interface values in the fewest iterations.

3-4.3 Transient Comparison

Finally, the imposed pressure drop case is executed using a time dependent pressure drop across the pipe. The pipe outlet pressure was held at a constant value of $10^5 Pa$ ($0Pa$ relative pressure), while the pipe inlet pressure was given by Eq. 3-3:

$$p_{in}(t) = \begin{cases} 1.001 \times 10^5 Pa, & t \leq 5.0s, \\ 10^5 Pa + 100.0\left[1 + \sin^4\left(\dfrac{t - 5.0s}{10.0\ s}\pi\right)\right] Pa, & 5.0\ s < t < 15.0s, \\ 1.001 \times 10^5 Pa, & t \geq 15.0s. \end{cases} \qquad 3\text{-}3$$

The computational results are shown in Fig. 3-19 for both the TS and TST cases, along with reference cases from both TRACE and STAR-CCM+ stand-alone results. The coupled cases produced lower mass flow rate because of the flat inlet profiles of velocity and turbulence quantities. The TST case features the shortest CFD component and hence most under-predicts developing flow effects, resulting in a higher mass flow rate for this case. As was stated

previously, it is not straightforward to perform a CFD simulation with a time-dependent imposed pressure drop, due to the formulation of “Pressure Outlet” BCs.

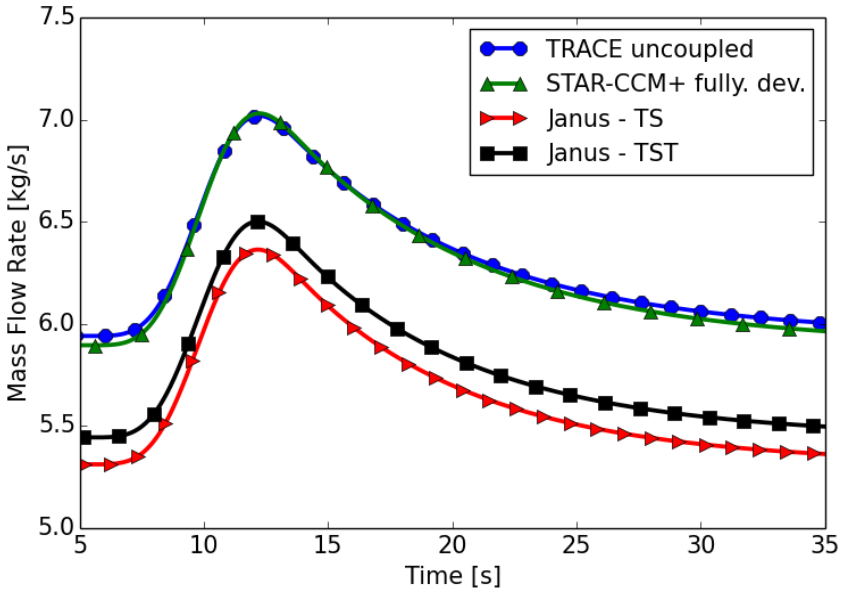

Fig. 3-19. Time dependent mass flow rates for domain decomposition coupling under imposed pressure drop.

3-5 Conclusions

In this section, the basic theory of domain decomposition coupling was laid out and the Janus implementation was verified with simple pipe test cases. The coupling is realized through so-called “surface interfaces” that connect STAR-CCM+ surface boundaries, such as mass flow inlets or pressure outlets to TRACE boundary condition components, such as the fill and break. Coupled simulations were found to match the analogous STAR-CCM+ standalone simulations in both steady state and transient scenarios.

The convergence of the coupling was found to depend strongly on the physics of the overall simulation. For example, cases with imposed mass flow rates achieved convergence in just a few iterations. Cases with an imposed pressure drop required a higher number of iterations as well as under-relaxation to achieve convergence because of the strong coupling between the pressure and the velocity field.

Chapter 4. 1-D Domain Overlapping Development, Implementation, and Verification

In this chapter, the fundamentals of the domain overlapping coupling algorithm developed within this dissertation are established. Similar to the approach taken with the domain decomposition method discussed in the previous section, verification studies are carried out in 1-D pipe geometries allowing for efficient calculations and a clear characterization of the coupling behavior. The theoretical framework discussed in this chapter has been developed for the on-the-fly correction of the TRACE momentum equation based on CFD data. In transients, the effects of time-varying velocities on the pressure gradient can be substantial. These effects are present in both CFD and STH codes, and passing CFD pressure gradient data without inertial adjustment will result in an over-estimation of these transient effects. Two inertial correction approaches are laid out in §4-4 and §4-6, with the second method being the primary focus. The domain overlapping method is then applied to a number of simulations similar to those analyzed in Chapter 2. Rudimentary comparisons begin to show the benefits of domain overlapping coupling over domain decomposition methods. A more rigorous analysis of these benefits is deferred to Chapter 5.

4-1 Domain Overlapping Approach

In the domain overlapping coupling paradigm, the entire flow domain is simulated with the system code, while a selected portion of the domain is also simulated with the CFD code. The codes are then volumetrically coupled in the overlapped region. The system code (TRACE) solution is corrected internally, based on data from the CFD code (STAR-CCM+). A properly validated CFD model is therefore a prerequisite to the appropriate application of this, or any, coupling algorithm.

A simplified version of the one-dimensional equation of motion implemented in TRACE is given in Eq. **Error! Reference source not found.**:

$$\frac{V_{j+1/2}^{n+1} - V_{j+1/2}^{n}}{\Delta t} + V_{j+1/2}^{n} \left.\frac{\partial V^{n+1}}{\partial x}\right|_{j+1/2} = -\frac{1}{\langle\rho\rangle_{j+\frac{1}{2}}^{n}} \frac{p_{j+1}^{n+1} - p_{j}^{n+1}}{\Delta x} - K_{j+\frac{1}{2}}^{n} \left[2V_{j+\frac{1}{2}}^{n+1} - V_{j+\frac{1}{2}}^{n}\right] \left|V_{j+\frac{1}{2}}^{n}\right|. \qquad 4\text{-}1$$

Here the superscript n refers to the old time step solution, $(n+1)$ to the new time step, $V_{j+1/2}^{n+1}$ refers to the velocity at the new time step defined at the edge between cells j and $j+1$, while $\langle\rho\rangle_{j+\frac{1}{2}}^{n}$ refers to the average liquid density between nodes j and $j+1$, p is node-averaged pressure, Δx is the distance between centers of neighboring cells, and $K_{j+1/2}^{n}$ is a coefficient used to model the effects of both form and frictional loss. For the purposes of this study, we focus on the frictional aspect of the coefficient.

Comparison to the Navier-Stokes momentum balance equations shows that the divergence of the stress tensor **T** is modeled as proportional to the square of a velocity:

$$-\frac{\nabla \cdot \mathbf{T}}{\rho} \approx KV^2 = 2f_F \frac{\Delta x}{D_h} V^2. \qquad 4\text{-}2$$

In TRACE, the constant of proportionality is calculated using the Churchill correlation for the Fanning friction factor [16]. Based on this analysis, a CFD-based friction factor, f_{CFD}, can be calculated from the definition of the Fanning friction factor [46], as shown in Eq. 4-3:

$$f_{CFD} = \frac{1}{2} \frac{D_h}{\rho_{TRC} \left(V_{j+1/2}^n\right)^2} \frac{\Delta p_{CFD}^n}{L_{LP}}. \qquad 4\text{-}3$$

The CFD friction factor defined in Eq. 4-3 is computed from the global pressure drop across the CFD component, ΔP_{CFD}. Because this pressure drop includes the convective pressure drop calculated in CFD, the associated term (form loss contribution to K in Eq. **Error! Reference ource not found.**) is eliminated from the TRACE momentum equation coefficients associated only with the coupled (overlapped domain) component. Division by a lumped parameter (LP) length scale L_{LP} yields the average pressure gradient of the overlapped component. The length scale L_{LP} is the length of the component as defined in TRACE and is automatically retrieved from the TRACE input data by the coupling interface. The average pressure gradient is then normalized by the hydraulic diameter (D_h) and the local TRACE values for density (ρ_{TRC}) and old time step velocity ($V_{j+1/2}^n$).

Combining Eqs. **Error! Reference source not found.** through 4-3, for steady state conditions, he pressure drop across the $j + 1/2$ face is calculated as shown in Eq. 4-4. Thus, the pressure drop across an edge (i.e. between adjacent CVs) is simply the total CFD pressure drop scaled down to the correct length for edge $j + 1/2$:

$$\Delta p_{j+1/2} = -\operatorname{sign}\left(V_{j+\frac{1}{2}}\right) \Delta p_{CFD} \left(\frac{\Delta x}{L_{LP}}\right). \qquad 4\text{-}4$$

However, the inertial term of the momentum equation cannot be neglected in transient simulations. The transient pressure drop between node *j* and *j+1* for TRACE is shown in Eq. 4-5, which includes, in addition to the contribution of the CFD pressure drop, an inertial contribution. The CFD pressure drop also includes an inertial contribution, leading to an overestimation of these effects and inconsistency between CFD and STH:

$$\Delta p_{j+1/2} = -\rho \Delta x \frac{V_{j+\frac{1}{2}}^{n+1} - V_{j+\frac{1}{2}}^{n}}{\Delta t} - \Delta x \frac{1}{\left(V_{j+\frac{1}{2}}^{n}\right)^2} \frac{\Delta p_{CFD}^{n}}{L_{LP}} \left(2V_{j+\frac{1}{2}}^{n+1} - V_{j+\frac{1}{2}}^{n}\right) \left|V_{j+\frac{1}{2}}^{n}\right|. \qquad 4\text{-}5$$

Accounting for the inertial contribution in the calculation of coupled friction factors is therefore necessary to maintain transient consistency between the coupled codes. Two approaches were experimented with: one formulated with spatial gradients, as explained in §4-4; and one formulated with temporal derivatives, as discussed in §4-6. In practice, the latter was found to be much more efficient and was used for the majority of the work presented in this dissertation. For completeness, both methods are included.

The acceleration and frictional pressure gradient contributions are easily excluded from the TRACE pressure balance by simply intercepting the appropriate terms in the code, allowing these effects to be aliased onto other terms, namely the friction factor. However, exclusion of the inertial term would essentially prevent TRACE from stepping forward in time. As a result, the coupling methods presented here use a pressure drop from CFD data augmented to exclude the inertial contribution.

4-2 Pressure Gradient Decomposition

Using the Navier-Stokes equations, the pressure gradient can be partitioned into three terms as shown in Eq. 4-6 **Error! Reference source not found.**:

$$\nabla p = -\rho \frac{\partial \mathbf{v}}{\partial t} - \rho \mathbf{v} \cdot \nabla \mathbf{v} + \nabla \cdot \mathbf{T}. \qquad 4\text{-}6$$

The first term on the right, the inertial contribution, results from unsteady velocities. The second term on the right, the convective pressure gradient, results from acceleration due to velocity gradients. Finally, the frictional pressure gradient resulting from viscous dissipation is the third term on the right. For turbulent flow, consider $\mathbf{v}$ to be the Reynolds-averaged velocity and $\mathbf{T}$ to include Reynolds stresses.

Since the coupling is currently limited to regions where the flow is incompressible, it is assumed that the difference between the inertial pressure drops computed by the CFD and STH codes for the overlapped domain is negligible as long as fluid velocities are consistent. Therefore, only the non-inertial pressure drop terms (acceleration and friction) need to be corrected. One approach is to use the CFD data to calculate only the non-inertial contribution to the pressure gradient. This method, referred to as the spatial inertial interface because the terms involve spatial derivatives ($\rho \mathbf{v} \cdot \nabla \mathbf{v}, \nabla \cdot \mathbf{T}$) is discussed in §4-4. The more successful method, the temporal inertial interface, instead subtracts the time-derivative term ($\rho \frac{\partial \mathbf{v}}{\partial t}$) from the total pressure gradient and is discussed in §4-6. In both cases, Δp_{CFD}^{n} in Eq. 4-3 is replaced with an augmented version of the pressure drop.

The remaining discussion in this chapter is restricted to 1-D pipe components. Such test cases provide convenient grounds for establishing proof-of-principle calculations. A more general interface applicable to 3D geometries, such as open regions with recirculation, based on the foregoing development is presented in Chapter 6.

4-3 Global 1-D Coupling

As previously discussed, TRACE applies friction factors at each edge of a component. While it is possible to calculate the factor corresponding to each edge from an accompanying CFD simulation, a "global" coupling approach for 1-D components was deemed expedient. Specifically, the pressure drop across the entire coupled component is used to calculate an average friction factor. The friction factor across every edge of a constant cross section channel is therefore identical. This was deemed consistent with the goals of the coupling because the more complete CFD solution is available, rendering the local TRACE data redundant.

To demonstrate the effects of global 1-D coupling, consider a straight $2.0\,m$ square pipe with $0.1\,m \times 0.1\,m$ cross section. The pipe is broken into 20 equally sized cubic cells with length $0.1\,m$. The pressure profile was calculated for both fully developed and flat inlet profiles. In Fig. 4-1, each curve shows the volume-averaged pressure for each cell, along with the surface average pressure at the inlet and outlet. In addition to the fully developed ("Fully Dev." in Fig. 4-1) and flat ("Flat" in Fig. 4-1) profiles, a linearized form of the flat velocity profile is included ("Lin. Flat" in Fig. 4-1).

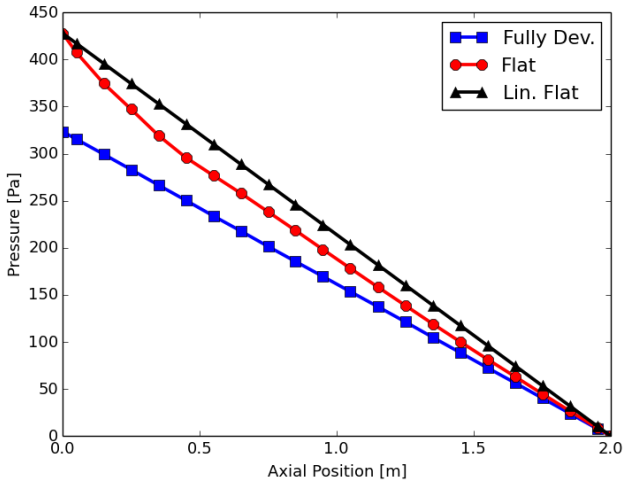

Fig. 4-1. Pressure profiles calculated for 2.0 m square pipe with inlet flow $\dot{m}_{in} = 15.0\frac{kg}{s}$.

The curves show that developing flow incurs a significantly larger pressure drop than a fully developed flow. The "extra" pressure loss occurs near the inlet and exhibits a nonlinear relationship with the ordinate variable. The pressure profile for the fully developed case exhibits a purely linear relationship with the ordinate, as would be expected. Comparing the "Lin. Flat" and "Fully Dev." curves illustrates the effect of global 1-D coupling. Both curves produce the

same total pressure drop, though they differ about individual cell pressures. In general, individual pressure drops throughout 1-D components are not expected to be important to the overall STH system.

4-4 Spatial Inertial Interface

The pressure gradient resulting from non-inertial processes can be directly calculated by neglecting the time derivative term of Eq. **Error! Reference source not found.**, resulting in a ormulation that relies only on spatial derivatives. Interfaces employing this method are therefore referred to as spatial inertial interfaces (SII). In order to map the more finely resolved CFD solution to the coarsely resolved STH grid, the CFD data are averaged over the analogous TRACE volume as shown in Eq. 4-7:

$$\langle \nabla p \rangle_{NI} = \langle \nabla \cdot \mathbf{T} \rangle - \rho \langle \mathbf{v} \cdot \nabla \mathbf{v} \rangle \qquad 4\text{-}7$$

in which the angle brackets denote a volume average, $\langle \cdot \rangle = \frac{1}{V} \iiint_V \cdot \, dV$. The calculation of second derivatives of the velocity field can be avoided by invoking the divergence theorem:

$$\langle \nabla \cdot \mathbf{T} \rangle = \frac{1}{Vol} \iiint \nabla \cdot \mathbf{T} dV = \frac{1}{Vol} \oiint (\mathbf{T} \cdot \mathbf{n}) dS. \qquad 4\text{-}8$$

If the geometry of a specific test case lies entirely along one coordinate, the proper pressure gradient can be calculated simply by dotting the previous expression with the proper unit vector. For example, the friction factor for a geometry aligned along the z direction would be computed with Eq. 4-9:

$$f_{CFD} = \frac{1}{2} \frac{D_h}{\rho_{TRC} \left(V^n_{j+1/2} \right)^2} \left[\frac{1}{Vol} \oiint (\mathbf{T} \cdot \mathbf{n}) \cdot \hat{\mathbf{e}}_\mathbf{z} dS - \frac{1}{Vol} \iiint \rho (\mathbf{v} \cdot \nabla \mathbf{v}) \cdot \hat{\mathbf{e}}_\mathbf{z} dV \right]. \qquad 4\text{-}9$$

Consider a flow path vector field $\hat{\boldsymbol{n}}_{fp}$ that, for 1-D flow, indicates the direction of mean flow across each cross section. For example, in axial flow $\hat{\boldsymbol{n}}_{fp} = \hat{z}$. This vector field is not directly extensible to 3-D geometries where a more sophisticated approach is required. Using this, a slightly different quantity is calculated in Eq. 4-10 that is valid for pipes with changes in flow direction.

$$\langle \nabla p \cdot \hat{\boldsymbol{n}}_{fp} \rangle^{1D}_{NI} = \langle (\nabla \cdot \overline{\overline{\mathbf{T}}}) \cdot \hat{\boldsymbol{n}}_{fp} \rangle - \rho \langle \mathbf{v} \cdot \left(\hat{\boldsymbol{n}}_{fp} \cdot \nabla \mathbf{v} \right) \rangle \qquad 4\text{-}10$$

The stress tensor is split into two parts in order to allow application of the divergence theorem in Eq. 4-11:

$$\frac{1}{V}\iiint (\nabla \cdot \bar{\bar{\mathbf{T}}}) \cdot \hat{\boldsymbol{n}}_{fp} dV = \frac{1}{V}\iiint \left[\boldsymbol{\nabla} \cdot \left(\mathbf{T} \cdot \hat{\boldsymbol{n}}_{fp}\right) - \mathbf{T} : \nabla \hat{\boldsymbol{n}}_{fp}\right] dV$$
$$= \frac{1}{V}\oiint \left[\left(\mathbf{T} \cdot \hat{\boldsymbol{n}}_{fp}\right) \cdot \mathbf{n}\right] dS - \frac{1}{V}\iiint \left[\mathbf{T} : \nabla \hat{\boldsymbol{n}}_{fp}\right] dV. \qquad \textit{4-11}$$

The volume-averaged non-inertial pressure gradient is then calculated with Eq. 4-12:

$$\langle \nabla p \cdot \hat{\boldsymbol{n}}_{fp} \rangle_{NI}^{1D} = \frac{1}{V}\oiint \left[\left(\mathbf{T} \cdot \hat{\boldsymbol{n}}_{fp}\right) \cdot \mathbf{n}\right] dS - \frac{1}{V}\iiint \mathbf{T} : \nabla \hat{\boldsymbol{n}}_{fp} dV$$
$$- \frac{1}{V}\iiint \rho \mathbf{v} \cdot \left(\hat{\boldsymbol{n}}_{fp} \cdot \nabla \mathbf{v}\right) dV. \qquad \textit{4-12}$$

This expression can be cast into a form more convenient for implementation by expanding the surface integral of the shear stress into contributions from different boundary types, as shown in Eq. 4-13:

$$\oiint \left[\left(\mathbf{T} \cdot \hat{\boldsymbol{n}}_{fp}\right) \cdot \mathbf{n}\right] dS = \iint_{wall} \left[\left(\mathbf{T} \cdot \hat{\boldsymbol{n}}_{fp}\right) \cdot \mathbf{n}\right] dS + \iint_{other} \left[\left(\mathbf{T} \cdot \hat{\boldsymbol{n}}_{fp}\right) \cdot \mathbf{n}\right] dS$$
$$= \iint_{wall} \left[\boldsymbol{\tau_w} \cdot \hat{\boldsymbol{n}}_{fp}\right] dS + \iint_{other} \left[\left(\mathbf{T} \cdot \hat{\boldsymbol{n}}_{fp}\right) \cdot \mathbf{n}\right] dS, \qquad \textit{4-13}$$

where $\boldsymbol{\tau_w}$ is the wall shear stress. The second contribution to the stress tensor relates to non-wall boundaries such as inlets, outlets, symmetry planes, etc. For most situations, the wall contribution would be expected to dominate this integral, potentially allowing for the remaining boundary contributions to be neglected. The total volume-averaged non-inertial pressure gradient is thus given in Eq. 4-14. This non-inertial gradient can then be normalized to calculate the coupled friction factor:

$$\langle \nabla p \cdot \hat{\boldsymbol{n}}_{fp} \rangle_{NI}^{1D} = \frac{1}{V}\iint_{wall} \left[\boldsymbol{\tau_w} \cdot \hat{\boldsymbol{n}}_{fp}\right] dS + \frac{1}{V}\iint_{other} \left[\left(\mathbf{T} \cdot \hat{\boldsymbol{n}}_{fp}\right) \cdot \mathbf{n}\right] dS$$
$$- \frac{1}{V}\iiint \mathbf{T} : \nabla \hat{\boldsymbol{n}}_{fp} dV - \frac{1}{V}\iiint \rho \mathbf{v} \cdot \left(\mathbf{n}_{fp} \cdot \nabla \mathbf{v}\right) dV. \qquad \textit{4-14}$$

4-5 Double Elbow Test Case

A double elbow test case, displayed in Fig. 4-2, was designed to induce strong velocity gradients with a curved flow path and to verify the SII formulation of Eq. 4-14. A representation of the flow path vector field $\hat{\boldsymbol{n}}_{fp}$ pointing from the inlet to the outlet is shown on the left of the figure, with dimensions shown on the right. The geometry is asymmetric, with the distance between the outlet and the bends larger than the distance between the inlet and the bends. Small buffer sections are present between the inlet/outlet boundaries and the region of interest.

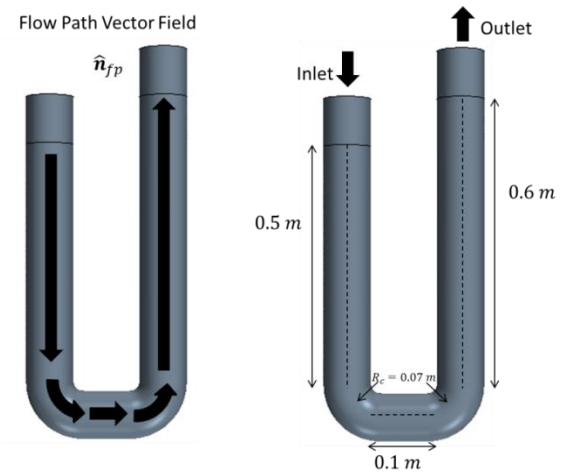

Fig. 4-2. Double elbow test case used for verification of SII. (LEFT) Flow path vector field near the bends. (RIGHT) STAR-CCM+ geometry with annotated dimensions.

4-5.1 Steady State Results

In order to test the SII formulation in steady state mode, the inlet mass flow rate of the geometry in Fig. 4-2 was varied and the pressure drop between the bounding surfaces of the region of interest was recorded as output. The non-inertial pressure drop was calculated by multiplying the volume-averaged non-inertial pressure gradient of Eq. 4-14 and the total centerline track length of the geometry. Because the flow is steady state, the inertial contribution to the pressure drop vanishes, and the total pressure drop equals the non-inertial pressure drop, shown on the left of Fig. 4-3. The pressure drop calculated from Eq. 4-14 ("SII Est." in Fig. 4-3) is shown to match closely with the value calculated from surface averages ("STAR-CCM+" in Fig. 4-3) over a wide range of flow rates. The error calculated with Eq. 4-15 is shown on the right of the figure:

$$\%Error = \frac{\Delta p_{SII} - \Delta p_{CCM}}{\Delta p_{CCM}} \times 100\%. \qquad 4\text{-}15$$

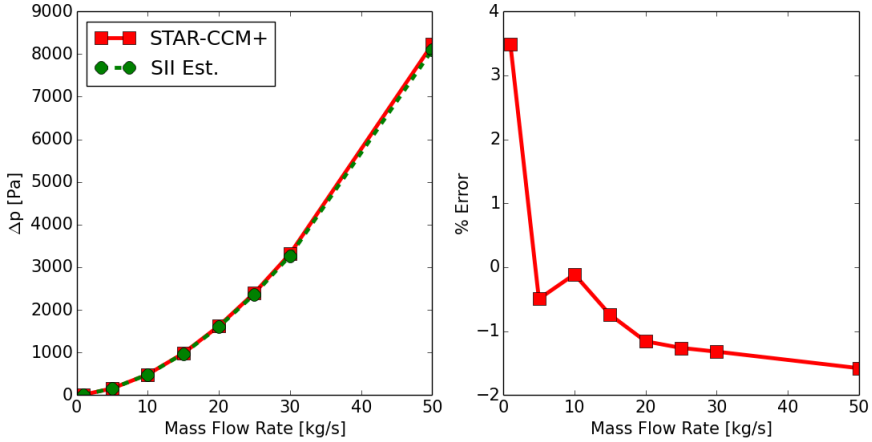

Fig. 4-3. (LEFT) Steady state pressure drops for double elbow verification case. (RIGHT) Error in the estimated spatially-calculated pressure drop.

A decomposition of the SII-calculated pressure drop into four normalized contributions based on Eq. 4-14 is shown in Fig. 4-4. The largest contributions are the wall shear term ("wsFrac") and the convective acceleration term ("vdvFrac"), with the remaining terms only making up a few percent of the pressure drop. For this test case, each contribution accounts for an approximately constant share of the pressure drop over a wide range of mass flow rates. The term resulting from non-wall boundaries ("inoutFrac") and the colon product with the flow path vector ("addFrac") are on the order of error and could potentially be neglected in a simplified implementation.

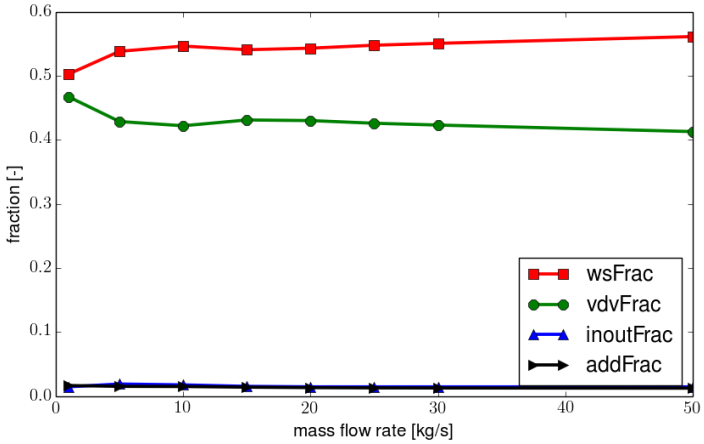

Fig. 4-4. Fractional contributions to steady state pressure drops for the double elbow verification case. Wall shear contribution (wsFrac): first term on right of Eq. 4-13. Convective acceleration term (vdvFrac): fourth term on right. Non-wall boundary term (inoutFrac): second term on right. Colon product term (addFrac): third term on right.

4-5.2 Transient Results

In order to test the transient behavior of the SII, the time-dependent inlet mass flow rate of Eq. **Error! Reference source not found.** was applied to the inlet:

$$\dot{m}(t) = \begin{cases} 10.0\dfrac{kg}{s}, & t \leq 1.0s, \\ 10.0\left[1 + \sin^4\left(\dfrac{t - 1.0s}{10.0s}\pi\right)\right]\dfrac{kg}{s}, & 1.0s < t < 11.0s, \\ 10.0\dfrac{kg}{s}, & t \geq 11.0s. \end{cases} \qquad \textit{4-16}$$

The total and non-inertial pressure drops are compared in Fig. 4-5, where inertial effects are clearly noted as the difference between the curves, demonstrating the necessity of calculating non-inertial pressure gradients.

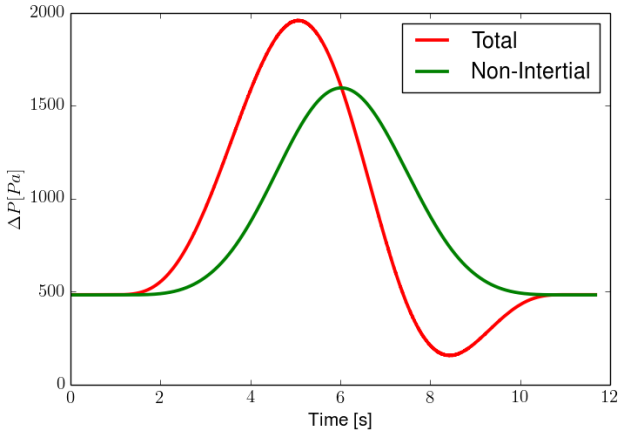

Fig. 4-5. Transient pressure drops for double elbow verification case calculated with a time step of $\Delta t = 1ms$

The non-inertial pressure drop is decomposed in Fig. 4-6, showing that the contribution of each term in Eq. 4-14 follows the shape of the mass flow rate. The wall shear stress term and the convective acceleration term together make up the majority of the pressure gradient, with other terms only contributing a few percent.

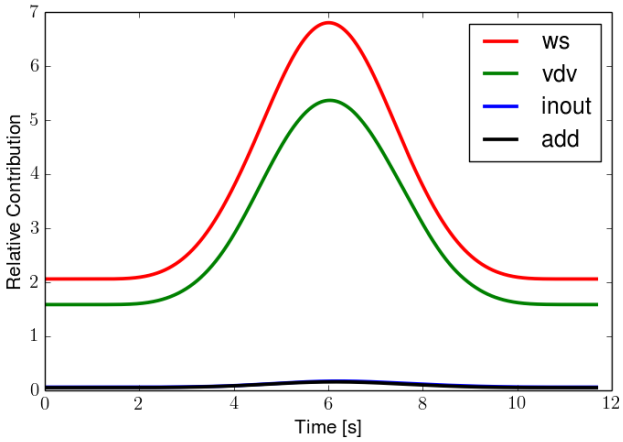

Fig. 4-6. Relative contributions to transient pressure drops for double elbow verification case

4-6 Temporal Inertial Interface

In addition to the SII introduced in §4-4, it is possible to formulate a non-inertial pressure gradient by calculating the total pressure gradient and subtracting the inertial contribution $\left(-\rho\frac{\partial \mathbf{v}}{\partial t}\right)$. Interfaces based on this methodology are referred to Temporal Inertial Interfaces (TII) because inertia-consistent pressure gradients are calculated using temporal, rather than spatial, derivatives. Similar to the procedure used to develop the SII, the non-inertial pressure gradient is dotted with a flow path vector $\hat{\boldsymbol{n}}_{fp}$, as shown in Eq. 4-17:

$$\langle \nabla p \cdot \hat{\boldsymbol{n}}_{fp} \rangle_{NI} = \langle \nabla p \cdot \hat{\boldsymbol{n}}_{fp} \rangle_{tot} - \langle \nabla p \cdot \hat{\boldsymbol{n}}_{fp} \rangle_{I} = \langle \nabla p \cdot \hat{\boldsymbol{n}}_{fp} \rangle_{tot} + \langle \rho \frac{\partial \mathbf{v}}{\partial t} \cdot \hat{\boldsymbol{n}}_{fp} \rangle \qquad 4\text{-}17$$

Once again, this vector field is related to the direction of the mean flow at each cross section and can be user-input or derived from geometric input data available to the STH code for 1-D components. Using this, a friction factor based on CFD data can be defined for the correction of the TRACE momentum equation, given by Eq. 4-18 in which **v** refers to the velocity vector field of the CFD solution:

$$f_{CFD} = \frac{1}{2} \frac{D_h}{\rho_{TRC} \left(V_{j+1/2}^{n} \right)^2} \left[\frac{\Delta p_{CFD}^{n+1}}{L_{LP}} - \frac{1}{\Delta t} \left(\frac{1}{Vol} \iiint \rho \mathbf{v}^{n+1} \cdot \hat{\boldsymbol{n}}_{fp} dV - \frac{1}{Vol} \iiint \rho \mathbf{v}^{n} \cdot \hat{\boldsymbol{n}}_{fp} dV \right) \right]. \qquad 4\text{-}18$$

This friction factor requires evaluation of three integrals at each time step for each coupled component: 1) inlet pressure, 2) outlet pressure, and 3) volume-averaged velocity. The old time (t^n) velocity integral must also be saved from the previous time step. The specific definitions of Δp_{CFD} and L_{LP} are discussed in greater detail in the next section. As a point of clarification, the reader is reminded that Eq. 4-18 is only applicable to pipe geometries in which $\hat{\boldsymbol{n}}_{fp}$ and L_{LP} are easily defined. The extension to cases in which these definitions are not straightforward, such as in 3-D open mixing regions, is discussed in Chapter 6 and Chapter 7.

Comparing the development of the TII to that of the SII in §4-4 suggests that the implementation of the TII is much easier. Additionally, the TII turns out to be more accurate due its formulation in terms of only primary variables (i.e. pressure and velocity) while the SII relies on spatial derivatives, which incur error without sophisticated calculations. The accuracy of SII was briefly touched upon in §4-5 and will be revisited in §6-2 for the 3-D formulation.

4-6.1 Considerations for Domain Overlapping Coupling

A consideration unique to domain overlapping coupling is the treatment of edges between components. Fig. 4-7 illustrates these so-called "connection edges" for a configuration in which a coupled TRACE component is flanked by two uncoupled components. As a design choice, the 1-D domain overlapping volume interfaces only affect edges internal to the coupled component. TRACE handles such edges with a donor approach in which the edge belongs to the downstream component. For example, the first edge from the left in the figure is assigned to the uncoupled component, while the second edge is assigned to the coupled component because the flow is directed from left to right. To account for this, Janus specifically checks if an edge is a connection edge and does not alter the TRACE momentum equation for this edge.

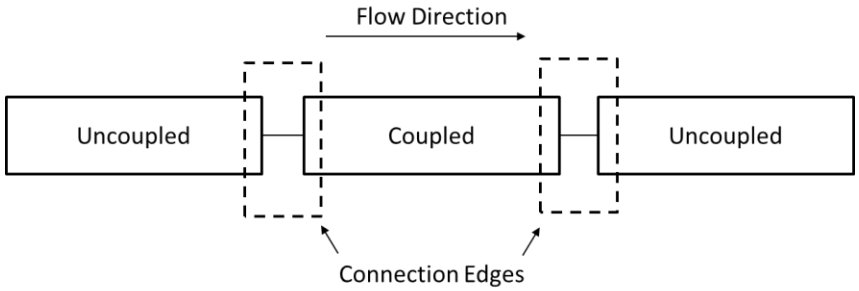

Fig. 4-7. Diagram of theoretical TRACE system illustrating the edges between components for a sample coupling configuration.

In the domain decomposition coupling approach, the interpretation of a coupled simulation as using STAR-CCM+ to replace the test section directly follows from the idea of coupling by boundary conditions data transfer. Essentially, the specific internal solution structure of each code could be ignored, as only boundary values are relevant. The implementation of the 1-D domain overlapping coupling method through so-called "volume interfaces" requires a more subtle interpretation because friction factors have a precise geometric interpretation in TRACE.

As previously discussed, TRACE uses a staggered grid with pressures defined at cell centers and velocities and friction factors defined at cell edges. The STAR-CCM+ pressure analogous to that of a TRACE cell is calculated by volume-averaging the pressure field over a sub-domain that corresponds with the TRACE cell. The diagram in Fig. 4-8 shows representative STAR-CCM+ and TRACE meshes and the pressure drops that are calculated from $\Delta p = p_{in} - p_{out}$, where p_{in} and p_{out} are volume-averages of the pressure field over the indicated regions for STAR-CCM+.

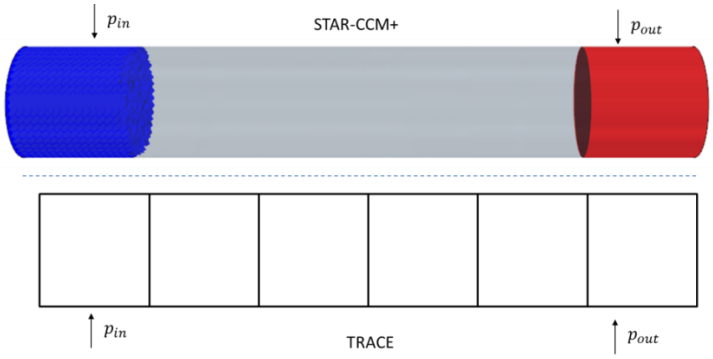

Fig. 4-8. Diagram showing pressure drops definitions in STAR-CCM+ and TRACE for the domain overlapping coupling.

In order to match TRACE's Δp to the CFD results, the lumped parameter length scale L_{LP} in Eq. 4-18 must measure the distance between the *center* of the inlet cell and the *center* of the outlet cell. For a pipe of length L with N cells, and the i^{th} cell has a length of Δx_i, the lumped parameter length scaled is then defined by Eq. 4-19:

$$L_{LP} = \frac{\Delta x_1}{2} + \frac{\Delta x_N}{2} + \sum_{i=2}^{N-1} \Delta x_i. \qquad 4\text{-}19$$

The value of L_{LP} is therefore equivalent to the total pipe length minus the half-cell lengths on each end.

4-7 Imposed Mass Flow Rate

The temporal 1-D domain overlapping method is first tested in systems in which a mass flow boundary condition is placed to the left of the pipe and a pressure boundary condition is set to the right of the pipe.

4-7.1 Full Pipe

First considered is the $1.8m$ long circular pipe shown in Fig. 3-2 and Fig. 3-3. The domain overlapping coupling configuration is given Fig. 4-9. The flow rate through the system is determined by a fill component to the left of the TRACE pipe. Mass flow rate data is passed from TRACE to the mass flow inlet of the CFD pipe. Once STAR-CCM+ receives a mass flow rate, a pressure gradient is calculated and passed to TRACE in the form of friction factors.

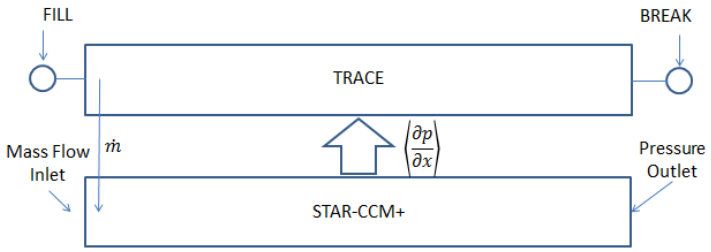

Fig. 4-9. Schematic diagram for domain overlapping coupling setup with imposed mass flow rate.

Data from this test care are displayed in Fig. 4-10. Once again, the pressure drops calculated with the volume interface collapse onto the standalone CFD results. Because the mass flow rate through the pipe is imposed through boundary conditions, convergence happens practically immediately. Even with poor initial conditions, STAR-CCM+ receives the correct mass flow rate from TRACE at the first data exchange. Then, STAR-CCM+ calculates the pressure drop across the pipe and passes the smeared pressure gradient to TRACE at the second data exchanged. Once the TRACE solver runs with the new friction factors, no further iteration is needed, provided that sufficient inner iterations have been performed for each code. An example of the iteration process is shown in Table 4-1,

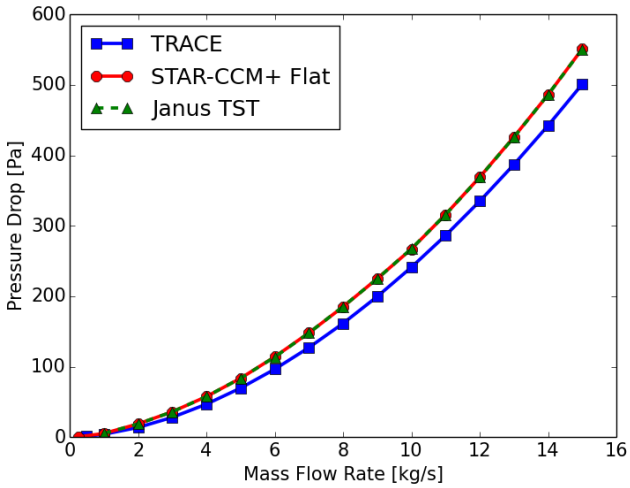

Fig. 4-10. Steady state pressure drop results for domain overlapping full pipe test case with imposed mass flow rate.

Table 4-1. Behavior of coupled cases as iteration proceeds.

	TRACE		STAR-CCM+	
Iteration	Δp	$\dot{m}$	Δp	$\dot{m}$
0	$\Delta p_{TRC}(\dot{m}_{TRC,0})$	$\dot{m}_{TRC,0}$	$\Delta p_{CFD}(\dot{m}_{CFD,0})$	$\dot{m}_{CFD,0}$
1	$\Delta p_{CFD}(\dot{m}_{CFD,0})$	$\dot{m}_{TRC,0}$	$\Delta p_{CFD}(\dot{m}_{TRC,0})$	$\dot{m}_{TRC,0}$
2	$\Delta p_{CFD}(\dot{m}_{TRC,0})$	$\dot{m}_{TRC,0}$	$\Delta p_{CFD}(\dot{m}_{TRC,0})$	$\dot{m}_{TRC,0}$

where $\Delta p_{TRC}(\dot{m})$ is the pressure drop across the TRACE component induced by a mass flow rate of $\dot{m}$, $\Delta p_{CFD}(\dot{m})$, is the same quantity for STAR-CCM+, $\dot{m}_{CFD,0}$ is the mass flow initial condition for STAR-CCM+, and $\dot{m}_{TRC,0}$ is the same for TRACE.

For a transient test case the time dependent mass flow rate of Eq. 4-20 was applied to the inlet of the pipe region:

$$\dot{m}_{in} = \begin{cases} 5.0\dfrac{kg}{s}, & t < 10.0s, \\ 5.0\dfrac{kg}{s} + (t - 10.0s)\dfrac{kg}{s^2}, & 10.0s \le t \le 15.0s, \\ 10.0\dfrac{kg}{s}, & t > 15.0s. \end{cases} \qquad 4\text{-}20$$

The pressure drop curves that result from the time dependent mass flow rate are shown in Fig. 4-11. At $t = 10s$ and $t = 15s$, the pressure drop abruptly changes due to the discontinuous inertial component of the pressure gradient. Due to the fully developed flow assumption, TRACE predicts a lower pressure drop throughout the transient. The Janus and STAR-CCM+ results calculated with flat inlet profiles match very closely, as expected.

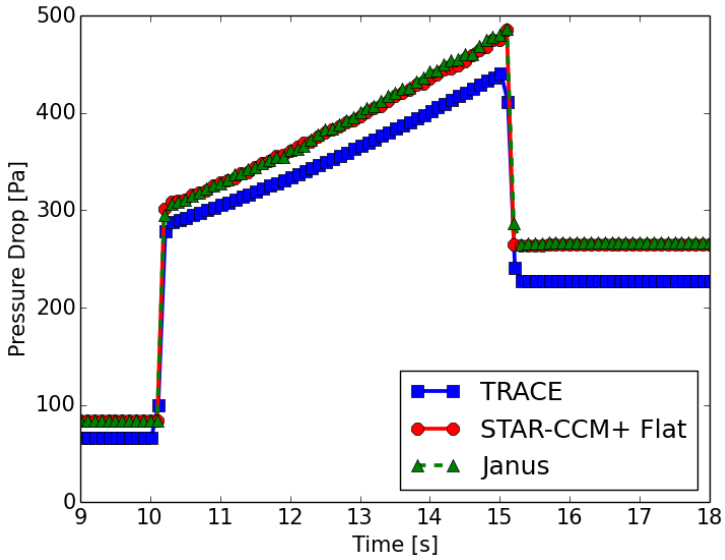

Fig. 4-11. Pressure drop across a $1.8m$ pipe as calculated with standalone software and a domain overlapping coupled simulation.

4-7.2 Partial Pipe Coupling – TST Configuration

For a more complex case, the full $1.8m$ TRACE pipe is broken into 3 segments of equal length. As indicated in Fig. 4-12 a domain overlapping interface is used to couple the central TRACE component to a $0.6m$ long STAR-CCM+ pipe.

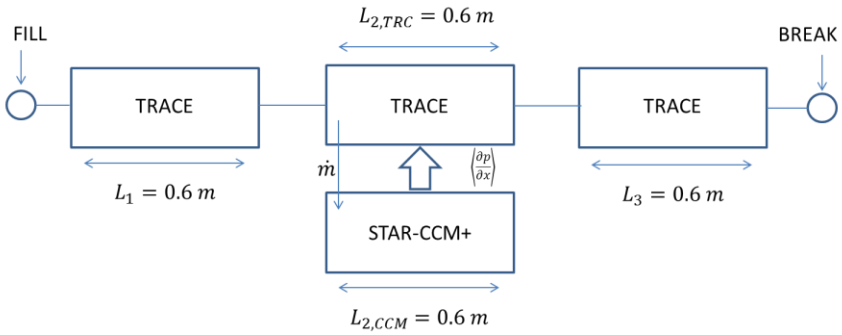

Fig. 4-12. Schematic diagram for domain overlapping coupling setup with imposed mass flow rate and three spatial segments.

Pressure drops calculated with various mass flow rates are plotted in Fig. 4-13. Some disagreement is apparently between the STAR-CCM+ and coupled curves because the length of the coupled pipe is not sufficient to fully capture developing flow.

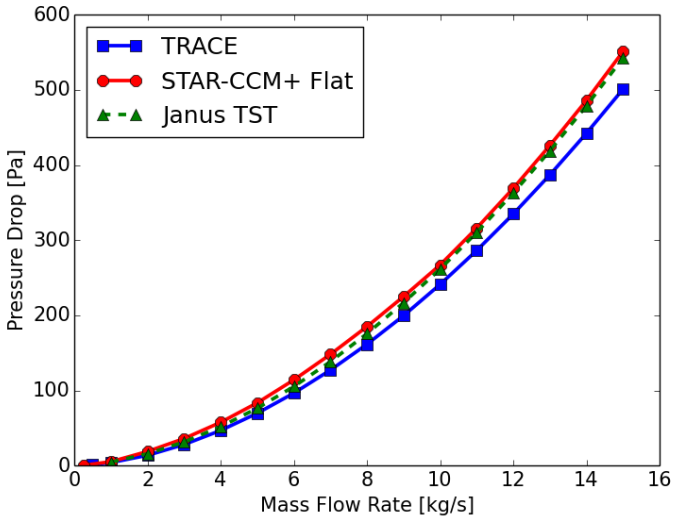

Fig. 4-13. Pressure drop vs. mass flow rate for imposed mass flow rate coupled cases.

For a transient test case, the time dependent mass flow rate of Eq. 4-20 was applied to the inlet of the domain. The total pressure drop resulting from the transient mass flow rate is plotted in Fig. 4-14. The coupled pressure drop does not directly overlap the CFD standalone results, though it is more CFD-like than the TRACE standalone results. The disagreement between the coupled results and the CFD is again a result of the coupled section not being long enough to fully capture the effects of developing flow.

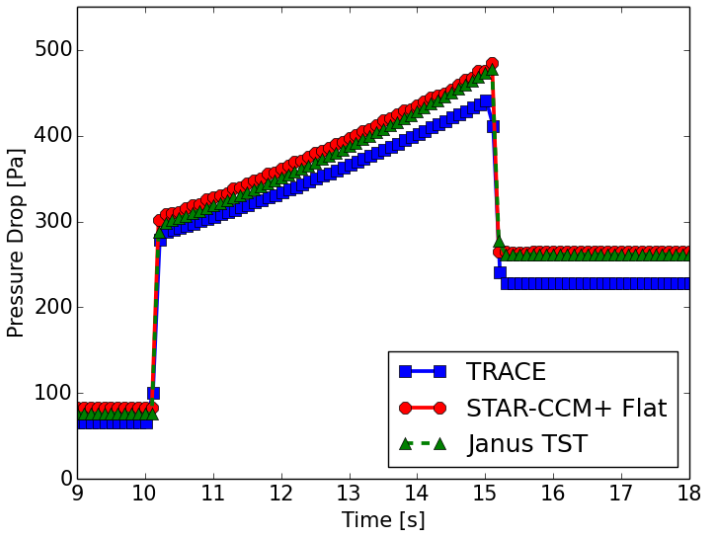

Fig. 4-14. Pressure drop vs. mass flow rate for the full pipe as calculated with standalone codes as well as with the domain overlapping coupling method in the TST configuration.

The pressure drop across each segment is plotted in Fig. 4-15, where it is clear that the domain overlapping coupling algorithm is indeed correctly implemented. The coupled pressure drops match the TRACE standalone pressure drops across the uncoupled left and right pipe segments.

In the coupled center segment, the coupled results closely overlay the CFD results, which diverge noticeably from the TRACE standalone results. The pressure drops across the edge that connects the left and center segments and the edge that connects the center and right segments are not shown here, but both are uncoupled and match the standalone TRACE results.

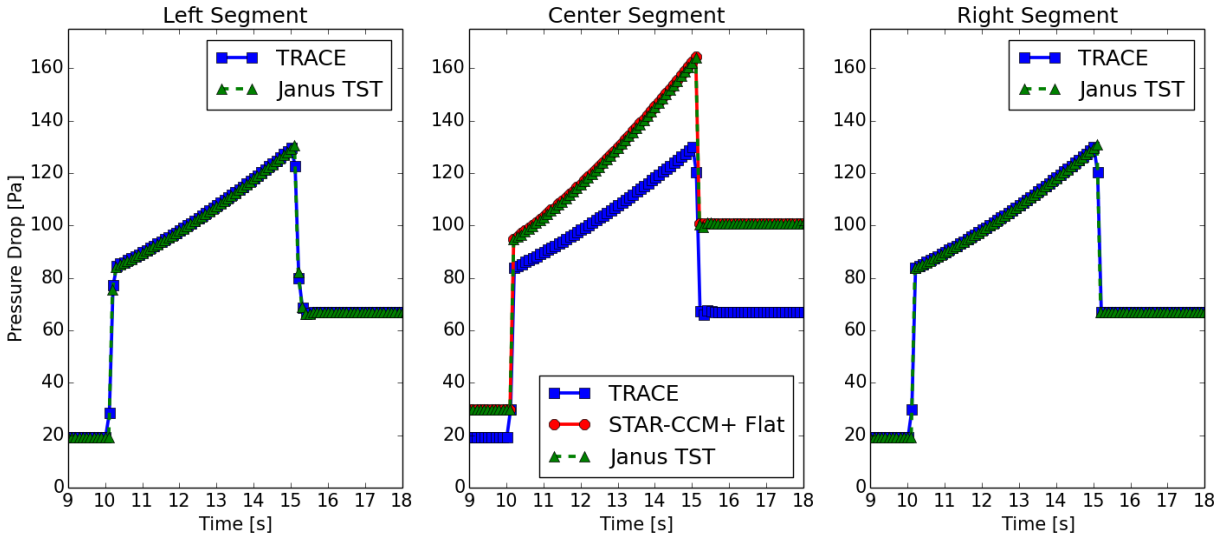

Fig. 4-15. Pressure drop vs. mass flow rate for each of the three pipe segments as calculated with standalone codes as well as with the domain overlapping coupling method.

4-8 Imposed Pressure Drop

In this section, cases in which flow is driven by imposed pressure drops are explored. Pressure boundaries are placed on either side of the pipe for these cases.

4-8.1 Full Pipe Coupling

Full system domain overlapping coupling is not possible for imposed pressure drop conditions. Consider, for example, the hypothetical coupling arrangement shown in Fig. 4-16. TRACE will initially calculate a mass flow rate that incurs a pressure drop sufficient to match the boundary conditions. This value is then passed to STAR-CCM+, which calculates a friction. If the CFD pressure drop is lower than the prescribed pressure drop, TRACE will attempt to lower the mass flow rate to match the pressure. Since the friction factors are no longer affected by the TRACE velocities, however, the lowered flow rates will not change the TRACE pressure drop, and the coupled simulation will not produce any useful results.

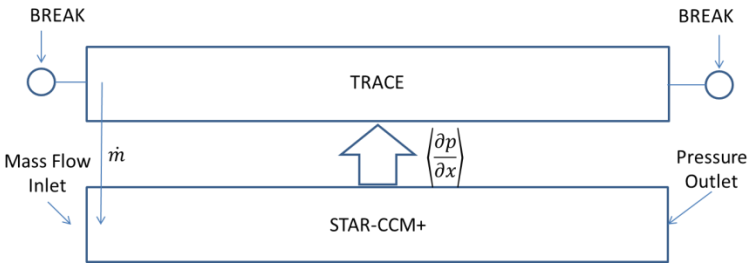

Fig. 4-16. Schematic diagram for hypothetical full pipe domain overlapping coupling setup with imposed pressure drop. This system is over-specified.

4-8.2 Partial Pipe Coupling – TST Configuration

Fig. 4-17 shows a domain overlapping coupling configuration in which STAR-CCM+ provides data for only a portion of the system. The TRACE file consists of 3 identical pipe segments of length $0.6m$, while a $0.6m$ CFD pipe section is coupled to the middle TRACE segment.

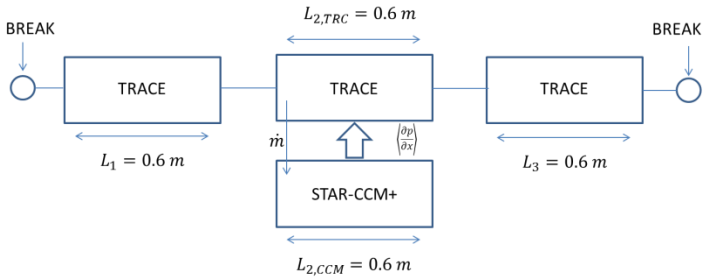

Fig. 4-17. Schematic diagram for domain overlapping coupling setup with pressure drop.

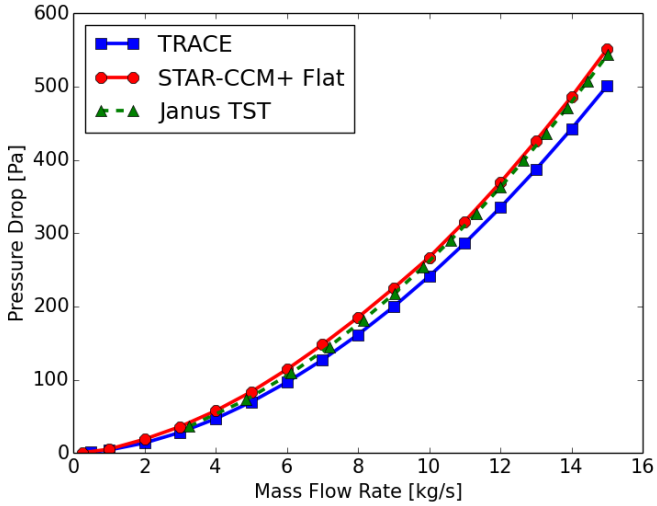

Fig. 4-18. Pressure drop vs. mass flow rate for imposed pressure drop coupled cases.

Convergence data from this case are shown in Fig. 4-19. Contrary to the analogous case with domain decomposition coupling, no under-relaxation is needed. The system's sensitivity was tested by varying the initial mass flow rate in the STAR-CCM+ pipe, as indicated by $\dot{m}_{init}$ in the

figure. As would be expected, convergence appears to happen more quickly for cases with starting conditions near the true value. The "$\dot{m}_{init} = 20.0 kg/s$" case is particularly interesting in that the pressure drop across the CFD component ($\sim 350 Pa$) is larger than the total prescribed pressure difference ($280 Pa$), resulting in TRACE passing zero mass flow rate back to STAR-CCM+.

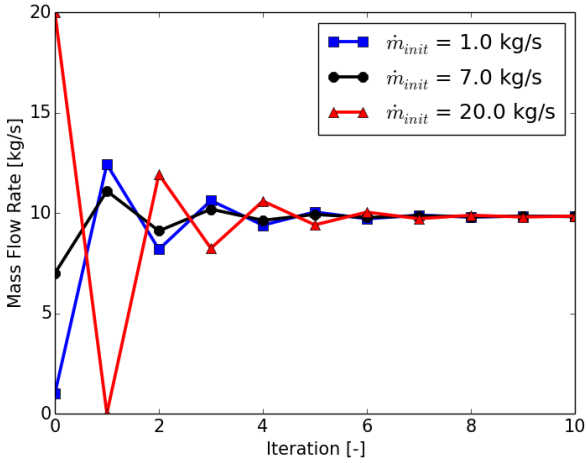

Fig. 4-19. Convergence patterns for 3 segment domain overlapping coupling cases with imposed pressure drop boundary conditions. Calculated by setting the left break at a pressure of 280 Pa relative to the right break.

For a transient test case of the imposed pressure drop coupling case, the time dependent pressure (relative to $10^5 Pa$) of Eq. 4-21 was applied to the inlet break component in the TRACE system. This transient allows sufficient idle time so that transient effects die out before coupling begins:

$$p_{break,left}(t) = \begin{cases} 40.0Pa, & t < 75.0s, \\ 40.0Pa + 48(t - 75.0s)\dfrac{Pa}{s}, & 75.0s \le t \le 80.0s, \\ 280.0Pa, & t > 80.0s. \end{cases} \qquad 4\text{-}21$$

The mass flow rates resulting from the time dependent boundary conditions are shown in Fig. 4-20. In this figure, the "STAR-CCM+" and "Janus" curves refer to the mass flow rate computed by the CFD and STH portion of the same coupled simulation, while the "TRACE" curve refers to an STH standalone computation. The former two curves are necessarily equal due to the interface configuration. The TRACE standalone case produces a higher mass flow rate due to the fully developed flow assumption.

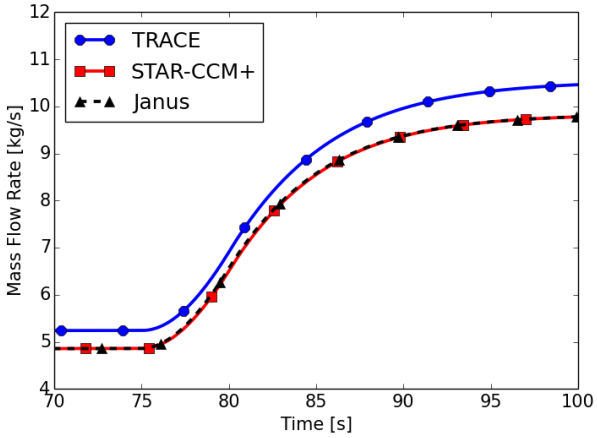

Fig. 4-20. Pressure drop vs. mass flow rate for imposed pressure drop coupled cases.

The pressure drop across each pipe segment during the coupled simulation is shown in Fig. 4-21 compared to TRACE standalone results. In the coupled center segment, the STAR-CCM+ and Janus curves match quite well. In the uncoupled segments, Janus tends to produce a somewhat lower pressure drop, due to the smaller mass flow rate of the coupled simulation.

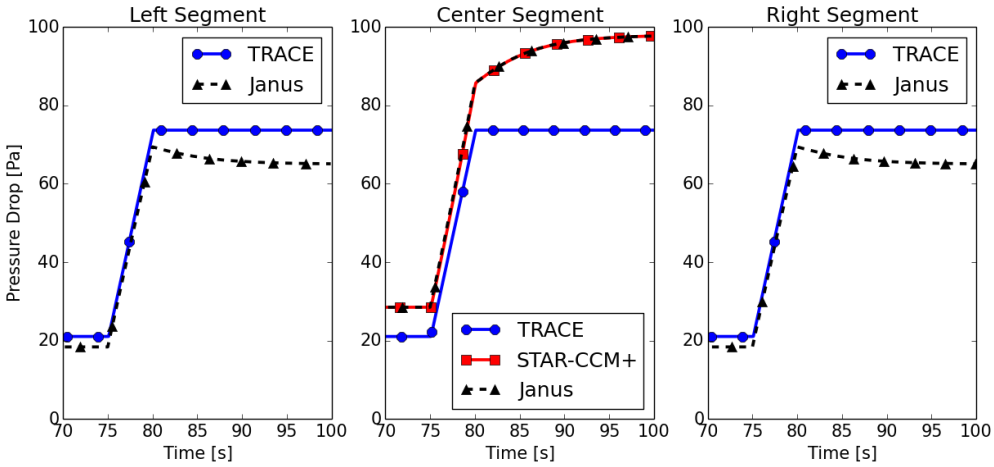

Fig. 4-21. Pressure drop curves for each pipe segment during domain overlapping coupled simulation.

4-9 Bent Pipe Test Case

The geometry of the previous test case was modified to include two bends (Fig. 4-22) to test the TII domain overlapping coupling in a case without a trivially define vector flow path. In this case the CFD solution does not have radial symmetry, as in the case of a straight pipe. In addition, the presence of a bend will give rise to localized frictional pressure drops, which in a 1D system code like TRACE are typically modeled with a user-defined form loss coefficient. The geometry of the test consists of a pipe of radius $0.03\ m$ with two right angle turns with centerline curvature $0.07\ m$. For the TRACE standalone simulations, a form factor $K = 0.16$ was input at each bend.

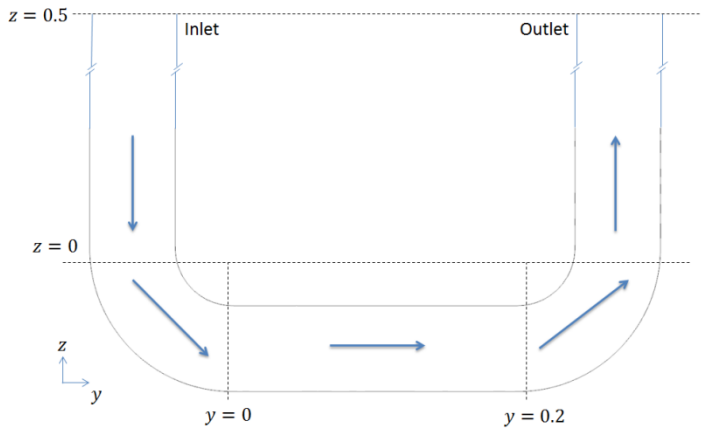

Fig. 4-22. Schematic illustration of flow path vector field used for the bent pipe test case.

Three simulations were run for this case: a TRACE standalone simulation, a STAR-CCM+ standalone simulation, and a coupled TRACE/CCM+ simulation. The results obtained for the pressure drop across the component as function of the mass flow rate $\dot{m}_{in}$ in steady state conditions are reported in Fig. 4-23. The comparison shows that the coupled TRACE/CCM+ results are consistent with STAR-CCM+ standalone simulations, justifying Eq. 4-18 under steady state conditions.

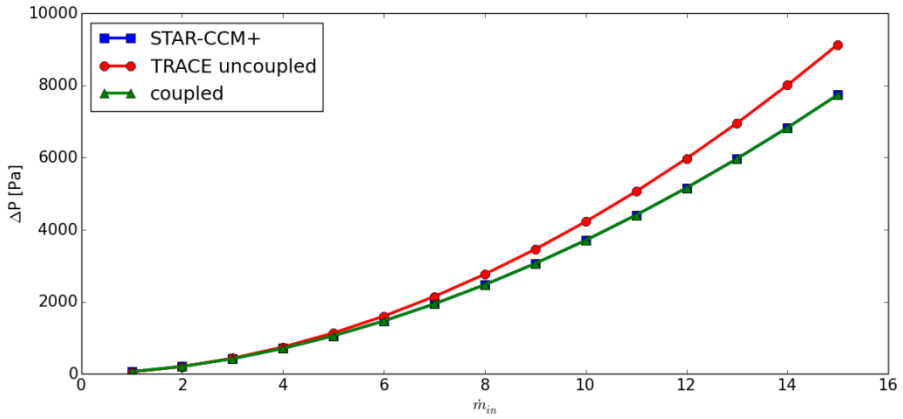

Fig. 4-23. Steady state results for bent pipe coupled case.

The friction factor definition of Eq. 4-18 reduces to a simple form for steady state cases, requiring transient operation to engage the inertial correction. In pursuit of this, the time dependent mass flow rate of Eq. 4-22 was applied to the inlet of the bent pipe, with the resulting time dependent pressure drop recorded as output:

$$\dot{m}_{in}(t) = \begin{cases} 10.0\,\frac{kg}{s}, & t \leq 10.0s, \\ t \times 1.0\,\frac{kg}{s^2}, & 10.0s < t < 15.0s, \\ 15.0\,\frac{kg}{s}, & t \geq 15.0s. \end{cases} \qquad \textit{4-22}$$

Data collected from a selected transient simulation ($\Delta t = 0.1\ s$) are displayed in Fig. 4-24 (left). The coupling is activated at $t = 9.0\ s$. After a short null transient that allows equilibration between CCM+ and TRACE to, the transient mass flow rate begins. The on-the-fly correction of the TRACE solutions using CFD data is shown to be successful in transient conditions. Similarly to the steady case, the standalone TRACE simulation differs from the CFD pressure drop, while the coupled solution closely follows the CFD solution.

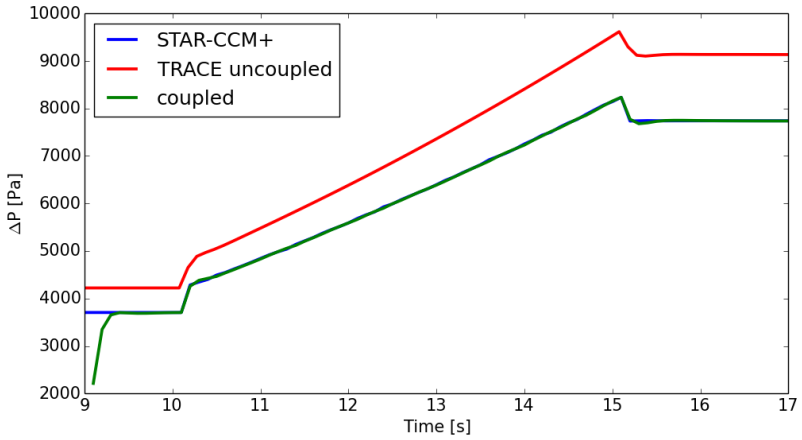

Fig. 4-24. Transient bent pipe coupling test case. Calculated with $\Delta t = 0.1\ s$.

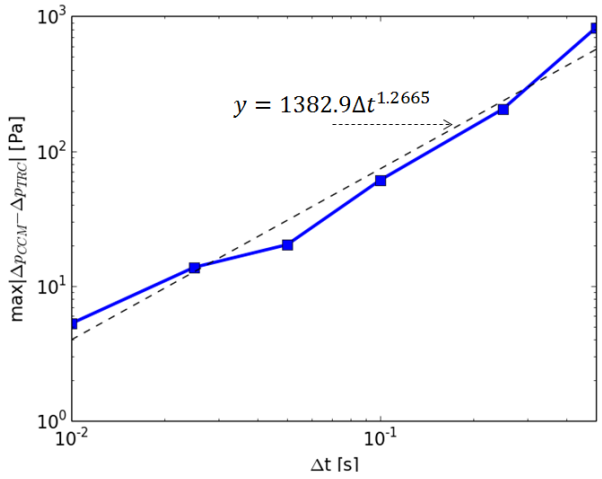

Fig. 4-25. L^{∞} error in agreement between TRACE and STAR-CCM+ for domain overlapping coupling of the bent pipe test case with power law data fit to show approximately linear diminishing of error.

In Fig. 4-24, some visible differences between the “STAR-CCM+” and the “coupled” curves are apparent. Because the codes calculate the inertial pressure drop independently, some error is introduced. We measure this error by calculating the maximum difference (L^{∞} norm error) between the two curves after the initial null transient. This error is included in Fig. 4-25 for several time steps and is observed to diminish approximately linearly with decreasing time step.

4-10 Conclusions

In this section, a domain overlapping coupling method was detailed for 1-D flow domains. Two potential formulations were discussed, one based on computing spatial derivatives and one based on temporal derivatives. Some rudimentary analysis suggested that the temporal method would be the most efficient, in terms of both implementation and accuracy. The temporal method was then applied to simple 1-D systems in a variety of configurations. Similarly to the domain decomposition method, the performance of the domain overlapping method was linked to the physics of the overall system. Convergence under imposed mass flow conditions is essentially trivial due to the lack of feedback between mass flow and pressure. The mass flow-pressure feedback is a factor for imposed pressure drop simulations where convergence required more iterations.

In general, the domain overlapping method requires significantly more theoretical development than the domain decomposition method of Chapter 2. However, comparison of the convergence of the two methods under challenging conditions would seem to justify the additional complexity. In particular, comparing Fig. 3-18 and Fig. 4-19 show that for a segmented pipe with an imposed pressure drop, the domain overlapping coupled simulation converges with far fewer iterations and without the need for under-relaxation. The two methods are compared more rigorously in the next chapter.

Chapter 5. 1D Domain Treatment Comparison

The domain decomposition method developed in Chapter 3 and the domain overlapping coupling method developed in Chapter 4 were both found to successfully couple simple 1-D systems. Before the methods can be extended to more complex systems, their mathematical and convergence properties must be explored more deeply. In this chapter, the approaches are applied to simple cases that allow for in-depth analysis. The methods are also directly compared to each other through calculations on identical systems to lay the foundation of developing an effect coupling method.

5-1 Open Loop Test Case

Consider the geometry in Fig. 5-1 in which a pipe of length L is broken into two sections of lengths L_1 and L_2. For $t < 0\ s$, the pipe is stagnant with $p_{in} = p_{out} = 1.0\ MPa$. Immediately after $t = 0\ s$, the outlet pressure drops and the total pressure drop across the pipe is held constant at $\Delta p = 10\ kPa$ for $t > 0\ s$.

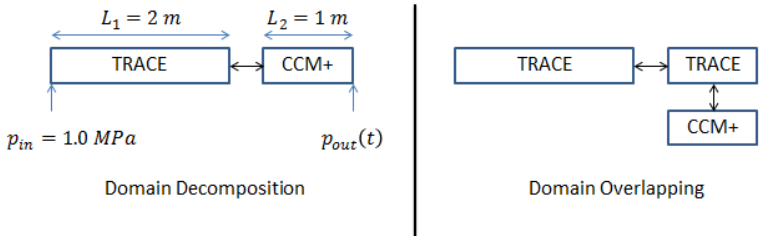

Fig. 5-1. Schematic diagrams of the abrupt pressure drop test case coupling configurations.

The abrupt pressure drop case was previously explored by Bertolotto [55], who utilized a 3 meter pipe with a radius of 0.025 meters. We reproduced this test case with the first 2 meters of the pipe simulated by TRACE, while the remaining meter is coupled to STAR-CCM+ through either domain decomposition (Fig. 5-1 left) or domain overlapping (Fig. 5-1 right) methods. The flow in the pipe is initially stagnant and at a constant pressure of $p_{init} = 1.0\ MPa$. At time $t = 0.0\ s$, the pressure at the outlet is abruptly lowered to $p_{out}(t \geq 0.0\ s) = 0.99\ MPa$.

The time dependent mass flow rates resulting from the abrupt pressure drop are shown in Fig. 5-2 for both coupling methods. Additionally, the data calculated by Bertolotto with semi-implicit domain decomposition coupling using ANSYS CFX/TRACE are plotted as a reference. Convergence is observed with larger time steps when domain overlapping is used. In addition, significant mass flow overshoots are observed for the domain decomposition approach (Fig. 5-2 bottom). These overshoots are present for all time steps tested, as shown in Fig. 5-3, with the

underlying cause discussed below. It is observed that the domain overlapping case converges with $\Delta t = 0.1s$, while the domain decomposition method requires an integration time step close to $\Delta t = 0.0025s$. Therefore, a significant savings in terms of integration time step, and hence computational resources requirements, is realized.

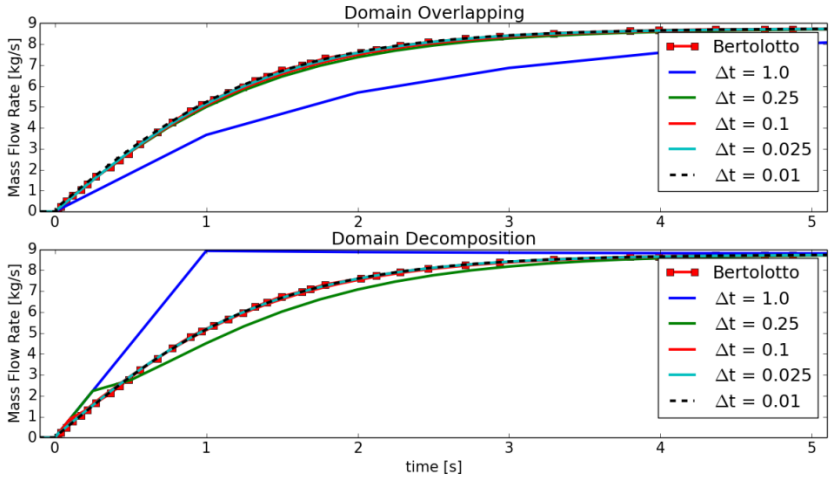

Fig. 5-2. Mass flow rates through the open loop as a function of time for both coupling methods.

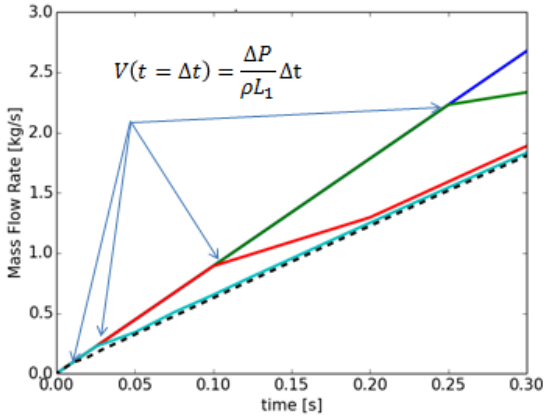

Fig. 5-3. Zoomed picture of domain decomposition mass flow rates from Fig. 5-2 to show overshoots.

In order to understand the cause of the mass flow overshoots in domain decomposition, it is useful to consider an accompanying simplified analytical model. Because the pipe cross section does not change along the pipe axis, the only contributions to the pressure drop are given by the inertial (Δp_I) and frictional (Δp_f) terms of the momentum equation. Utilizing the Fanning friction factor to model the frictional terms yields Eq. 5-1 as a model governing equation of the system, where $L = L_1 + L_2$ is the total length of the system as shown in Fig. 5-1:

$$\Delta p = 10\ kPa = \Delta p_f + \Delta p_I = 2f_F \frac{L}{D}\rho V^2 + L\rho \frac{\partial V}{\partial t}. \qquad 5\text{-}1$$

At the beginning of the transient, the pressure drop is dominated by the inertial term, so that the initial velocity gradient can be estimated using Eq. 5-2:

$$\left.\frac{\partial V}{\partial t}\right|_{t=0} = \frac{\Delta p}{\rho L}. \qquad 5\text{-}2$$

It is useful to apply Eq. 5-2 to the first iterative cycle of an explicit domain decomposition coupled calculation. Before any iteration occurs, the mass flow rate of STAR-CCM+ is set to zero and the pressure everywhere is uniform. The pressure of the outlet (STAR-CCM+) is then lowered abruptly, but the mass flow rate is still everywhere zero due to the CFD inlet relying on TRACE for mass flow. The STAR-CCM+ outlet pressure is thus translated to the outlet of the TRACE section. TRACE then calculates the new velocity based on the entire pressure drop but only across the TRACE portion of the pipe as estimated in Eq. 5-3.

$$\left.\frac{\partial V}{\partial t}\right|_{t=0} = \frac{\Delta p}{\rho L_1} > \frac{\Delta p}{\rho L} \qquad 5\text{-}3$$

Thus, it is expected that an explicit domain decomposition coupling will overestimate the velocity at the first timestep by a factor of L/L_1, which is 1.5 in the case of the geometry in Fig. 5-1. In the domain overlapping coupling, the governing equation of the 1D system is Eq. 5-4, in which the Fanning friction factor has been replaced with the factor calculated from CFD data.

$$10\ kPa = 2f_{CFD} \frac{L}{D}\rho V^2 + L\rho \frac{\partial V}{\partial t} \qquad 5\text{-}4$$

Because the entire length of the component is available to TRACE in this case, the effect of Eq. 5-3 does not occur. While generally $f_F \neq f_{CFD}$, the two factors are expected to be of the same magnitude, at least to such an extent as to not significantly alter the mathematical structure of the governing equation. Thus, it is concluded that, for reasonable f_{CFD}, the coupled solution will evolve in a geometrically consistent manner ($\left.\frac{\partial V}{\partial t}\right|_{t=0} = \frac{\Delta p}{\rho L}$). The analysis of this simple system suggests that, in the case of abrupt pressure drops, the domain overlapping method will outperform the domain decomposition method as long as $f_{CFD} \sim f_F$. While the instantaneous pressure drop is a special case, continuously changing systems become abrupt under temporal discretization. Thus, the domain overlapping method appears to better suited for larger timesteps, potentially allowing for improved computational efficiency.

5-2 Pump Driven Closed Loop Test Case

The test case is made progressively more challenging by closing the loop to include feedback effects. The loop considered in this section, as shown in Fig. 5-4 (top), consists of three pipe sections, a pump, and a pressure set-point to prevent runaway pressures from building up within

the loop. The pump is driven by a custom pump head curve designed to produce the desired mass flow rates.

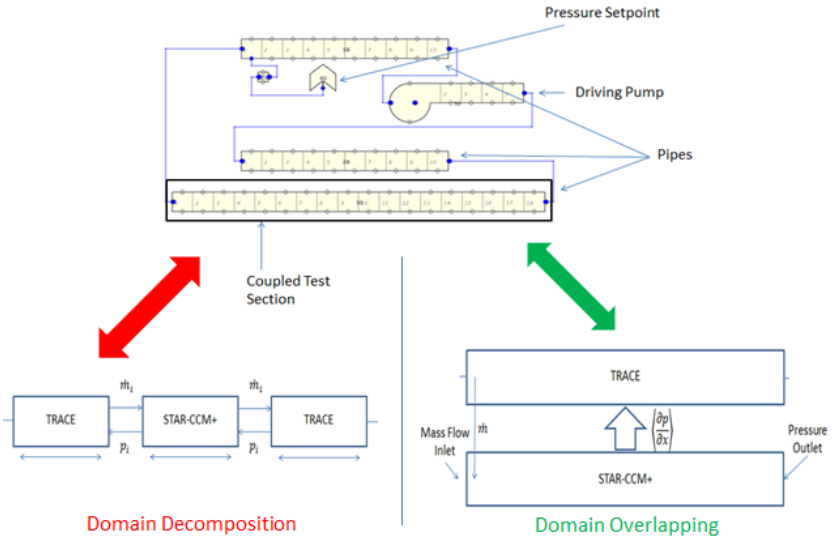

Fig. 5-4. TRACE model of closed, pump driven loop with employed coupling schemes indicated. Both coupling schemes are used in separate calculations to replace the solution in the coupled test section with CFD-based results.

The coupled test section modeled with CFD is indicated in Fig. 5-4 and consists of a 1.8 m long circular pipe with a diameter of 0.1 m. For the domain overlapping approach, this section is also modeled within TRACE using 18 cells of equal length. The accompanying STAR-CCM+ component is a circular tube of the same dimensions as the TRACE pipe and is composed of approximately 23000 cells. True consistency between CFD and system code simulations would require fully developed velocity and turbulence profiles at the CFD inlet because TRACE assumes the fully developed flow state. However, for the current test case, flat inlet velocity profiles with default turbulence parameters are imposed at the CFD inlet. With this assumption, a given mass flow rate will result in a lower TRACE (standalone) pressure drop compared to CFD. The effects are observed to be quite small, and thus it is deemed acceptable to test the coupling implementation.

5-2.1 Interfacing

The domain overlapping technique is applied through one volumetric interface connecting the test section in the complete TRACE model to the CFD model of the component as shown in Fig. 5-4 (bottom right). The left side of the STAR-CCM+ pipe is a mass flow inlet held at the same mass flow rate as the TRACE pipe. With each coupling iteration, information about the average non-inertial pressure gradient (denoted by $\langle \partial p/\partial x \rangle$ in Fig. 5-4) is passed from CFD to TRACE in the form of a friction factor calculated by Eq. 4-18. The right side of the CFD model is held at a constant pressure, while the right and left sides of the TRACE model are connected to pipes as shown in Fig. 5-4.

Domain decomposition coupling techniques are applied to the closed loop by removing the test section (outlined in Fig. 5-4) from the TRACE model, using STAR-CCM+ for this region instead, and communicating pressure and mass flow data via two interfaces at either end of the CFD component as shown in Fig. 5-4 (bottom left). The left side of the STAR-CCM+ component is a mass flow inlet receiving an interfacial mass flow rate ($\dot{m}_i$) from TRACE and, in turn, providing a pressure (p_i). The right side of the CFD component is a pressure boundary that receives a pressure (p_i) from a FILL component (mass flow rate boundary) in TRACE and, in turn, provides a mass flow rate ($\dot{m}_i$) to TRACE.

5-2.2 Steady State

First, TRACE standalone and coupled solutions using both domain decomposition and domain overlapping methodologies are compared for steady state cases. The resulting mass flow rates are plotted as functions of the pump rotation speed in Fig. 5-5. The data all collapse onto approximately the same line, indicating that the CFD inlet profiles have minimal effect on the solution.

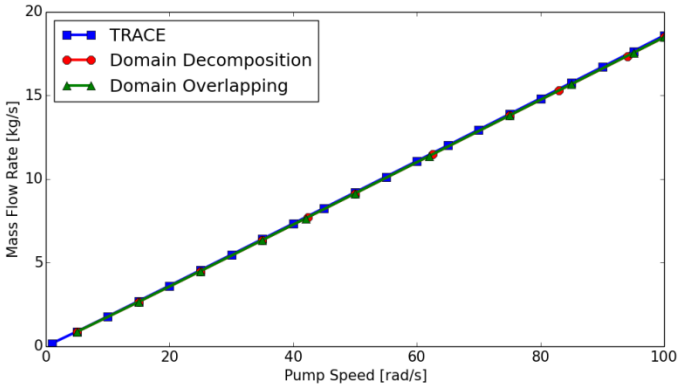

Fig. 5-5. Steady state mass flow rates achieved via both coupling methodologies as compared to those calculated via TRACE standalone simulation.

We investigated the convergence performance of the two coupling methodologies by recording the number of iterations required to achieve convergence. The results are reported in Fig. 5-6 for representative pump rotation rates. On the horizontal axis the guessed mass flow rate $\dot{m}_{init}$ at the beginning of the simulation is normalized by the final steady state flow rate $\dot{m}_{ss}$. The vertical axis displays the number of iterations required to achieve convergence. The i^{th} iteration is deemed converged if the criteria of Eq. 5-5 are met:

$$\left|\dot{m}^{i} - \dot{m}^{i+1}\right| < \dot{m}^{i+1} \times 10^{-3} \; and \; \left|\dot{m}^{i+1} - \dot{m}^{i+2}\right| < \dot{m}^{i+1} \times 10^{-3}. \qquad 5\text{-}5$$

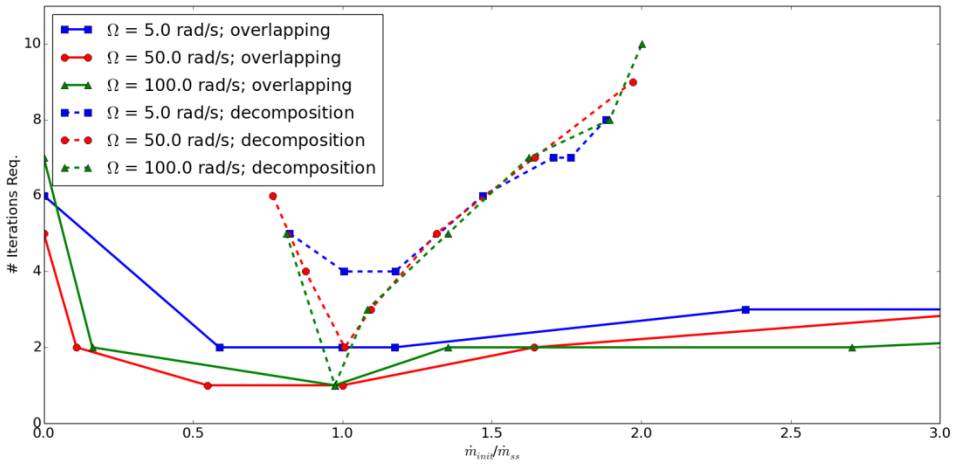

Fig. 5-6. Iterations required for convergence of 6 coupling scenarios with varied initial mass flow rates. Solid lines refer to domain overlapping; dashed lines refer to domain decomposition. Three representative pump rates are indicated by the line color.

The initial mass flow rate was applied to domain decomposition cases by setting the values at the STAR-CCM+ inlet and the TRACE FILL component. In the domain overlapping cases, the values were only required in the STAR-CCM+ input. The domain decomposition coupling was not found to converge in all cases, and the data shown in Fig. 5-6 approximately represent the range over which convergence was achieved. Identical TRACE numerical settings were used in both cases (i.e. convergence criteria and maximum pressure iterations both left as default). In contrast, the domain overlapping coupling was found to converge for all cases tested, demonstrating the superior robustness of this coupling methodology. Not only was the domain overlapping method less sensitive to initial guesses, but it also achieved convergence in fewer iterations for most conditions.

The less favorable performance of the domain decomposition approach results from the inability of TRACE to calculate a system-wide pressure balance within a single coupled iteration, requiring several iterations for the system pressure to equilibrate. The domain decomposition simulations require multiple iterations for even the best initial mass flow rates, due to the effects of imperfect initial pressures set at the interface. Initial interface pressures were set to approximately correct values, but even small perturbations in the steady state pressure profiles require additional iterations. This process is evidently exacerbated for low-flow regimes in which the pressure drop is more sensitive to the flow rate. With starting conditions near $\dot{m}_{init}/\dot{m}_{ss} \approx 2.0$, the pressure rebalancing becomes too unstable and the TRACE iteration fails. To be sure, under-relaxation would improve convergence in these cases, but this is not considered here as the domain overlapping method required no such assistance. A further benefit of the domain overlapping method is that it depends only upon changes in pressure, and not on absolute pressure at the interface, eliminating a dimension of sensitivity.

5-2.3 Transient

With steady state convergence data in hand, the question of transient performance is now addressed. The pump impeller rotation rate was pulsed according to the function in Eq. 5-6:

$$\Omega(t) = \begin{cases} 50.0\frac{rad}{s}, & t \leq 100.0s, \\ 50.0\left[1 + \sin^4\left(\frac{t - 100.0s}{10.0\ s}\pi\right)\right]\frac{rad}{s}, & 100.0s < t < 110.0s, \\ 50.0\frac{rad}{s}, & t \geq 110.0s, \end{cases} \qquad 5\text{-}6$$

designed to be smooth up to at least the first derivative. The mass flow rate through the loop and the pressure drop across the coupled test section (highlighted in Fig. 5-4) were recorded as system response functions. Response functions for the mass flow rate and pressure drop across the test section are shown in Fig. 5-7 alongside temporal convergence data. As expected, the mass flow rate appears to converge to a function resembling the pump impeller rotation rate, while the pressure drop converges to a function resembling the time derivative of the mass flow rate. An unphysical secondary pressure peak is observed for large integration time steps ($\Delta t \gtrsim 1.0\ s$).

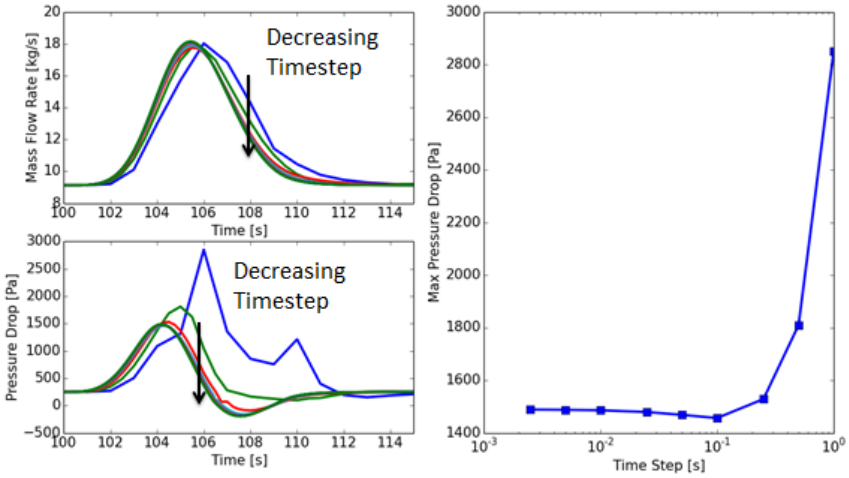

Fig. 5-7. Transient response functions (left) and temporal convergence data (right) for domain decomposition coupling pump driven close loop test case. Multiple time steps are shown with the trend of decreasing time steps indicated.

The maximum pressure drop is plotted on the right of Fig. 5-7 for each time step tested, giving an indication of the temporal convergence of the pressure response function. Significant error reduction is evident in the region $\Delta t \in [10^{-1}s, 10^{0}s]$, while the reduction drops off markedly for $\Delta t < 10^{-1}s$.

The results for the domain overlapping coupled model and corresponding convergence data are shown in Fig. 5-8. The unphysical secondary peak in the pressure drop of Fig. 5-7 is not observed in this case for any time step used.

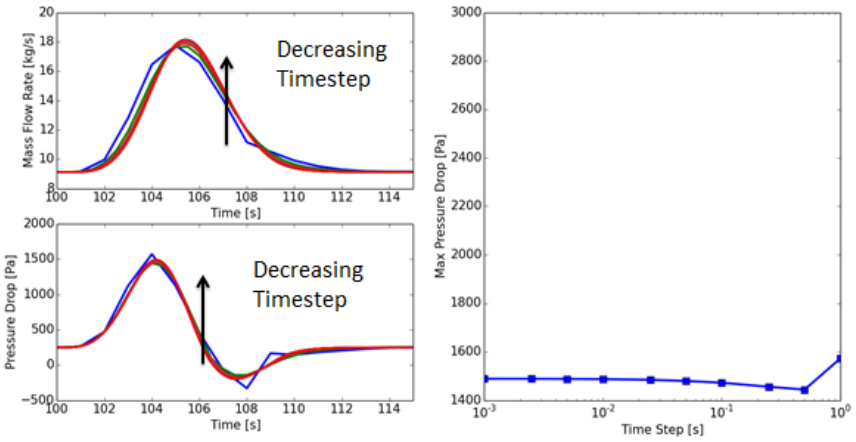

Fig. 5-8. Mass flow rate and pressure drop response functions alongside temporal convergence data for the domain overlapping pump driven close loop transient test case. Multiple time steps are shown with the trend of decreasing time steps indicated.

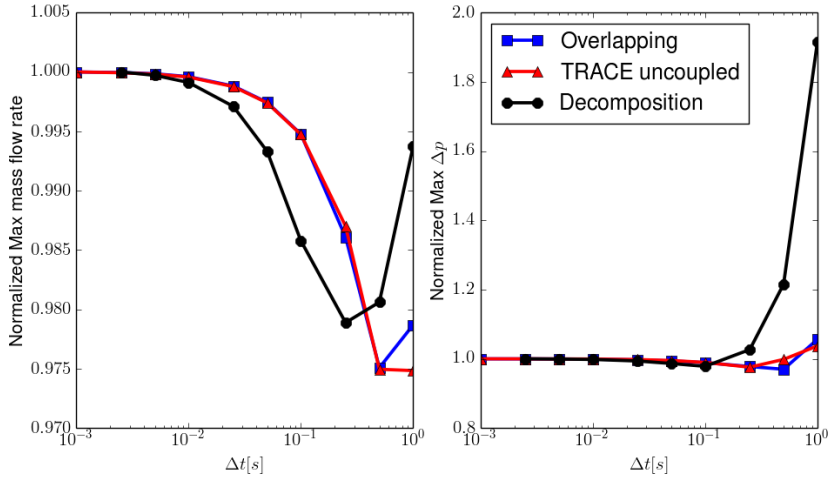

Fig. 5-9. Plots of (normalized) maximum values of mass flow rate (left) and pressure drop (right) across the coupled section against the time step used for each transient case tested.

The comparison between TRACE standalone simulations and the two coupling methodologies is presented in Fig. 5-9. The maximum values of mass flow rate and pressure drop are plotted against time step used for the cases tested in Fig. 5-9. As expected, the converged solutions of domain decomposition and domain overlapping are identical (Fig. 5-9 left). This value is somewhat higher than the TRACE standalone case, due to the developing flow conditions at the CFD inlet. In this case, the difference allows for visual verification that the domain overlapping method is implemented correctly. The domain decomposition coupling requires smaller time steps to converge and produces highly inaccurate results for large time steps. Additionally, we found that the domain decomposition simulations became unstable for $\Delta t = 1\ ms$. At this level, perturbations to the velocity cause the inertial velocity derivative to become unstable, as discussed below in §5-2.4. Remarkably, the convergence of the coupled solution when using

domain overlapping methods is limited only by the convergence of TRACE, as can be observed in Fig. 5-9.

5-2.4 Domain Decomposition Stability

To consider the cause of the domain decomposition instability observed at small time steps in the previous section, consider once more the 1D model given by Eq. 5-1. In one iteration, STAR-CCM+ calculates a new pressure drop, estimated in Eq. 5-7, based on the previous velocity and the velocity just passed to it:

$$\Delta p_{CFD} = 2 f_{CFD} \frac{L_{CFD}}{D} \rho V^n V_0 + \frac{\rho L_{CFD}}{\Delta t} (V^{n+1} - V^n), \qquad 5\text{-}7$$

where f_{ccm} is a friction factor characterizing the frictional losses of the CFD portion of the simulation. For this analysis, we linearize the friction term based on the initial velocity V_0. The transient calculation of the previous section were preceded by several seconds of null transient with a mass flow rate of approximately $9.13\ kg/s$, making V_0 simple to calculate. Using this pressure drop, the next time step velocity calculated by TRACE is estimated with Eq. 5-8:

$$\rho L_{TRC} \frac{V^{n+2} - V^{n+1}}{\Delta t} = \Delta p_{CFD} - 2 f_{TRC} \frac{L_{TRC}}{D} \rho V^{n+1} V_0. \qquad 5\text{-}8$$

Combining Eqs. 5-7 and 5-8 yield the recurrence relation shown in Eq. 5-9:

$$V^{n+2} = V^{n+1} \left(1 + \frac{L_{CFD}}{L_{TRC}} - \frac{2 f_{TRC} \Delta t}{D} V_0\right) + V^n \frac{L_{CFD}}{L_{TRC}} \left(\frac{2 f_{CFD} \Delta t}{D} V_0 - 1\right). \qquad 5\text{-}9$$

Performing a rudimentary Von Neumann stability analysis ($V^{n+1} = V^n e^{\lambda \Delta t}$) yields the error amplification factor of Eq. 5-10:

$$G \equiv \frac{V^{n+1}}{V^n} = e^{\lambda \Delta t} = \frac{L_{CFD}}{L_{TRC}} \left(1 + \frac{L_{CFD}}{L_{TRC}} - \frac{2 f_{TRC} \Delta t}{D} V_0\right) \left(\frac{2 f_{TRC} \Delta t}{D} V_0 - 1\right) \qquad 5\text{-}10$$

While this model is too crude to accurately predict the stability bounds, it does predict that stability ($|G| \leq 1$) requires that the time step used fall within a specific range, since G is quadratic in Δt. The upper bound of this range represents the familiar stability limit of explicit time stepping, while the lower bound represents a limit at which perturbations to the velocity cause unstably large perturbations to the inertial term. The domain overlapping method was found to be stable for all timesteps tested.

5-3 Thermosiphon-Driven Closed Loop Test Case

5-3.1 Test Case Description

As a particularly challenging test case for coupled codes, a natural circulation loop was selected. Because the loop is closed and the flow rate results from a pressure balance over the entire

system, a tighter coupling between the CFD and system code domains results than would be the case for open loops or forced circulation conditions. The selected test case is characterized by a rectangular loop of width $w = 0.2\,m$ and length $H = 3.0\,m$. The radius of the pipe is $0.03\,m$ and the radius of curvature of the bends is $0.07\,m$. Heated and cooled sections of the riser and downcomer legs, respectively, with lengths $l = 1.0\,m$, offset $0.5\,m$ from the bends, are used to drive the flow through a balance of buoyant and frictional forces, rather than imposed flow rates through boundary conditions.

In order to achieve natural circulation, a temperature dependent water density over a temperature range $T \in [400\,K, 605\,K]$ at a pressure of $P = 1.5 \cdot 10^7\,Pa$ was compiled and used as an interpolation table from STAR-CCM+ [56]. TRACE uses IAPWS data for the fluid's equation of state by default.

The goal of this case is to verify the implementation of Janus and ensure that the TRACE solution is corrected, based on STAR-CCM+ data in the absence of imposed mass flow rate or pressure drop and thus no attempt is made to validate with experimental data. For the purposes of this study, the CFD solution will serve as the reference solution. Other researchers have found that CFD methods perform adequately in similar thermosiphon flows [57]. In order to properly assess the coupled results, four models were created: a STAR-CCM+ standalone, a TRACE standalone, and two coupled Janus models. The TRACE model is shown alongside an annotated diagram illustrating the loop in Fig. 5-10.

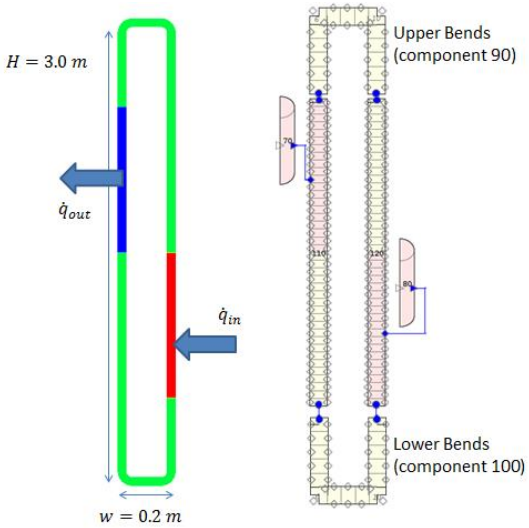

Fig. 5-10. Geometry of the natural circulation loop for STAR-CCM+ (left) and TRACE(right.)

The first Janus case examined in the study applies a volume interface to the lower set of bends (component 100 in TRACE), while a second case applies interfaces to both sets of bend (components 90 and 100).

5-3.2 Steady State Results

The mass flow rates obtained from various heating rates for four test cases are shown in Fig. 5-11. As a first observation, the TRACE and STAR-CCM+ standalone results differ substantially. In particular, the TRACE model overestimates the mass flow rate with respect to STAR-CCM+. This is due to the the assumption of fully developed flow used in TRACE, to the fact that multi-dimensional effects are not taken into account, and to the lack of appropriate localized loss coefficients for the bends. In the present work, no attempt is made to reduce the differences between standalone TRACE and CFD simulations, as the aim of the section is to illustrate the impact of the coupling scheme. Using the CFD solution to correct for the pressure drops in the bottom bends (JANUS-bottom in Fig. 5-11) and in both bottom and top bends (JANUS-all in Fig. 5-11 have the effect of consistently bringing the results closer to the CFD standalone solution. While some difference still remains in the predicted mass flow rates with respect to the CFD standalone reference solution, Fig. 5-11 shows that the difference has been significantly reduced through the applied coupling methods. The remaining discrepancy is likely caused by small density differences that are exacerbated by the large gravity pressure drops through the vertical sections.

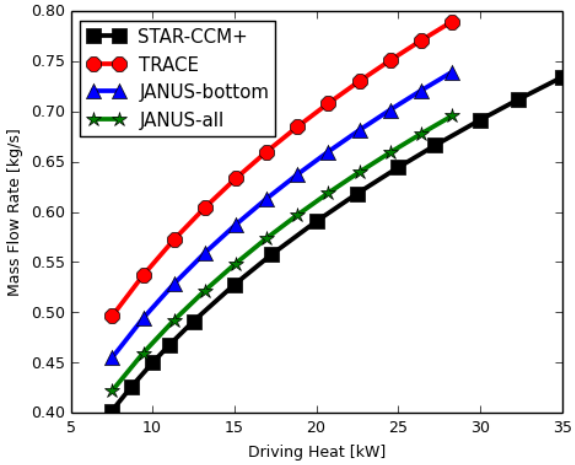

Fig. 5-11. Mass flow rates resulting from 4 different models of the natural circulation loop.

The effect of coupling is more clearly established in Fig. 5-12, where the pressure drop across selected loop components are plotted against the loop mass flow rate. Curves from coupled components collapse onto the STAR-CCM+ curve, while those from uncoupled components collapse onto the TRACE curve, verifying the implementation of the Janus coupling interfaces.

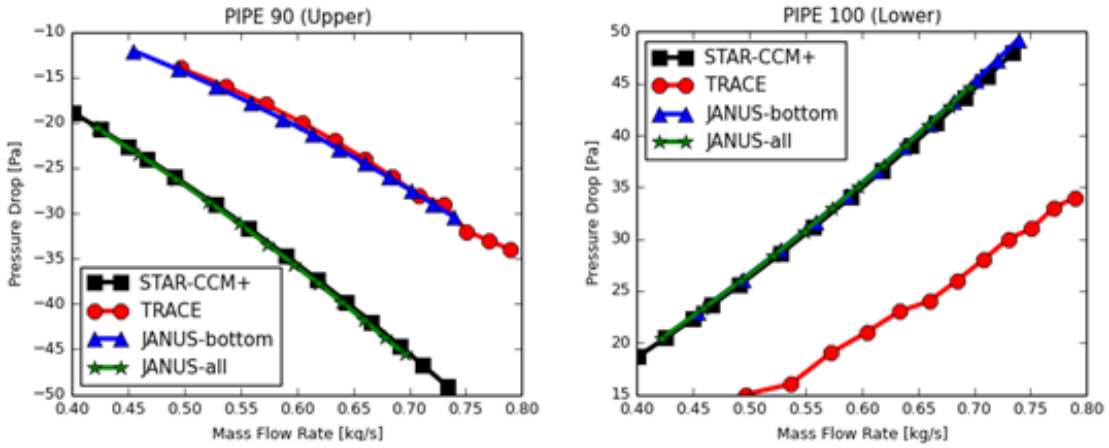

Fig. 5-12. Pressure drops as functions of mass flow rates for the top and bottom sections of the natural circulation loop.

5-3.3 Stability and Convergence

Variables passed between TRACE and STAR-CCM+ over several coupled iterations are normalized to their ultimate value and plotted in Fig. 5-13 to Fig. 5-15. Fig. 5-13 contains mass flow rates (normalized to converged value for ease of comparison) passed from TRACE to STAR-CCM+ over the course of iteration for three selected powers spanning the range of heating used in this study. The three cases behave quite similarly and are essentially converged after just 4 coupled iterations.

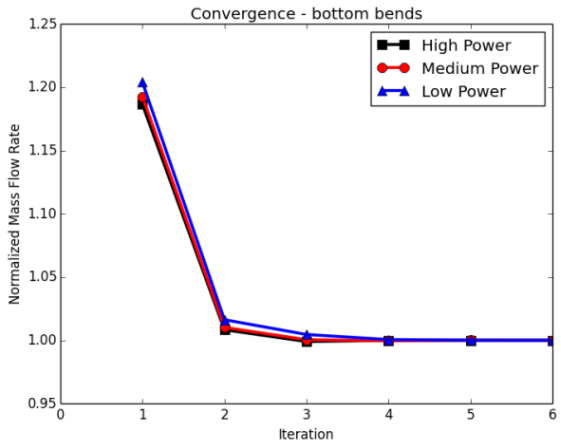

Fig. 5-13. Flow rate convergence for selected cases.

The next variable considered was the friction factor passed from STAR-CCM+ to TRACE as shown in Fig. 5-14. Again, results are normalized to converged values.

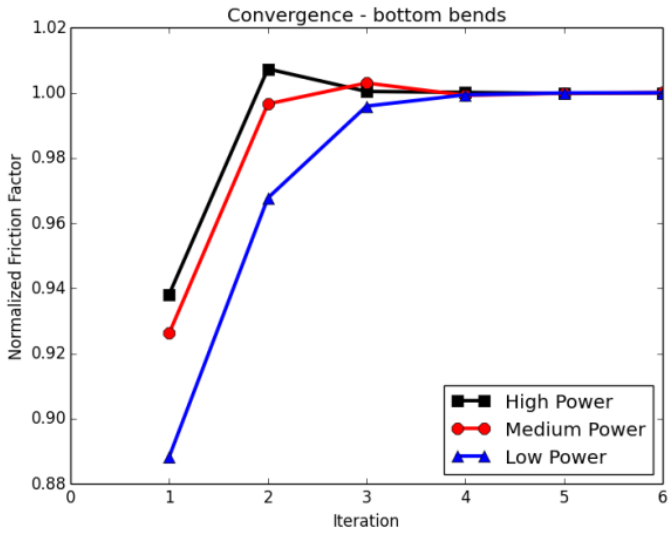

Fig. 5-14. Friction factor convergence for selected cases.

In all cases, the initial conditions in the STAR-CCM+ portion of the simulation consisted of a mass flow rate of $0.5\,kg/s$ at a temperature of $550.0\,K$. In order to test the stability of the solution to perturbations in the initial conditions, the initial mass flow rate in the STAR-CCM+ simulation was varied over a large range with the results plotted in the Fig. 5-15.

Fig. 5-15 shows that Janus is robust to a large range of initial conditions. The results converge within a few iterations (less than 10) for all tested initial conditions. As expected, for the simulations to which Janus has been applied, the vast majority of the computation time has been used by STAR-CCM+ iterations. Except in rare cases, the time required for TRACE calculation and data transfer has proven to be practically negligible. The previous cases were run on a desktop PC (8x Intel Core i7-2600 CPU @ 3.40 GHz) with five parallel STAR-CCM+ processes. The total elapsed time for a coupled simulation was approximately 72 seconds. For comparison, a standalone STAR-CCM+ simulation for the entire loop required more than two hours on the same system.

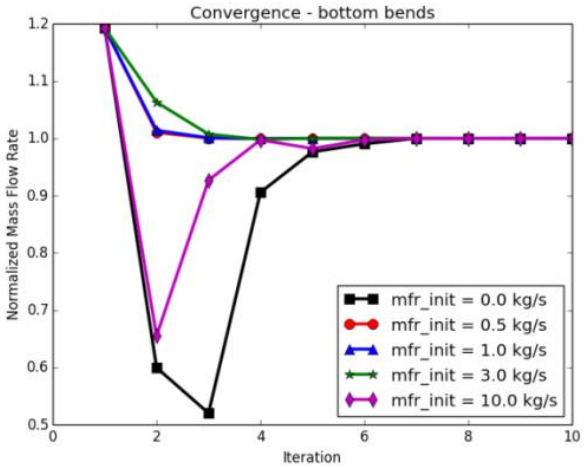

Fig. 5-15. Convergence sensitivity of loop flow rate to initial mass flow rate.

5-4 Conclusions

In this chapter, a novel domain overlapping method is presented for the coupling of CFD and 1D system codes. The method allows on-the-fly correction of non-inertial pressure drops in the momentum equations of the 1D code, based on the CFD solution which is markedly more accurate under certain flow conditions. The performance of the novel method is compared to a domain decomposition coupling scheme using a variety of test cases. Consistency, stability, and convergence characteristics of the two coupling methods are compared with the objective of identifying strengths and weaknesses.

The proposed domain overlapping method proved feasible and accurate for all cases tested, both in steady state and transient conditions. Results showed that the developed domain overlapping coupling method exhibits superior convergence and numerical stability when compared to the domain decomposition approach. We showed that domain decomposition coupling results in a geometric discrepancy that requires additional iterations to overcome. In transient mode, this discrepancy can disrupt the entire simulation and result in unphysical results for large time steps. Additionally, since the domain overlapping method relies on changes in pressure rather than absolute pressures, a dimension of sensitivity is avoided. Conversely, the implementation of a domain decomposition approach is significantly easier than domain overlapping methods and automatically enforces consistency between the two codes.

Most modern best-estimate system codes also include a pseudo-3D formulation of the momentum equation to model 3D components such as the reactor pressure vessel. These components are instrumental in the simulation of reactor transients. While additional complexity is added by the inability to easily define cross section-averaged flow paths, many of the ideas presented here are extensible to 3D geometries. The extension of our domain overlapping approach to the coupling with system code 3D components will be reported in the next chapter.

Chapter 6. Domain Overlapping Coupling Methods for 3-D Systems

The 1-D simulations of the previous sections provided an excellent platform for verification, exhibition, and simple analysis of domain overlapping coupling fundamentals. In particular, the idea of coupling by friction factors adjusted to allow inertial contributions to be calculated independently by TRACE and STAR-CCM+ was explored in the context of several systems in steady state and transient modes. The domain overlapping method was found to outperform domain decomposition in terms of convergence and stability, justifying the added complexity of the method.

However, many scenarios that motivate NPP simulation such MSLB and ATWS, involve aspects that are irreducibly multi-dimensional, such as the transport properties of the lower plenum of a reactor vessel. In this chapter, the ideas developed in previous chapters are extended to more complex formulations. TRACE models higher dimensional flow domains like reactor pressure vessels with components called "vessels" that support simple geometries in Cartesian and cylindrical coordinates. A complication arises in the assumption that both codes calculate the same inertial contribution to the pressure drop as a result of the multi-dimensional nature of the coupled region. In 1-D geometries, ensuring that both domains kept the same mass flow rate at the inlet was sufficient to ensure consistent velocity fields, and therefore inertial consistency, because only one possible flow path existed. In general 3-D geometries, distinct flow paths do not exist, and a more sophisticated approach to inertial consistency is necessary.

In this chapter, two domain overlapping coupling methods based on Temporal Inertial Interfacing (TII) are introduced. The Inertial Domain Overlapping (IDO) method is an approach that calculates inertia-corrected friction factors and uses a rudimentary approach to velocity field consistency. The Stabilized Inertial Domain Overlapping (SIDO) method improves on IDO by adding correction factors to both the friction factor and the velocity field consistency formulation that more closely integrates the coupling into the nonlinear iteration procedure used by TRACE. A method based on Spatial Inertial Interfacing (SII) is also briefly discussed.

6-1 Coupling Strategy

6-1.1 Momentum Equation Coupling

Under isothermal incompressible three-dimensional single phase liquid water flow conditions (applicable to test cases used here), the discretized TRACE momentum equation in the α direction (where α can be $x, y, z, r,$ or θ) reduces to Eq. 6-1, along with analogous equations for the other two accompanying directions:

$$\frac{V^{n+1}_{\alpha,i+\frac{1}{2},j,k} - V^{n}_{\alpha,i+\frac{1}{2},j,k}}{\Delta t} + (V \cdot \nabla V)_{\alpha,i+\frac{1}{2},j,k} = -\frac{1}{\rho}\frac{p^{n+1}_{i+1,j,k} - p^{n+1}_{i,j,k}}{R_\alpha \Delta\alpha_{i+\frac{1}{2},j,k}} - K^{n}_{\alpha,i+\frac{1}{2},j,k}\left[2V^{n+1}_{\alpha,i+\frac{1}{2},j,k} - V^{n}_{\alpha,i+\frac{1}{2},j,k}\right]\left|V^{n}_{\alpha,i+\frac{1}{2},j,k}\right|, \quad 6\text{-}1$$

where $V^{n}_{\alpha,i+\frac{1}{2},j,k}$ is the α-component of velocity at the edge between adjacent cells with indices (i,j,k) and $(i+1,j,k)$, Δt is the timestep, $p_{i,j,k}$ is the volume-averaged pressure of cell (i,j,k), ρ is the density, Δt is the timestep, $\Delta\alpha$ is the mesh size in the α direction, and R_α is a length multiplier that is unity for all directions except $\alpha = \theta$ in which R_α is the radius at which the cell centers lie. All three directions are coupled through the convective acceleration terms $V \cdot \nabla V$, as well as through mass conservation, or continuity This formulation is valid for both Cartesian and cylindrical coordinate systems. The effects of friction and turbulence are modeled through the coefficient $K^{n}_{\alpha,i+\frac{1}{2},j,k}$ which is calculated through correlations, such as the Churchill correlation [16]. For brevity, unnecessary indices will be omitted for the remainder of this chapter. Comparison to the continuous Navier-Stokes equations makes clear the role of the coefficient as a model for the divergence of the stress tensor **T**, including both viscous and turbulent stresses. As shown in Eq. 6-2 the K coefficient can be related to the *Fanning* friction factor f_F used in TRACE (not to be confused with the Darcy friction factor which is 4 times larger):

$$-\frac{\nabla \cdot \mathbf{T}}{\rho} \rightarrow KV^2 = 2f_F \frac{R_\alpha \Delta\alpha}{D_h} V^2. \quad 6\text{-}2$$

The friction factor can be written as a normalized pressure gradient as shown in Eq. 6-3 [46].

$$f_F = -(\nabla p \cdot \hat{\boldsymbol{e}}_{\boldsymbol{\alpha}})_{fric} \frac{D_h}{2\rho V^2} \quad 6\text{-}3$$

where D_h is the hydraulic diameter, ρ is the fluid density (water in this report), $\hat{\boldsymbol{e}}_{\boldsymbol{\alpha}}$ is a unit vector in the α direction, and V is the mean fluid velocity. A primary objective of the proposed coupling method is to adjust the TRACE momentum equation in a specific region to reproduce the results of higher fidelity CFD models. Rather than accomplishing this through adding a momentum source to Eq. 6-1, we instead modify friction factors in TRACE for three reasons: 1) the friction factor is essentially a normalized pressure gradient and is thus easily interpreted, 2) the friction factors used in TRACE are evaluated at the previous time step, making it straightforward to modify the term in a consistent way, and 3) the stability of TRACE has already been thoroughly studied by its developers for the friction factor as currently implemented; utilizing the same structure allows us to leverage this work.

STH codes such as TRACE often use a staggered grid discretization, defining scalar quantities like pressure and temperature, interpreted as averages over the control volumes (CVs), in the center of the CVs [58] [16]. Defined at the boundaries of the CV are vector quantities such as velocity, as well as friction factors that account for the frictional pressure difference between

adjacent cells. With staggered grids, interpolation is necessary to calculate the velocity at the center of a CV or the pressure at the CV boundary.

6-1.2 TRACE Solution by Nonlinear Iteration

The general outline of the TRACE solution procedure is given in Fig. 6-1.

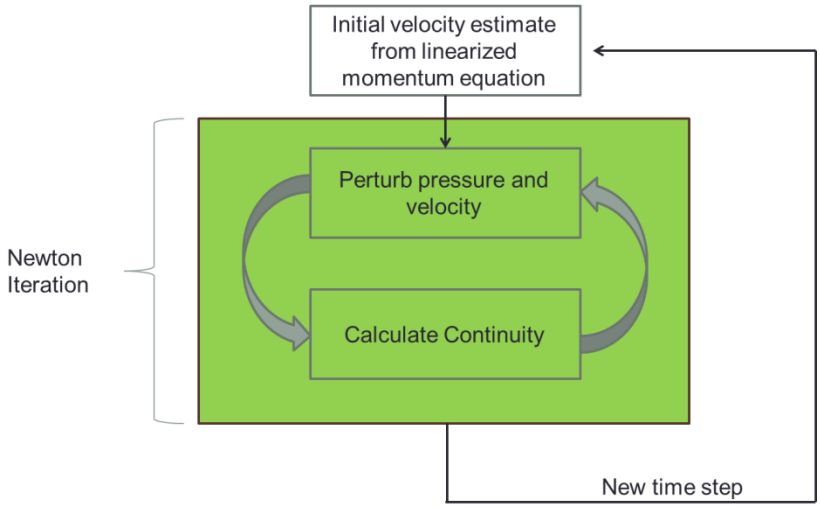

Fig. 6-1. Schematic of nonlinear iteration used in the TRACE solution procedure

TRACE begins a time step by calculating an initial estimate of the new time velocity ($\tilde{V}_\alpha^{n+1,0}$, where the 0 superscript signifies the initial, unadjusted estimate and the tilde represents the intermediate nature of the value) from a version of Eq. 6-1 built from previous time step pressures (i.e. replace p^{n+1} with p^n in Eq. 6-1). As shown in Eq. 6-4, this equation is linear in $\tilde{V}_\alpha^{n+1,0}$ and can be solved directly:

$$\tilde{V}_\alpha^{n+1,0}\left[1+2\Delta t K^n_{\alpha,i+\frac{1}{2},j,k}\right] = V^n_{\alpha,i+\frac{1}{2},j,k} - \Delta t\left[\frac{1}{\rho}\frac{p^n_{i+1,j,k}-p^n_{i,j,k}}{R_\alpha \Delta\alpha_{i+\frac{1}{2},j,k}} - K^n_{\alpha,i+\frac{1}{2},j,k} V^n_{\alpha,i+\frac{1}{2},j,k}\left|V^n_{\alpha,i+\frac{1}{2},j,k}\right|\right]. \quad 6\text{-}4$$

After calculating $\tilde{V}_\alpha^{n+1,0}$, the variable given by Eq. 6-5 is stored, characterizing the relationship of changes in pressure drop between adjacent cells and the velocity across the edge shared by the adjacent cells:

$$\left.\frac{dV}{d\Delta p}\right|_{j+\frac{1}{2}} = \frac{\Delta t}{\rho R_\alpha \Delta\alpha\left[1+\Delta t\left(2K^n_{j+\frac{1}{2}}\left|V^n_{j+\frac{1}{2}}\right| + \beta\nabla_{j+\frac{1}{2}} V^n_{j+\frac{1}{2}}\right)\right]}. \quad 6\text{-}5$$

Eqs. 6-4 and 6-5 are built from a linearized version of the momentum equation. The fully nonlinear equations of motion are solved with a Newton-Raphson iteration cycle, which can be conceptualized as adjusting the pressure field based on a new velocity estimate, followed by

adjusting the velocity field based on the newest pressure field estimate. Specifically, a set of equations is built by perturbing the pressure and velocity variables in the mass and energy conservation equations with the as yet unknown pressure perturbation δp_j^m. The pressure variable is replaced with Eq. 6-6:

$$p_j^{n+1,m+1} = p_j^{n+1,m} + \delta p_j^m. \tag{6-6}$$

where j refers to a cell and m refers to the iteration number of the Newton cycle. The velocity perturbation shown in Eq. 6-7 is built from the pressure perturbation using Eq. 6-5:

$$V_{j+\frac{1}{2}}^{n+1,m+1} = V_{j+\frac{1}{2}}^{n+1,m} + \left.\frac{dV}{d\Delta p}\right|_{j+\frac{1}{2}} \left(\delta p_j^m - \delta p_{j+1}^m\right). \tag{6-7}$$

For incompressible isothermal flow, the linearized mass conservation equation with perturbed values is shown in Eq. 6-8:

$$\frac{\left.\frac{dV}{d\Delta p}\right|_{j+\frac{1}{2}} \left(\delta p_j^m - \delta p_{j+1}^m\right) - \left.\frac{dV}{d\Delta p}\right|_{j-\frac{1}{2}} \left(\delta p_{j-1}^m - \delta p_j^m\right)}{\Delta x} = \frac{V_{j+\frac{1}{2}}^{n+1,m} - V_{j-\frac{1}{2}}^{n+1,m}}{\Delta x}. \tag{6-8}$$

The 3-D version is built by adding analogous terms for the remaining two directions. Applying the perturbed balance equation to each cell yields a system of expressions to be solved simultaneously for the pressure perturbations δp_j^m, which are used to update the pressure and velocity fields. This cycle continues until convergence, given by ($\lim_{m\to\infty} \tilde{V}_\alpha^{n+1,m} = V_\alpha^{n+1}$, $\lim_{m\to\infty} \delta p_j^m \to 0$), or a maximum number of iterations is reached.

6-2 Spatial Inertial Interfaces

Similar to the 1-D inertial interface discussed in §4-4, the 3-D friction factors can be formulated by considering the spatial derivative terms of the pressure gradient. In the 1-D formulation, the vector equation Eq. 6-9 was converted to a scalar equation by dotting the integrand with a flow path vector field:

$$\langle \nabla p \rangle_{NI} = \langle \nabla \cdot \mathbf{T} \rangle - \rho \langle \mathbf{v} \cdot \nabla \mathbf{v} \rangle. \tag{6-9}$$

No such vector field is easily identifiable in general 3-D geometries, we instead proceed by individually considering each component of the vector equation. In order to correctly reproduce system wide pressures with such a formulation, friction factors must be based on local pressure drops, rather than the global formulation that was possible for 1-D components. This process is now illustrated for the axial direction of a Cartesian grid.

The Cartesian version of the vessel component breaks a region into a user-specified number of parallelepiped regions based on x,y, and z coordinates. Each face of each cell is connected to

either zero cells or exactly one, meaning that no cell face is interfaced with more than one other cell, significantly simplifying flux calculations. For the local non-inertial pressure gradient coupling, only the pressure drop between adjacent cells is of concern. Based on this, the derivation for the non-inertial pressure drop begins by integrating the non-inertial pressure gradient over two cells, starting from their shared face. This is depicted in Fig. 6-2 for the example of the z direction.

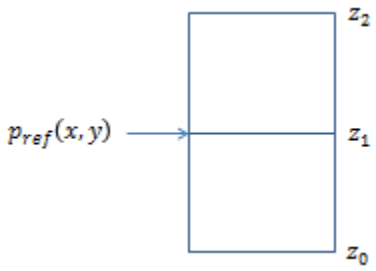

Fig. 6-2. Depiction of cell geometry to be integrated over for non-inertial pressure gradient coupling

The change in volume-averaged pressure between the two cells is given by Eq. 6-10:

$$\Delta\langle p\rangle_{ccm}^{V} = \frac{1}{V_2}\iiint_{V_2} p(\vec{r})d^3\,\vec{r} - \frac{1}{V_1}\iiint_{V_1} p(\vec{r})d^3\,\vec{r}. \qquad 6\text{-}10$$

Integration by parts of this equation yields Eq. 6-11, an expression for the change in volume-averaged pressure in terms of the pressure gradient:

$$\Delta\langle p\rangle^{V} = \frac{1}{V_2}\iiint_{V_2}(z_2 - z)\frac{\partial p}{\partial z}dxdydz - \frac{1}{V_1}\iiint_{V_1}(z - z_0)\frac{\partial p}{\partial z}dxdydz. \qquad 6\text{-}11$$

The formulation in Eq. 6-11 can be used to calculate non-inertial pressure drops by replacing $\partial p/\partial z$ with the non-inertial pressure gradient:

$$\langle p\rangle_1^V - \langle p\rangle_2^V = \langle f(z)\frac{\partial p}{\partial z}\rangle_{NI}^{\mathbf{1+}} + \langle f(z)\frac{\partial p}{\partial z}\rangle_{NI}^{\mathbf{2-}}, \qquad 6\text{-}12$$

where

$$\langle f(z)\frac{\partial p}{\partial z}\rangle_{NI} = \frac{1}{V}\oiint fT_{zj}n_j dS - \frac{1}{V}\iiint_V T_{zz}\frac{\partial f}{\partial z}dV - \frac{1}{V}\iiint_V \rho f v_i\frac{\partial v_z}{\partial x_i}dV. \qquad 6\text{-}13$$

The "1 +" and "2 −" superscripts of Eq. 6-12 refer to the cell number as well as whether $f(z)$ is increasing or decreasing with z. The function $f(z)$ refers to the linear function included in the integrands of Eq. 6-11 (i.e. the "+" superscript → $f(z) = z - z_0$ and the "-" superscript → $f(z) = z_2 - z$). As shown in Fig. 6-3, the value of $f(z)$ is 0 at the edges away from the interface cell and Δz at the interface. Cells are not required to have the same value of Δz and to maintain

functional continuity, $f(z)$ must be thought of as only being defined over each cell, rather than over the two adjoined cells.

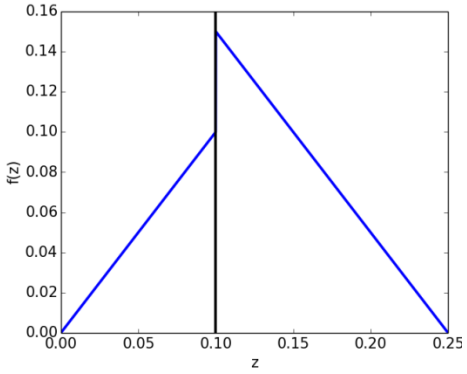

Fig. 6-3. Example of linear piecewise continuous function f(z) for the case of two cells of different lengths.

The non-inertial friction factor for a face in the z direction is then given by Eq. **Error! eference source not found.**:

$$f_{NI,z} = \frac{1}{\Delta s_\alpha}\frac{D_h}{2\rho V^2}\left[\frac{1}{V}\oiint f T_{zj} n_j dS - \frac{1}{V}\iiint_V T_{zz}\frac{\partial f}{\partial z}dV - \frac{1}{V}\iiint_V \rho f v_i \frac{\partial v_z}{\partial x_i}dV\right]. \qquad 6\text{-}14$$

An unfortunate characteristic feature of the SII friction factor is its sensitivity to the specific form of the stress tensor **T**, which can change significantly with turbulence model choice.

6-3 Temporal Inertial Interface

In addition to the SII, the non-inertial friction factor can be calculated with a temporal formulation. In this section, the principles of friction factor coupling developed in §6-1.1 are applied to the solver described in §6-1.1 in order to construct two domain overlapping approaches. A base formulation, referred to as the Inertial Domain Overlapping (IDO) coupling method is built by forming a non-inertial pressure gradient and directly applying that to the coupled friction factor calculation. A more advanced method, referred to as the Stabilized Inertial Domain Overlapping (SIDO) coupling method, is formulated by performing a deeper analysis of the mathematical structure of the TRACE solver and correcting for secondary effects of the coupling on the TRACE flow solver. The two methods are found to behave quite similarly, except for challenging conditions in which the SIDO method exhibits superior stability properties.

6-3.1 Computing Friction Factors from CFD data

Starting from the continuous Navier-Stokes equations, a pressure gradient vector-valued function can be defined as a combination of three terms as shown in Eq. 6-15. The first term on the right of the equality, the inertial contribution, describes the effects of unsteady velocities. The second

term captures the effects of acceleration due to velocity gradients and is referred to as the acceleration or convective pressure gradient. Finally, the frictional pressure gradient resulting from viscous dissipation is the third term on the right. In cases of turbulent flow, consider **v** to be the Reynolds-averaged velocity and for **T** to include Reynolds stresses:

$$\nabla p = -\rho \frac{\partial \mathbf{v}}{\partial t} - \rho \mathbf{v} \cdot \nabla \mathbf{v} + \nabla \cdot \mathbf{T}. \qquad 6\text{-}15$$

The TRACE momentum balance of Eq. 6-1 is comprised of directly analogous terms, each of which must be specifically addressed by a successful coupling formulation. In TRACE, the convective term, $(V \cdot \nabla V)_{x,i+\frac{1}{2},j,k}$ in Eq. 6-1 is easily eliminated from the momentum equation for edges in the coupled region. Similarly, the term $\beta \nabla_{j+\frac{1}{2}} V^n_{j+\frac{1}{2}}$ can be easily omitted from Eq. 6-5. The combined effects of friction, turbulence, and convective acceleration computed with CFD are therefore combined into the friction coefficient used in TRACE. The inertial term, however, is a byproduct of the calculation procedure of Eqs. 6-1, 6-6, and 6-7 and cannot be excluded from TRACE. The term is instead corrected through velocity field manipulation via the velocity-matching functionality introduced in §6-3.2. Therefore, only the non-inertial (NI) pressure drop terms (acceleration and friction) are to be corrected through a modified friction coefficient. Based on this, a NI pressure gradient is defined by subtracting the inertial contribution from the total pressure gradient:

$$\nabla p_{NI} = \nabla p_{tot} + \rho \frac{\partial \mathbf{v}}{\partial t}. \qquad 6\text{-}16$$

We recall that the friction factor can be interpreted as a normalized pressure gradient, and that TRACE pressure is consistent with a volume-averaged pressure in STAR-CCM+. A friction factor computed from CFD data must thus be based on changes in volume-averaged pressure with respect to the volumes that make up the TRACE nodalization. The geometric definitions of TRACE are automatically passed to STAR-CCM+, which uses the data to overlay the TRACE mesh on the STAR-CCM+ mesh. Specifically, the Janus interface that couples STAR-CCM+ with TRACE builds data structures with elements for each cell and edge of the TRACE geometry.

During coupling startup procedures, sub-surfaces are automatically built in the CFD model for each cell face of the 3D system. During the time between STAR-CCM+ and TRACE execution, surface integrals are performed over the faces to calculate the area-averaged CFD velocity analogous to the TRACE velocity across the same edge. More information on how integrals are calculated can be found in Appendix D.

Once values for the velocity normal to each cell face and average pressure of each cell are calculated and stored, it is possible to calculate the non-inertial pressure gradients needed for the volumetric coupling. The first step is to calculate the volume-averaged pressure for each cell.

Next $\Delta p_{i\to j}$, the pressure drop across the edges defined by each pair of adjacent cells V_i and V_j is calculated as shown in Eq. 6-17:

$$\Delta p_{i\to j} = \iiint_{V_i} p(\vec{x}) d^3\vec{x} - \iiint_{V_j} p(\vec{x}) d^3\vec{x}. \qquad 6\text{-}17$$

The portion of the pressure drop resulting from inertia, $\Delta p_{I,\alpha}$, is then estimated from area-averaged velocities as shown in Eq. 6-18:

$$\Delta p_{I,\alpha} = -R_\alpha \frac{\Delta\alpha_{V_2} + \Delta\alpha_{V_1}}{2} \frac{\rho}{\Delta t} \frac{1}{A_\Omega} \left[\iint_\Omega v_\alpha^{n+1} dS - \iint_\Omega v_\alpha^n dS \right], \qquad 6\text{-}18$$

where α again refers to any coordinate among (x, y, z, r, θ), Ω refers to the surface defining the edge, A_Ω is the surface area of the edge, while $R_\alpha = \frac{r_{max}+r_{min}}{2}$ for the θ coordinate (where r_{max} is the radius defining the upper bound of the cell and r_{min} defines the lower bound) and $R_\alpha = 1$ for all other coordinates (x, y, z, r). A non-inertial friction factor for use in the STH momentum equation for coupled components can then be formed as shown in Eq. 6-19:

$$f_{NI,i\to j} = \frac{\Delta p_{NI}}{\Delta s_\alpha} \frac{D_h}{2\rho V^2} = \frac{\Delta p_{i\to j} - \Delta p_{I,\alpha}}{\Delta s_\alpha} \frac{D_h}{2\rho V^2}, \qquad 6\text{-}19$$

where Δs_α is shorthand for the distance between centers of the two cells adjoining the edge:

$$\Delta s_\alpha = R_\alpha \frac{\Delta\alpha_{V_2} + \Delta\alpha_{V_1}}{2}. \qquad 6\text{-}20$$

In coupled simulations, Δp_{NI} is the actual value passed to TRACE from STAR-CCM+ and all other variables in Eq. 6-19 are as defined in TRACE.

6-3.2 Velocity Field Coupling

A general velocity field is determined based on three primary influences: boundary conditions, continuity, and the pressure field. Through these mechanisms, a pressure-velocity feedback is established, an example of which is higher velocities yielding higher frictional losses. In a coupled simulation, where TRACE friction factors are specified from an outside source, this feedback is disrupted. For example, in a coupled steady-state simulation, any nonzero velocity across a face can produce any pressure drop across that face, depending only on the friction factor. The consequences of this effect are further explored in §7-1.

"Velocity Matching Faces" (VMFs) are implemented in Janus to reinstate the pressure-velocity feedback. Ideally, a VMF applied to a specific edge causes TRACE to calculate the same velocity as the equivalent STAR-CCM+ edge. VMFs are user-specified for an array of faces such that consistency is enforced between TRACE and STAR-CCM+, but also such that enough faces are left unconstrained to allow TRACE to independently enforce mass conservation. For

VMF configurations that fully dictate the flow field, the effects of the specific configuration are minimal, as will be demonstrated.

As a prelude to discussing the specific VMF implementation, the Newton iteration implemented in TRACE is more closely examined. Eq. 6-7 can be rearranged to form Eq. 6-21, an expression for the change in pressure drop across an edge at the m^{th} step of the iteration:

$$d\Delta P^{m}_{j+\frac{1}{2}} = \left(\delta p^{m}_{j} - \delta p^{m}_{j+1}\right) = \frac{\tilde{V}^{n+1,m+1}_{\alpha,j+\frac{1}{2}} - \tilde{V}^{n+1,m}_{\alpha,j+\frac{1}{2}}}{\left.\frac{dV}{d\Delta p}\right|_{j+\frac{1}{2}}}. \qquad 6\text{-}21$$

The relationship for the new time pressure drop across the edge is shown in Eq. 6-22, calculated by summing over all inner iterations:

$$\Delta P^{n+1}_{j+\frac{1}{2}} = \Delta P^{n}_{j+\frac{1}{2}} + \sum_{m=1}^{M} d\Delta P^{m}_{j+\frac{1}{2}} = \Delta P^{n}_{j+\frac{1}{2}} + \left(\left.\frac{dV}{d\Delta p}\right|_{j+\frac{1}{2}}\right)^{-1}\left(V^{n+1}_{\alpha,j+\frac{1}{2}} - \tilde{V}^{n+1,0}_{\alpha,j+\frac{1}{2}}\right), \qquad 6\text{-}22$$

where M is the maximum number of inner iterations allowed by TRACE. Restated, Eq. 6-22 represents two useful relationships. First, the difference between the initial estimate of the velocity and the final new time velocity is shown in Eq. 6-23:

$$\left(V^{n+1}_{\alpha,j+\frac{1}{2}} - \tilde{V}^{n+1,0}_{\alpha,j+\frac{1}{2}}\right) = \left(\Delta P^{n+1}_{j+\frac{1}{2}} - \Delta P^{n}_{j+\frac{1}{2}}\right)\left.\frac{dV}{d\Delta p}\right|_{j+\frac{1}{2}}. \qquad 6\text{-}23$$

Additionally, the total change in pressure drop in a time step ($\Delta\Delta p$) is shown in Eq. 6-24:

$$\Delta\Delta p_{j+\frac{1}{2}} = \left(\left.\frac{dV}{d\Delta p}\right|_{j+\frac{1}{2}}\right)^{-1}\left(V^{n+1}_{\alpha,j+\frac{1}{2}} - \tilde{V}^{n+1,0}_{\alpha,j+\frac{1}{2}}\right). \qquad 6\text{-}24$$

In the IDO coupling method, $\tilde{V}^{n+1,0}_{\alpha,j+\frac{1}{2}}$ is replaced with a velocity calculated from STAR-CCM+ for the analogous edge, V_{CFD}. The new time velocity can then be estimated from Eq. 6-23 as shown in Eq. 6-25:

$$V^{n+1}_{\alpha,j+\frac{1}{2}} = V_{CFD} + \left(\Delta P^{n+1}_{j+\frac{1}{2}} - \Delta P^{n}_{j+\frac{1}{2}}\right)\left.\frac{dV}{d\Delta p}\right|_{j+\frac{1}{2}}. \qquad 6\text{-}25$$

Generally $\left.\frac{dV}{d\Delta p}\right|_{j+\frac{1}{2}}$ is very small and $V^{n+1}_{\alpha,j+\frac{1}{2}} \approx V_{CFD}$. The IDO method does not further consider the consequences of $\tilde{V}^{n+1,0}_{\alpha,j+\frac{1}{2}}$ replacement. The VMF implementation used in the SIDO method is realized by instead replacing $\tilde{V}^{n+1,0}_{\alpha,j+\frac{1}{2}}$ with V_1, a "corrected" velocity defined in Eq. 6-26:

$$V_1 = V_{CFD} - \frac{\left(\Delta P^{n+1}_{j+\frac{1}{2}} - \Delta P^{n}_{j+\frac{1}{2}}\right)\Delta t}{\rho \Delta s_\alpha \left(1 + 2\Delta t K^n_{j+\frac{1}{2}} \left|V^n_{j+\frac{1}{2}}\right|\right)}. \qquad 6\text{-}26$$

Performing this substitution in Eq. 6-23 leads to Eq. 6-27, suggesting that the new time velocity can be driven to match the CFD velocity, assuming that the value used for $\left(\Delta P^{n+1}_{j+\frac{1}{2}} - \Delta P^{n}_{j+\frac{1}{2}}\right)$ is accurate:

$$\left(V^{n+1}_{\alpha,j+\frac{1}{2}} - V_{CFD}\right) = 0. \qquad 6\text{-}27$$

The SIDO method further considers the action of $\tilde{V}^{n+1,0}_{\alpha,j+\frac{1}{2}}$ substitution on the pressure drop change in a time step, an expression for which can be calculated by subtracting the value of $\Delta\Delta p$ that results from a VMF from the unaffected equivalent, shown in Eq. 6-28:

$$E(\Delta\Delta p) = \frac{\tilde{V}^{n+1,0}_{\alpha,j+\frac{1}{2}} - V_1}{\left.\frac{dV}{d\Delta p}\right|_{j+\frac{1}{2}}}. \qquad 6\text{-}28$$

The $E(\Delta\Delta p)$ term can be used to calculate a stabilized friction factor for VMF faces as shown in Eq. 6-29:

$$f_{NI} = \frac{\Delta p_{tot} - \Delta p_{I,\alpha} - E(\Delta\Delta p)}{\Delta s_\alpha} \frac{D_h}{2\rho V^2}. \qquad 6\text{-}29$$

The stabilized friction factor used in the SIDO method adjusts the pressure drop incoming from STAR-CCM+, already augmented to account for inertial contributions, to mitigate the effects of VMF application on pressure drop across the affected edge.

In order to properly calculate $E(\Delta\Delta p)$, Eq. 6-28 must be evaluated simultaneously with Eqs. 6-4 and 6-5, since the K coefficient in the latter equations depends on f_{NI} which depends on $E(\Delta\Delta p)$. In TRACE, these three equations are linear in their unknowns $\left(E(\Delta\Delta p), \tilde{V}^{n+1,0}_{\alpha,j+\frac{1}{2}}, \left.\frac{dV}{d\Delta p}\right|_{j+\frac{1}{2}}\right)$, and algebraic manipulation can yield an explicit expression for $E(\Delta\Delta p)$ with the specific form dependent on a number of variables internal to TRACE.

6-3.3 Domain Overlapping Method Summary

The IDO and SIDO methods are summarized in Table 6-1. Each method is distinguished by the friction factor and VMF formulation. Both methods attempt to predict the inertial contribution to the pressure drop between two adjacent cells so that it can be removed from the total pressure

drop in order to calculate a non-inertial friction factor. Both methods also seek to allow for velocity field and inertial pressure consistency through VMFs. The SIDO method includes extra correction factors that more closely integrate it into the TRACE nonlinear iteration solution procedure.

Table 6-1. Summary of formulations for the Inertial Domain Overlapping (IDO) coupling method and the Stabilized Inertial Domain Overlapping (SIDO) coupling method.

Method	Friction Factor	Velocity Matching Face
IDO	$f_{NI,i\to j} = \dfrac{\Delta p_{i\to j} - \Delta p_{I,\alpha}}{\Delta s_\alpha}\dfrac{D_h}{2\rho V^2}$	$\tilde{V}^{n+1,0}_{\alpha,j+\frac{1}{2}} \to V_{CFD}$
SIDO	$f_{NI,i\to j} = \dfrac{\Delta p_{i\to j} - \Delta p_{I,\alpha} - E(\Delta\Delta p)}{\Delta s_\alpha}\dfrac{D_h}{2\rho V^2}$	$\tilde{V}^{n+1,0}_{\alpha,j+\frac{1}{2}} \to V_{CFD} - \dfrac{\left(\Delta P^{n+1}_{j+\frac{1}{2}} - \Delta P^{n}_{j+\frac{1}{2}}\right)\Delta t}{\rho\Delta s_\alpha\left(1 + 2\Delta t K^{n}_{j+\frac{1}{2}}\left\lvert V^{n}_{j+\frac{1}{2}}\right\rvert\right)}$

6-4 Data Mapping

It is beneficial to discuss specifically how the data are calculated, as well as the geometry of data transfer. An adjacent pair of representative cells is shown in Fig. 6-4 along with their shared edge for a cylindrical configuration. In this figure, the TRACE nodalization is shown on the right with the CFD equivalent on the left. As indicted in the figure, a volume-averaged pressure is calculated for a region of the CFD mesh corresponding to a TRACE node. Additionally, an area-integrated velocity (units of volume over time) is calculated for a planar section corresponding to the face between the cells. These three quantities are combined to calculate a non-inertial friction factor that is passed to TRACE.

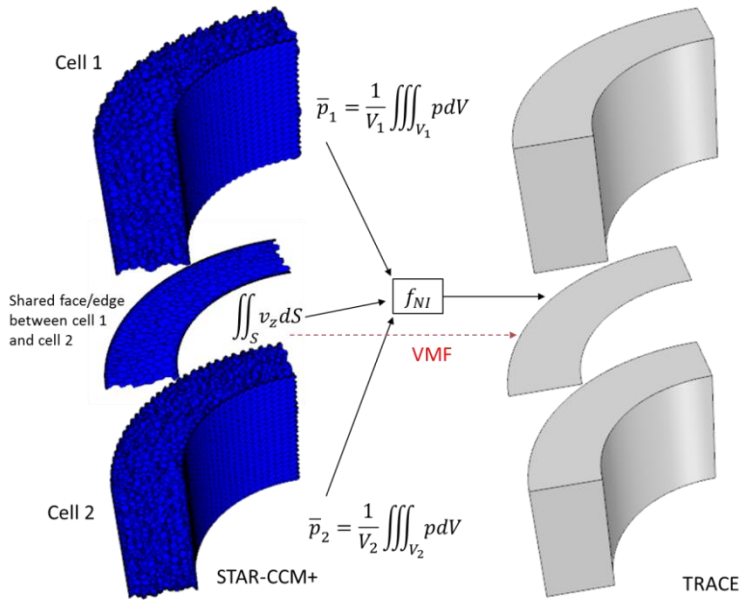

Fig. 6-4. Data transfer schematic for VESSEL coupling interface.

The diagram in Fig. 6-4 further demonstrates that the IDO and SIDO coupling methods affect only edges, since the coupling method seeks to correct pressure differences rather than absolute pressures. The diagram also demonstrates the disparity in mesh resolution. Even with the relatively coarse CFD mesh pictured in Fig. 6-4, there are hundreds to thousands of CFD cells per each TRACE volume. Under such circumstances, the CFD solution can be essentially considered to be continuous in comparison to the STH solution, and only the TRACE discretization is discussed in detail in this dissertation.

6-5 Developing Channel Flow

The simplest useful test case for the Cartesian TII formulation is pipe flow. Shown in Fig. 6-5, a $1.0m$ long straight pipe with a square $0.1\ m \times 0.1\ m$ cross section broken into 10 cells of equal length is used as an initial test case with the goal of enforcing a developing flow pressure profile on the TRACE domain.

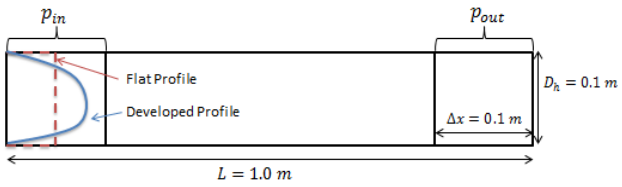

Fig. 6-5. Schematic diagram of test case for developing channel flow

Verification in the steady state mode was carried out by varying the mass flow rate through the pipe with the difference in pressure between the first and last cells ($\Delta p = p_{in} - p_{out}$ as labeled in Fig. 6-5) recorded as an output variable. The data in Fig. 6-6 show that the CFD simulation consistently produced a higher pressure drop for each mass flow rate, as expected due to developing flow. Further, the pressure drops calculated from the coupled simulations collapse directly onto the CFD results, suggesting proper implementation of the friction factor coupling method.

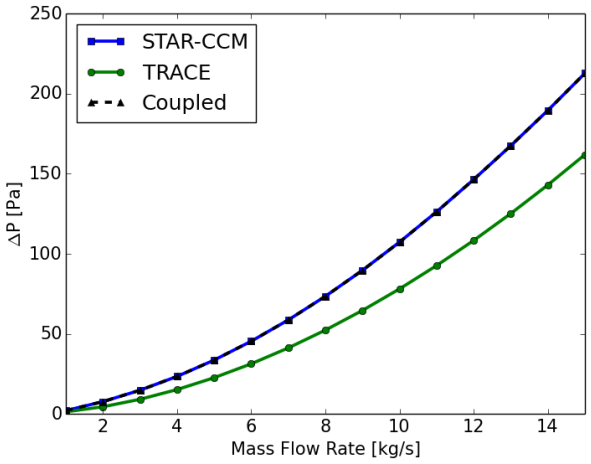

Fig. 6-6. Steady state pressure drops from straight pipe test case.

The pipe was subjected to the mass flow rate of Eq. 6-30 for a transient test case:

$$\dot{m}_{in}(t) = \begin{cases} 10.0\dfrac{kg}{s}, & t \leq 10.0s, \\ 10.0\dfrac{kg}{s} + (t - 10.0s)\dfrac{kg}{s^2}, & 10.0s < t < 15.0s, \\ 15.0\dfrac{kg}{s}, & t \geq 15.0s. \end{cases} \qquad \textit{6-30}$$

During the period $t \in (10.0s, 15.0s)$ the inlet flow rate increases linearly with time. At the edges of this interval, the time derivative of $\dot{m}_{in}(t)$ is discontinuous Fig. 6-7 shows the pressure drop across the coupled pipe. At $t = 9.5s$ the coupling is activated and the TRACE pressure drop jumps from a fully developed value to a developing profile value. Upon incipience of the linearly increasing mass flow at $t = 10.0s$, the pressure drop abruptly jumps due to the suddenly nonzero inertial pressure drop $\nabla p_t = -\rho\frac{\partial \vec{v}}{\partial t}$. At $t = 15.0s$, the transient flow rate is completed and the inertial term vanishes and both pressure drops quickly settle to a flat value with time.

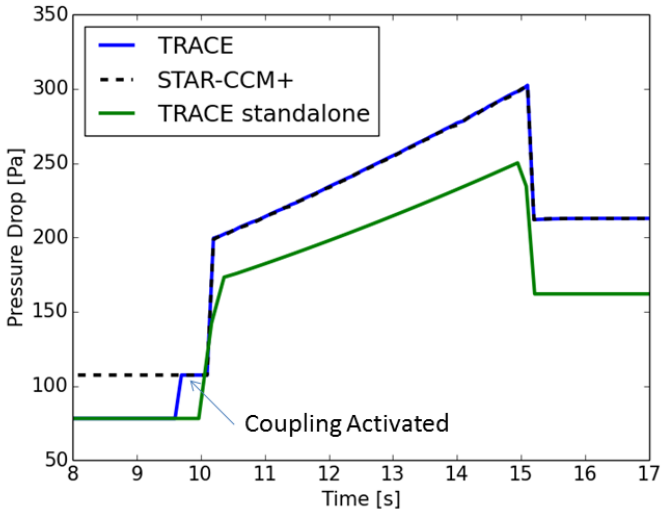

Fig. 6-7. Time dependent pressure drop for coupled solution of the straight pipe transient.

Similar to what was observed in the steady state case, the CFD pressure drop is higher than the TRACE standalone pressure drop due to the effects of flow development. Further, the coupled pressure drop function again falls directly over the STAR-CCM+ pressure drop.

6-6 Cylindrical coupling examples

6-6.1 Radial Direction

The geometry of Fig. 6-8 was created to isolate the radial direction for verification of the 3-D domain overlapping coupling method. The flow domain consists of three radial cells of differing length. Because the region of interest is drained by a square channel with a significant difference in flow area, the CFD velocity field is quite complex. As metrics, two pressure drops, Δp_1 and Δp_2, were defined as shown in Eq. 6-31:

$$\begin{cases} \Delta p_1 = \dfrac{1}{V_2}\iiint_{V_2} p dV - \dfrac{1}{V_1}\iiint_{V_1} p dV\,, \\ \Delta p_2 = \dfrac{1}{V_3}\iiint_{V_3} p dV - \dfrac{1}{V_2}\iiint_{V_2} p dV\,. \end{cases} \qquad 6\text{-}31$$

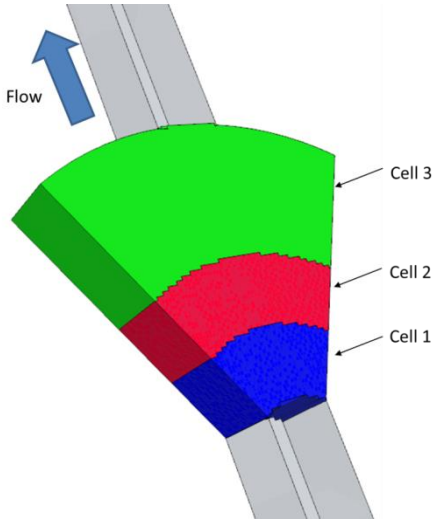

Fig. 6-8. Geometry built to isolate the radial coordinate for coupling verification.

Steady state test cases were performed by varying the inlet mass flow rate and recording pressure drops. Shown in Fig. 6-9, the results demonstrate that STAR-CCM+ and TRACE differ significantly in their standalone predictions of pressure drop, but that the coupled results match STAR-CCM+ very well. The disagreement in standalone solutions owes to the fact that the pressure drop is largely determined by abrupt area changes, which are intrinsically multi-dimensional and distributed.

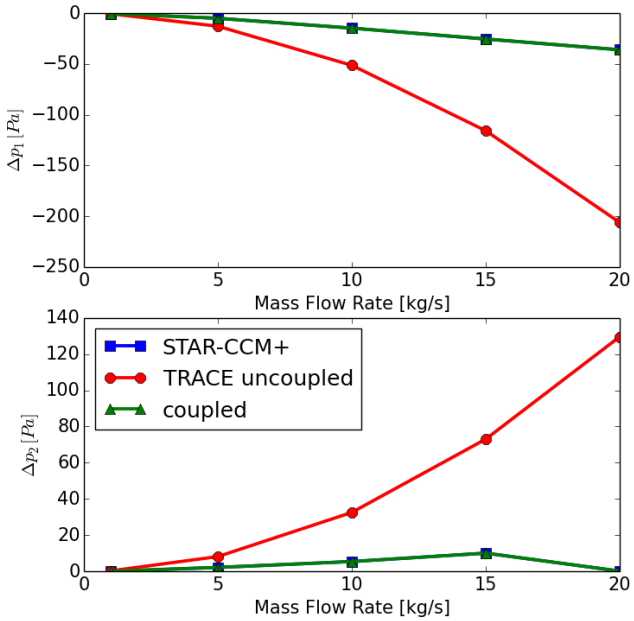

Fig. 6-9. Radial pressure drops calculated in steady state.

For a transient test case, the mass flow rate of Eq. 6-32 was applied to the inlet of the flow domain:

$$\dot{m}_{in}(t) = \begin{cases} 10.0\,\frac{kg}{s}, & t \leq 10.0s, \\ (10.0 + t \times 1.0s^{-1})\,\frac{kg}{s}, & 10.0s < t < 15.0s, \\ 15.0\,\frac{kg}{s}, & t \geq 15.0s. \end{cases} \qquad 6\text{-}32$$

Transient pressure drops, shown in Fig. 6-10, exhibit similar behavior as the steady state results. The standalone results again differ substantially due to the multi-dimensional and distributed nature of the pressure field. The activation of the coupling at $t = 9.0s$ is clearly visible in the figure. Additionally, the pressure drop of the coupled simulation appears to lag the CFD solution somewhat, due to the effects of explicit time stepping. Aside from this effect, the coupled solution matched the CFD solution very well.

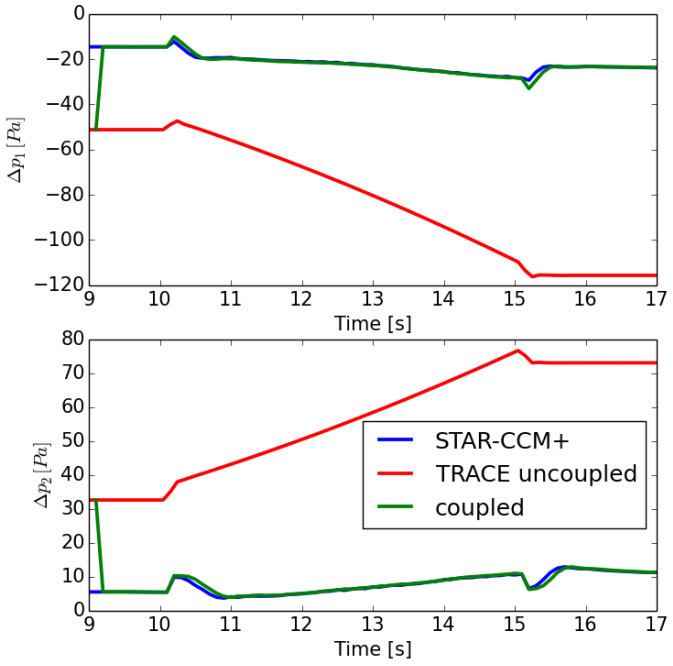

Fig. 6-10. Radial pressure drops calculated with a time dependent simulation. Calculated with a time step of $\Delta t = 0.1s$

6-6.2 Azimuthal Direction

The geometry of Fig. 6-11 was created to verify the 3-D coupling in the azimuthal direction. A semi-circular arc with an inner radius of $0.1m$ is divided into 4 cells of unequal size as shown.

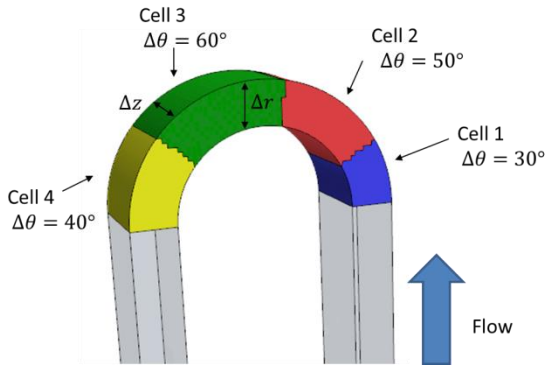

Fig. 6-11. Geometry for verifying the azimuthal implementation of the 3-D coupling. $\Delta r = 0.05m$. $\Delta z = 0.1m$.

For a steady state test case, the mass flow rate through the system was varied and the pressure drop between each set of adjacent cells was recorded and plotted in Fig. 6-12. The standalone TRACE results differ substantially from STAR-CCM+ results. This is not an indictment of TRACE, since this type of application is outside the scope of the vessel component. The coupled pressure drops collapse directly over the CFD results, indicating that the coupling method is correctly implemented for azimuthal faces.

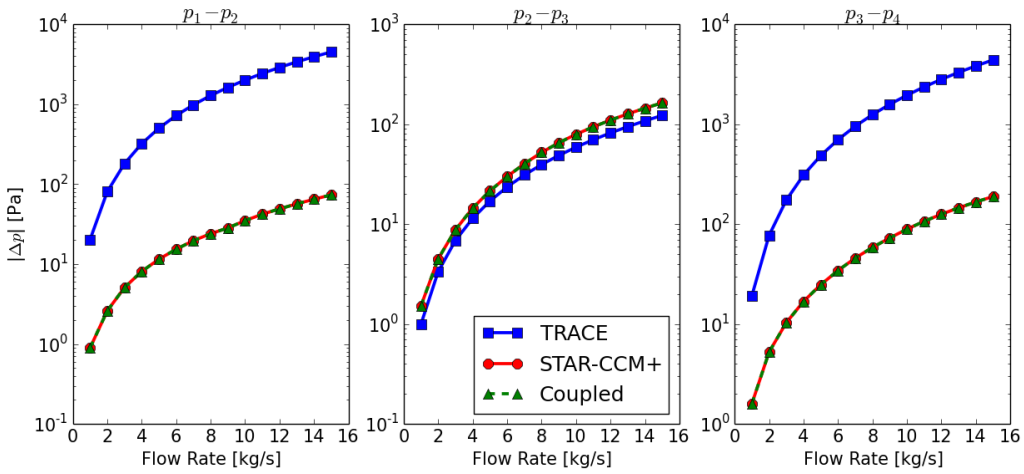

Fig. 6-12. Steady state pressure drops across the azimuthal test section.

For a transient test case, the mass flow rate of Eq. 6-33 was applied to the flow inlet:

$$\dot{m}_{in}(t) = \begin{cases} 10.0\,\dfrac{kg}{s}, & t \le 10.0s, \\ (10.0 + t \times 1.0s^{-1})\,\dfrac{kg}{s}, & 10.0s < t < 15.0s, \\ 15.0\,\dfrac{kg}{s}, & t \ge 15.0s. \end{cases} \qquad 6\text{-}33$$

The three pressure drops resulting from the time-dependent flow rate are shown in Fig. 6-13. Similar to the steady state case, TRACE predicts much larger pressure drops for the two outer pressure drops. The coupled results match the CFD curve very well, verifying the 3-D coupling method for the azimuthal direction in transient mode.

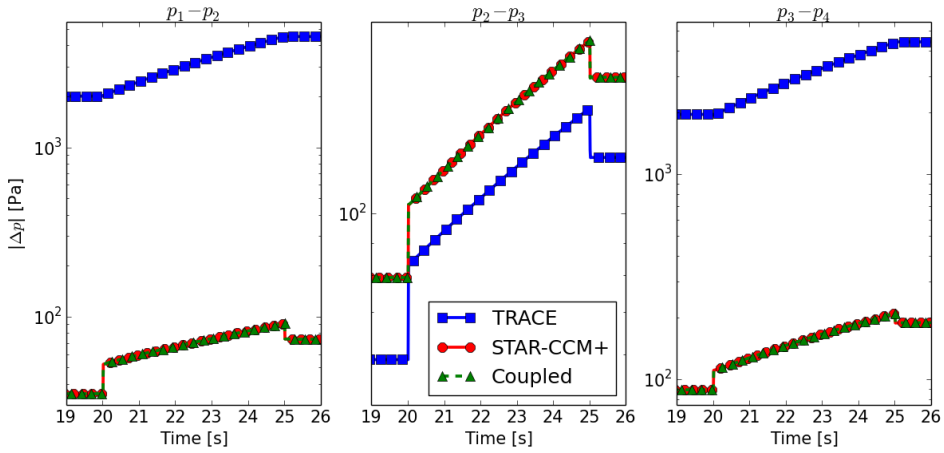

Fig. 6-13. Transient pressure drops across the azimuthal test section. Calculated with $\Delta t = 0.01s$.

6-7 Conclusions

In this chapter, the domain overlapping coupling method was extended to 3-D regions. Spatial and temporal formulations were laid, with the latter being the focus due to its simplicity of implementation and improved accuracy. The coupling is designed to correct local pressure and velocity profiles instead of the global design used in 1-D components. Coupling is implemented through CFD-calculated friction factors applied to the STH momentum equation. Friction factors are adjusted to exclude the contributions of inertia. Velocity consistency is maintained through a VMF functionality that consequently also maintains consistency of the inertial contribution to the pressure field.

Two domain overlapping methods are laid: the IDO and SIDO methods. The IDO method is a basic approach that only adjusts CFD data to account for inertia. The SIDO method elaborates on the IDO method by utilizing correction factors calculated from in depth analysis of the TRACE nonlinear iteration solution procedure. The methods are then applied to very simple geometries to verify their performance. More in-depth verification and analysis is deferred until the next chapter.

Chapter 7. Verification of IDO and SIDO 3-D Coupling Methods

In the previous chapter, the IDO and SIDO methods were introduced and briefly discussed. The methods were verified in extremely simple conditions that were essentially 1-D, in that the TRACE model being coupled only allowed for advection in one direction; the CFD models were fully 3-D. In this chapter, the methods are verified under more complex situations. We begin with a Cartesian flow-splitter that includes two well-defined flow paths. While simple, this model provides an excellent introduction to the use of VMFs.

The majority of the analysis in this chapter is carried out on annular flow splitter geometry. The TRACE model for this test case allows flow in azimuthal and axial direction. Coupled results from 6 transients are analyzed in detail. The transients used were designed to span a range of conditions with relevant parameters being Reynolds number and the time-derivative of velocity changes. Cases with low Reynolds numbers and high velocity time-derivatives were identified as the most challenging. In one particular case, the IDO method was unable to produce a useful solution, while the SIDO method performed much better due to the additional correction factors that characterize the method.

7-1 Cartesian Flow Splitter

The Cartesian geometry shown in Fig. 7-1 was designed as an initial verification case for the IDO coupling method and as a demonstration for VMF application. Referred to as a "flow splitter", the geometry includes two possible flow paths, designated as the lower and upper legs, as well as four changes in stream direction, two dictated by geometry and two by pressure balance. The TRACE geometry is only one cell deep in the z direction, so no open mixing regions exist and the model is effectively two-dimensional. Each cell is cubic, with dimensions of $0.1\,m \times 0.1\,m \times 0.1\,m$. While the STAR-CCM+ model is three-dimensional, there are no nonzero flow faces in the z direction in the TRACE model and so the coupled case is not considered to be fully three-dimensional. The quality of the coupling is quantified with the pressure drop between the inlet and outlet ($\Delta p = p_{in} - p_{out}$, as indicated in Fig. 7-1) as well as the mass flow through each leg.

The dual flow path configuration of this geometry provides an ideal introduction to the VMF functionality and its verification. The flow through each leg is determined by the balance between the frictional and form losses incurred along each path. The coupling method used here does not allow TRACE to influence the friction factor and therefore disrupts this balance. However, guiding the velocity field with VMFs reinstates the pressure-velocity feedback through the CFD solution. Because only two possible flow paths exist, one VMF is sufficient to determine flow through both legs, as the conservation of mass will ensure the non-VMF leg

receives the correct flow rate. Using multiple VMFs would be redundant, producing an over-specified system. As a consequence of continuity, the precise location of the VMF is essentially immaterial for this geometry. Fig. 7-1 shows the two VMF configurations used in this analysis.

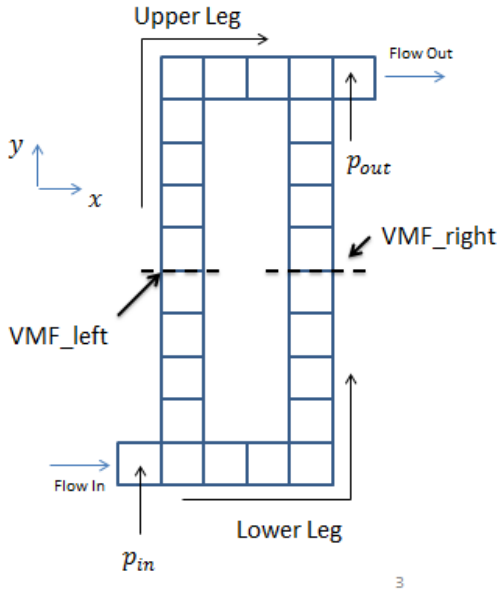

Fig. 7-1. Schematic diagram of Cartesian flow splitter test case with two potential VMF locations. VMF_left and VMF_right are only activated separately. The upper left and lower right corners are geometry-dictated stream direction changes. The stream direction changes at the lower left and upper right corners are dictated by pressure balance.

7-1.1 Steady State

For steady state verification, the inlet mass flow rate through the flow splitter was varied in the range $\dot{m}_{in} \in (0\frac{kg}{s}, 15.0kg/s]$. Mass flow rates through each loop are shown in Fig. 7-2 and total pressure drops are shown in Fig. 7-3. Coupled results were calculated with the IDO method. TRACE assumes fully-developed flow throughout the flow domain, while STAR-CCM+ calculates specific velocity profiles throughout. Based on this, TRACE would be expected to under-predict the pressure drop, but instead TRACE over-predicts the total splitter pressure drop as well as the amount of flow through the lower leg of the flow splitter. Evidently, TRACE over-estimates the pressure penalty incurred by diverting flow and is more "reluctant" to change flow direction when not bound by geometry. Pressure drops resulting from flow changes are both distributed and multi-dimensional, and can only be approximated by the TRACE formulation. The coupled results collapse directly onto the STAR-CCM+ results, simultaneously confirming both the friction factor coupling and the VMF implementation. No differences are found between the VMF_left and VMF_right cases, confirming that the Newtonian iteration of Eqs. 6-5 through 6-7 has not been unduly disrupted and that the particular selection of VMF does not affect the coupled solution in this case.

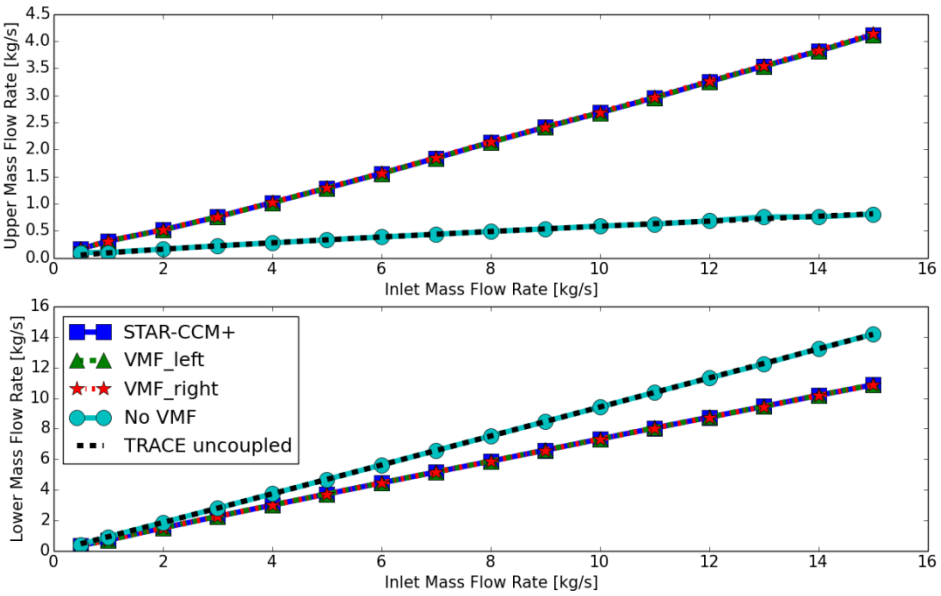

Fig. 7-2. Mass flow rates through each leg of the Cartesian flow splitter.

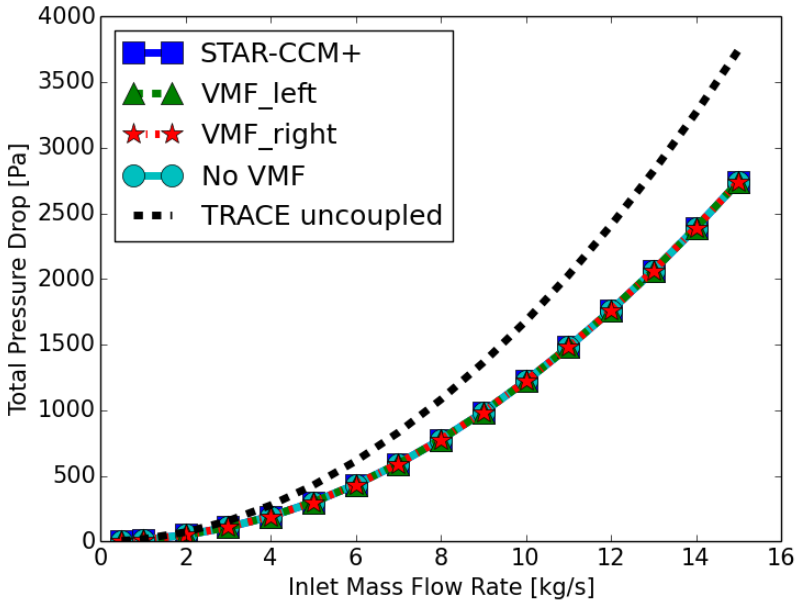

Fig. 7-3. Steady state global pressure drops across Cartesian flow splitter.

The behavior of the simulations performed with coupled friction factors, but without any VMFs, ("No VMF" in Fig. 7-2 and Fig. 7-3) is also of note. As evidenced in Fig. 7-2, the "No VMF" case produces the same mass flow distributions as TRACE standalone, while Fig. 7-3 shows that this case produces the same total pressure drop of STAR-CCM+. This result is clearly erroneous. Because the coupling algorithm allows TRACE to initialize unperturbed, the STH begins the coupled iteration with a standalone TRACE solution. Once CFD friction factors are passed to TRACE, the pressure drop in each leg is forced to match that of STAR-CCM+. Because the

pressure-velocity feedback has effectively been disabled in the process, the STH solver does not change the velocities through the legs to match the pressure balance and hence the coupled solution produces the velocity field of standalone TRACE. This demonstrates that VMF is necessary to make sure that a consistent velocity-pressure field is computed by the coupled code.

7-1.2 Non-inertial pressure gradient comparison

Two methods of calculating the non-inertial contribution to the pressure gradient were developed in §6-2 and §6-3. The Cartesian flow splitter provides an effective test case for the evaluation of the two methods. Steady state pressure drops calculated with both methods are shown in Fig. 7-4 along with standalone results from STAR-CCM+ and TRACE. Both SII and TII cases match the STAR-CCM+ data quite well, however there is a small but distinct difference between them, measured with Eq. 7-1:

$$\%\text{Error} = \frac{\Delta p_{CFD} - \Delta p_{Janus}}{\Delta p_{CFD}} \times 100\%. \qquad 7\text{-}1$$

The error is then plotted in Fig. 7-5. From this perspective, it is clear that the temporal method for non-inertial pressure gradient formulation offers substantially reduced error over the spatial method.

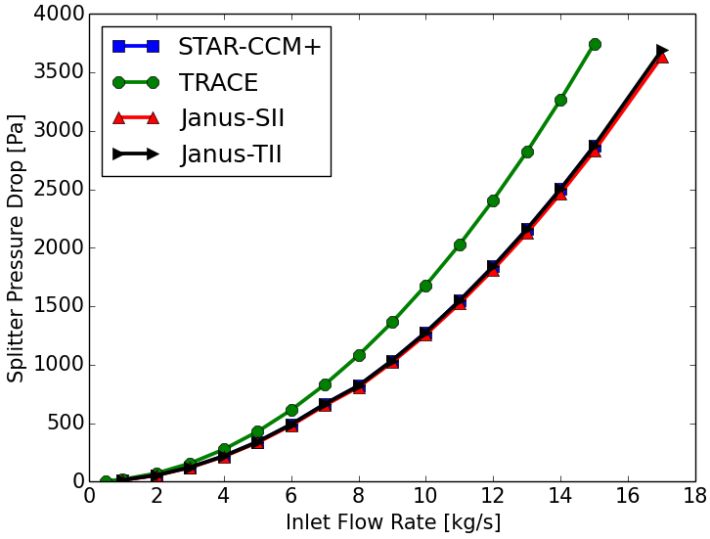

Fig. 7-4. Total pressure drop of Cartesian flow splitter as calculated with both spatial (SII) and temporal (TII) inertial interfaces.

In theory, the temporal and spatial methods are equivalent. Both were derived from the same sets of equations. However, the spatial method involves a significant number of spatial derivatives. While these terms are part of the governing equation and therefore theoretically extractable from the solution, this is not an easy task. For this work, spatial derivatives were computed from the CFD solution with an operator built in to STAR-CCM+. This operator uses a least squares approach to gradient calculation, while the STAR-CCM+ solver uses a two-pass Gauss

algorithm. Additionally, the gradient operator has access to less boundary data than does the solver. In accordance with the objective of developing a user-friendly coupling method, this analysis motivated the decision to exclusively use to temporal method as it provides better accuracy with a significantly simpler implementation.

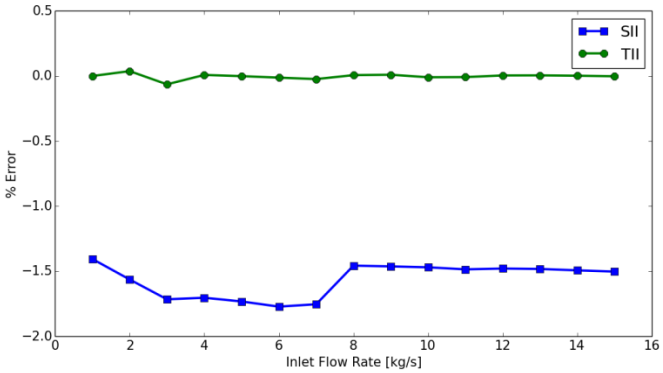

Fig. 7-5. Error comparison for spatial (SII) and temporal (TII) inertial interfaces.

7-1.3 Transient

A time-dependent mass flow rate, given by Eq. **Error! Reference source not found.**, was pplied to the inlet of the flow splitter to verify the IDO method in transient conditions:

$$\dot{m}_{in}(t) = \begin{cases} 5.0\frac{kg}{s}, & t \leq 150.0s, \\ 5.0\frac{kg}{s} \times \left[1.0 + \sin^4\left(\frac{t - 150.0\ s}{10.0\ s}\pi\right)\right], & 150.0s < t < 160.0s, \\ 5.0\frac{kg}{s}, & t \geq 160.0s. \end{cases} \qquad 7\text{-}2$$

Converged solutions for the system-wide pressure drop are shown in Fig. 7-6, while the accompanying mass flow rate distributions are shown in Fig. 7-7.

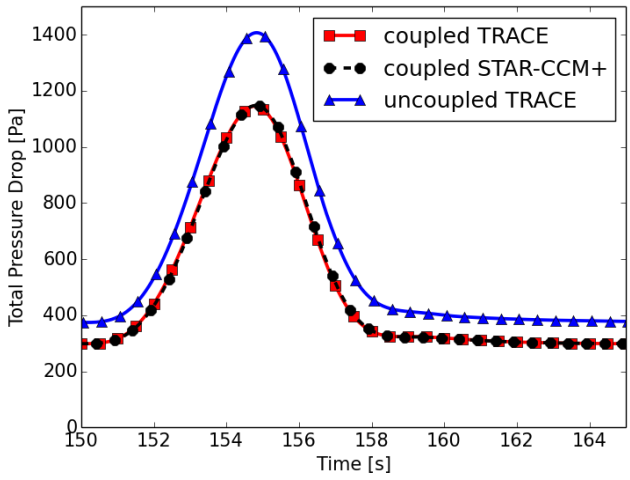

Fig. 7-6. Total system pressure drop for coupled and standalone simulations of the flow splitter transient.

TRACE over-predicts the total pressure drop and the flow rate through the lower leg throughout the transient, consistent with steady state observations. Additionally the upper mass flow rate in the uncoupled TRACE solution drops below zero, indicating recirculating flow, which is not predicted by STAR-CCM+. For both the pressure drop and mass flow distributions, the coupled TRACE solution matches the STAR-CCM+ solution very well.

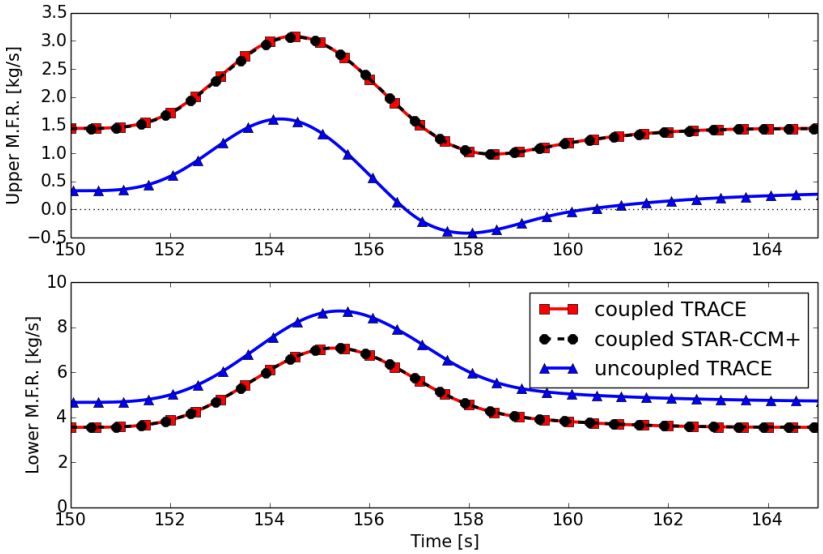

Fig. 7-7. Mass flow rates through the upper (top) and lower (bottom) legs of the flow splitter geometry under transient conditions.

The mass flow rate through the upper leg and the total pressure drop are shown in Fig. 7-8 for three selected integration time steps. The plots show that the coupling is not exact, due to the explicit nature of the numerical coupling, and the two codes exhibit some disagreement at larger time steps. The ∞-norm error, calculated with Eq. 7-3, is plotted in Fig. 7-9:

$$Err = \frac{\max\limits_{150s \le t \le 170s} |\Delta p_{TRC}(t) - \Delta p_{CCM}(t)|}{\max\limits_{150s \le t \le 170s} |\Delta p_{CCM}(t)|}. \qquad 7\text{-}3$$

The error in the system pressure drop agreement levels off below 1% around an integration time step of $\Delta t = 0.01\ s$. The error in mass flow rate agreement is relatively large for large time steps, but decreases steadily with time step.

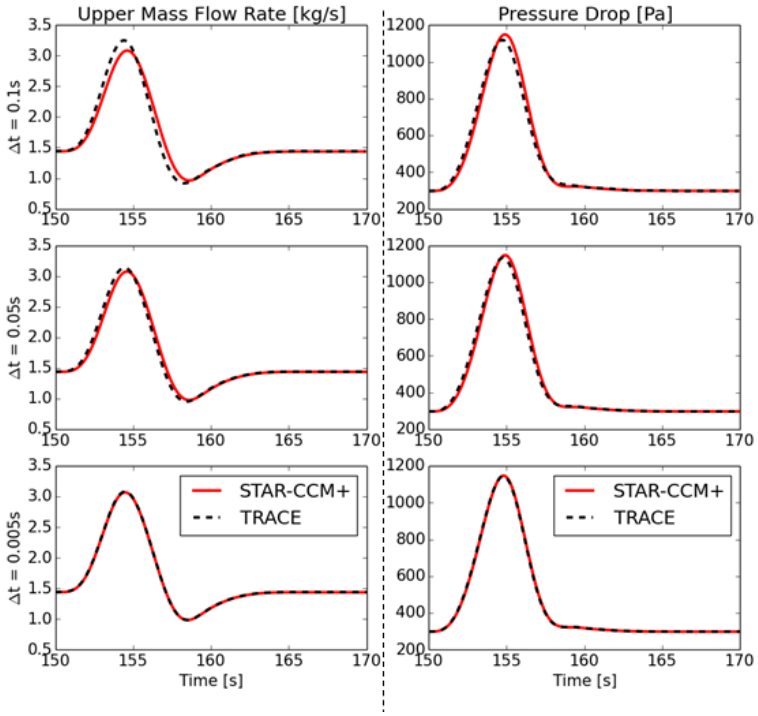

Fig. 7-8. Flow rate through upper leg (left) and system wide pressure drop (right) for the flow splitter test case. Both STAR-CCM+ and TRACE data sets are from coupled simulations.

Since the IDO method is used, no corrective action is taken for the CFD velocity applied to VMFs for this test case, and some additional error is introduced. Using the binomial theorem, the error can be estimated by as shown in Eq. **Error! Reference source not found.**:

$$\left(V_{j+\frac{1}{2}}^{n+1} - V_{CFD}\right) = \frac{(\Delta P^{n+1} - \Delta P^{n})\Delta t}{\rho \Delta s_{\alpha}\left(1 + 2\Delta t K_{j+\frac{1}{2}}^{n}\left|V_{j+\frac{1}{2}}^{n}\right|\right)} = \frac{(\Delta P^{n+1} - \Delta P^{n})}{\rho \Delta s_{\alpha}}\Delta t\left[1 - 2\Delta t K_{j+\frac{1}{2}}^{n}\left|V_{j+\frac{1}{2}}^{n}\right| + \cdots\right]. \quad 7\text{-}4$$

The predicted linear behavior is approximately observed in Fig. 7-9.

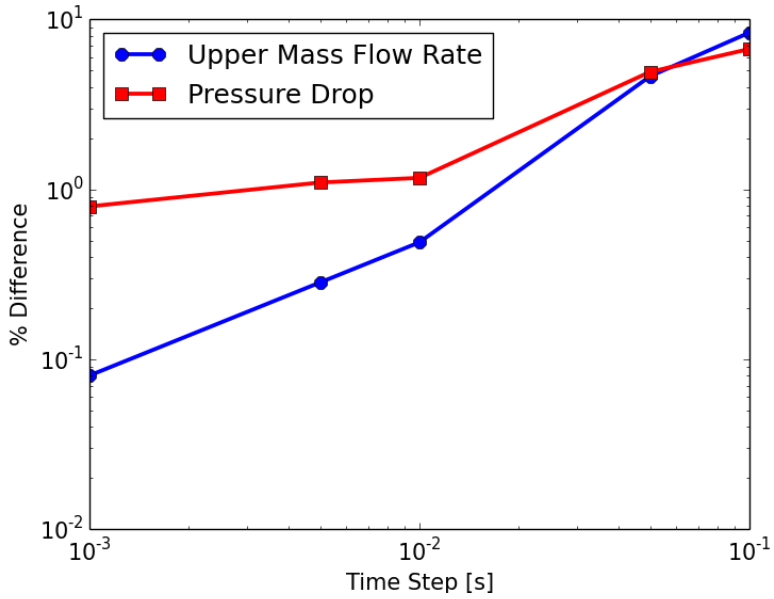

Fig. 7-9. L^{∞} error [%] for upper mass flow rate and system wide pressure drop for the flow splitter test case.

7-2 Annular Flow Splitter Verification Case

The Cartesian geometry of the previous section presented ideal conditions for introducing VMFs and multi-dimensional coupling, but the well-defined flow paths provided significant simplification. In order to expand to geometries more representative of NPPs, an annular test case was devised. Dimensions of the base annulus are shown in Fig. 7-10 with overlaid TRACE nodalization. Flow enters the domain through a pipe attached to the third quadrant (Q3 in Fig. 7-10) on the highest axial level (see Fig. 7-10 right) and exits through the first quadrant (Q1) on the lowest axial level.

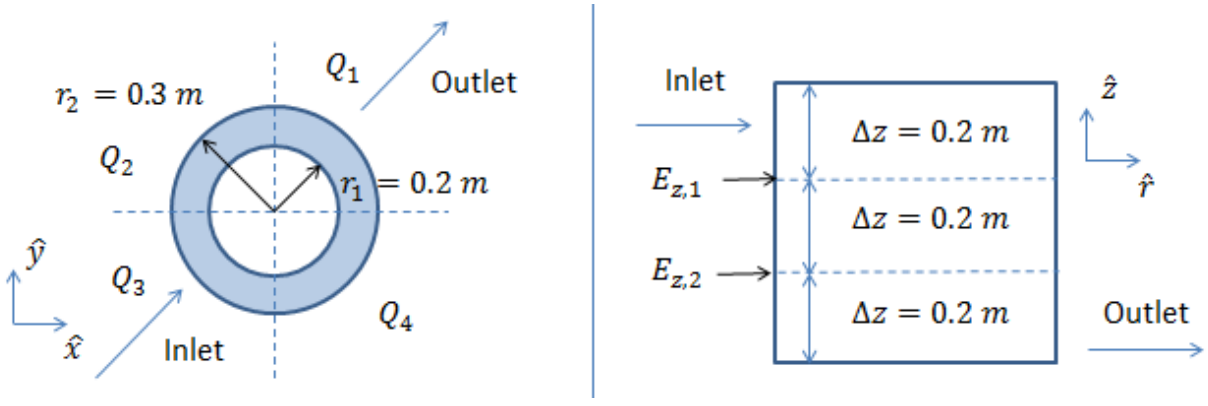

Fig. 7-10. Schematic diagram of annular geometry. (LEFT) Top down view showing annular rings divided into 4 azimuthal quadrants. (RIGHT) side view showing axial dimensions divided into 3 segments of equal length; labeled edges ($E_{z,i}$) also shown.

The corresponding TRACE and STAR-CCM+ meshes are shown in Fig. 7-11. The CFD mesh is composed of 173,022 cells, mostly polyhedral in nature with 2 layers of prismatic cells near wall boundaries. A standard k-ϵ turbulence model is used to satisfy closure. While the CFD mesh is relatively coarse, the purpose of this work is to verify the coupling method and to explore numerical behaviors. We seek only to demonstrate that a STH code can be corrected to produce CFD-like results in a coupled configuration. In this case, minimizing computational time is prioritized over physical accuracy. Once the coupling method is fully established and verified, a fully validated CFD model is required in order for results to be trustworthy.

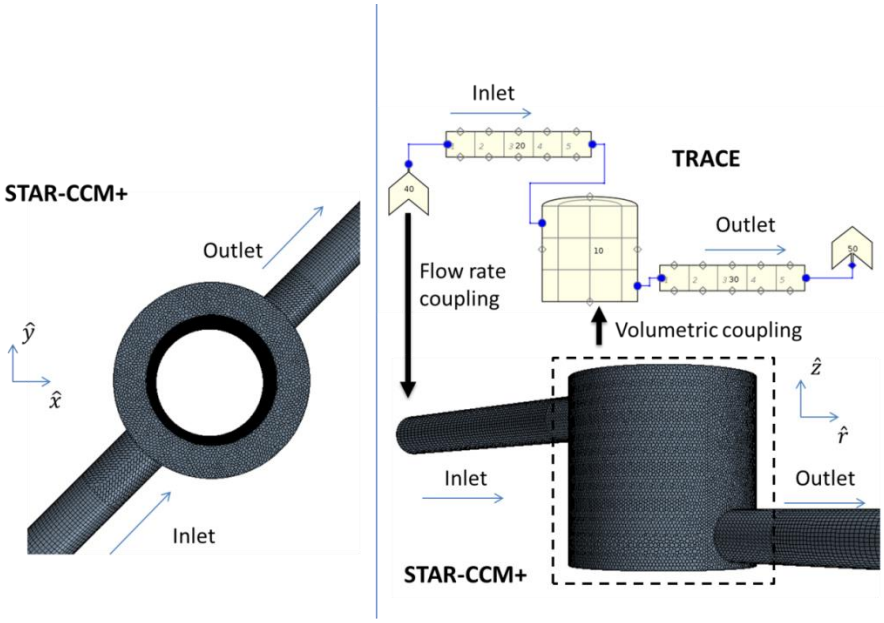

Fig. 7-11. Views of TRACE and STAR-CCM+ implementations of the annulus geometry. (LEFT) Top down view of CFD mesh. (TOP RIGHT) TRACE nodalization as displayed by the Symbolic Nuclear Analysis Package (SNAP). (BOTTOM RIGHT) side view of CFD mesh showing axial locations of inlet and outlet channels.

The coupling for this test case was realized through 2 interfaces, as indicated on the right side of Fig. 7-11. A surface interface passes mass flow rate data from a TRACE "fill" component to a STAR-CCM+ mass flow inlet. Additionally, a volumetric interface passes friction factor and velocity data from the STAR-CCM+ region to the TRACE "vessel" component. With both interfaces working together, the coupling is two-way.

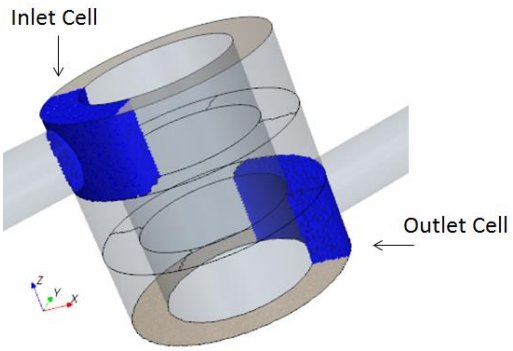

Fig. 7-12. Highlighted inlet/outlet cells showing definition of "global" pressure drop.

A set of pressure drops is defined to quantify the accuracy of the coupling with respect to the pressure field. Each pressure drop is defined in STAR-CCM+ as the difference in volume-averaged pressure between two cells. The TRACE definition of a pressure drop is identical, but TRACE pressure values are natively defined as volume averages, so no averaging needs to be carried out. A global pressure drop is defined as the difference between the "Inlet Cell" and "Outlet Cell" as denoted in Fig. 7-12. In more complex cases, a global pressure drop must include the losses incurred by flowing into inlet cells and out of outlet cells, since there is an abrupt change in flow area at these locations. However, the goal of this chapter is the verification of coupling in 3-D geometry, and treatment of entry/exit effects is deferred to future work with closed loop flow configurations in which the local pressure drops have a substantial effect on the system.

It is secondarily desired to characterize the behavior of the coupling on a more localized scale. At each edge, or boundary between adjacent cells, a velocity is defined in TRACE. Additionally, a pressure drop can easily be defined at the edge as the difference in volume-averaged pressure between the adjacent cells. As shown in Fig. 7-10, the annulus has 8 internal axial edges (2 edges per quadrant with 4 quadrants) and 12 internal azimuthal edges (3 faces per azimuthal division with 4 divisions) for a total of 20 internal edges. The quality of coupled solutions is therefore based on a combination of global and local pressure drops, along with local velocity profiles.

In order to quantify the fidelity of the coupling with respect to the pressure field, the error functions of Eqs. 7-5 and 7-6 are defined. Because of the explicit time stepping between the CFD and STH code data exchange, the STAR-CCM+ curves are shifted by one time step. This has minimal effect on the value of Err_2, but it allows Err_∞ to produce more useful values, as will be demonstrated. All transients tested in this chapter are driven by inlet mass flow rates with time dependence that begins, arbitrarily, at $t = 75.0\,s$ and ends at $t = 80.0\,s$. The error function integrates the pressure drop functions beginning $3.0\,s$ before and after these times in order to capture redistribution effects. Eq. 7-5, based on the 2-norm, can be interpreted as the time-averaged difference between the CFD and STH pressure drops:

$$Err_2 = \frac{1}{11.0s}\int_{t=72.0\ s}^{t=83.0\ s} |\Delta p_{TRC}(t') - \Delta p_{CCM}(t' + \Delta t)|dt', \qquad 7\text{-}5$$

while Eq. 7-6, based on the ∞-norm, is interpreted as the maximum value of the difference over the course of the transient:

$$Err_\infty = \max_{72.0\ s \le t \le 83.0\ s} |\Delta p_{TRC}(t) - \Delta p_{CCM}(t + \Delta t)|. \qquad 7\text{-}6$$

Analysis of both types of error will provide a better picture of convergence for transients with, for instance, abrupt changes in the time derivative of the total flow rate through the system, as will be encountered in §7-2.3.1 and §7-2.4.1. Convergence in the sense of Err_∞ is a stronger statement than convergence in the sense of Err_2.

A similar approach is adopted for the velocity field, although an ∞-norm error function was not deemed necessary due to smoothness of the velocity fields encountered in this chapter. Eq. 7-7 is employed to quantify error in the velocity field on a global scale:

$$Err_{vel} = \sum_{i=1}^{20} \frac{1}{11.0s}\int_{t=72.0\ s}^{t=83.0\ s} \left|v_{i,TRC}(t') - v_{i,ccm}(t' + \Delta t)\right|dt'. \qquad 7\text{-}7$$

The summation ranges over all faces in the system, both velocity-matched and open. With units of velocity, this quantity has the interpretation of the time-averaged total difference in velocity between TRACE and STAR-CCM+. While dividing by 20 would yield the average error per face, it is found in practice that the majority of the error is confined to specific faces, causing such an interpretation to be misleading.

7-2.1 Velocity Matching Face Configurations

In the Cartesian case of §7-1, the placement of VMFs was relatively straightforward, due to the existence of two distinct flow paths. In true reactor geometry, flow enters an annular downcomer primarily travelling downward, then makes a turn in the lower plenum and finally rises through the core and riser. Although the geometry of this section was designed to represent a downcomer, the configuration of the inlet and outlet create much more azimuthal flow than would be expected in a NPP. The VMF configurations devised for this case were based on decomposing the geometry into 4 "pseudo flow paths" corresponding with the 4 azimuthal sections of the annulus. Each path therefore consists of two axial pressure drops. This VMF scheme was chosen because the authors expect such a strategy to be directly extensible to more realistic NPP geometries. We applied VMFs to the axial faces along these paths for 3 of the 4 pseudo flow paths as shown in Fig. 7-13 (left). This allows the TRACE continuity equation to determine the flow through the 4th face, preventing an overdetermined system. In this configuration, the azimuthal direction is entirely left to the TRACE continuity solver.

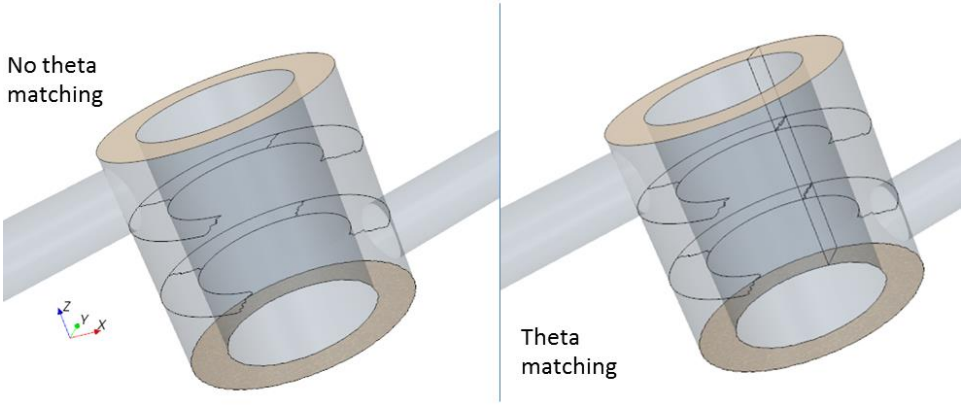

Fig. 7-13. Diagram showing VMF (outlined) placement for annular geometry. (LEFT) only axial matching faces. (RIGHT) theta matching faces included

In the VMF configuration shown in Fig. 7-13 (right), the three azimuthal faces of one sector are also included in the VMF configuration. In broad terms, one of the ultimate goals of this coupling methodology is to ensure proper velocity profiles at the core inlet and correct total pressure drops throughout the downcomer and inlet plenum regions. Correct matching of azimuthal velocities is not necessarily required to achieve this goal. As such, we included both cases to understand the effect that granting full control over azimuthal velocity to TRACE would have on stability and accuracy. The authors believe that study of these two configurations will lay the groundwork for a reasonable process for determination of VMF placement for reactor-like geometries.

7-2.2 Steady State

In order to provide a general idea of how the annular system behaves and how TRACE and STAR-CCM+ solutions differ, a rudimentary steady state analysis is performed. The inlet mass flow rate was varied with the resulting pressure drops across each axial edge (as indicated in Fig. 7-10) recorded as output. The data shown in Fig. 7-14 demonstrate that while TRACE standalone pressure drops behave similarly to those of STAR-CCM+, the magnitude of the pressure drops differ substantially. The coupled results, however, overlap the CFD results, verifying the correctness of the steady-state coupling. The inclusion of θ-matching faces was found to have no effect and Fig. 7-14 results are representative of both VMF configurations shown in Fig. 7-13.

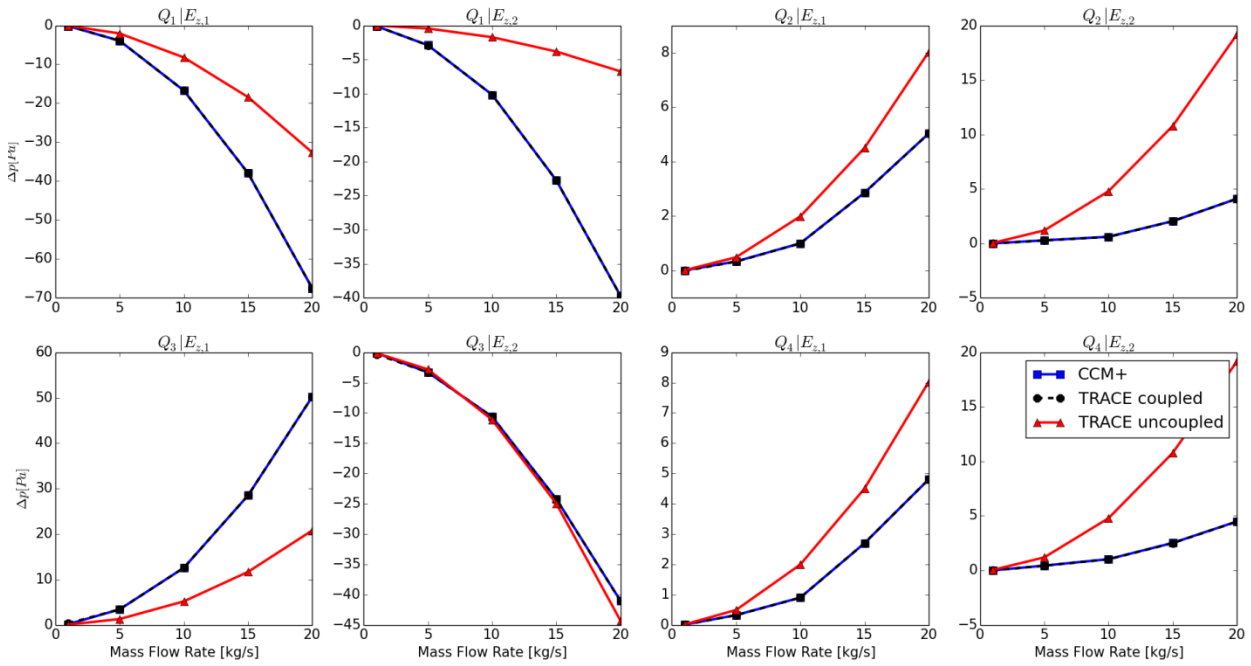

Fig. 7-14. Steady state pressure drop across each axial face for the annular test case.

The velocity field behaved similarly to the pressure field in that the uncoupled TRACE results differed noticeably from the CFD results, but the coupled version of TRACE was found to overlap STAR-CCM+ quite closely. In contrast to the pressure field, the velocity field does depend somewhat on the VMF configuration. Cases without θ-matching can see different flows in the azimuthal direction. This behavior will be discussed in §7-2.3.1 and is not shown here to avoid undue redundancy.

7-2.3 High Flow Transient

Coupling performance in transient mode is additionally sensitive to the rates of change of flow, rather than just the flow rate itself, as in steady state. In order to be sufficiently broad in our analysis, we executed simulations with three types of transient inlet mass flow rates in a high and a low flow regime respectively. This section discusses the "high flow regime" in which the initial mass flow rate is 15.0 kg/s, while a "low flow regime" is discussed in §7-2.4. Higher flow rates provide a greater stabilizing influence of frictional loss compared to the potentially destabilizing effect of the inertial component of the pressure gradient. The ratio of these two effects is the Reynolds number, which takes on a value in the range $Re \in [1.28 \cdot 10^4, 1.95 \cdot 10^5]$ for each face at the initial mass flow rate. Transients in this class are therefore considered to be less challenging than those of §7-2.4. The specific transients considered in this section are driven by the time dependent inlet mass flow rates shown in Fig. 7-15 (TOP). The time derivatives of the same functions are shown in Fig. 7-15 (BOTTOM). The "linear" test case is characterized by a mass flow rate that increases proportionally with time during the transient. The "sin^4" functions are both based on quartic sinusoids designed to have continuous first-order time derivatives. The

quartic sinusoids are further classified by the relative size of their first order time derivatives. The function with the higher value derivative is referred to as "fast" or "tall", while the function with the lower value derivative is referred to as "slow" or "short." As can be seen in Fig. 7-15, the time derivative of the tall quartic sinusoid reaches a rather high value compared to the other two functions, which have similar maxima.

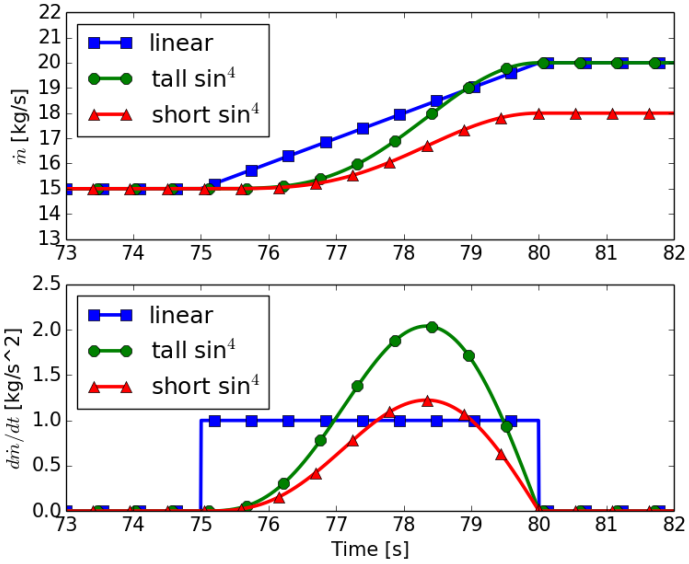

Fig. 7-15. (TOP) Time dependent mass flow rates used for transient test cases. (BOTTOM) derivative w.r.t. time for the transient mass flow rates.

7-2.3.1 Linear Mass Flow Rate

For the linear mass flow rate in the high flow regime, the time dependent mass flow rate of Eq. 7-8 is applied to the flow inlet

$$\dot{m}_{in}(t) = \begin{cases} 15.0\frac{kg}{s}, & t \leq 75.0s, \\ 15.0\frac{kg}{s} + (t - 75.0s)\frac{kg}{s^2}, & 75.0s < t < 80.0s, \\ 20.0\frac{kg}{s}, & t \geq 80.0s. \end{cases} \qquad 7\text{-}8$$

As shown in Fig. 7-15, the defining features of this transient are the discontinuities in the time derivative of the mass flow rate at $t = 75s$ and $t = 80s$. The convergence pattern for the global pressure drop (from inlet to outlet as defined in Fig. 7-12) for this transient is shown in Fig. 7-16. A striking feature of these curves is the oscillatory behavior near $t = 75s$ and $t = 80s$. As the time step is refined, the decay ratio increases and the error decreases noticeably, especially away from the time derivative discontinuities. However, the oscillations near the discontinuities persist with seemingly constant amplitude for even very small time steps, similar to the familiar Gibbs phenomenon.

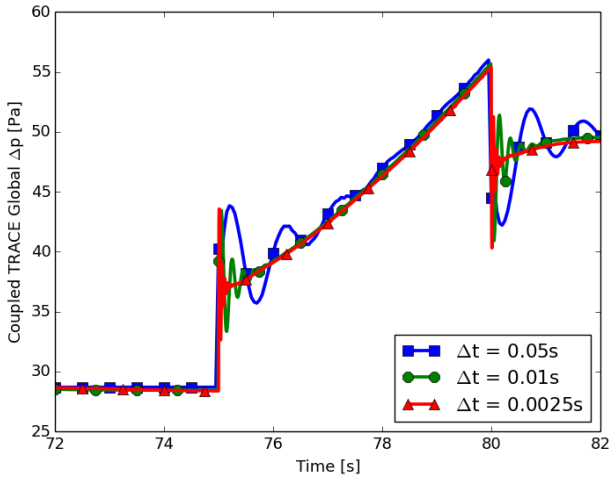

Fig. 7-16. Typical convergence pattern for global pressure drop subject to the linear mass flow rate in the high flow regime as computed with selected representative time steps.

The oscillatory response can be explained by examining VMFs in greater detail. Consider an explicit time stepping coupling configuration with N_{VMF} velocity-matched faces out of a total of N faces subject to the transient of Eq. 7-8. During the time step in which the linearly increasing mass flow rate is first engaged (i.e. $t^n = 75.0s, t^{n+1} = 75.0s + \Delta t$ in TRACE), the total mass flow rate through the system increases by $\Delta\dot{m} = \Delta t \frac{kg}{s^2}$. Broadly approximated, in an uncoupled solution the additional mass flow rate will be split evenly among all N edges of the system:

$$\Delta\dot{m}_{face} \sim \frac{\Delta\dot{m}}{N}, \qquad 7\text{-}9$$

where $\Delta\dot{m}_{face}$ is the amount the mass flow rate increases during the time step across each face. However, in a coupled case, the VMFs are still held at the velocities calculated with CFD at $\dot{m}_{in} = 15.0 \frac{kg}{s}$, since the mass flow rate increase had not been communicated to CFD during the previous time step. The faces that are not velocity-matched must therefore compensate, resulting in an over-estimated inertial pressure that reverberates through the entire system. By continuity, a total flow rate $N_{VMF}\,\Delta\dot{m}_{face}$ needs to be made up by uncoupled faces. An open face flow rate given by Eq. 7-10 is calculated by assuming that the makeup flow rate is evenly distributed among the unmatched faces:

$$\Delta\dot{m}_{openface} \sim \frac{\Delta\dot{m}}{N} + \frac{N_{VMF}\,\Delta\dot{m}_{face}}{N - N_{VMF}} = \frac{\Delta\dot{m}}{N}\left[\frac{N}{(N - N_{VMF})}\right] = C_{VMF}\Delta\dot{m}_{face}. \qquad 7\text{-}10$$

The accompanying inertial pressure drop can therefore be estimated by Eq. 7-11 which predicts an over-prediction of the inertial pressure drop by a factor of C_{VMF}:

$$\Delta p_I \sim \frac{\Delta x}{\Delta t}\frac{\Delta\dot{m}_{openface}}{A_{face}} = C_{VMF}\frac{\Delta x}{\Delta t}\frac{\Delta\dot{m}_{face}}{A_{face}}. \qquad 7\text{-}11$$

where A_{face} is the area of the face and Δp_I is the change in inertial pressure during the time step. For the case without θ-matching, $N = 20$ and $N_{VMF} = 6$, leading to $C_{VMF} \approx 1.43$. Including azimuthal VMFs, $N_{VMF} = 9$ and $C_{VMF} \approx 1.82$. While this analysis is extremely simplified, it predicts that the inertial pressure drop will be initially over-predicted by about 40% with θ-matching and by about 80% without θ-matching. These predictions match up well with the observations in Fig. 7-17, which shows the initial portion of the transient calculated with each coupling method for two selected time steps. Also apparent in Fig. 7-17 is the motivation for shifting the STAR-CCM+ results by one time step in Eqs. 7-5 and 7-6. The CFD data clearly lags the STH data by a time step, and the shifting effectively excludes the error that results from the lag. The value of Err_2 is only minimally affected, while the shift allows Err_∞ to characterize the initial pressure overshoot rather than just the pressure of the first time step. Without the shift, Err_∞ was found to characterize the time step lag rather than the inertial pressure overshoot.

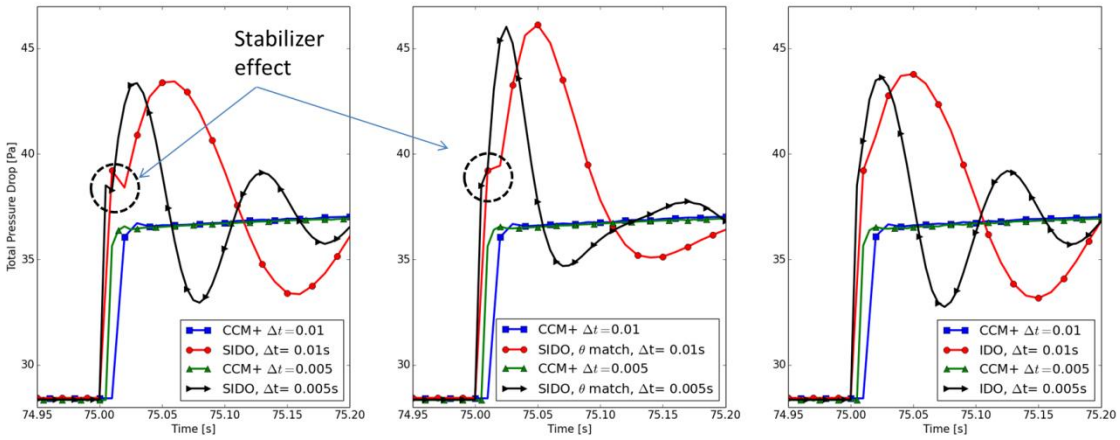

Fig. 7-17. Plots of coupling behavior near the beginning of the high flow linear transient. (LEFT) Case with friction factor and VMF correction. (CENTER) SIDO case with θ-matching. (RIGHT) Coupled case without friction factor or VMF correction. Red/blue curves calculated with $\Delta t = 0.01s$. Black/green curves calculated with $\Delta t = 0.005s$.

In the SIDO cases (left and middle), there is a clear error reduction effect in that the TRACE curves (black and red) exhibit an abrupt direction change toward the STAR-CCM+ curves (blue and green). This stabilizer effect is less striking in the θ-matched case (middle) and absent from the IDO case (right). While the effect seems rather small in Fig. 7-17, the effect on the ∞-norm error is substantial, as can be observed in Fig. 7-18 (left), where the difference between the SIDO and IDO curves is readily apparent for all time steps. The SIDO method with θ-matching resulted in the least 2-norm (left) error at large time steps and the most error at small time steps. At small time steps, the SIDO method without θ-matching and the IDO method converge to the same value. The θ-matching leads to significantly higher error in the ∞-norm (Fig. 7-18 right) as predicted by Eq. 7-11.

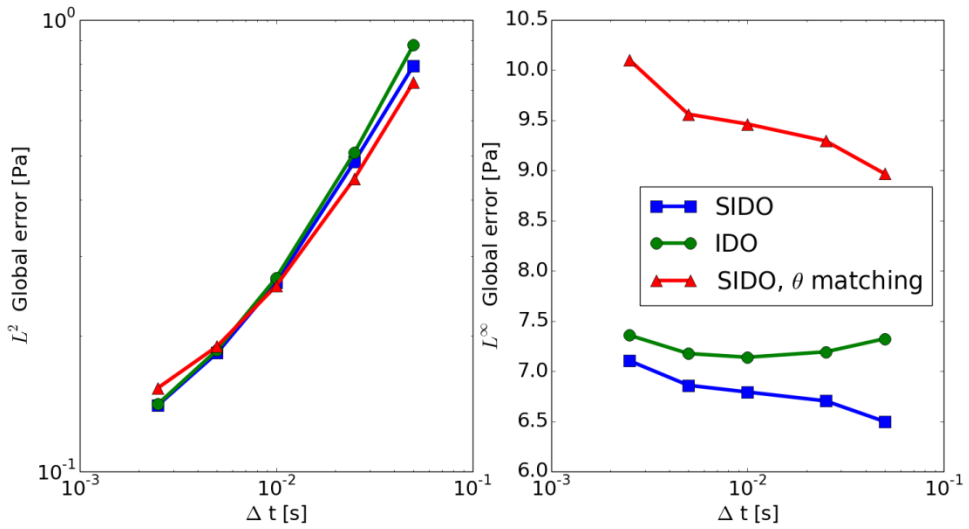

Fig. 7-18. Pressure convergence data for linear transient in the high flow rate regime. (LEFT) 2-norm error data. (RIGHT) ∞-norm error.

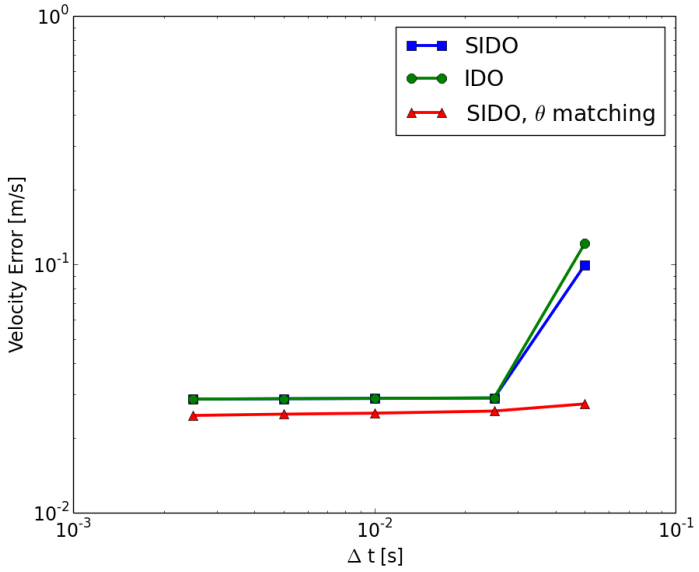

Fig. 7-19. Velocity convergence data for linear transient in high flow regime.

The velocity field error is shown Fig. 7-19 and is essentially constant, except for the large time step cases. The error is small but non-vanishing. As the time step is refined, the TRACE velocities on VMFs quickly match the STAR-CCM+ velocities, and the error reaches the ultimate value around $\Delta t \approx 0.025s$. Unmatched faces are primarily responsible for the persistent error, as can be observed in Fig. 7-20. The figure shows the velocities across the 4 azimuthal faces on the lowest axial level of the annulus calculated with $\Delta t = 0.05s$. In the θ-matched case, the $\theta_0 z_0$ face is velocity-matched, while the other 3 faces are open. In the cases without θ-matching, all 4 azimuthal faces are open. From these curves, it is apparent that open faces are the primary contributors to Err_{vel}. The θ-matched case shows significantly less error for all faces,

while the SIDO case without θ-matching appears to provide some error relief over an IDO case without θ-matching. The data in Fig. 7-20 are indicative of the remainder of the faces in the system. In all cases, axial velocities are matched quite well due to the heavy velocity-matching in this direction. The primary goals of the coupling are to match overall system pressure drop and flow rate through important interfaces, such as the core inlet. The remainder of the TRACE solution is essentially discarded, so internal consistency between TRACE and STAR-CCM+ is not necessarily required.

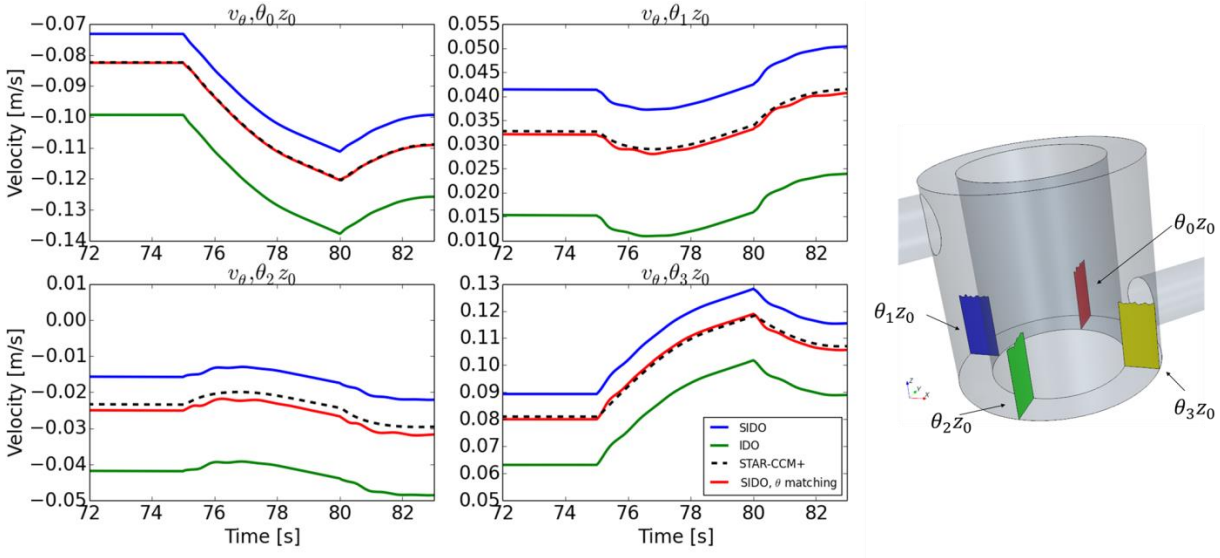

Fig. 7-20. (LEFT) Azimuthal velocities on the lowest axial level for the linear transient in the high flow regime. Calculated with $\Delta t = 0.05s$. (RIGHT) Diagram showing location of VMF planes.

Coupled results for the SIDO method with and without θ-matching and for IDO are shown in Fig. 7-21 compared to a reference standalone STAR-CCM+ curve. The curves are essentially indistinguishable from each other except near the discontinuities of the time derivative, at $t = 75s$ and $t = 80s$, verifying all employed coupling methods for this transient.

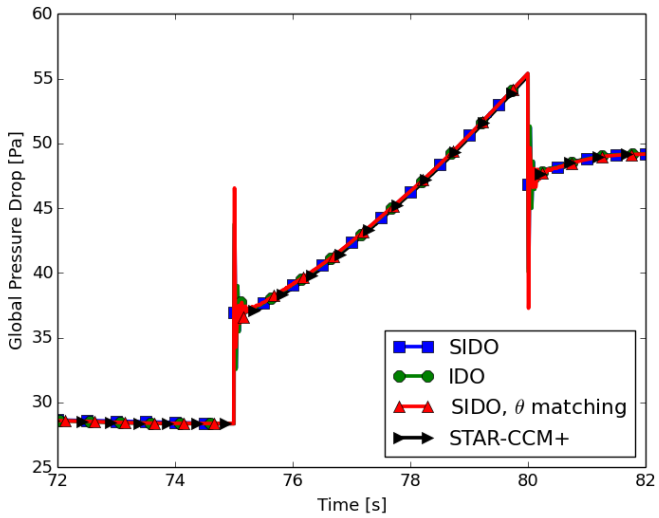

Fig. 7-21. Global pressure drop functions calculated with $\Delta t = 0.0025s$ for the linear inlet mass flow rate in the high flow regime.

7-2.3.2 Fast Smooth Transient

In the high flow regime, a fast, smooth transient is realized with a mass flow boundary condition set by Eq. 7-12. In contrast to the linear transient, this function presents no discontinuity in the inertial pressure drop:

$$\dot{m}_{in}(t) = \begin{cases} 15.0\dfrac{kg}{s}, & t \leq 75.0s, \\ 15.0\dfrac{kg}{s}\left[1 + \sin^4\left(\dfrac{t - 75.0s}{10.0\,s}\pi\right)\right], & 75.0s < t < 80.0s, \\ 20.0\dfrac{kg}{s}, & t \geq 80.0s. \end{cases} \qquad \textit{7-12}$$

A typical convergence pattern for this class of transient is shown in Fig. 7-22. The solution does not appear to change significantly for time step refinements below $\Delta t = 0.01s$. The lower time step solutions appear to lag the higher time step solution, due to the combined effects of explicit time stepping and VMFs through Eq. 7-11.

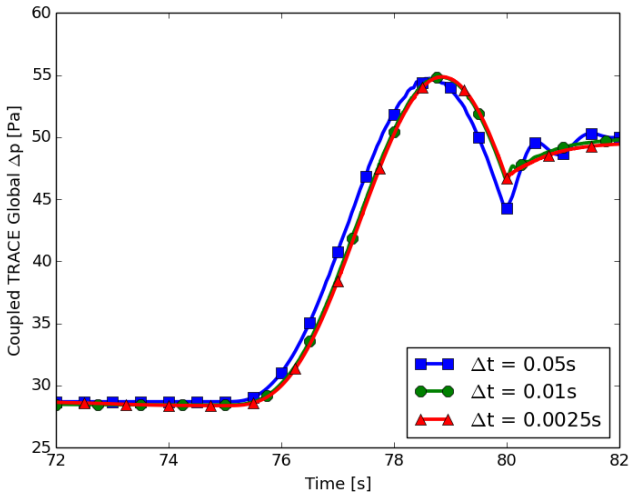

Fig. 7-22. Convergence pattern for fast smooth transient in the high flow regime. Results shown are as gathered from TRACE during a coupled simulation for selected time steps.

The pressure convergence behavior is shown in Fig. 7-23 calculated with both the L^2 (LEFT) and L^∞ (RIGHT) norms. In this case the inclusion of the stabilizer term in the friction factor does not appear to have a substantial effect. The VMF-induced error described by Eq. 7-11 is apparent in these results, but is much less dramatic due to the smoother nature of the time derivative of the mass flow rate. The error in the velocity field, shown in Fig. 7-24, behaves quite similarly to the previous case in that the error quickly levels off to a constant value that results from unmatched faces.

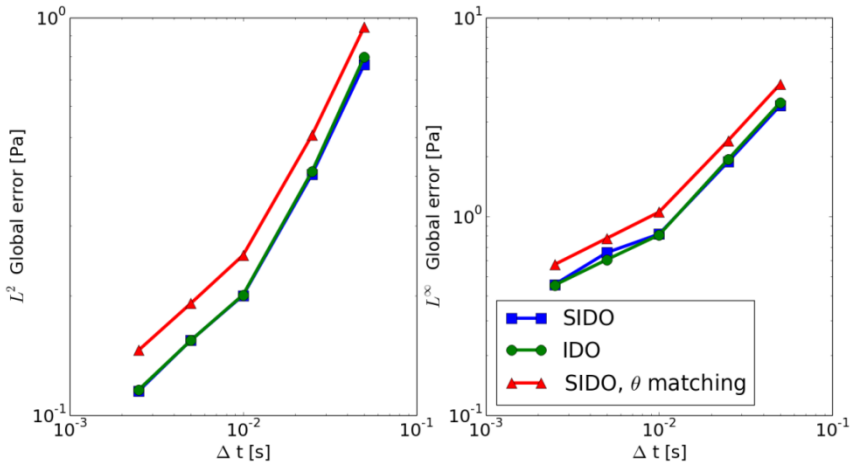

Fig. 7-23. Pressure convergence data for fast smooth transient in the high flow rate regime. (LEFT) 2-norm error data. (RIGHT) ∞-norm error.

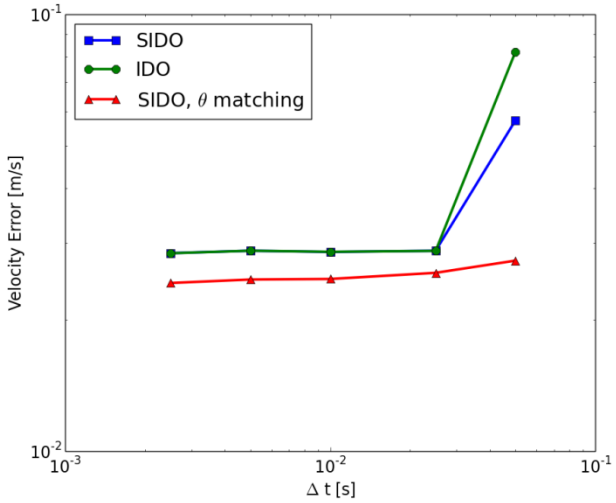

Fig. 7-24. Velocity convergence data for fast smooth transient in high flow regime.

Coupled results for the SIDO method with and without θ-matching and for IDO are shown in Fig. 7-25 compared to a reference STAR-CCM+ curve. The curves are essentially indistinguishable throughout the transient, confirming the methods for this transient. Due to the smooth nature of the transient and the strong stabilizing effect of friction resulting from high flow rates, no oscillatory behavior is observed in the coupled solutions.

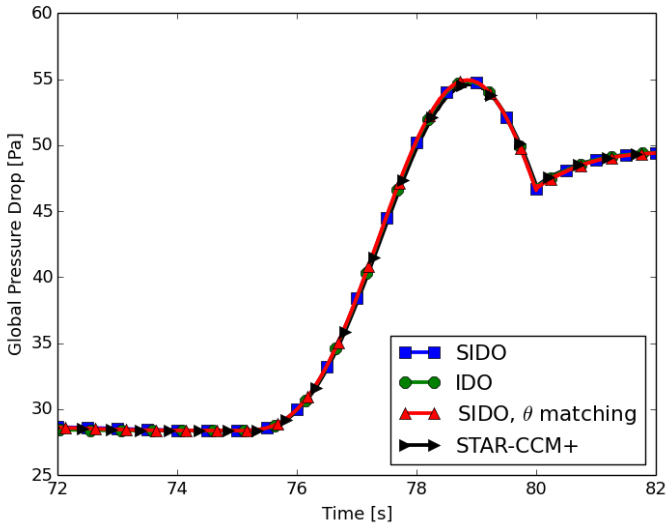

Fig. 7-25. Global pressure drop functions calculated with $\Delta t = 0.0025s$ for the fast smooth inlet mass flow rate in the high flow regime.

7-2.3.3 Slow Smooth Transient

In the high flow regime, a slow smooth transient is realized through a mass flow boundary condition set by Eq. 7-13. The mass flow function has the same form as the in the fast smooth

transient of the previous section, but it reaches a lower maximum value over the same time period and hence has a lower time derivative:

$$\dot{m}_{in}(t) = \begin{cases} 15.0\dfrac{kg}{s}, & t \le 75.0s, \\ 15.0\dfrac{kg}{s}\left[1 + \dfrac{3}{5}\sin^4\left(\dfrac{t - 75.0s}{10.0\,s}\pi\right)\right], & 75.0s < t < 80.0s, \\ 18.0\dfrac{kg}{s}, & t \ge 80.0s. \end{cases} \qquad \textit{7-13}$$

Under higher flow conditions, the slow smooth transient does not behave appreciably different than the fast smooth transient. The effects of stabilizer corrections on friction factors and VMFs do not have a strong effect in either the 2-norm or the ∞-norm, as shown by the similarity of the IDO and SIDO method in Fig. 7-26. The velocity field error of Fig. 7-27 shows a leveling off of error around $\Delta t = 0.025s$.

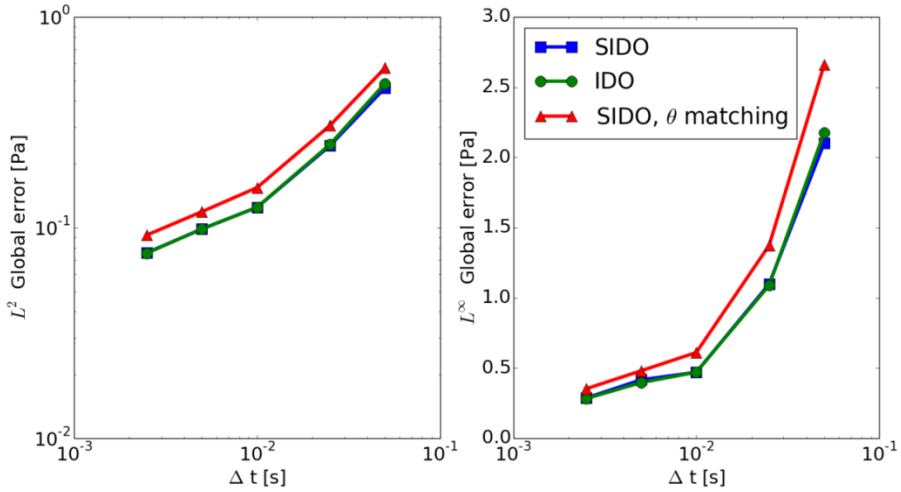

Fig. 7-26. Pressure convergence data for slow smooth transient in the high flow rate regime. (LEFT) 2-norm error data. (RIGHT) ∞-norm error.

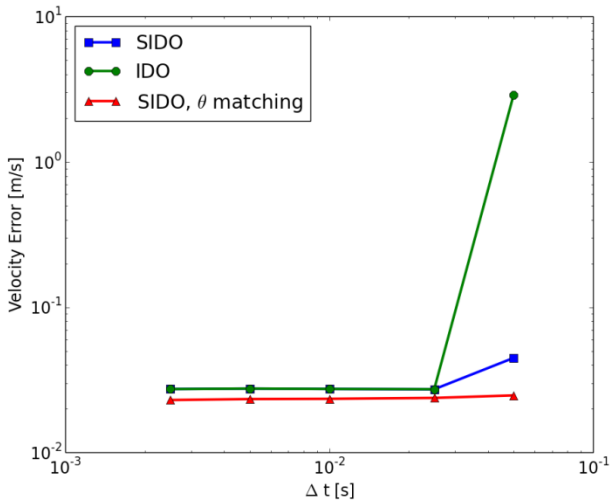

Fig. 7-27. Velocity convergence data for slow smooth transient in high flow regime.

This simulation is the least challenging, due to the strong stabilizing effects of friction and the weak time derivatives involved. Coupled results for SIDO with and without θ-matching and for IDO are shown in Fig. 7-28 compared to a reference STAR-CCM+ curve. The pressure drop resulting from this transient looks quite similar to that of the fast smooth transient of the previous section, but with smaller ultimate values. The coupled solutions all match quite well with the reference CFD solution, confirming their applicability to this transient.

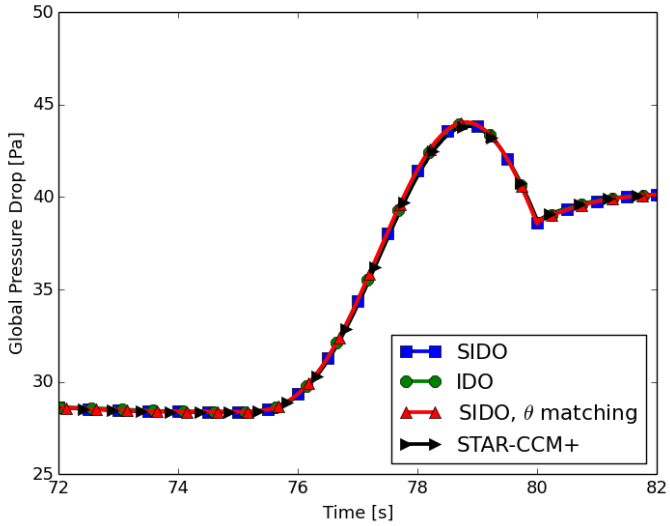

Fig. 7-28. Global pressure drop functions calculated with $\Delta t = 0.0025s$ for the slow smooth inlet mass flow rate in the high flow regime.

7-2.4 Low Flow Transient

Low flow transients analyzed in this chapter are characterized by an initial mass flow rate of $5.0\,kg/s$, with Reynolds numbers for each face falling in the range $Re \in [4.48 \cdot 10^3, 6.49 \cdot$

10^4]. Due to the diminished stabilizing effect of frictional losses compared to the inertial pressure gradient, transients in this flow regime are significantly more challenging than their counterparts in the higher flow regime. Analogous to the previous section, three transient mass flow rates (shown in Fig. 7-29 (TOP), with their respective time derivatives shown in Fig. 7-29 (BOTTOM)) are employed to test the IDO and SIDO methods under diverse conditions.

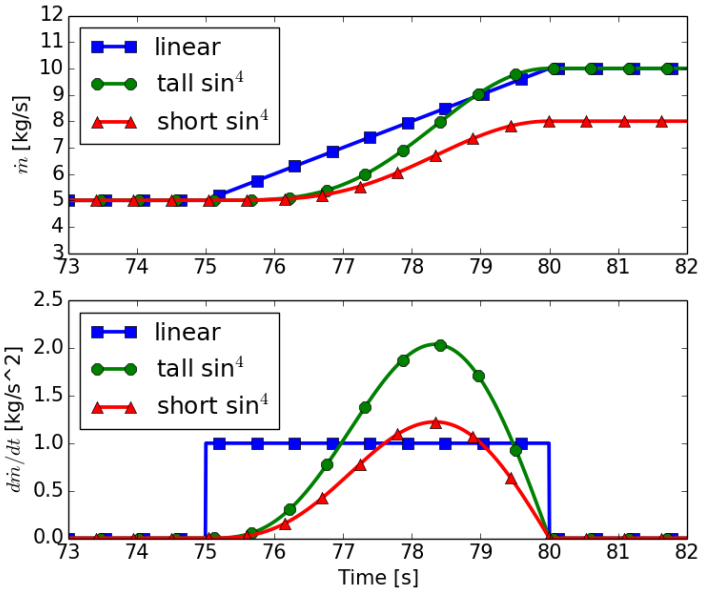

Fig. 7-29. (TOP) Time dependent mass flow rates used for transient test cases. (BOTTOM) derivative w.r.t. time for the two transient mass flow rates.

7-2.4.1 Linear Transient

For the linear transient in the low flow regime, Eq. 7-17 was applied to the flow domain inlet. Similar to §7-2.3.1, this function is characterized by a discontinuous time derivative at $t = 75s$ and $t = 80s$. The magnitude of the time derivative is the same as the analogous case in the high flow regime, but the relative magnitude compared to the underlying stabilizing friction loss is much larger:

$$\dot{m}_{in}(t) = \begin{cases} 5.0\dfrac{kg}{s}, & t \leq 75.0s, \\ 5.0\dfrac{kg}{s} + (t - 75.0s)\dfrac{kg}{s^2}, & 75.0s < t < 80.0s, \\ 10.0\dfrac{kg}{s}, & t \geq 80.0s. \end{cases} \qquad 7\text{-}14$$

Pressure convergence data are shown in Fig. 7-30. The test case behaves similarly to the linear transient in the high flow regime. The SIDO cases again appear to be less sensitive to the ∞-norm error introduced resulting from the effects described by Eq. 7-11. Using the θ-matched

VMF configuration significantly increases the ∞-norm error for all time steps and the 2-norm error at small time steps.

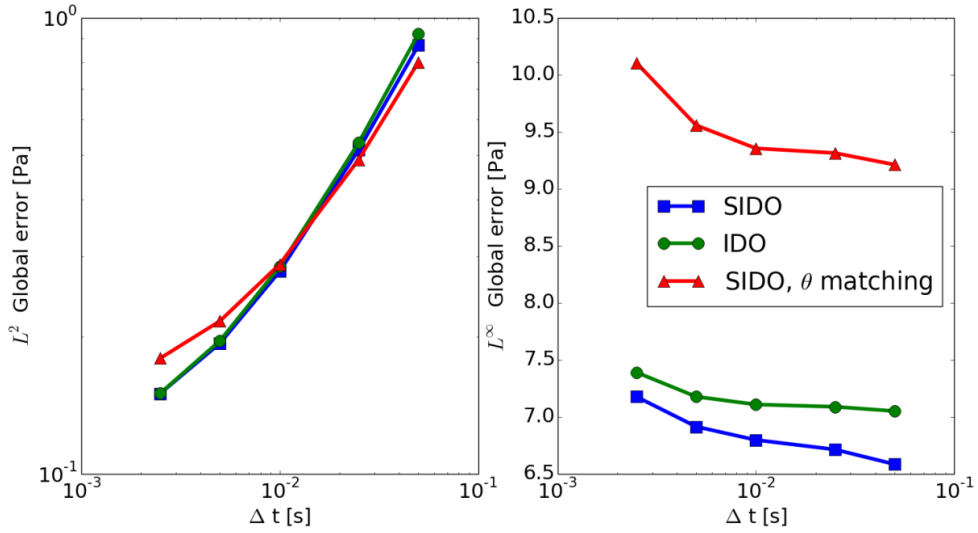

Fig. 7-30. Pressure convergence data for linear transient in the low flow rate regime. (LEFT) 2-norm error data. (RIGHT) ∞-norm error.

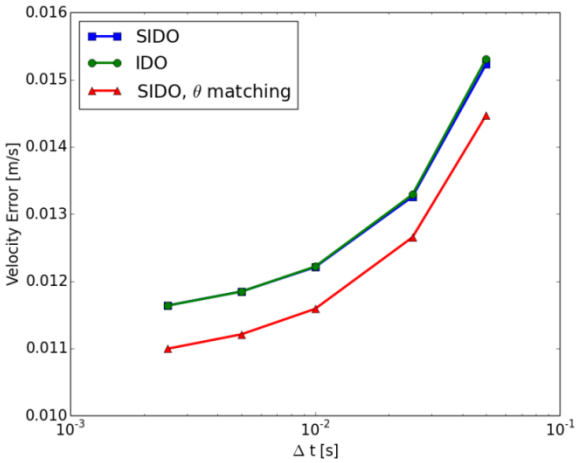

Fig. 7-31. Velocity convergence data for linear transient in low flow regime.

The velocity convergence data in Fig. 7-31 show that the θ-matched VMF configuration leads to the least velocity error, as would be expected. The IDO and SIDO methods without θ-matching lead to quite similar error in the velocity. Coupled results for SIDO with and without θ-matching and for IDO are shown in Fig. 7-32, compared to a reference STAR-CCM+ curve. Similar to the linear transient in the high flow regime, the coupled results match the STAR-CCM+ results very well away from the discontinuities in the time derivative of the inlet mass flow rate at $t = 75s$ and $t = 80s$.

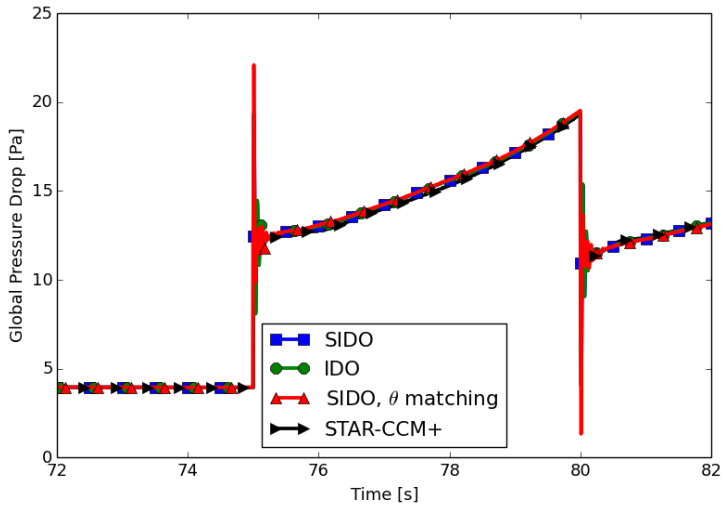

Fig. 7-32. Global pressure drop functions calculated with $\Delta t = 0.0025s$ for the linear inlet mass flow rate in the low flow regime.

7-2.4.2 Fast Smooth Transient

For the fast smooth transient in the low flow regime, Eq. 7-15 was applied to the inlet of the flow domain:

$$\dot{m}_{in}(t) = \begin{cases} 5.0\dfrac{kg}{s}, & t \leq 75.0s, \\ 5.0\dfrac{kg}{s}\left[1 + \sin^4\left(\dfrac{t - 75.0s}{10.0\ s}\pi\right)\right], & 75.0s < t < 80.0s, \\ 10.0\dfrac{kg}{s}, & t \geq 80.0s. \end{cases} \qquad \textit{7-15}$$

Due to the diminished stabilizing effects of frictional loss and the high temporal derivative of mass flow rate, this transient turned out to be the most challenging test case discussed in this chapter, and indeed motivated the development of the stabilized coupling method. The data shown in Fig. 7-33 illustrate an unusual convergence pattern in both norms. The error for the IDO coupling implementation increases substantially at $\Delta t = 0.01s$, while the θ-matched SIDO case shows a similar behavior incipient at smaller time steps. The SIDO coupling without θ-matching shows much more favorable convergence behavior.

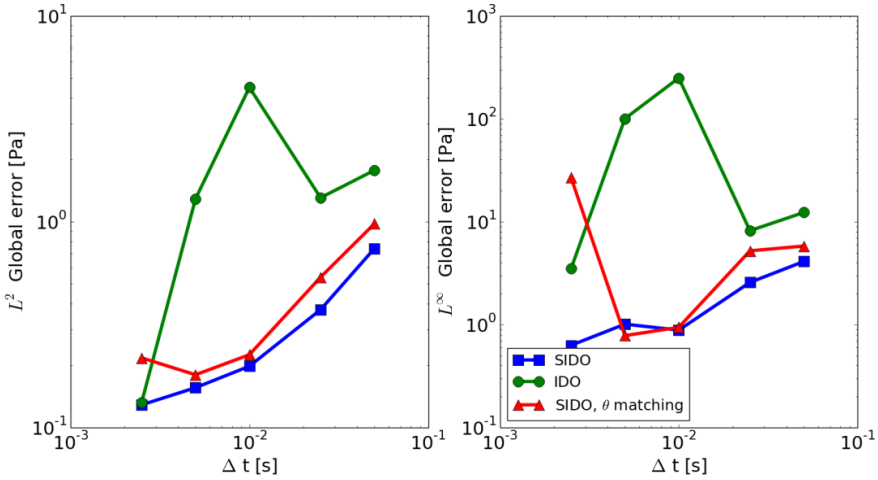

Fig. 7-33. Pressure convergence data for fast smooth transient in the low flow rate regime. (LEFT) 2-norm error data. (RIGHT) ∞-norm error.

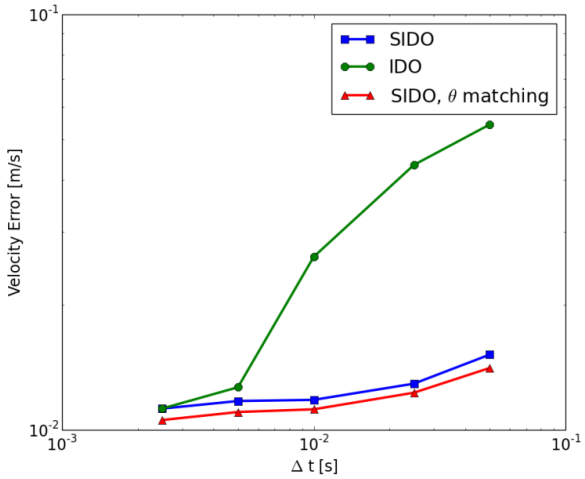

Fig. 7-34. Velocity convergence data for fast smooth transient in low flow regime.

The velocity error data in Fig. 7-34 shows a departure from the behavior observed in previous sections. Substantial error is noted for the IDO coupling case for all but the smallest of time steps. The unique behavior of the velocity data suggests that the velocity field plays an important role in the solution stability, an idea that will be corroborated by a deeper examination of the solution of the continuity equation.

The form of the convergence data is better understood upon inspection of Fig. 7-35, in which an instability is observed for the IDO case calculated with $\Delta t = 0.01s$. Near the end of the transient, large oscillations of high frequency appear in the pressure drop response functions that essentially destroy the usefulness of the coupling. The instability appeared to manifest at a time step of $\Delta t = 0.01s$. Close inspection of this test case revealed that certain edges were

accompanied by a value of $E(\Delta\Delta p)$ (Eq. 6-28) similar in size to the total pressure drop across the edge.

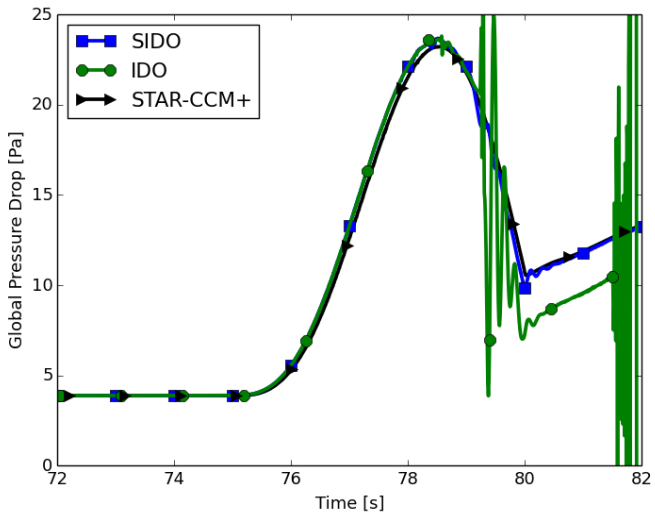

Fig. 7-35. Total pressure drop for the fast smooth transient in the low flow rate regime calculated with $\Delta t = 0.01s$.

As is observed in Fig. 7-35, the stabilization term has almost no effect on the total pressure drop until the peak of the function around $t \approx 78.5s$, where the SIDO and IDO curves begin to exhibit different behavior. On the downward slope, the stabilizer effect is apparent in rather dramatic fashion. A deeper discussion of continuity is beneficial to the understanding this behavior. We define a cell-based continuity function, F shown in Eq. 7-16:

$$F = (\bar{v}_{x-}^{TRC} A_{x-}^{TRC} - \bar{v}_{x+}^{TRC} A_{x+}^{TRC}) + \left(\bar{v}_{y-}^{TRC} A_{y-}^{TRC} - \bar{v}_{y+}^{TRC} A_{y+}^{TRC}\right) + (\bar{v}_{z-}^{TRC} A_{z-}^{TRC} - \bar{v}_{z+}^{TRC} A_{z+}^{TRC}). \quad \textit{7-16}$$

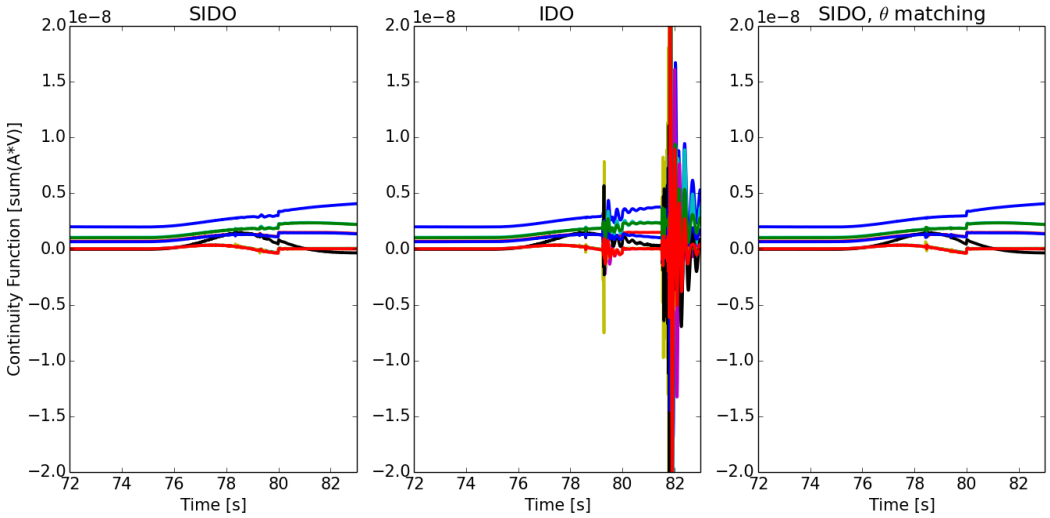

Fig. 7-36. Plots of continuity function F for 10 (of 12 total) cells from the fast smooth transient in the low flow test case.

Data in Fig. 7-36 show the continuity function from Eq. 7-16 as calculated for 10 cells (out of 12 total) for the annular geometry. The cells with external connections (i.e. the inlet and outlet cells shown in Fig. 7-12) have been omitted for simplicity. While the F values are nonzero, they are generally extremely small and within TRACE's tolerance for convergence. Upon inspection of the figure, the unstable character of the data in the center plot, calculated without stabilizer terms, can be clearly seen. As the transient progresses, the value of F tends to drift, which can lead to a mass flow rate correction as TRACE attempts to enforce continuity. In the IDO case, the velocity correction is abrupt enough to cause strong perturbations to the inertial pressure drop. In the SIDO case, the stabilizer correction factors serve to balance incoming velocity and pressure data to account for the perturbation.

Coupled results for SIDO with and without θ-matching and for IDO are compared in Fig. 7-37 to a reference standalone STAR-CCM+ solution. Even though Fig. 7-33 appears to show that the IDO method behaves better than SIDO with θ matching, a noticeable disruption in the coupled solution remains at the small time step. Additionally, the spike in the SIDO with θ-matching convergence curve is evident in this figure as a disruption in the coupled solution near the peak of the transient.

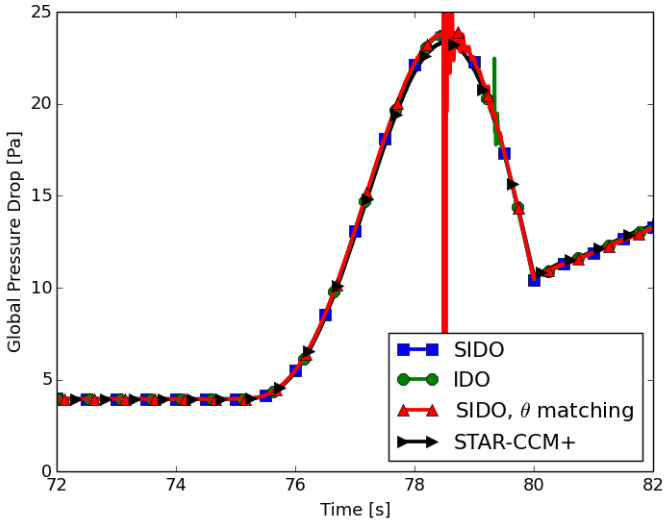

Fig. 7-37. Global pressure drop functions calculated with $\Delta t = 0.0025s$ for the fast smooth inlet mass flow rate in the low flow regime.

7-2.4.3 Slow Smooth Transient

For the slow smooth transient in the low flow regime, Eq. 7-17 was applied to the inlet of the flow domain. The mass flow rate function is of the same shape as that used in the previous section, but with a smaller amplitude, leading to a smaller time derivative and a smaller ultimate flow rate. The maximum time derivative is somewhat higher than the derivative of the linear function used in §7-2.4.1, but is lower on average:

$$\dot{m}_{in}(t) = \begin{cases} 5.0\dfrac{kg}{s}, & t \leq 75.0s, \\ 5.0\dfrac{kg}{s}\left[1 + \dfrac{3}{5}\sin^4\left(\dfrac{t - 75.0s}{10.0\ s}\pi\right)\right], & 75.0s < t < 80.0s, \\ 8.0\dfrac{kg}{s}, & t \geq 80.0s. \end{cases} \qquad 7\text{-}17$$

The pressure drop convergence data in Fig. 7-38 and the velocity field convergence data Fig. 7-39 show that this test case is not plagued with the same instability as the fast smooth transient in the low flow regime, suggesting that the high time derivative of mass flow rate is a strong factor affecting the stability. Both types of error exhibit behavior similar to both the fast and slow smooth transients in the high flow regime. The relative "gentleness" of this transient does not require any abrupt velocity corrections for TRACE to maintain continuity. Additionally, there are no time derivative discontinuities to exacerbate the VMF error.

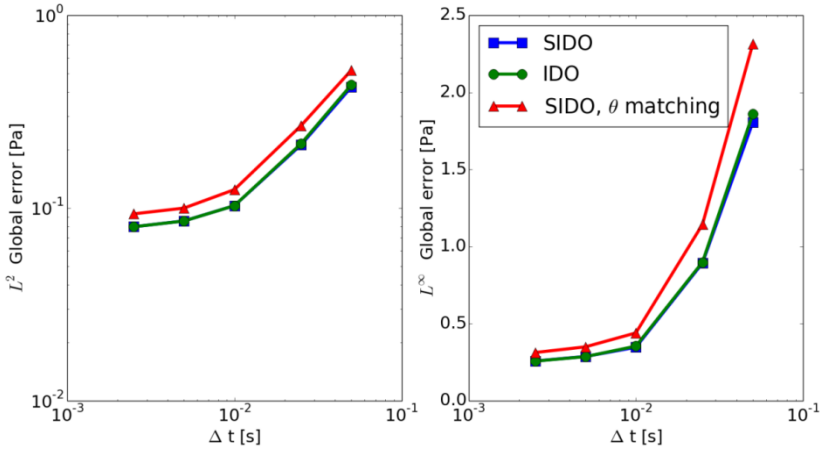

Fig. 7-38. Pressure convergence data for slow smooth transient in the low flow rate regime. (LEFT) 2-norm error data. (RIGHT) ∞-norm error.

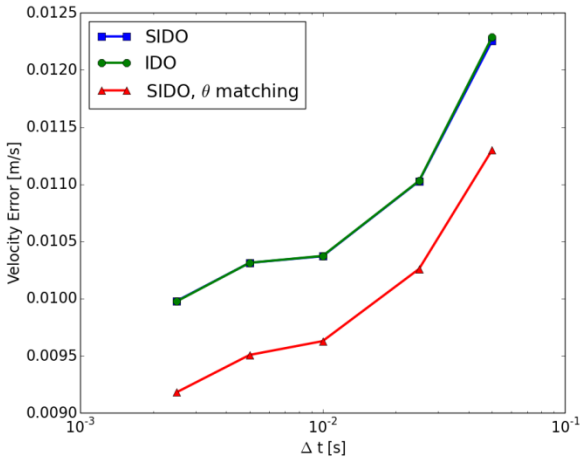

Fig. 7-39. Velocity convergence data for slow smooth transient in low flow regime.

Coupled results for SIDO with and without θ-matching and for IDO are shown in Fig. 7-40 compared to a reference STAR-CCM+ curve. In stark contrast to the previous case, no disruptions are apparent in any of the coupled solutions, which match the CFD solution quite well throughout the entire transient.

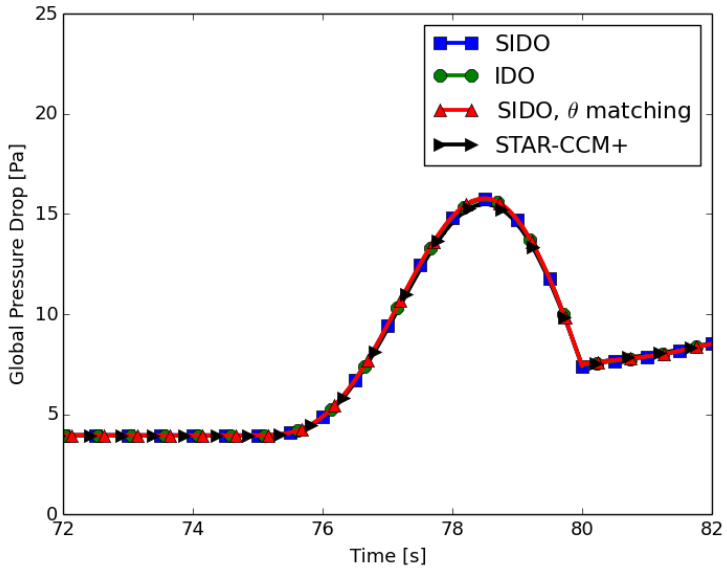

Fig. 7-40. Global pressure drop functions calculated with $\Delta t = 0.0025s$ for the slow smooth inlet mass flow rate in the low flow regime.

7-2.5 Pseudo-Implicit Transient

A dominant portion of the error that accompanies the coupling method presented in this chapter is either caused or exacerbated by the explicit time stepping employed in the data exchange between the two coupled codes. Based on this, it is appropriate to explore the use of an implicit scheme. In general, it is not an easy task to accomplish efficient implicit coupling with closed source software such as STAR-CCM+. Performing time step backups efficiently with CFD presents an additional difficulty, especially with fine meshes. However, since the cases explored in this chapter use prescribed flow conditions, it is possible to perform a sort of "pseudo-implicit coupling" in which both the STAR-CCM+ and TRACE sides of the coupled simulations are preconfigured with identical mass flow boundary conditions (in contrast with the previous cases analyzed in this chapter, in which the flow rate functions were implemented in TRACE and passed to STAR-CCM+ through boundary coupling). This type of pseudo-implicit coupling is not possible for more realistic cases in which the coupled region is part of a broader system in which feedback mechanisms determine the flow conditions, rather than prescribed functions. However, the pseudo-implicit time stepping exercise is worthwhile to further explore the root cause of coupling error and to lay down groundwork for future efforts aimed at error reduction.

In §7-2.3 and §7-2.4, it was observed that the STAR-CCM+ solution lagged the TRACE solution by a time step. When the flow rate through the system is changing, this lag can cause considerable error through VMF interaction as estimated in Eq. 7-11. By performing this pseudo-implicit transient, we demonstrate that the primary error associated with the coupling method presented herein arises from the action of velocity-matching faces under explicit time-stepping schemes. Error resulting from the imperfect estimate of $\Delta P_{j+\frac{1}{2}}^{n+1} - \Delta P_{j+\frac{1}{2}}^{n}$ in $E(\Delta\Delta p)$ (Eq. 6-28)

still remains, however. This section therefore also serves to motivate the development of advanced VMF formulations or another velocity profile coupling method altogether.

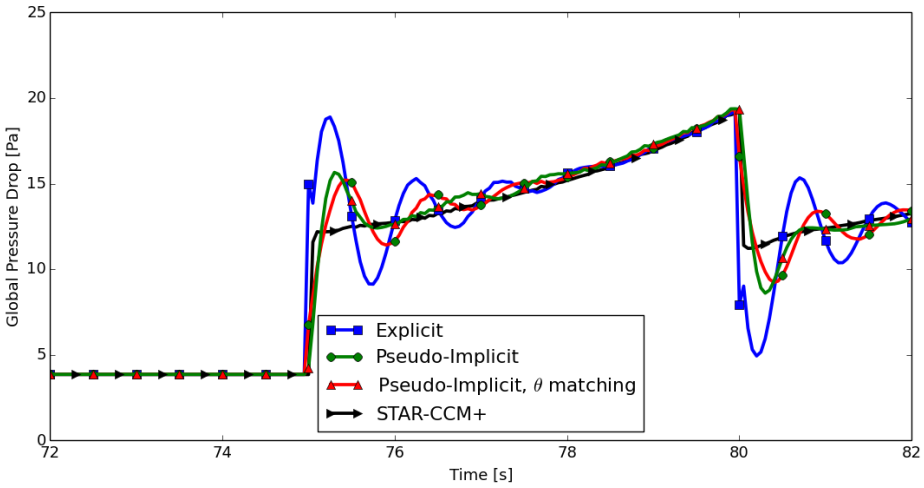

Fig. 7-41. Comparison of explicit and pseudo-implicit schemes for the linear transient in the low flow regime. Computed with $\Delta t = 0.05s$.

In Fig. 7-41, the pseudo-implicit method is compared to the SIDO method without θ-matching and explicit time stepping. The cases shown were calculated with the largest time step examined for the annulus test case $\Delta t = 0.05$s. At this time step level it is clear that the pseudo-implicit method significantly reduces the oscillations that result from discontinuities in the inertial pressure drop. Additionally, the larger oscillations predicted by Eq. 7-11 for θ-matched cases are no longer present. Convergence data shown in Fig. 7-42 demonstrate that the pseudo-implicit substantially reduces error in both the 2-norm and the ∞-norm. As would be expected, the benefit diminishes as the time step is refined. Based on these results, it is reasonable to expect that a fully implicit method would show even further improvement.

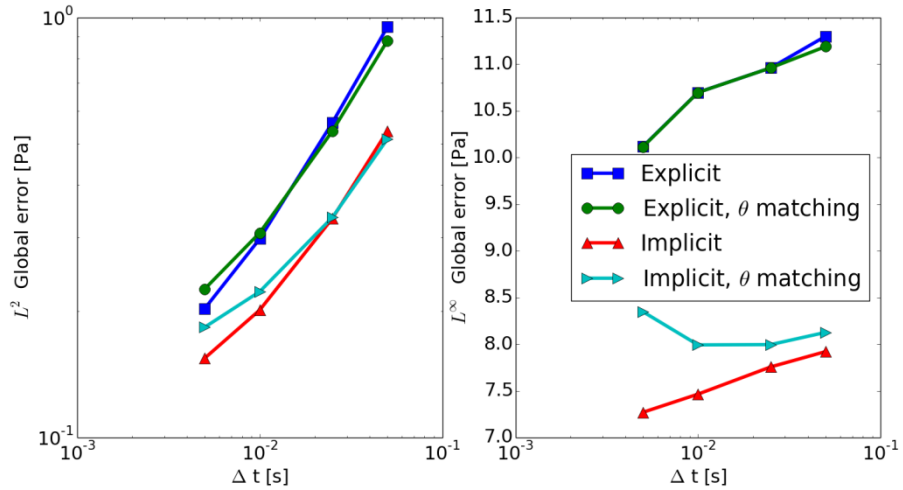

Fig. 7-42. Pressure drop convergence data showing effects of pseudo-implicit coupling. (LEFT) 2-norm error data. (RIGHT) ∞-norm error.

7-3 Conclusions

In this chapter, we described the theoretical framework of a novel domain overlapping coupling methodology between CFD and thermal-hydraulic system codes applicable to multi-dimensional regions. We showed that the STH internal solution for a 3-D component can be corrected on-the-fly to match an accompanying CFD solution. In order to correct the STH code's momentum equation, friction factors calculated on-the-fly from CFD data were used to account for the effects of convective acceleration, friction, and turbulence. A velocity-matching functionality was implemented to drive consistency between the STH and CFD velocity fields, thereby accounting for the effects of inertia on the momentum equation.

The application of the coupling method to a simple Cartesian flow splitter was straightforward. A relatively naïve approach to velocity-matching which ignored the coupling's effect on the nonlinear iteration of the TRACE solver, was found to be sufficient due to the simplicity of the geometry. In steady state, coupled simulations without velocity matching were found to produce CFD-like pressure drops, but STH-like velocity profiles due to the disruptive effect of the coupling on the pressure-velocity feedback intrinsic to fluid flow. Coupled simulations with velocity matching, however, produced CFD-like pressure drops and CFD-like velocity profiles, verifying the IDO method and motivating velocity-matching.

A more complex annular flow splitter test case was then simulated over a range of transients at both high and low Reynolds numbers. Transients featuring large time-derivatives of velocity in a low flow environment were identified as the most challenging cases. In these, perturbations from the velocity-matching implementation had a destabilizing influence on the coupled solution. Through analysis of the interaction between the IDO coupling method and the nonlinear iteration of the TRACE solver, correction factors were identified, leading to the SIDO method. Including azimuthal velocity-matching was found to produce more accurate velocity fields, but at the cost

of reduced stability for challenging transients and slowing temporal convergence in other transients.

While this method was developed and implemented with the TRACE and STAR-CCM+ code pair, the formulation is sufficiently general to be applicable to any CFD-STH pair. The proposed coupling method stands to appreciably improve the fidelity of simulations of transients involving the simulation of multi-dimensional regions with complex flow phenomena, such as those present in the downcomer in the pressure vessel of a nuclear reactor.

Chapter 8. 3-D Coupling of RPV Simulant with Simplified Internals

8-1 Introduction

In Chapter 6 the formulation of the Stabilized Inertial Domain Overlapping (SIDO) coupling interface designed for 3-D geometries was laid out, and in Chapter 7 the implementation was verified in sample Cartesian and cylindrical geometries. It was shown that the local pressure-velocity feedback in 3-D systems characterized by open regions is more challenging than what was found for the simpler cases discussed in Chapter 3 and Chapter 4. However, the systems analyzed in Chapter 7 consisted of open loop systems, and therefore the performance of the coupling methodology in the presence of global pressure-velocity feedback mechanisms was not tested. In this chapter the methods developed in the previous chapters are applied to closed flow systems subject to global feedback effects.

In NPPs, coolant is transported to and from the reactor core through multiple closed flow loops driven by independent pumps. The multi-loop configuration benefits reactor safety by maintaining core coolant in the event of a pump failure. However, the dynamics of multi-loop systems can be significantly more complex than single loop systems. The SIDO method is therefore applied to both single and dual loop configurations. Domain decomposition coupled simulations are used for direct comparison under conditions resembling typical NPP systems. The analysis is restricted to explicit time stepping.

The inlet plenum of a reactor is not an open region, but is populated with internal structures for core support and with a perforated drum or mixing plate for the optimization of the flow distribution at the core inlet. A simplified perforated drum is included in the lower plenum of the RPV model to take into account the effects of reactor internals. The core region of the flow domain is left open, since the primary targets of the SIDO coupling method are the downcomer and inlet plenum sections of the RPV. More details on the geometry used in the chapter can be found in Appendix A.

8-2 Single Loop Vessel with Simplified Internals

The TRACE model for the single loop test case is shown in Fig. 8-1. The loop consists of 6 primary components: one pump, 4 pipes, and a vessel. Additionally, a break component is attached to the pump component to act as a pressurizer. Pressures reported in this chapter are relative to the pressure of the break ($1MPa$). The pump is modeled with a homologous curve that gives the pressure rise across the component based on a rotation rate Ω with units of rad/s. In order to fully account for the effects of the vessel, the coupled region includes the vessel and sections of the cold and hot legs directly adjacent to the vessel. The two pipe segments are

referred to as inlet and outlet pipes depending on their position with respect to flow. The standard k-ϵ turbulence model was used for the single loop cases in this section.

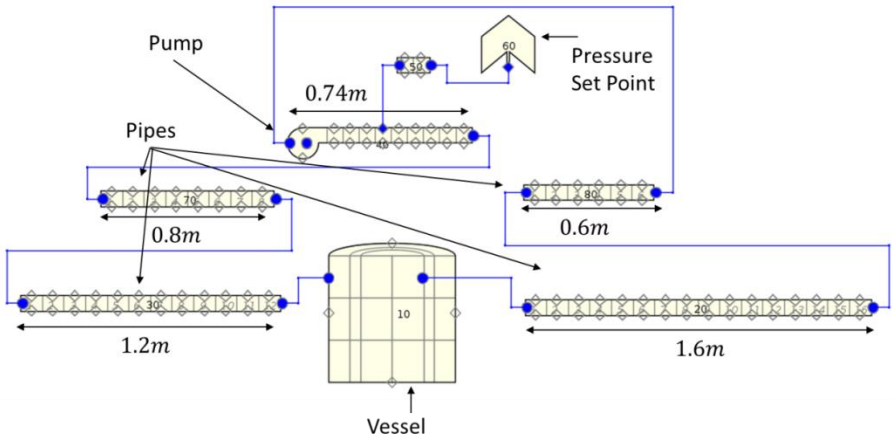

Fig. 8-1. TRACE model of single loop structure with labeled components. Fluid moves from left to right through all primary components.

8-2.1 Domain Decomposition

A domain decomposition simulation of the single loop RPV model is realized by removing the vessel and adjacent pipes from the TRACE standalone model and replacing them with the accompanying CFD model. As shown in Fig. 8-2, a fill and a break were added to the TRACE model for interfacing with the outlet and inlet of the CFD region, respectively. The main benefit of domain decomposition coupling is the straightforward implementation of the data exchange between CFD and STH codes. As apparent from Fig. 8-2, the TRACE model for the coupled simulation is simplified into an open loop system, requiring a mass flow at the fill component labeled “30” in the figure and a pressure at the break component labeled “10”. The execution time of the TRACE model is reduced compared to the TRACE standalone deck, and therefore to the TRACE deck of the domain overlapping case. However, in both coupling methods, the total runtime is dominated by the CFD code (STAR-CCM+) and the time-savings is not significant

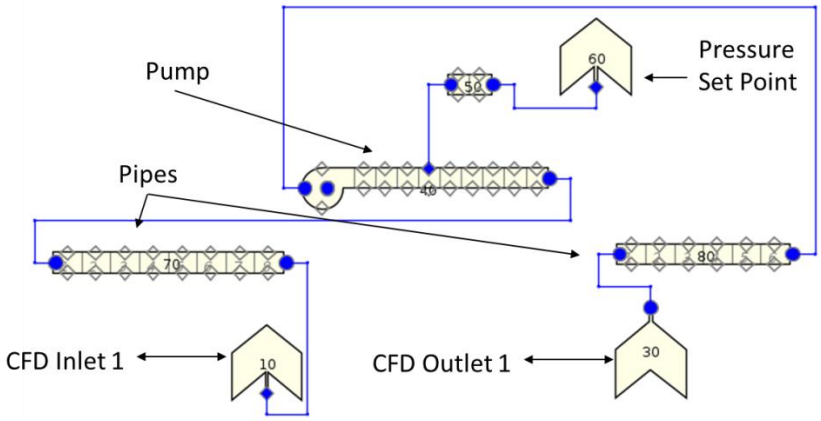

Fig. 8-2. TRACE model of single loop structure for domain decomposition coupling.

8-2.1.1 Steady State

For steady state testing, the pump impeller rotation rate Ω was varied with converged interface conditions plotted in Fig. 8-3. The mass flow rate through the loop is plotted in Fig. 8-3 (top). Also included in Fig. 8-3 (bottom) is the pressure at the interface between CFD Outlet 1 and the break component labeled "30" in Fig. 8-2. Both quantities exhibit monotonic relationships with pump speed.

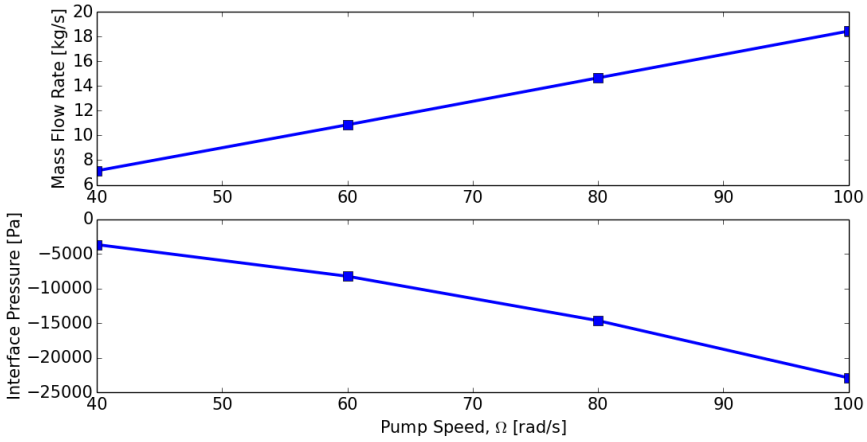

Fig. 8-3. (TOP) Mass flow rates calculated from domain decomposition coupled simulations with varied pump rotations rates. (BOTTOM) Relative pressure at the CFD outlet.

Some insight into convergence behavior can be gained upon inspection of Fig. 8-4, where the data passed at each CFD/STH iteration during a coupled simulation is reported. Under-relaxation factors (urf) were applied to the data passed from TRACE to STAR-CCM+. Convergence is achieved in all cases, even though an oscillatory behavior is present for the first few iterations when higher urfs are employed.

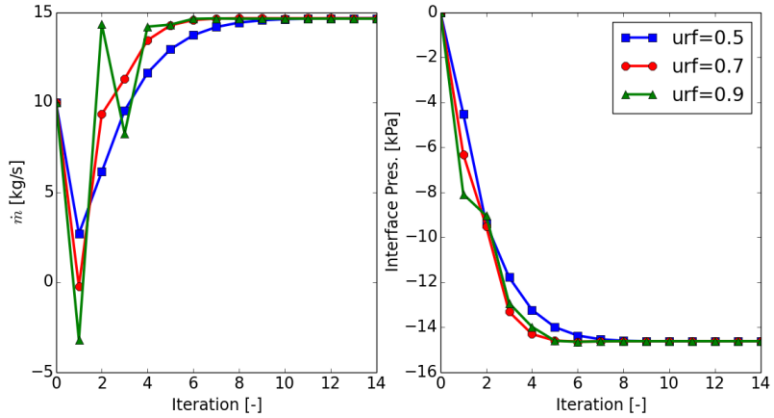

Fig. 8-4. (LEFT) Mass flow rate passed versus iteration. (RIGHT) Relative interface pressure passed from TRACE to STAR-CCM+ versus iteration. Calculated with $\Omega = 80\ rad/s$.

8-2.1.2 Transient

The domain decomposition method was tested under null transient conditions with the pump rotation rate set at a constant $\Omega(t) = 60 rad/s$. In most cases presented in this thesis, transient calculations are first initialized from a steady state solution. The coupled simulation then begins at a time somewhat before the onset of the transient ($t = 75s$ in this case) so that the solution is allowed to stabilize under null transient conditions. This is because the steady state and unsteady solvers of STAR-CCM+ will produce slightly different results, and the null transient will allow for the effects of these differences to die out. However, we found that the domain decomposition method was unstable, and no converged solution could be obtained. This case will be examined in more detail in §8-2.3. This result is not surprising, as other authors using coupled CFD/STH code based on decomposition methods have experienced similar convergence issues.

8-2.2 Domain Overlapping

The interface structure shown in Fig. 8-5 was applied to the TRACE model in Fig. 8-1 for a SIDO calculation. Pipe and connection interfaces are required to capture the distributed pressure drop that results from flow entering and exiting the vessel geometry. The connection interfaces couple the edges that attach the inlet and outlet pipes to the vessel. The pressure difference across this edge is often substantial, but insufficient to fully capture entry/exit effects. Therefore, the inlet (left in Fig. 8-5) and outlet pipes (right in Fig. 8-5) are also coupled to ensure the proper pressure drop across the entire system is reproduced in TRACE.

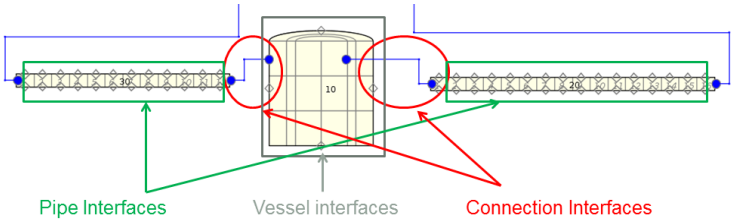

Fig. 8-5. Relevant portion of TRACE part of single loop model showing interface configuration.

Four pseudo flow paths are defined, based on the four azimuthal partitions of the vessel, to quantify the performance of the vessel interface on a component scale. Each path consists of 7 total cells and is assigned an "in" cell and an "out" cell, as shown in Fig. 8-6. The difference between the pressures of these two cells is used to provide insight into the coupling of the pressure field within the RPV geometry.

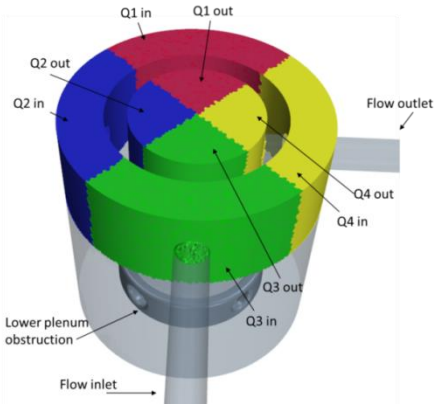

Fig. 8-6. Diagram showing the definition of "quadrant" pressure drops for each pseudo flow path.

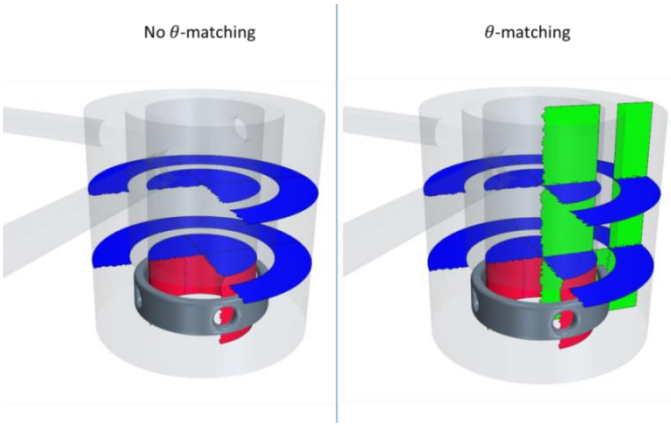

Fig. 8-7. Diagram showing VMF configurations for RPV simulant. Axial faces are blue, radial faces are red, and azimuthal faces are green. (LEFT) VMF configuration for test case without azimuthal matching. (RIGHT) VMF configuration with azimuthal matching.

The analysis of the annular geometry in Chapter 7 provided some intuition for VMF configurations. A system tended to be more stable without θ-matching, but excluding these faces meant that velocity field conformity between TRACE and STAR-CCM+ was not guaranteed. However, the goal of the coupling is only to match global pressure drops and the velocity distribution at the core. Since the STAR-CCM+ solution is already available, the TRACE velocity field does not need to reproduce it as long as the primary objectives are satisfied. The two configurations shown in Fig. 8-7 were used for the RPV simulant geometry. The case without θ-matching on the left is comprised of 18 VMFs, while the θ-matched case on the right uses 25 VMFs.

8-2.2.1 Steady State

The rotation rate of the pump impeller was varied with the resulting loop mass flow rates plotted in Fig. 8-8. The steady state convergence behavior can be observed in Fig. 8-9, where the computed mass flow-rate circulating in the closed loop is reported as function of the iteration step. In the simulations used to compute the data, an urf was placed on the mass flow rate passed from TRACE to STAR-CCM+. It is clear that this system requires significant under-relaxation compared to domain decomposition for steady state convergence.

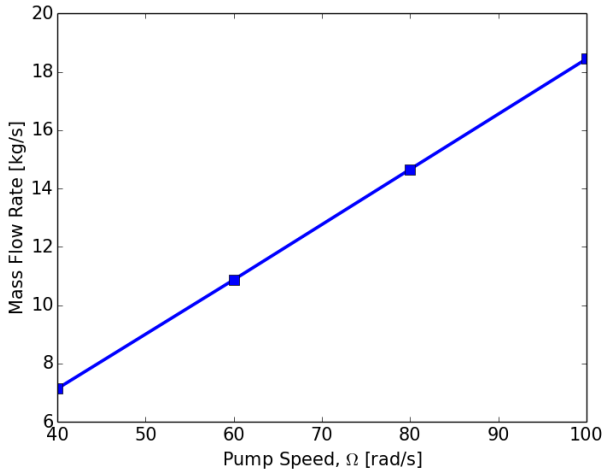

Fig. 8-8. Mass flow rates calculated from domain overlapping coupled simulations with varied pump rotations rates.

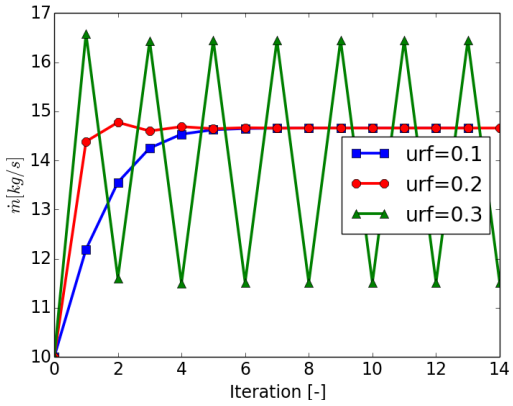

Fig. 8-9. Loop mass flow rate at each iteration for domain overlapping coupled simulations with selected under-relaxation factors. Calculated with $\Omega = 80\ rad/s$

8-2.2.2 Transient

In order to test the coupling under transient conditions, the pump was driven by a time-dependent rotation rate given by Eq. 8-1:

$$\Omega(t) = \begin{cases} 60\dfrac{rad}{s}, & t < 75s, \\ 60\dfrac{rad}{s} + 2(t - 75s)\dfrac{rad}{s^2}, & 75s \le t \le 80s, \\ 70\dfrac{rad}{s}, & t > 80s. \end{cases} \qquad \textit{8-1}$$

We first consider the VMF configuration that excludes azimuthal velocity-matching (Fig. 8-7, left). The mass flow rate through the system is shown in Fig. 8-10. The top of the figure shows the mass flow rate entering the RPV, while the bottom shows the mass flow rate leaving the region. The STAR-CCM+ inlet mass flow rate is set by one-way surface interface to match the flow through the loop in TRACE. Continuity requires that the outlet flow rate matches the inlet.

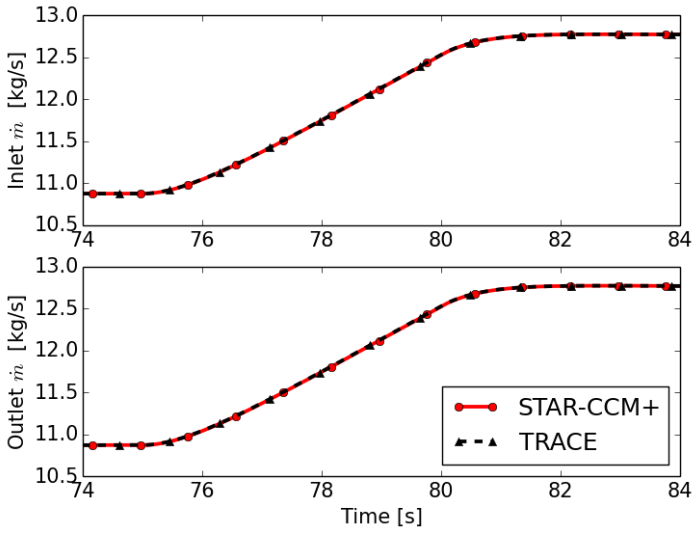

Fig. 8-10. Mass flow rates through the coupled section. (TOP) Mass flow into vessel. (BOTTOM) Mass flow out of vessel. Calculated with $\Delta t = 0.01s$.

The total pressure drop across the coupled section, defined by the difference in pressure between the first cell of the inlet pipe and the last cell of the outlet pipe, is given in Fig. 8-11. This value encompasses the effects of all 5 interfaces. The pressure drops calculated by both STAR-CCM+ and TRACE during the simulation match very well.

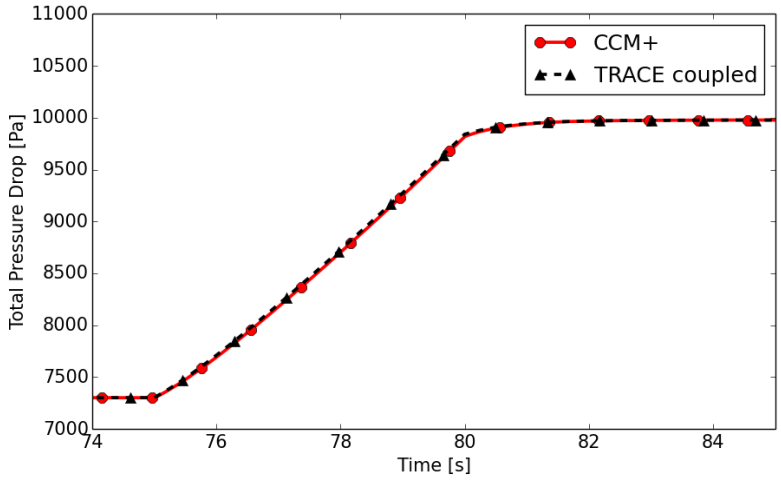

Fig. 8-11. Total pressure drop across the coupled section. Calculated with $\Delta t = 0.01s$ and without azimuthal velocity-matching.

Fig. 8-12 shows the velocity distribution at the core inlet. The matched faces, Q1-Q3, show very good CFD/STH consistency, while there is some error on the unmatched face, Q4. This error results from interpolation error in the CFD code. More details can be found in §A-5 in Appendix A. The data in Fig. 8-11 and Fig. 8-12 show that the coupling succeeds in its stated goals of reproducing the total system CFD pressure drop and core inlet velocity distributions in TRACE.

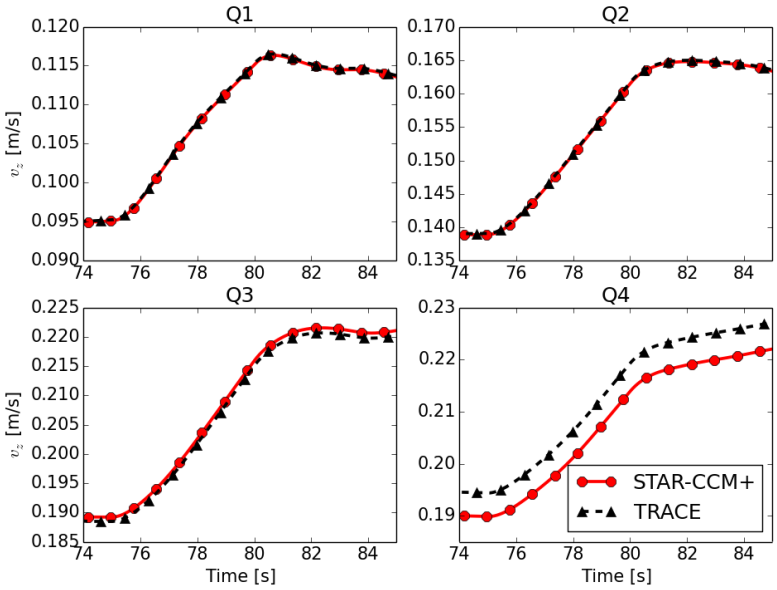

Fig. 8-12. Velocity distribution at core inlet. Calculated with $\Delta t = 0.01s$ and without azimuthal velocity-matching.

The consequences of excluding azimuthal VMFs can be seen in Fig. 8-13, which shows the pressure drops across each quadrant (as defined in Fig. 8-6) of the RPV simulant. The flows internal to the TRACE vessel are not completely consistent with STAR-CCM+ in this case and therefore do not necessarily produce the same inertial pressure drop.

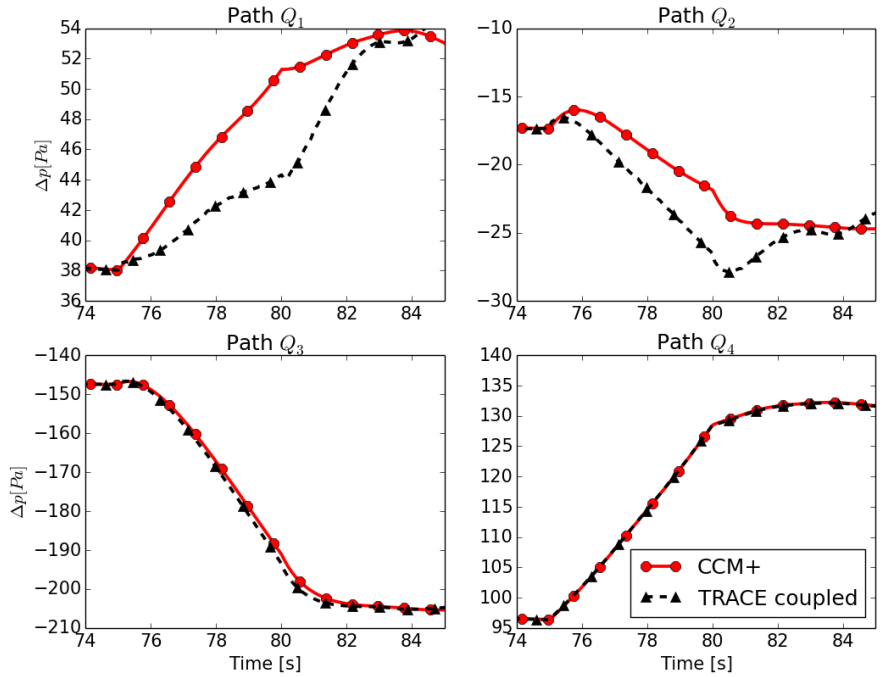

Fig. 8-13. Pressure drops across each quadrant of the vessel component during a transient simulation without azimuthal velocity matching faces. Calculated with $\Delta t = 0.01s$.

The inlet and outlet are attached to Quadrants 3 and 4, respectively, making them the most necessary for prediction of the total pressure drop across the component. While there is clearly some inconsistency in the pressure drops across Q1 and Q2, this does not appear to adversely affect the variables of interest, the global pressure drop and the velocity distribution at the core inlet.

The same transient was carried out with the addition of azimuthal velocity-matching to more fully explore the effects of VMFs. The total system pressure drop is shown in Fig. 8-14. Again, the values calculated by STAR-CCM+ and TRACE match closely. The velocity distribution across the core inlet is shown Fig. 8-15, which shows similar behavior as the same data for the un-matched case.

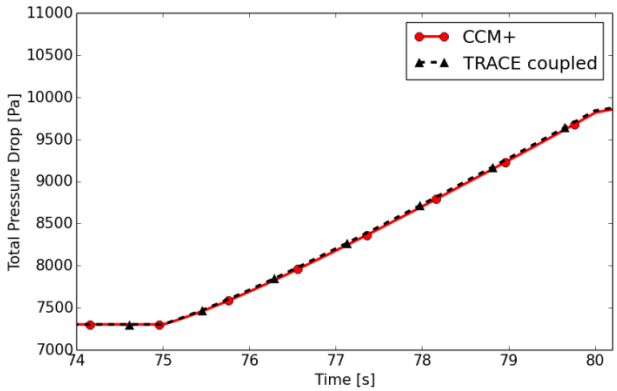

Fig. 8-14. Total pressure drop across the coupled section. Calculated with $\Delta t = 0.01s$ and with azimuthal velocity-matching.

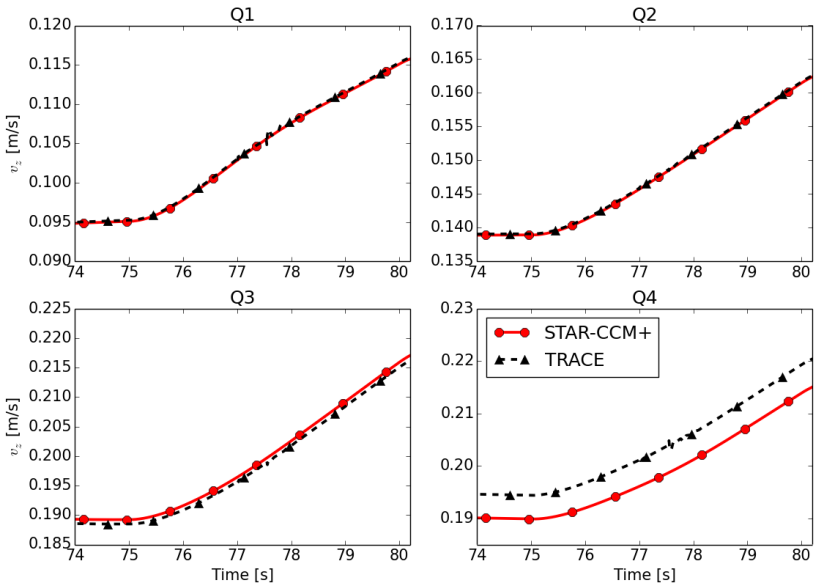

Fig. 8-15. Velocity distribution at core inlet during a transient simulation with azimuthal velocity matching faces. Calculated with $\Delta t = 0.01s$.

The pressure drops across the pseudo flow paths are shown in Fig. 8-16. Compared to Fig. 8-13, the pressure drops across quadrants Q1 and Q2 match more precisely for most of the transient. However, near the middle of the transient, some instability is apparent. While this does not strongly affect the total pressure drop and core inlet velocity, such behavior is generally indicative of unfavorable numerical properties of the system.

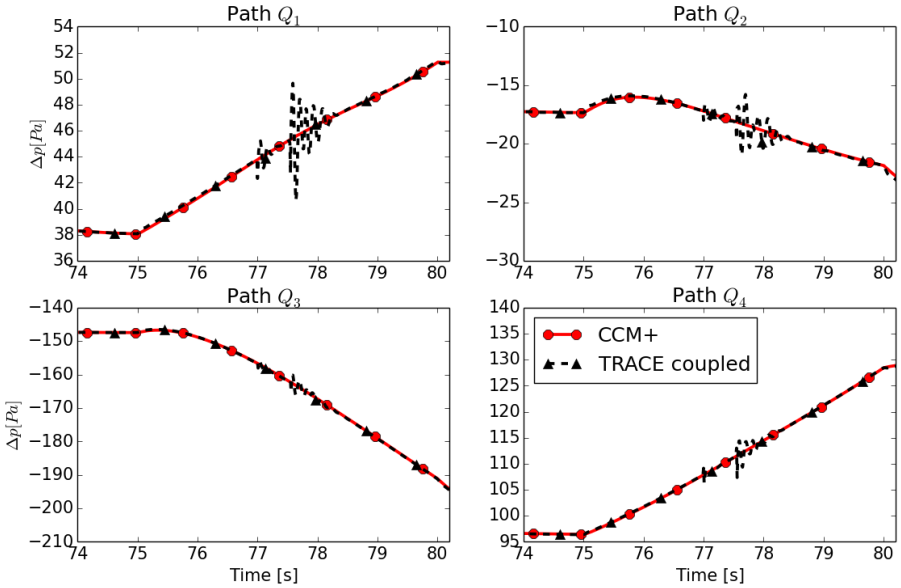

Fig. 8-16. Pressure drops across each quadrant of the vessel component during a transient simulation with azimuthal velocity matching faces. Calculated with $\Delta t = 0.01s$.

The same calculation with azimuthal velocity matching was carried out with a smaller time step of $\Delta t = 0.005s$, with the total pressure drop shown in Fig. 8-17 and the core inlet velocity distribution given in Fig. 8-18. Once again, these values match quite well with no significantly different behavior than in the previous two cases.

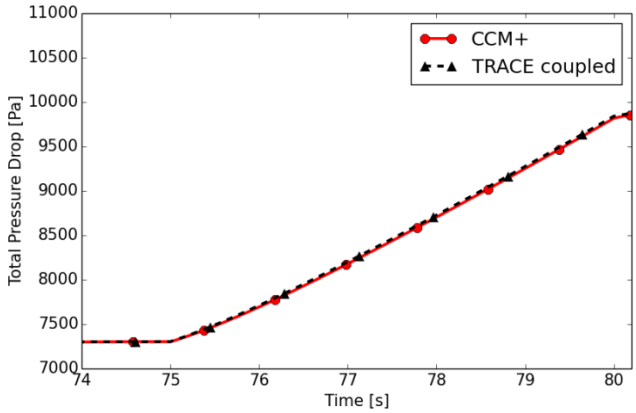

Fig. 8-17. Total pressure drop across the coupled section. Calculated with $\Delta t = 0.005s$ and with azimuthal velocity-matching.

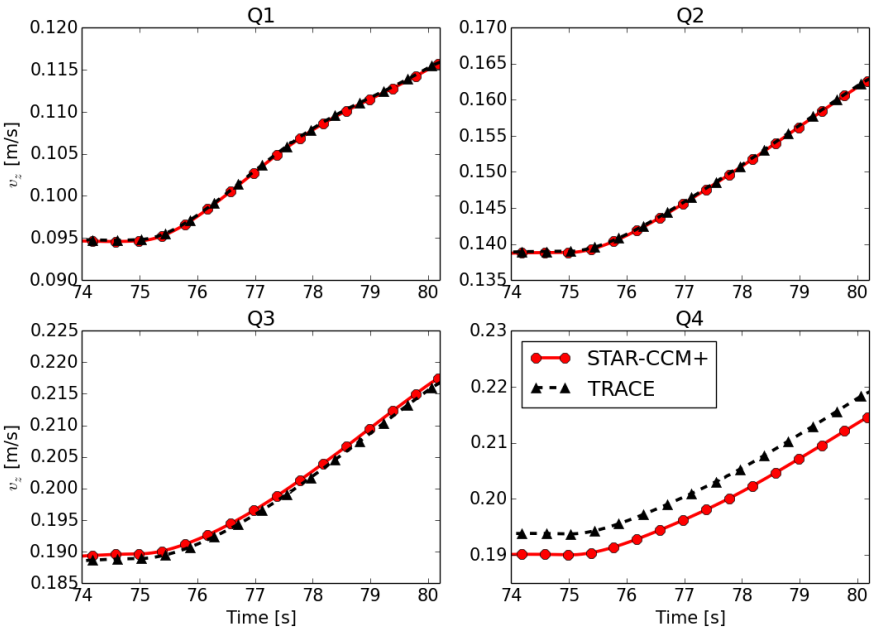

Fig. 8-18. Velocity distribution at core inlet during a transient simulation with azimuthal velocity matching faces. Calculated with $\Delta t = 0.005 s$.

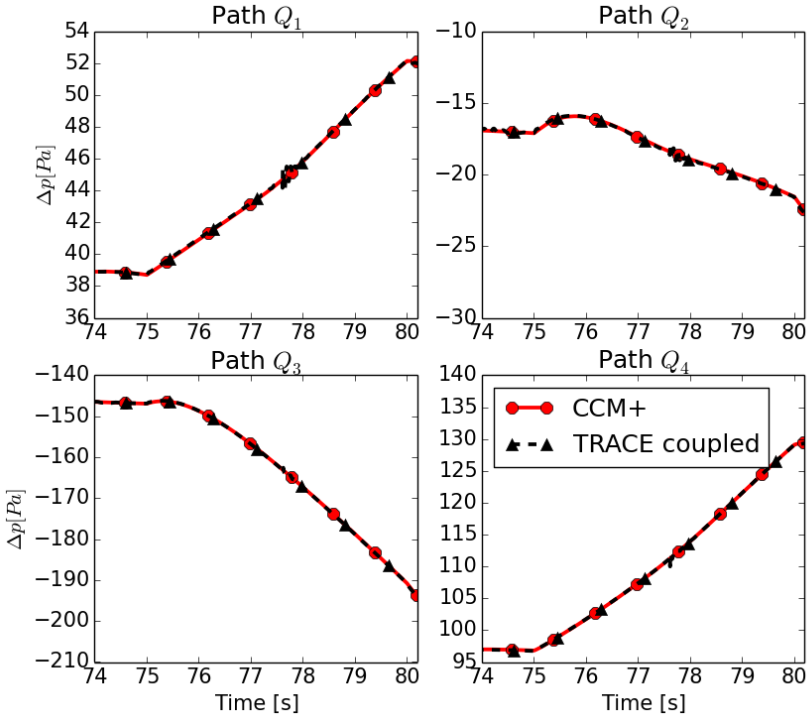

Fig. 8-19. Pressure drops across each quadrant of the vessel component during a transient simulation with azimuthal velocity matching faces. Calculated with $\Delta t = 0.005 s$.

The pressure drops across each quadrant are shown in Fig. 8-19. The instability is apparent near the middle of the transient, though is it much more subdued in the case with the smaller time

step. Based on the foregoing analysis, it can be concluded that, for the single loop system, adding azimuthal VMFs decreases the stability of the solution with no readily apparent increase in accuracy of the global pressure drop and core inlet velocity profile. The VMF configuration with azimuthal matching did lead to improved consistency in the predicted pressure drops across the quadrants in the vessel component. However, this information is already available in STAR-CCM+, and the improved consistency therefore does not justify the cost to stability.

8-2.3 Method Comparison

Now that the abilities and limitation of the domain decomposition and domain overlapping coupling methods have been discussed in the context of closed loop flow through an RPV simulant, it is of interest to directly compare the coupling methods. Mass flow rates from both domain overlapping and domain decomposition coupling methods are plotted against pump speed in Fig. 8-20. The mass flow rates match almost identically for all pump speeds tested.

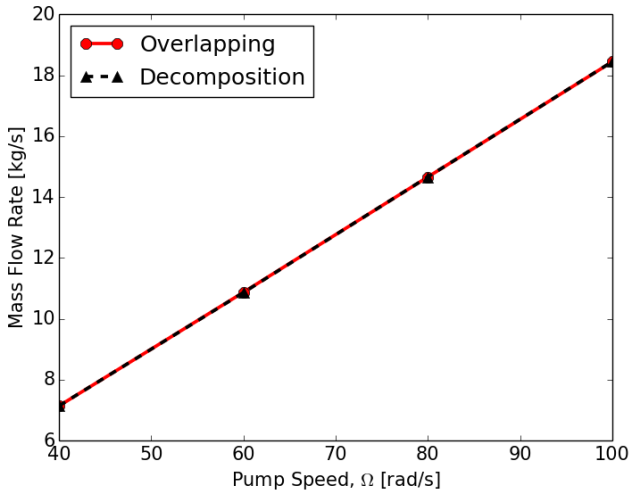

Fig. 8-20. Comparison of steady state mass flow rates calculated from domain overlapping and domain decomposition coupled simulations.

The steady state convergence of the two methods is compared in Fig. 8-21, showing the mass flow rates passed during iteration. The domain overlapping method is observed to reach the converged mass flow rate significantly faster.

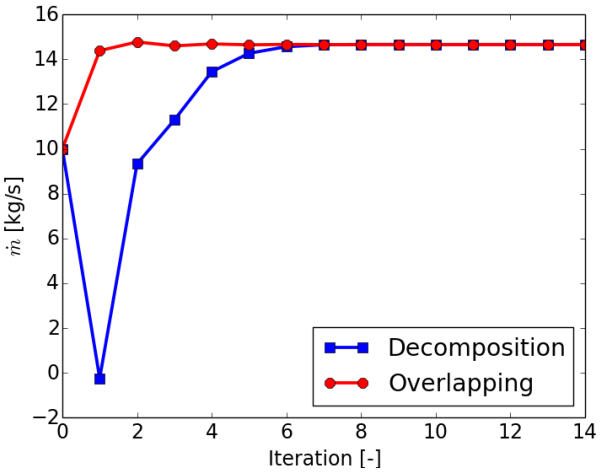

Fig. 8-21. Comparison of steady state mass flow rates calculated from domain overlapping and domain decomposition coupled simulations.

The transient performance of the two methods is compared in Fig. 8-22. Because the domain decomposition method was found to be unstable, only the first $2.0s$ of the coupled simulation are shown. Due to reasons discussed in §8-2.1.2, a perturbation is expected after the onset of the coupling. All SIDO simulations recover from the initial perturbation, while the domain decomposition method exhibits oscillatory behavior with increasing amplitude, suggesting that the solution is unstable. The pressures passed at the CFD outlet interface exhibit similar behavior.

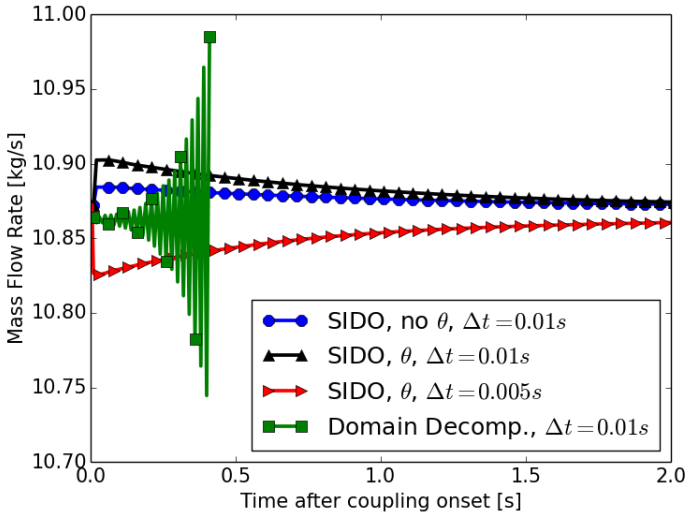

Fig. 8-22. Comparison of mass flow rate through loop for various coupling methods during a null transient simulation.

8-3 Dual Loop Vessel with Simplified Internals

The closed loop model was made more complex by adding a second loop and corresponding recirculation pump, as shown in Fig. 8-23. The secondary inlet and outlets pipes are attached to the vessel directly opposite from their original counterparts. The two pumps are driven independently. A pressurizer is only required on one loop, consistent with NPP configurations. The simulations with symmetric pump rotation rates were carried out with the standard k-ϵ model, while the k-ω model was used for asymmetric pump rates. More details can be found in §A-2.2 of Appendix A.

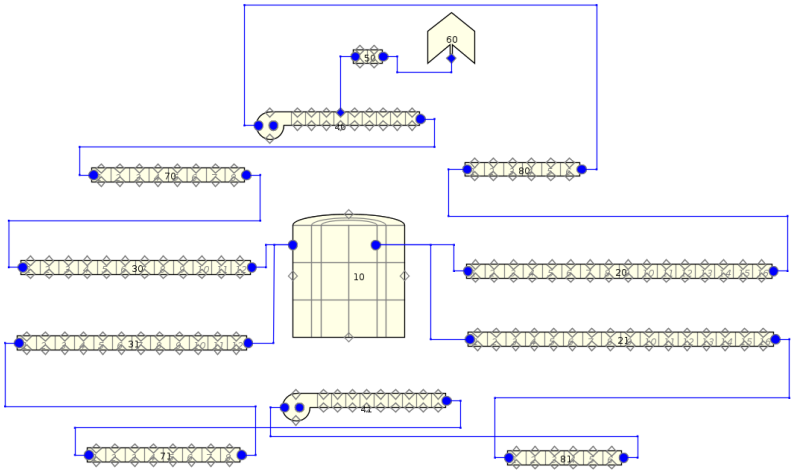

Fig. 8-23. TRACE model of dual loop test case.

8-3.1 Domain Decomposition

A domain decomposition approach to the dual loop RPV simulant is realized with the configuration shown in Fig. 8-24. The vessel component has been replaced with two fill components and two break components that interface with the CFD inlets and outlets as indicated. The pressure set-point is maintained on the first loop. No pressurizer is required for the second loop, as pressure data is communicated between the loops through the CFD simulation.

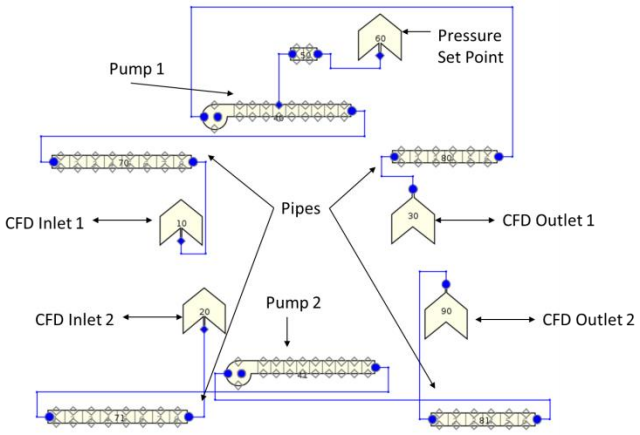

Fig. 8-24. TRACE model of dual loop structure for domain decomposition coupling.

8-3.1.1 Steady State

Steady state results for the domain decomposition coupling of the dual loop system are shown in Fig. 8-25 for symmetric pump configurations. Fig. 8-25 (top) shows the mass flow rate through each loop as recorded at the CFD inlets, while in Fig. 8-25 (bottom) the interface pressures for each loop as recorded at the CFD outlets is presented. The two loops are essentially identical, as would be expected from the symmetric pump configuration.

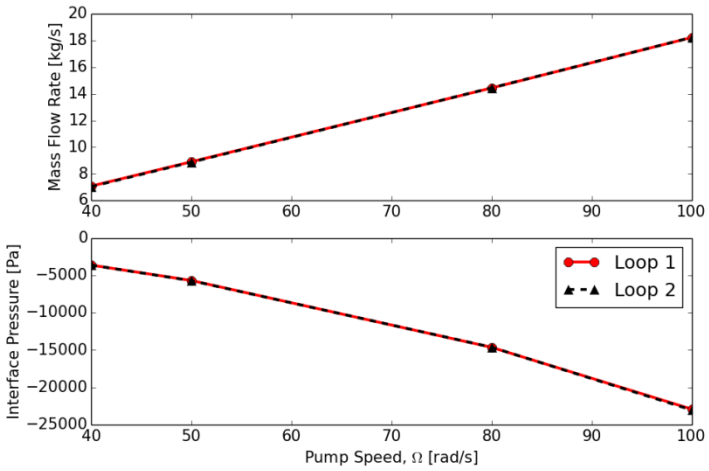

Fig. 8-25. Domain decomposition coupling results for symmetric pump cases.

Fig. 8-26 shows the effects of varying the initial guess of outlet pressures. For these cases, both pumps were operated at a rotation rate of $\Omega_1 = \Omega_2 = 50 rad/s$ and both CFD inlets were initialized to $\dot{m}_1 = \dot{m}_2 = 10 kg/s$. The cases only differed by the pressures to which the CFD outlets were initialized. As would be expected, it is possible to significantly aid convergence of the domain decomposition method with a better initial guess at the converged solution.

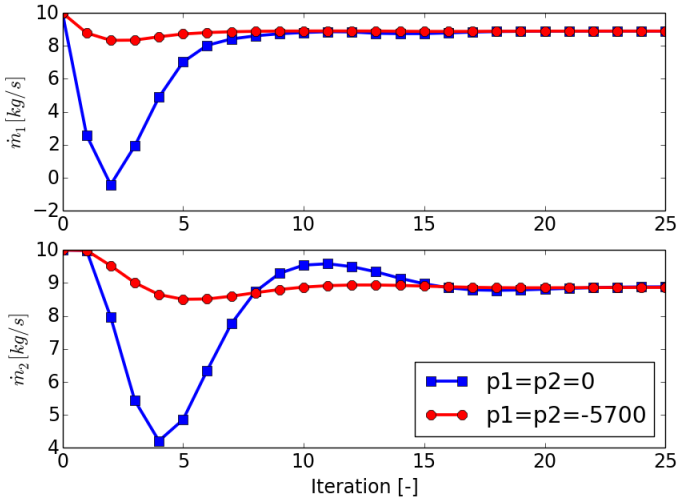

Fig. 8-26. Mass flow rates through each loop through each iteration. Cases shown had different initial conditions for outlets pressures in STAR-CCM+

Steady state simulations were also carried out with asymmetric pump conditions by setting $\Omega_1 = 50 rad/s$ and varying Ω_2. The resulting mass flow rates are shown in Fig. 8-27 (top) while the relative pressure at each interface are shown in Fig. 8-27 (bottom). The loop 1 values do not change significantly, while the loop 2 values vary similarly to the behavior observed for the single loop case indicating the independence of the loops.

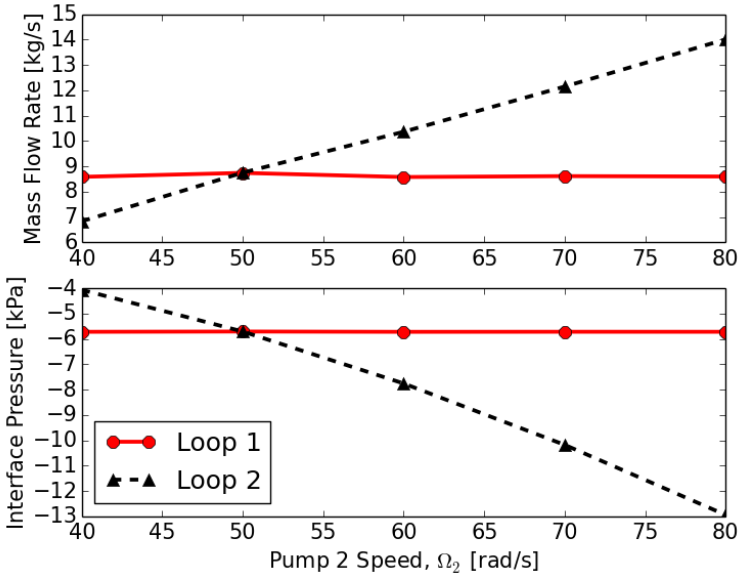

Fig. 8-27. Domain decomposition coupling results for asymmetric pump cases.

Convergence data from an asymmetric pump simulation are shown in Fig. 8-28 for selected urfs. In each case, the indicated under-relaxation factor was applied to the data passed from STAR-CCM+ to TRACE for all four interfaces. Using a large urf resulted in larger oscillations in the

interface data. In this case $urf = 0.7$ was taken to be an optimum configuration for convergence.

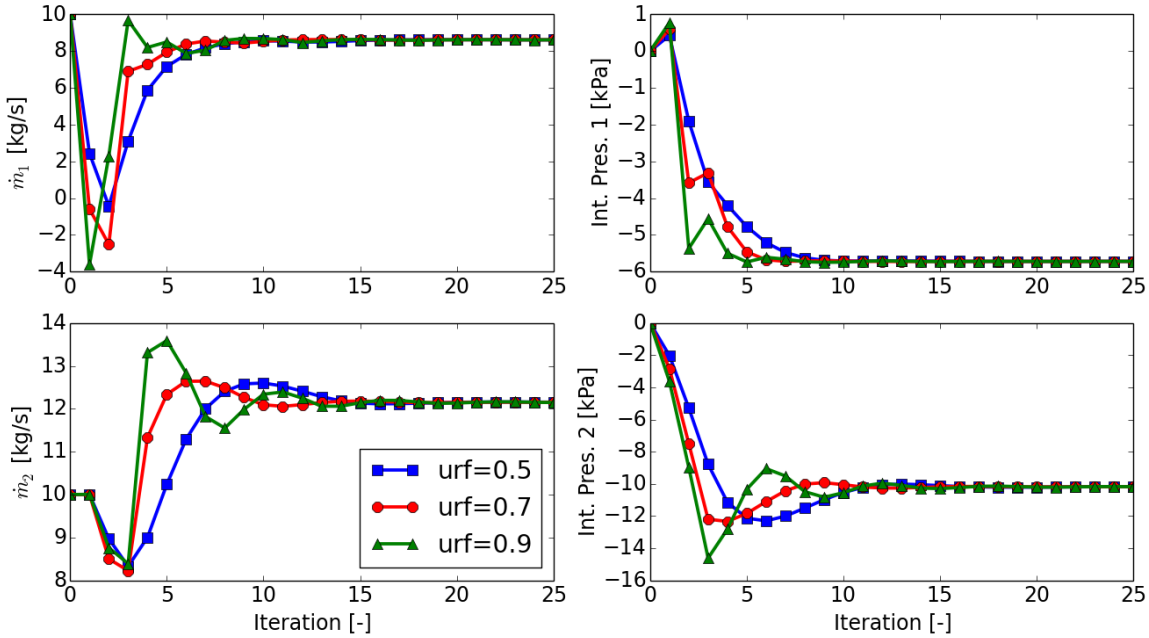

Fig. 8-28. Steady state convergence data for dual loop test case. Calculated with k-ω model and asymmetric pump rate $\Omega_1 = 50 rad/s$ and $\Omega_2 = 70 kg/s$.

8-3.2 Domain Overlapping

A domain overlapping test case is carried out with the single loop interface configuration of Fig. 8-5 essentially duplicated (except for the vessel interface) to connect to the second loop. However, the presence of multiple outlets presents an additional complication. When only one outlet is considered, the boundary simply acts as a set-point for pressure, which is sufficient because the domain overlapping coupling method only depends on pressure differences. While the coupling method continues to rely solely on pressure differences with multiple outlets, the pressure differential between the outlets becomes important for the correct redistribution of the mass flow-rate among the outlets.

Consider a case in which the rotation rate of pump 1 is significantly larger than the rotation rate of pump 2 ($\Omega_1 \gg \Omega_2$). Under such circumstances, it would be expected that the mass flow rate through loop 1 is significantly larger than the flow through loop 2 ($\dot{m}_1 \gg \dot{m}_2$). However, if there is no pressure difference between the two outlets, there will not be a relative flow rate between them and the CFD model would always predict $\dot{m}_1 = \dot{m}_2$, regardless of pump speed. Therefore, some information regarding the relative pressures of the two outlets is required for coupling under asymmetric pump speed configurations. The two outlets of the CFD simulation correspond to the surface between two adjacent cells. For example, consider Fig. 8-29, which shows the

geometry of a surfaces pressure p_s relative to a cell on the left with pressure p_l and a cell on the right with pressure p_s.

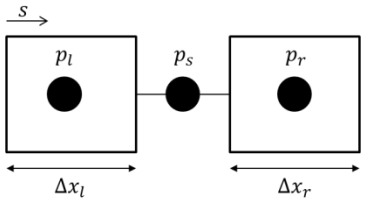

Fig. 8-29. Interpolation scheme for calculation of the pressure at the surface between adjacent cells.

We can approximate the surface pressure with a simple linear interpolation, shown in Eq. 8-2:

$$p_s = p(s = \Delta x_l) = \frac{(p_r - p_l)}{\left[\left(\Delta x_l + \frac{\Delta x_r}{2}\right) - \frac{\Delta x_l}{2}\right]}\left(\Delta x_l - \frac{\Delta x_l}{2}\right) + p_l = \frac{p_r \Delta x_l + p_l \Delta x_r}{\Delta x_l + \Delta x_r}. \qquad 8\text{-}2$$

Based on this, we can use a surface interface to match the outlet pressures with the appropriate surface from the STH nodalization. However, since only the pressure difference is relevant, a degree of freedom can be removed by keeping one outlet at a reference pressure and setting the remaining outlets to pressure relative to that outlet. This strategy is employed in this test case with CFD Outlet 1 is taken as reference. The cells used to calculate pressure differences for the dual loop model are shown in Fig. 8-30.

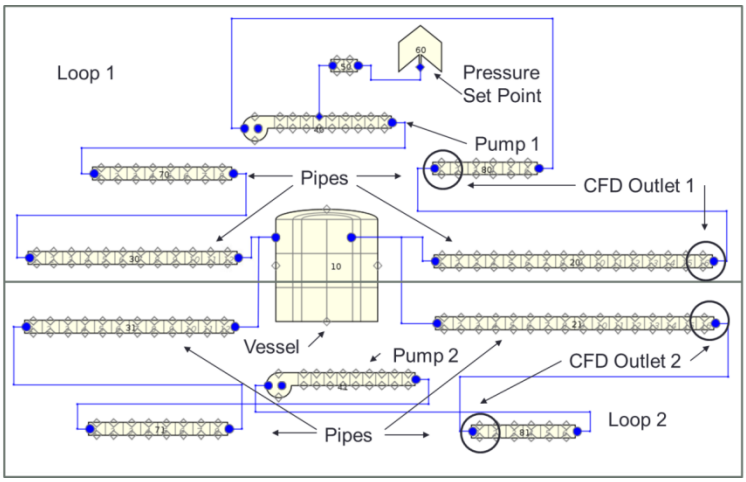

Fig. 8-30. TRACE model of the two loop test case with indicated cells for pressure calculation.

Additionally, it is necessary to ensure that flow through the outlets in TRACE matches the flow through the STAR-CCM+ outlets. When there are multiple outlets, the faces connecting the pipes and vessel components suffer from the same disruption in pressure-velocity feedback, as do the faces internal to the vessel component. Therefore, velocity matching must also be applied

to the set of outlets that remove flow from the vessel. The inlet connections are held consistent by the interfaces that pass mass flow rates from TRACE to the CFD inlets.

Outlet velocity matching is accomplished through a similar method as vessel velocity matching. In NPP systems we expect outlet connections to be relatively few in number (i.e. many commercial plants are of the 4-loop variety), and so some simple optimization strategies can be employed. First, because we are considering incompressible flow, it is not necessary to calculate the velocity at the connection from the precisely corresponding surface in the CFD model. For this particular case, we calculate the velocity at the CFD outlet. The velocity field at the surface that joins the outlet pipe to the riser is quite complex, whereas the velocity at the CFD outlet is essentially fully developed and much simpler. Calculating an average velocity at the latter location therefore reduces a source of error.

Secondly, to minimize any disagreement between CFD and STH outlet flows, instead of directly matching velocity, we instead match fractional flows. As was observed in the previous core inlet velocity distributions (i.e. Fig. 8-15), the velocities at VMFs were quite consistent between STAR-CCM+ and TRACE. The unmatched face, however, showed some error. Using fractional velocities acts to spread this error between outlets:

$$V_1 = \left(\sum_{outlets} AV_{TRC} \right) \times AV_{CFD} \times \left(\sum_{outlets} AV_{CFD} \right)^{-1} . \qquad 8\text{-}3$$

where AV refers to the produce of area and velocity. To accomplish this, the initial iterant for the velocity field in the Newton-Raphson iteration is replaced with Eq. 8-3 which, for a specific outlet, multiplies the total TRACE mass flow through all outlets by the ratio of the mass flow through the corresponding CFD outlet to the total mass flow through all CFD outlets.

8-3.2.1 Steady State

Pump speeds were initially varied symmetrically ($\Omega_1 = \Omega_2$), with the resulting loop mass flow rates and CFD outlet pressure differences plotted in Fig. 8-31. The mass flow rates through loops 1 and 2 match closely and exhibit an approximately linear relationship with the pump rotation rate, as would be expected. The CFD outlets remain at essentially the same pressure, with some difference resulting from numerical effects of the mesh.

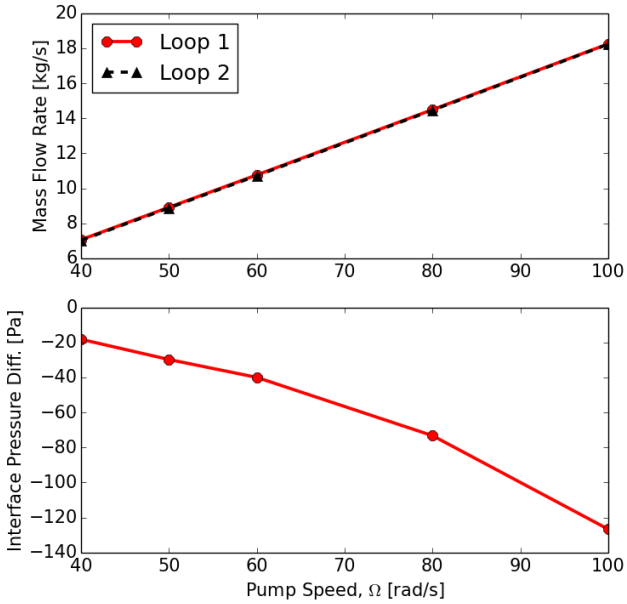

Fig. 8-31. Domain overlapping coupling results for symmetric pump cases. (TOP) Mass flow rates through each loop. (BOTTOM) Pressure of outlet 2 relative to outlet 1.

The system was tested under asymmetric conditions with $\Omega_1 = 50 rad/s$ and variable Ω_2, with results shown in Fig. 8-32. As would be expected, the flow rate through loop 1 remains mostly constant, and the loop 2 flow rate varies with Ω_2. The interface pressure differential decreases with Ω_2.

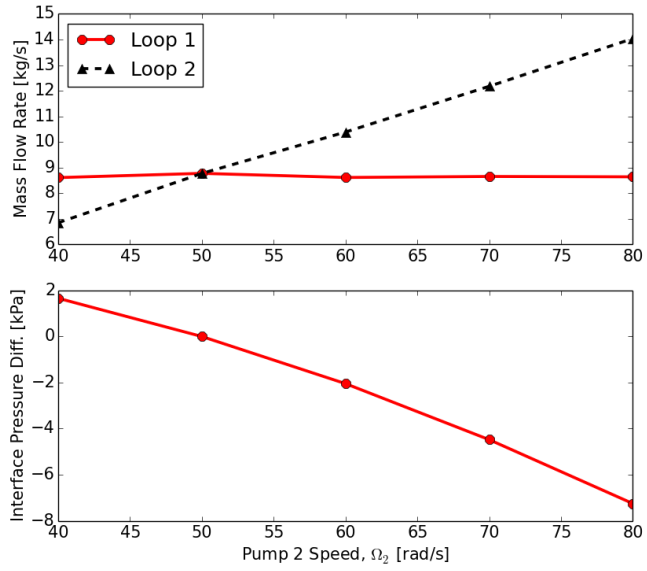

Fig. 8-32. Domain overlapping coupling results for asymmetric pump cases. Calculated with k-ω model and with $\Omega_1 = 50 rad/s$.

Fig. 8-33 shows data passed at each iteration during an asymmetric coupled simulation with selected under-relaxation factors. Under-relaxation factors were applied in three places: the mass flow rates passed from TRACE to STAR-CCM+ for inlets 1 and 2 as well as the for the pressure differential between the two outlets. In the "$urf = 0.1$"," $urf = 0.2$", and "$urf = 0.3$" cases, the same factor was used for each. In the remaining case, the value urf_m was used for the mass flow rates while urf_p was used for the pressure differential. Similar to the single loop case, convergence is achieved in all cases. However the coupled iteration appears to lose stability around $urf = 0.3$. The convergence of the pressure differential is improved significantly by increasing urf_p to 0.7. The "$urf\_m = 0.2, urf\_p = 0.7$" configuration is taken as optimal for steady state convergence.

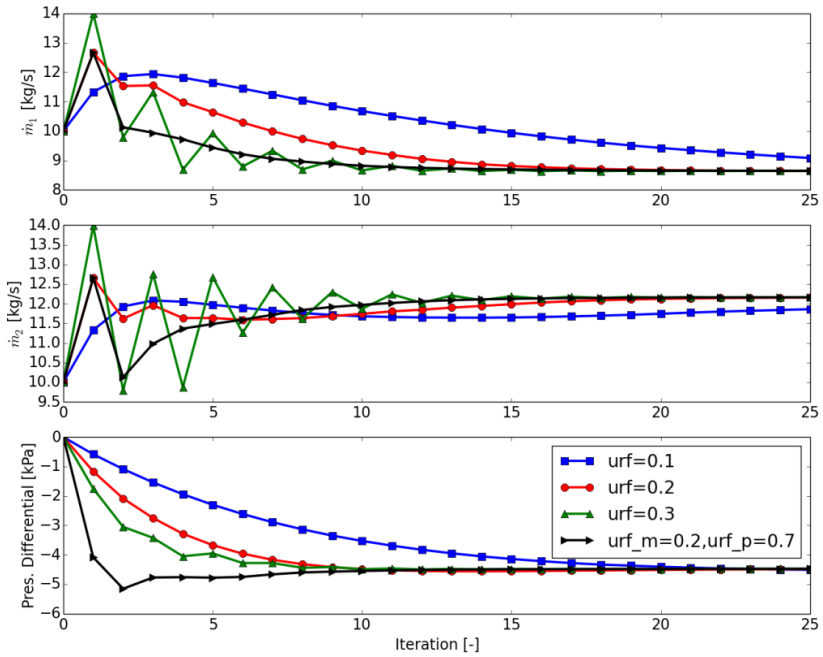

Fig. 8-33. Domain overlapping convergence data for steady state cases calculated with k-ω turbulence model. Asymmetric pump rates of $\Omega_1 = 50 rad/s$ and $\Omega_2 = 70 rad/s$. (TOP) Flow rate through loop 1. (CENTER) Flow rate through loop 2. (BOTTOM) Pressure differential between CFD outlets.

8-3.2.2 Transient

For a transient test case, pump 1 is kept at $\Omega_1 = 40 rad/s$, while the pump 2 is driven by the time dependent rotation rate of Eq. 8-4:

$$\Omega_2(t) = \begin{cases} 40\dfrac{rad}{s}, & t < 75s, \\ 40\dfrac{rad}{s} + (t - 75s)\dfrac{rad}{s^2}, & 75s \le t \le 80s, \\ 45\dfrac{rad}{s}, & t > 80s. \end{cases} \qquad 8\text{-}4$$

The transient was carried out with azimuthal velocity-matching. The mass flow rates into and out of the RPV simulant are shown in Fig. 8-35. The inlet flow rates are maintained consistent by the interfaces that set flow inlet conditions to the CFD simulation. The outlet flow rates in TRACE are governed by the velocity-matching of Eq. 8-3.

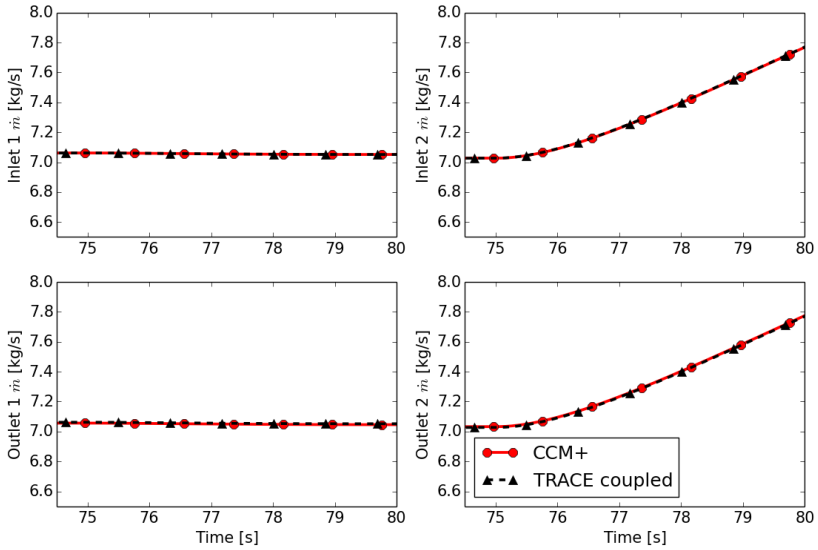

Fig. 8-34. Mass flow rates into (top plots) and out of (bottom plots) of the vessel region.

The total pressure drop through each loop is shown in Fig. 8-35. Some error is clearly apparent through the loop 1 value once the transient begins. However, compared to the value of the pressure drop, the error is quite small. The pressure drop through loop 2 experiences similar levels of error, though the scale of the abscissa obfuscates it somewhat.

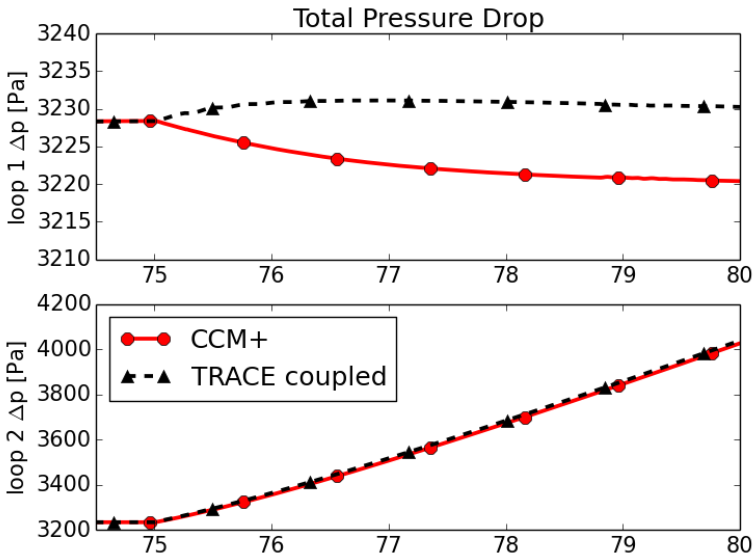

Fig. 8-35. Total pressure drops across each loop during the transient.

The pressure drop across each vessel-pipe connection is given in Fig. 8-36. The pressure drops across the inlet connections match very well. However, the source of error in the total pressure drop is clearly evident in the outlet connection pressure drops where the velocity-matching is applied. While this error appears quite significant for the "Out. Conn. 1 Δp" plot in Fig. 8-36 (top right), consider that the difference between the two curves is approximately $10 Pa$, which is less than 0.5% error.

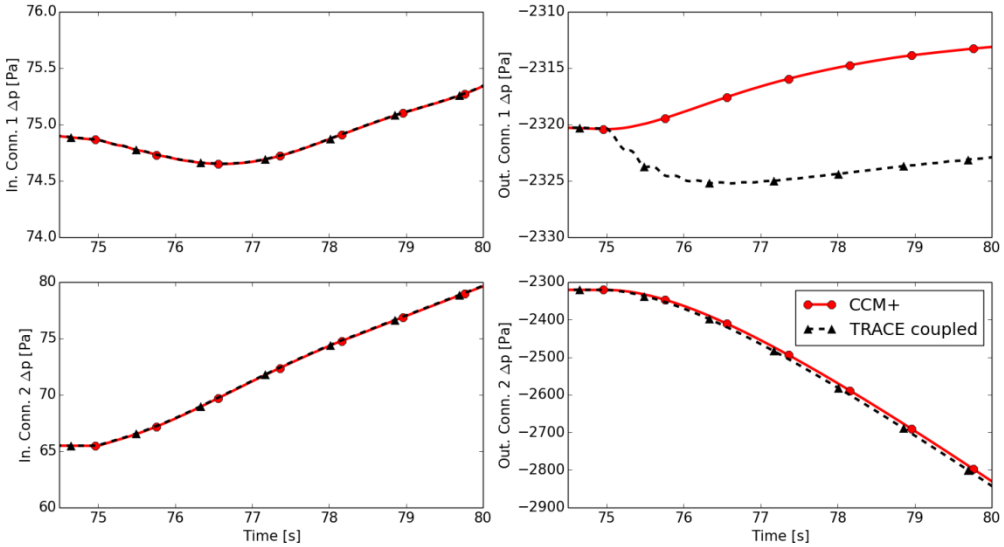

Fig. 8-36. Vessel-pipe connection pressure drops during transient operation.

The core inlet velocity distribution is given in Fig. 8-37. The velocity-matched faces Q1-Q3 show good CFD/STH consistency, while some error is apparent on the unmatched face, Q4.

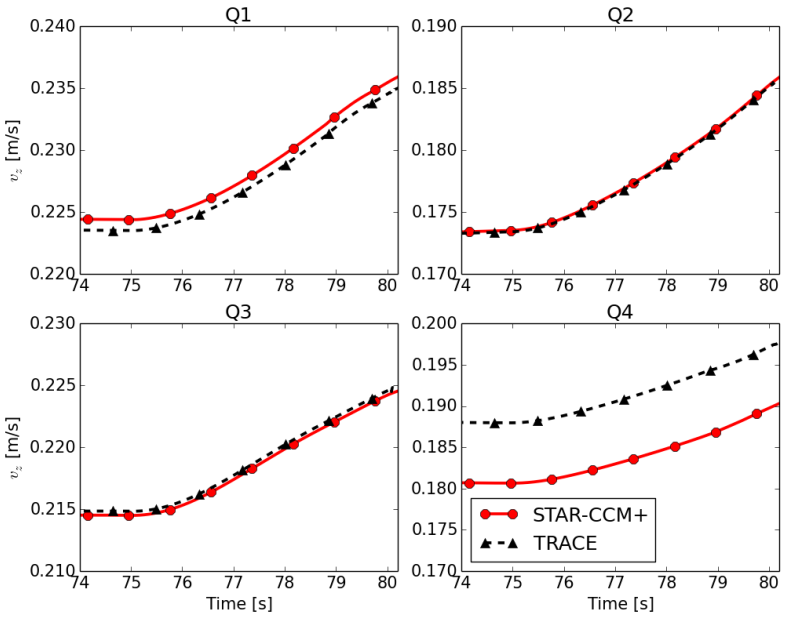

Fig. 8-37. Velocity distribution at core inlet during dual loop transient simulation with azimuthal velocity matching faces. Calculated with $\Delta t = 0.01s$.

As illustrated by Fig. 8-35 and Fig. 8-37, the SIDO method accomplishes its stated goals of inducing TRACE to calculated the same global pressure drop and core inlet velocity as CFD.

8-3.3 Method Comparison

Converged results for symmetric pump configurations are shown in Fig. 8-38 for both domain overlapping and domain decomposition coupled simulations. The top two plots compare the mass flow rates through loops 1 and 2, respectively. The bottom plot compares the difference in pressure between the two CFD outlets. The mass flow rate quantities match up almost perfectly, while some discrepancy in the outlet pressure difference quantity is clearly observable. However, this difference is very small when compared to the total pressure drops across the system.

Asymmetric pump configurations were implemented by holding the rotation rate of pump 1 at a constant $\Omega_1 = 50 rad/s$ and varying the rotation rate of pump 2, Ω_2. Results from these cases are shown in Fig. 8-39 for both domain decomposition and overlapping approaches. As would be expected, the flow through loop 1 is not strongly affected by the rotation rate of pump 2. The flow rate through loop 2, however, varies approximately linearly with Ω_2. The pressure at the CFD outlet for loop 2 decreases relative to the loop 1 interface significantly with increasing Ω_2.

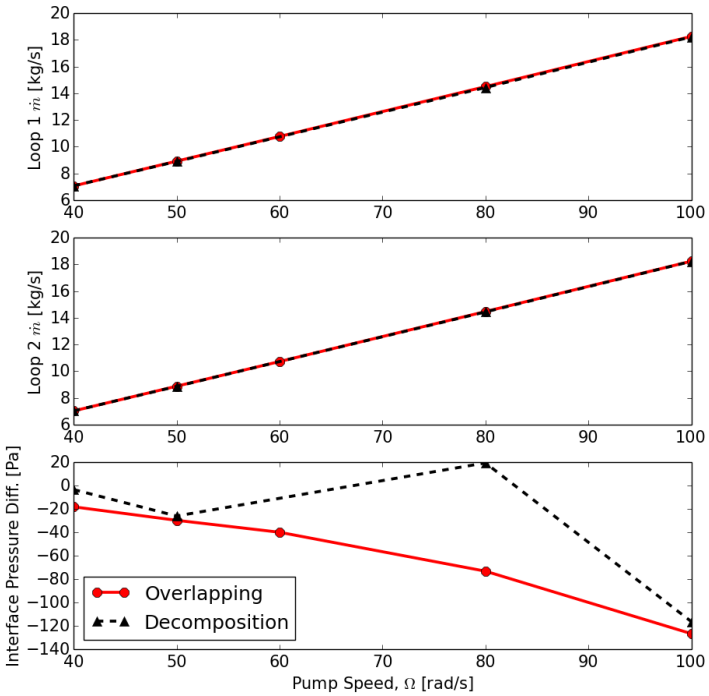

Fig. 8-38. Comparison of coupling methods for steady state symmetric pump rotation rates. Calculated with *k*-ϵ turbulence model. (TOP) Loop 1 flow rate. (CENTER). Loop 2 flow rate. (BOTTOM) interface pressure differential.

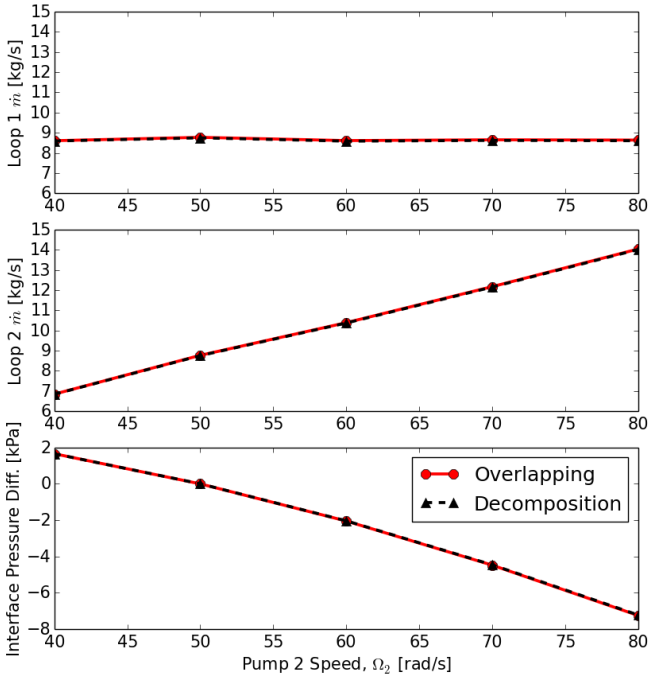

Fig. 8-39. Comparison of coupling methods for asymmetric pump rotation rates. Calculated with *k*-ω turbulence model. (TOP) Loop 1 flow rate. (CENTER). Loop 2 flow rate. (BOTTOM) interface pressure differential.

The convergence of the two methods is compared in Fig. 8-40. The SIDO method requires fewer iterations to converge than the domain decomposition method. A key observation is that the SIDO method calculates the outlet pressure differential much more quickly than the domain decomposition method, because the former method only needs the difference between the two outlets, while the domain decomposition method must calculate the pressure of both outlets.

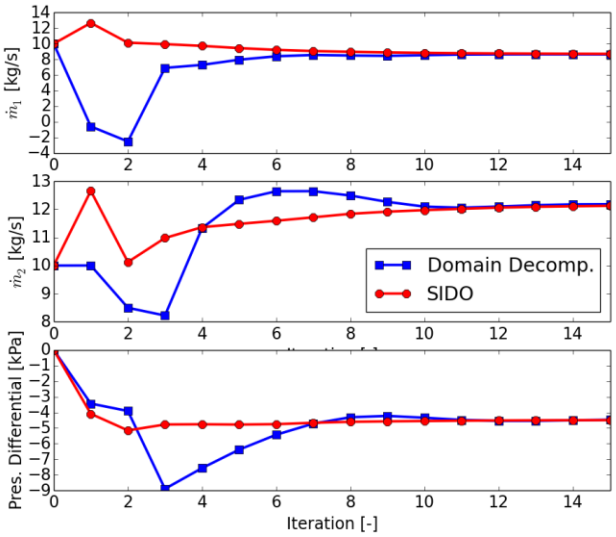

Fig. 8-40. Convergence data for steady state cases calculated with k-ω turbulence model. Asymmetric pump rates of $\Omega_1 = 50 rad/s$ and $\Omega_2 = 70 rad/s$. (TOP) Flow rate through loop 1. (CENTER) Flow rate through loop 2. (BOTTOM) Pressure differential between CFD outlets.

8-4 Conclusions

In this chapter, the SIDO method was applied to an RPV simulant in a closed loop configuration. Fluid flow was pump-driven in both single and dual loop configurations. Simulations were carried out under both steady state and transient conditions. In general, the domain overlapping method required heavier under-relaxation in steady state cases. However, the domain decomposition method usually required more coupled iterations to achieve convergence. Domain decomposition coupling was found to be unstable in transient mode. Several single-loop transients were undertaken with the SIDO method to establish the effects of VMF configuration. All cases produced good CFD/STH consistency for the total system pressure drop as well as the core inlet velocity distribution. Adding azimuthal VMFs had adverse effects on solution stability.

The dual-loop configuration was examined in both symmetric and asymmetric pump configurations. For all steady state cases tested, the converged results of SIDO and domain decomposition coupling were essentially indistinguishable. The SIDO method was found to converge in fewer iterations, depending on choice of under-relaxation factors. A transient was carried out in the dual loop configuration with asymmetric pump rates. The total system pressure drop and core inlet pressure velocity distribution showed good CFD/STH consistency.

Chapter 9. Conclusions and Future Work

9-1 Conclusions

The research reported in this dissertation was aimed at developing a theoretical framework for a novel coupling scheme applicable to existing CFD and thermal-hydraulic system codes. System codes like TRACE are designed to simulate the entire nuclear power plant, modeled as a network of diverse components (pipes, valves, pumps, etc.). Considerable simplifications to the governing equations of fluid flow are necessary in codes like TRACE, such as the approximation of 1-D flow, large integration volumes and neglect of intra-fluid shear forces. Closure of the two-fluid model in STH codes require use of a significant number empirical correlations for many sub-grid processes like heat transfer, viscous effects, and form losses. Additionally, the coarse grid used by STH codes like TRACE precludes it from sensitivity to small scale geometric details, such as those resulting from structures internal to RPVs, especially in the lower plenum.

CFD codes like STAR-CCM+, on the other hand, offer improved fluid simulation capabilities. While CFD generally requires modeling of turbulence, these correlations are at a much lower level than those used in TRACE, and higher flow resolution is possible. The meshes used in CFD are much finer than those used in STH codes, allowing for much improved sensitivity to intricate geometric details. These benefits of CFD come at a much higher computational cost, however. The practice of CFD/STH coupling therefore seeks to use each code to its advantage in simulating NPPS.

In Chapter 2, it was shown that the transport of both passive and active scalars is not correctly captured by TRACE in reactor components where three-dimensional effects are important. Additionally, TRACE was found to be essentially insensitive to the geometric details of flow obstructions in the lower plenum, as expected. Phenomena such as 3-D mixing and sensitivity to geometric details can be important under certain accident scenarios, such as those found in MSLB and ATWS conditions. This has motivated the development of the coupling scheme between CFD and STH codes described in this dissertation. The coupling scheme described in this dissertation differs from what already published in the literature, as it is designed to correct transient STH solutions on-the-fly for the 3-D component of interest without iterative controls.

9-1.1 One-Dimensional Coupling

The newly-developed coupling scheme was first verified and assessed against various one-dimensional pipe configurations, for multiple types of boundary conditions and spatial partitions. The capability of the coupling scheme to induce a CFD-like solution into the TRACE solver was

verified, and its convergence characteristics were shown to be superior to the more widely-used domain decomposition methods published in the open literature.

The 1-D domain overlapping coupling method was implemented by correcting the STH friction factors under the assumptions that the STH and CFD codes compute the same inertial contribution to the pressure gradient, a reasonable approximation for incompressible flows. Two formulations of the domain overlapping method were explored: a spatial and a temporal formulation. Both methods were used to calculate a pressure gradient from CFD data that excluded inertial contributions. The latter formulation turned out to be significantly easier to implement and less sensitive to the approximations in spatial derivatives, and was therefore selected as the basis for the majority of coupled simulations presented in this dissertation.

For the first time, the convergence characteristics of domain overlapping methods were systematically compared to domain decomposition methods. It was found that domain overlapping coupling, though more cumbersome to implement, can provide a much more computationally efficient platform for complex calculations than currently existing methods based on domain decomposition.

Both open and closed loops were analyzed, using explicit time stepping for the data exchange between STH and CFD codes. It was found that domain decomposition methods were stable only within a certain range of integration time steps and user-specified initial conditions. At very small time steps, the pressure drop resulting from changes in velocity became unstable to small perturbations, while large time steps led to the common instability found in explicit methods. When the user-specified initial conditions were too far from the steady-state solution, convergence was not achieved. The domain overlapping method, on the other hand, was shown to be stable for a much wider range of time steps and produce more accurate solutions at intermediate to large time steps. Its convergence was also shown to be relatively insensitive to the user-defined initial conditions.

9-1.2 Multi-Dimensional Coupling

The theoretical framework for inertial domain overlapping coupling method introduced on 1-D geometries was further extended to more complex multi-dimensional Cartesian and cylindrical geometries, where pressure and velocity distributions in a TRACE multi-dimensional vessel component need to be corrected on the basis of the CFD solution. A so-called velocity-matching face (VMF) functionality was developed to ensure correct flow distribution and inertial consistency throughout the coupled domain. Two formulations for 3-D domain overlapping coupling were devised and presented in this dissertation: the Inertial Domain Overlapping (IDO) method and a more sophisticated Stabilized Inertial Domain Overlapping (SIDO) method.

The SIDO and IDO methods were first verified against 2-D (annular flow splitter test case) geometry. Both steady-state and transient conditions were analyzed. As would be expected, it was found that low flow conditions with high velocity time-derivatives were the most

challenging cases. In such cases, the IDO method was unable to produce a useful solution due to an instability that resulted from interaction of velocity-matching with the TRACE mass conservation equation. The SIDO method, however, was found to produce much better solutions in these challenging cases. In less challenging cases, both SIDO and IDO methods were found adequate.

Two types of VMF configurations were explored: with and without azimuthal velocity matching. The cases without azimuthal matching proved to be more stable and sufficiently accurate for the quantities of interest, namely the global pressure drop and velocity distribution across a specific interface. Velocity-matching faces were found to be the primary cause of error in 3-D coupling, with the error being exacerbated by strong time-derivatives of velocity. A pseudo-implicit method was found to reduce this error.

The SIDO method was then applied to a reactor vessel geometry with simplified internals in single- and dual-loop configurations. Domain decomposition calculations were also performed as reference. It was found that the SIDO and domain decomposition methods produced identical results in steady state, but that SIDO requires fewer coupled iterations to reach convergence. The superiority of the SIDO method developed in this dissertation becomes more evident when applied to transient cases. For transient scenarios, the domain decomposition method was found to be unstable, at least to explicit time-stepping and it was not possible to achieve converged solutions. The SIDO method, on the other hand, was successfully used to simulate a variety of transients.

9-2 Future Work

The coupling methodology presented in this dissertation successfully accomplished the goals driving its development. However, there are multiple avenues for developing improved iterations of the SIDO method.

9-2.1 Improved Numerical Methods

The coupling method described in this work can potentially benefit from improved numerical methods in two ways. First, the 3-D coupling to the multi-dimensional vessel component in TRACE is currently only developed for the semi-implicit (in time) method. The stability-enhancing two-step (SETS) method is available within TRACE and generally allows for the use of larger time steps. Extending the domain overlapping coupling to the SETS numerical scheme is expected to be a fairly straightforward process that could potentially offer improved performance of the SIDO method developed within the framework of this dissertation.

A further avenue for improved coupling performance would be the implementation of more sophisticated time stepping schemes between the CFD and STH codes. The majority of the time-dependent coupled calculations performed for this dissertation were carried out with explicit time stepping. A pseudo-implicit method application in Chapter 7 showed that a semi- or fully implicit temporal scheme could potentially offer significant improvement in coupling accuracy

and would potential allow the use of larger time steps for the data exchange between STH and CFD codes. In particular, the error resulting from velocity-matching faces could be expected to be substantially reduced with an implicit method. Additionally, a staggered explicit scheme could potentially offer improvement as well. In particular, allowing the CFD and STH codes to differ by a half time step and interpolating exchanged data could serve to alleviate VMF-induced error by increasing mass flow consistency between the codes.

As computational resources continue to become more affordable, CFD practitioners are likely to increasingly use Large Eddy Simulation (LES). LES is characterized by a much finer resolution, both spatially and temporally. The SIDO method is actually directly applicable to LES as currently formulated since the friction factor formulation only requires a pressure drop and a velocity. However, LES simulations require much smaller time steps than do RANS simulations and this resolution may not be necessary in the TRACE system. The SIDO method could therefore potentially be refined for use with LES by, for instance, allowing CFD to execute uncoupled for several time steps and then averaging the relevant data over this time. Additionally, LES is considerably more sensitive to boundary conditions than RANS. Data passed from STH to CFD could potentially be adjusted by adding turbulent fluctuations.

9-2.2 Improved Velocity-Matching Functionality

The need for velocity-matching faces (VMFs) was laid out in Chapter 7. Without this functionality, the velocity field inside a multi-dimensional region is decoupled from frictional and form loss feedbacks. In true reactor simulations, this would result in incorrect mass flow distributions at the core inlet, and incorrect pressure drops during transient operation. It was additionally concluded that VMFs can significantly exacerbate error in explicit time stepping configurations. Further, there is a certain *ad hoc* nature to VMF arrangement, especially in geometries without clear and distinct flow paths. A general theory of VMF specification was laid out, but a more a generalized formulation has still to be developed.

Moreover, the VMF formulation laid out for the vessel interface in this thesis is considered a strong formulation because it requires the user to select specific faces for velocity-matching. These faces are driven to match a specific CFD velocity. One possible way to improve the VMF functionality is to employ a weak formulation instead, similar to that employed for mixing regions with multiple outlets in §8-3.2. This method can theoretically be implemented in such a way as to require no user input.

During the time that the Janus coupling interface sets up interfaces at beginning of a coupled simulation, an algorithm would collect and information on all faces of the coupled TRACE region with nonzero flow areas. The faces are to be sorted into 3 types of geometric groups:

1. All axial faces at each radial and axial position
2. All radial faces at each radial and axial position
3. All azimuthal faces at each radial and axial position

A geometry with N_r radial levels, N_θ azimuthal levels, and N_z axial levels would result in $N_r \times N_z$ groups, each with N_θ elements. A fully conforming VMF configuration can be formed by selecting $(N_\theta - 1)$ faces from each axial and radial group and 1 face from each azimuthal group. Rather than attempting to set the TRACE velocity to match the STAR-CCM+ velocity, a weak formulation would instead attempt to match the fractional velocity, based on the total flow rate in each group.

9-3 Thermal Coupling

The coupled simulations presented in this dissertation were primarily isothermal, with the exception of the case in §5-3. Naturally, the flows in true nuclear systems are not isothermal. In order to prepare the SIDO method, the implementations of inertial pressure gradients and VMFs would need to be hardened to account for temperature dependent densities. Additionally, the establishment of a surface interface for heat transfer would have applications for steam generator or open pool cooling. In particular, heat transfer coefficients for pipe wall sections could be dynamically calculated from CFD simulations and passed to TRACE as thermal boundary conditions.

The current formulation of the SIDO method also assumes single phase flow. TRACE and STAR-CCM+, however, support multiphase flow. Extending the SIDO method to this regime would require accounting for void fractions within fluid as well as other phenomena such as interfacial drag.

9-4 Considerations for Advanced Coupling Applications

In this thesis, the idea of coupling STAR-CCM+ to TRACE has been examined through a primarily academic lens. While these scenarios have proven quite useful for analyzing the efficacy of the coupling methods, they involve considerable simplifications with respect to actual situations encountered in real power plant STH simulations. In this section, we address the question of extending the coupling methods to situations more relevant to the nuclear power industry.

9-4.1 Reduced-Order Model Coupling

All coupled simulations presented in this thesis use the STAR-CCM+ software. However, the behavior of CFD can theoretically be reproduced by reduced order models (ROMs). TRACE essentially sees STAR-CCM+ as an operator that turns a certain set of inputs into outputs based on the type of interface. Any software that can perform such actions can be used in the SIDO method. Complicated, multidimensional CFD models can potentially be replaced by sets of ordinary differential equations generated from processes such as proper orthogonal decomposition (POD). POD results in a set of eigenfunctions ordered by their contribution to the total energy of the system. A ROM is built by considering a truncated set of eigenfunctions that can then be propagated in time to emulate CFD. Using ROMs in place of true CFD software can potentially produce very significant time savings.

9-4.2 Porous Media Approaches

In all the test cases considered in this dissertation, the coupling methods have been applied to the entire TRACE component. This has provided verification that the methods perform well with diverse geometry and many flow conditions. However, in some cases it is unnecessary and even infeasible to perform useful CFD calculations for the entirety of certain TRACE components. For example, consider a reactor pressure vessel with an active core region. In realistic cases, the core consists of tens of thousands of individual fuel pins that directly interface with the coolant. A CFD model that accurately resolves the flow field would be exceptionally expensive and cumbersome. Further, adding the necessary thermal and neutronic effects to properly model feedback with the nuclear fuel suggests a very high level of complexity. Moreover, the flow fields in the core region are often well-described with 1-D methods, especially in BWRs with canned fuel bundles. In such cases, it is advisable to provide the capability to allow TRACE to solve for the flow fields in certain sub-regions without any interference from CFD.

In simulations in which a sub-region is left uncoupled, it is often insufficient to simply exclude this sub-region from the CFD simulation. Except in conditions of choked flow, the downstream flow properties can substantially affect the flow in the region of interest. The liquid flow in a reactor vessel is generally very far from choked, requiring that some model of the flow downstream of the region of interest be incorporated. When only the upstream effects are important, however, it is not necessary to fully resolve the downstream flow field. In such cases, porous media methods may be employed.

Porous media methods in STAR-CCM+ are implemented with a lumped parameter approach in which the effects of internal structure are modeled through resistance coefficients of a source term $\vec{f}_p$ in the momentum equations, given by Eq. 9-1 [45]:

$$\vec{f}_p = -\bar{\bar{P}} \cdot \vec{v}, \qquad 9\text{-}1$$

where $\bar{\bar{P}}$ is the porous resistance tensor, which is further broken down into Eq. 9-2:

$$\bar{\bar{P}} = \bar{\bar{P}}_v + \bar{\bar{P}}_i |\vec{v}|, \qquad 9\text{-}2$$

where $\bar{\bar{P}}_v$ and $\bar{\bar{P}}_i$ are the viscous and inertial resistance tensors, respectively. The former is used to model porous effects that are linear in velocity, while the latter is for quadratic effects. The finite volume momentum equations for a porous medium are given by Eq. 9-3:

$$\frac{\partial}{\partial t}\iiint_V \rho\chi\vec{v}dV + \oiint_A \rho\vec{v}\cdot(\vec{v}\cdot\hat{n})dA = \oiint_A p\,\bar{\bar{I}}\cdot\hat{n}dA + \oiint_A \bar{\bar{T}}\cdot\hat{n}dA + \iiint_V \vec{f}_p, \qquad 9\text{-}3$$

where χ is the porosity, $\hat{n}$ is an outward pointing normal vector, $\bar{\bar{I}}$ is the identity tensor, and $\bar{\bar{T}}$ is the combined viscous and turbulent stress tensor. While there are multiple methods for specifying$\bar{\bar{P}}_v$ and $\bar{\bar{P}}_i$, the approach discussed here is referred to as the "principal tensor profile

method". In this method, the tensors are simply specified with the diagonal components with respect to the principal axes of the tensors. This requires the specification of 5 components: the diagonal XX, YY, and ZZ components of the principal tensor, as well as the vectors giving the XX and YY axes of the principal coordinates. The ZZ axis is then derived from the XX and YY axes, assuming a right-handed orthogonal coordinate system.

While some porous media found in nuclear engineering are isotropic, such as pebble bed reactors, the sub-regions discussed in this section, namely reactor cores and steam generator U-tubes, are highly anisotropic in that flow is much more restricted in the radial direction than the axial direction. In these cases the diagonal components of the principal tensor will vary significantly. In cases where radial flow is not permitted at all, such as in steam generator tube bundles, the transverse tensor components are set to a coefficient that is 2-3 orders of magnitude higher than the primary.

9-4.3 Active Core Reactors

During most accident conditions, it is imperative to capture the interaction of the nuclear fuel with the coolant. Correctly predicting fuel and cladding temperatures requires accurate prediction of the heat generated within the fuel and the heat transferred to the coolant. The heat generated in the fuel in turn depends on the density of the coolant, and the heat transferred depends on the coolant temperature. In cases with natural circulation, the flow rate through the core depends on heat transfer and the fluid temperature field. As stated above, explicitly modeling each fuel pin surface in STAR-CCM+ is prohibitively expensive for lengthy transients. A porous media approach can significantly decrease the computational cost. Such an approach has been taken, for instance, in the calculation of duct wall temperatures for a fuel assembly of a sodium fast reactor [59].

In realistic transient simulations of NPPs, it is expected that only the downcomer and lower plenum regions will be of coupling interest. It is in these locations that the flow patterns have the mostly strongly multi-dimensional characteristics. The flow in these regions also has the largest effects on the reactor core itself.

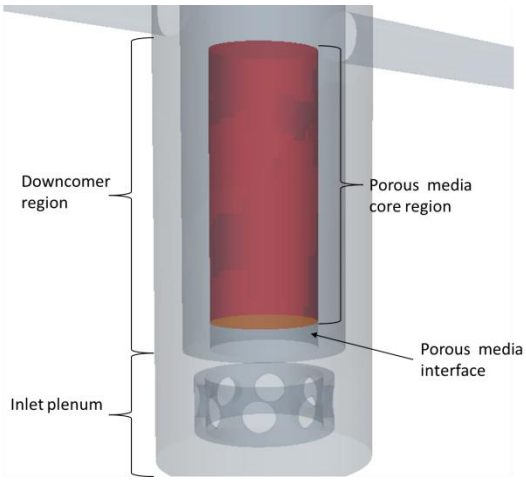

Fig. 9-1. Geometry of RPV simulant CFD model with porous media core region.

9-4.4 Steam Generators

Severe accident conditions such as station blackout (SBO) can lead to core uncovering under full pressure. In this case, a mixture of superheated steam flows through the primary leg and steam generator. When water accumulates in the loop seal, it can essentially block gas flow out of the steam generator, leading to the development of a natural circulation flow pattern. Rather than simulating flow from the many tubes of the steam generator, it is possible to use a porous media method to simplify the model [60]. For example, consider the simplified steam generator geometry shown in Fig. 9-2. On the left, less dense hot fluid enters the top portion of the steam generator inlet pipe, while denser cool flow leaves the domain. As highlighted in the figure, the U-tube portion the domain is modeled with porous media methods.

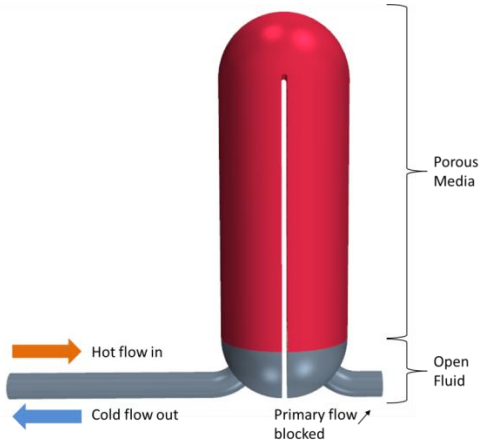

Fig. 9-2. Geometry of steam generator CFD model.

Because U-tube bundles do not allow transverse flow, the porous media resistance tensor must be anisotropic. The vector field displayed in Fig. 9-3 shows the function used to determine the

XX axis of the principal tensor. The XX component of the tensor would then be set to some known value for flow through such steam generators.

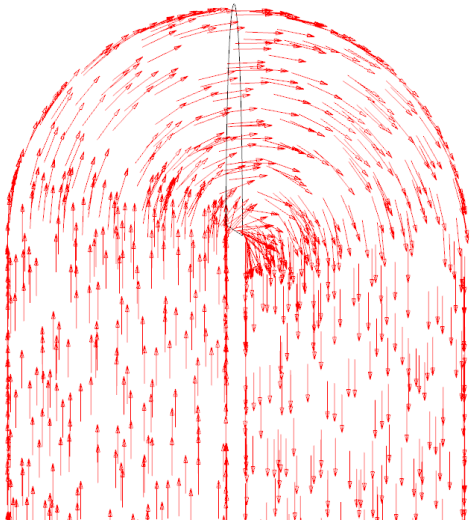

Fig. 9-3. Sample of the principal axis vector function for the steam generator example.

In TRACE simulations, steam generator U-tubes are often modeled using a small number (less than 10) of representative pipes with multiplicative factors applied so that each pipe represents a section of the entire tube bundle. Tubes near the outside of the bundle are longer and reach higher elevations, which can have important implications when buoyant effects are relevant or in case of small break loss of coolant accidents, when natural circulation in the tallest tubes might become interrupted. Tubes are often sorted by total length to capture these effects. One potential coupling method would involve placing a plane at the interface between the porous medium and the open flow region, shown in Fig. 9-4. A separate mapping function or table would then be used to describe which sub-surfaces of this interface are applied to each TRACE pipe. In this particular case, which features localized reversed flow, it would be imperative that the appropriate flow is assigned to the correct representative tube bundle.

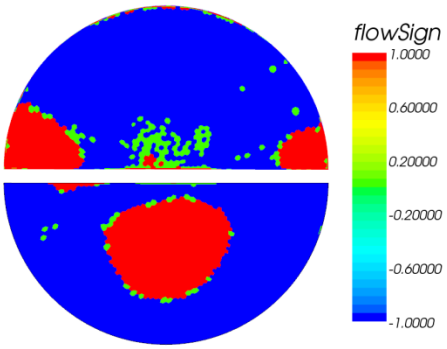

Fig. 9-4. Direction of flow at interface of porous medium and open flow regions. (TOP) Sign of the flow rate at the steam generator on the blocked side. (BOTTOM) Sign of the flow rate on the open side of the steam generator.

In a true steam generator, heat is transferred to the secondary fluid from the primary fluid through the surfaces of the many tubes in the U-tube assembly. Application of the porous media approximation prevents such surface heat transfer. The test simulation performed here used a volumetric heat sink in STAR-CCM+. Coupling of the volumetric heat sink in CFD to the surface heat transfer in TRACE could be accomplished by a simple scaling:

$$q''' = q'' \frac{S_{trc}}{\chi V_{CFD}}, \qquad 9\text{-}4$$

where q''' is the volumetric heat transfer of STAR-CCM+, q'' is the surface heat transfer in TRACE, S_{trc} is the surface area in TRACE, and V_{CFD} is the volume of the porous media sub-domain in CFD.

Appendices

Appendix A. Reactor Pressure Vessel Simulant

A-1 Introduction

The flow domain of a typical reactor pressure vessel (RPV) is characterized by several prominent features. Cool flow from an inlet pipe, or cold leg, enters the RPV through the downcomer, which is essentially an annular region surrounding the core that directs flow downward. After the downcomer, the flow enters the inlet plenum, where it changes direction for upward flow through the core. Flow in the inlet plenum can be quite complicated, due to the presence of flow-shaping devices as well as structural supports that act as internal flow obstructions. After the inlet plenum, the flow enters the core which is relatively densely packed with fuel rods that result in primarily 1-D flow. Strong temperature gradients are also present in this region. After the core, the heated flow exits the RPV through an outlet pipe, or hot leg.

The geometry presented in this appendix, an "RPV simulant", was devised to test the 3-D coupling methods presented in this thesis under conditions representative of a RPV. While the dimensions of the simulant are not representative of a true RPV, the geometry induces flow phenomena that are intended to be representative. The actual geometry and flow conditions were designed based on computational expediency. The core region of the RPV simulant was left empty because the coupling methodology developed in this dissertation is aimed primarily at the downcomer and inlet plenum sub-regions.

A-2 Base Geometry

The RPV simulant is based on the region shown in Fig. A-1. In the top left of the figure, three concentric circles represent the major radial regions. The downcomer is confined to the region given by $0.2m = r_2 < r < r_3 = 0.3m$, while the core region is confined to $0 \leq r < r_1 = 0.15m$. The top right of the figure, where no-flow boundaries are outlined in red, shows a general schematic of the flow path taken through the RPV simulant. In order to model the effects of reactor internals on the flow, an obstruction is introduced into the lower plenum region with location indicated in the bottom left of the figure. Axially, the geometry is broken into three equal sections as shown in the bottom right of Fig. A-1. Four equal azimuthal sections, referred to as quadrants are defined as indicated in the top left. The quadrants are labeled based on $Q_i = \left\{(r, \theta, z) \middle| (i-1)\frac{\pi}{2} < \theta \leq i\frac{\pi}{2}\right\}$.

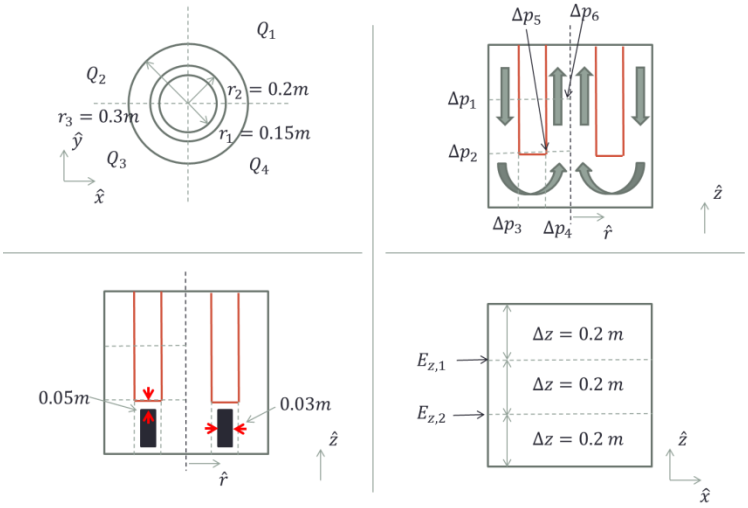

Fig. A-1. (TOP LEFT) Radial and azimuthal meshing. (TOP RIGHT) Axial and radial labeled by the pressure drops across them. (BOTTOM LEFT) obstruction geometry. (BOTTOM RIGHT) Axial meshing with edge labels.

A detailed view of the lower plenum flow obstruction is given in Fig. A-2. While not specifically representative of true RPV internals, the obstruction is meant to produce strong velocity gradients in the lower plenum. As shown in Fig. A-1 (bottom left), the obstruction is centered in the ring region given by $0.15m = r_1 < r < r_2 = 0.2m$. The obstruction feature 4 bypass holes, each of radius $0.03m$. A fillet with radius $0.01m$ was applied to each otherwise sharp edge. The obstruction occupies just over 25% of the lower plenum volume.

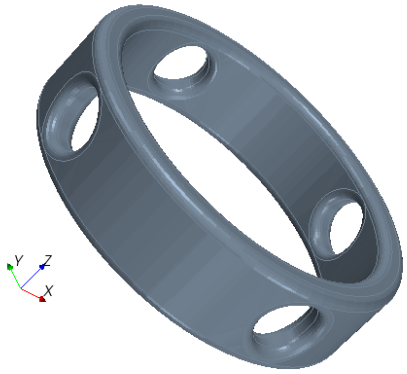

Fig. A-2. Obstruction that appears in lower plenum.

A-2.1 Single Loop Configuration

The base geometry described in the previous section is connected to an external system through an inlet cold leg and an outlet hot leg. Similar to a true RPV, the cold leg directly drains into the downcomer, while the hot leg provides suction to the region above the core. The hot and cold

legs are at the same elevation, requiring that the hot leg penetrate the downcomer annulus. The penetration reduces the size of the relevant node by about 6.5%. The hold and cold leg configuration is shown in Fig. A-3. In this case, the cold leg is connected to the downcomer in Q3, as labeled in Fig. A-1, while the hot leg is connected through Q3.

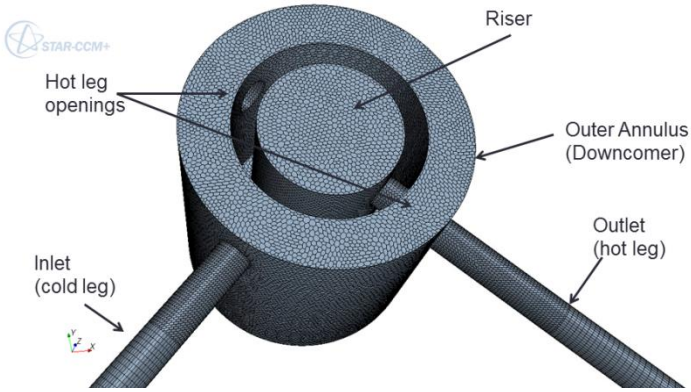

Fig. A-3. Annotated STAR-CCM+ mesh of the coupled region for the single loop test case.

A-2.2 Dual Loop Configuration

For a dual loop configuration, the hot and cold legs of the single loop are retained. Additional hot and cold legs are added directly opposite their counterpart as shown in Fig. A-4. This symmetric flow configuration introduces the possibility of flow bifurcations.

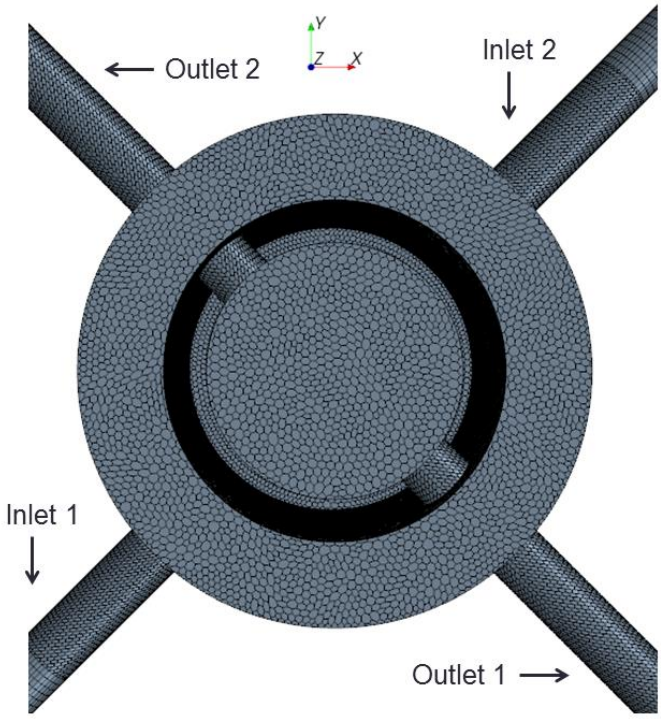

Fig. A-4. View from top of STAR-CCM+ mesh of two loop test case

A steady state solution would be expected to resemble the left of Fig. A-5, in which the flow from each inlet essentially splits into two streams equally distributing the flow between the outlets. However, it is possible that this solution is dynamically unstable. In such a case, the true solution is not steady and oscillates between multiple states, similar to the right of Fig. A-5 in which the flow field is asymmetric. In a computer-generated solution, error resulting from the mesh or from truncation can result in the solution collapsing to one of these degenerate states. Because of these considerations, care must be taken in such symmetric solutions with complex flow domains. In practice, some degree of asymmetry is often intentionally inserted to prevent instability. In the cases presented in this thesis, we simply choose the turbulence model and discretization to avoid instability.

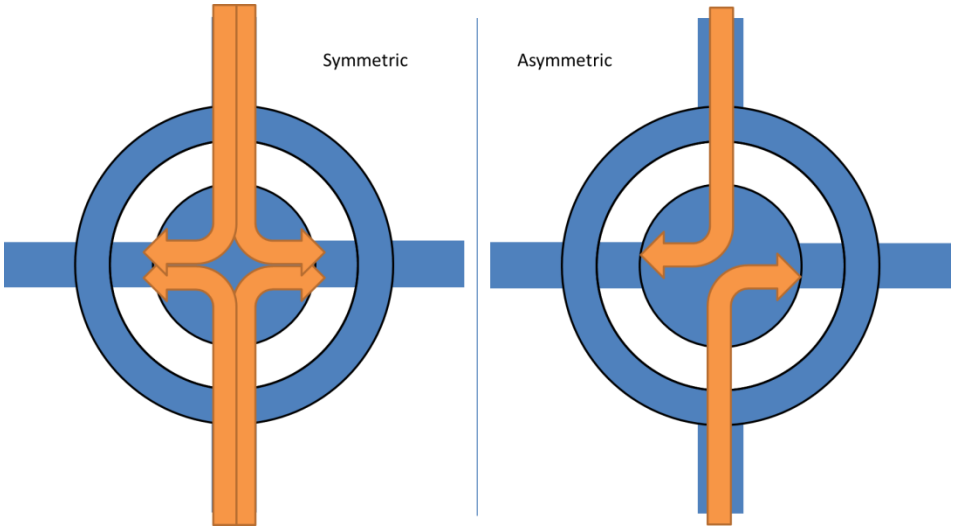

Fig. A-5. Schematic of flow bifurcation in dual loop test case.

A-3 CFD Mesh and Stability

The meshes used for the single and dual-loop CFD domains were built from polyhedral elements with a prismatic cell layer near wall boundaries. This type of mesh was chosen for its applicability to complex regions as discussed in greater detail in Appendix C. Two layers of prismatic cells were used in the mesh for the k-ϵ model. It is generally recommended that k-ω models are used with lower wall distances and the mesh used for this model had three layers of prismatic cells near the wall. Because stronger spatial gradients are expected near the flow obstruction in the lower plenum, the mesh was refined as shown in Fig. A-6. For both the k-ϵ and k-ω models, the cell density was somewhat increased in this region, and 3 cells of prismatic layers were used. The meshes for k-ϵ and k-ω therefore only differed by the number of prismatic layers in the unrefined region and were composed of 860977 and 927523 cells, respectively.

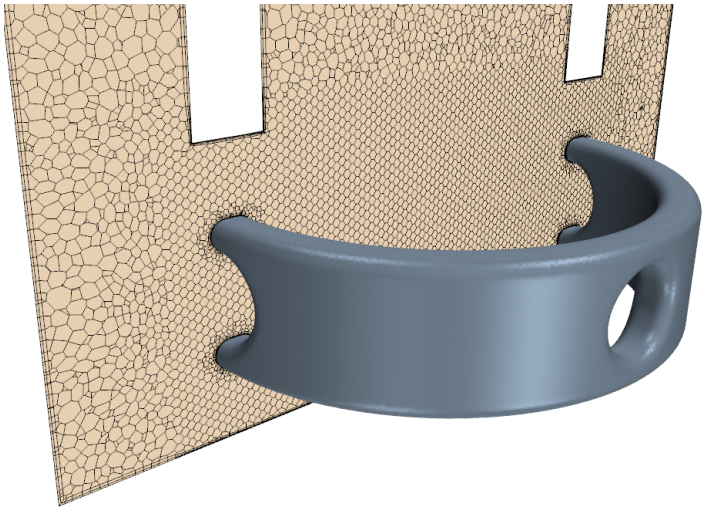

Fig. A-6. Mesh refinement in lower plenum near flow obstruction.

Additionally, in the k-ω model, a first-order upwind scheme was used to calculate the convective flux. This introduced dissipative error, which stabilized the solution. For a demonstration of the stability properties of the present models, simulations were carried with asymmetric flow conditions based on results calculated in §8-3.3 with pump rotation rates of $\Omega_1 = 50 rad/s$ and $\Omega_2 = 70 rad/s$. The boundary conditions for the dual loop test case are given in Table A-1.

Table A-1. Boundary conditions for asymmetric test case.

Boundary	Value
Inlet 1	$8.65\ kg/s$
Inlet 2	$12.17\ kg/s$
Outlet 1	$0\ Pa$
Outlet 2	$-4480.24\ Pa$

The mass flow rates through each of the outlets for maximally converged simulations are shown in Fig. A-7, plotted versus iteration. The two 1st order simulations reach a stable solution, while the 2nd order k-ϵ simulation appears to have reached a limit cycle.

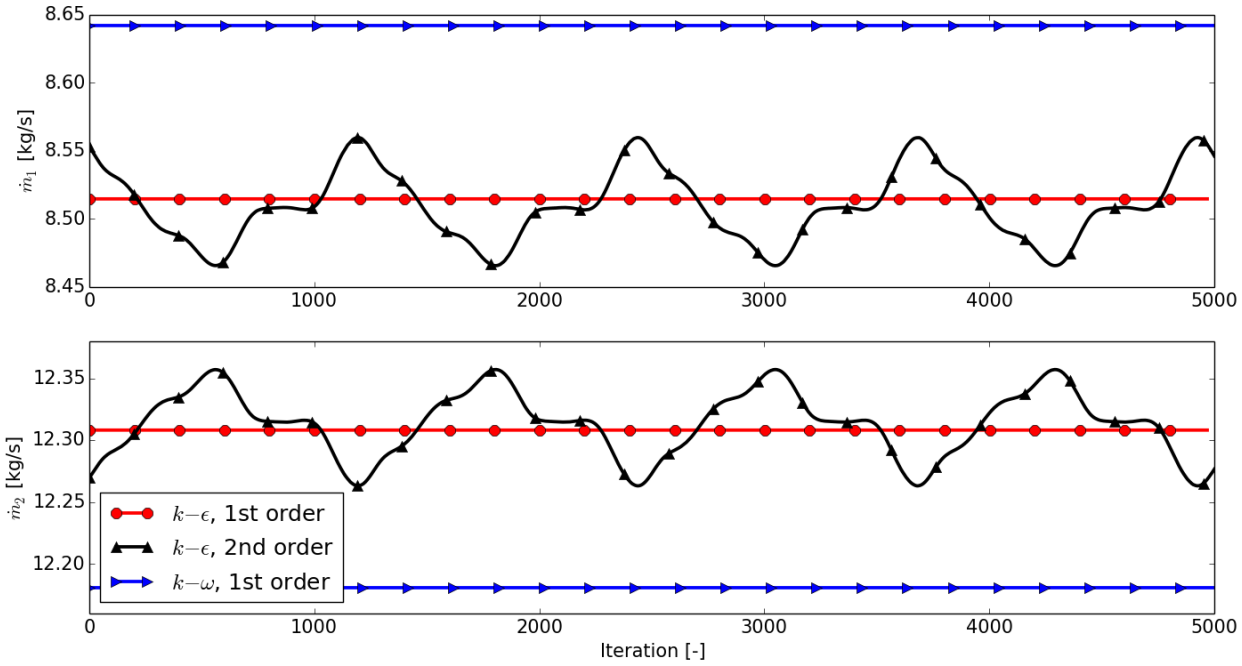

Fig. A-7. Mass flow rates through the outlets for selected models.

For an idea of convergence quality, the maximum residual reported by STAR-CCM+ are included. The values reported by STAR-CCM+ are actually RMS values, since a residual is calculated in each cell for each iteration. In the k-ϵ model with 2nd order convection, the maximum residual turned out to be from the transport equation for ϵ, while the equation for ω provided the largest residual for the k-ω model. In the k-ϵ model with 1st -order convection, the maximum residual resulted from the continuity equation.

Table A-2. Maximum residual values for test cases.

Test Case	Maximum Residual
Standard k-ϵ, 2nd order convection	10^{-4} *to* 10^{-3}
Standard k-ϵ, 1st order convection	$\sim 2 \times 10^{-7}$
k-ω, 1st order convection	$\sim 2 \times 10^{-15}$

Table A-2 shows the maximum residual value for each method. The values presented here are only meant to be evaluated relative to each other. As might be expected from Fig. A-7, the convergence of the second order k-ϵ model is rather poor. While both first order methods show much better convergence, the k-ω method apparently reaches the level of machine accuracy. Based on these results, the 1st-order k-ω method was determined to be the most stable for asymmetric flow conditions.

A-4 TRACE Mesh

The TRACE nodalization of the RPV simulant is shown in Fig. A-8. The mesh is composed of 3 radial divisions, 4 azimuthal divisions, and 3 axial divisions for a total of 36 cells. The radial

nodalization is based on three radial regions with upper limits given by $r_1 = 0.15m, r_2 = 0.2m, r_3 = 0.3m$. The 4 azimuthal divisions split 2π evenly, while the axial nodalization splits $0.6m$ uniformly.

In order to separate the downcomer from the core and riser section, all the radial faces above the first axial levels are set to no-flow faces (i.e. they have zero flow area), as indicated by a red line in the figure. In addition, the lowest level internal axial faces in the second radial division are set to zero flow area, forcing the flow to travel downward through the downcomer, into the lower plenum, and finally through the core. The locations of inlet and outlet connections are indicated by blue lines. The inlet pipes are connected to the outermost radial faces, while the outlet pipes are connected to the innermost radial faces. All pipes are connected to the vessel at the highest axial level.

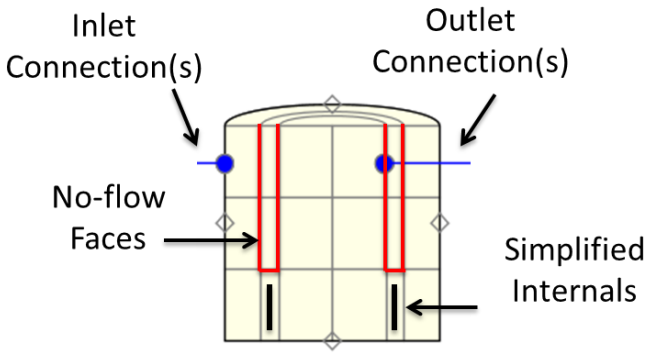

Fig. A-8. TRACE nodalization of RPV simulant geometry

Some of the cells in the TRACE mesh are obstructed. Either one or two cells of the outer ring of the top axial level are penetrated by an outlet pipe, depending on whether the vessel is in a single or dual loop configuration. Additionally some cells in the lower plenum are obstructed by the simplified reactor internals. The volume fractions for each set of cells are included in Table A-3.

Table A-3. Fraction of cells available for fluid flow.

Cell Penetrated by Outlet Pipe	Cell with L.P. Flow Obstruction	All other cells
0.935	0.745	1.0

A-5 Mass Conservation

STAR-CCM+ and TRACE both solve mass conservation equations, which are generally well-satisfied. For example, consider the single-loop transient discussed in §8-2.1.2. The mass flow rates into and out of the coupled test section are indicated in Fig. A-9. Both CFD and STH codes show identical mass flow rates, indicating that mass is conserved.

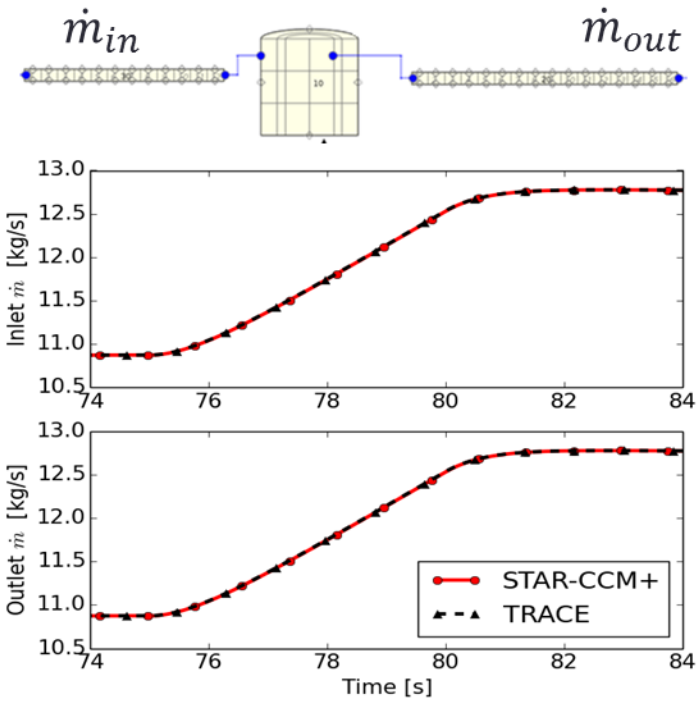

Fig. A-9. Mass flow rates into and out of vessel section.

However, STH and CFD codes do not represent the geometry identically. Consider for example the core inlet, shown in Fig. A-10 for both CFD and STH meshes. In this case, the STH mesh is constructed such that it exactly represents the core inlet plane. Specifically, the staggered grid arrangement allows for the edges, at which velocities are defined, to be exactly aligned with the core inlet plane. The CFD mesh, on the other hand, does not exactly correspond with the plane. Fig. A-10 shows the mesh elements that intersect with the core inlet plane. As is clear from the figure, some cells lie somewhat above the plane and some lie below the plane. As a result, the velocities at the plane are interpolated, introducing some error. Fig. A-11 shows the result of the velocity interpolation by plotting the total mass flow rate through the core inlet plane as calculated by STAR-CCM+ and TRACE. In this case, the velocity interpolation error is manifest as a slight (~2.5%) under-prediction of mass flow rate. The error can be potentially be alleviated through finer meshing or advanced interpolation schemes.

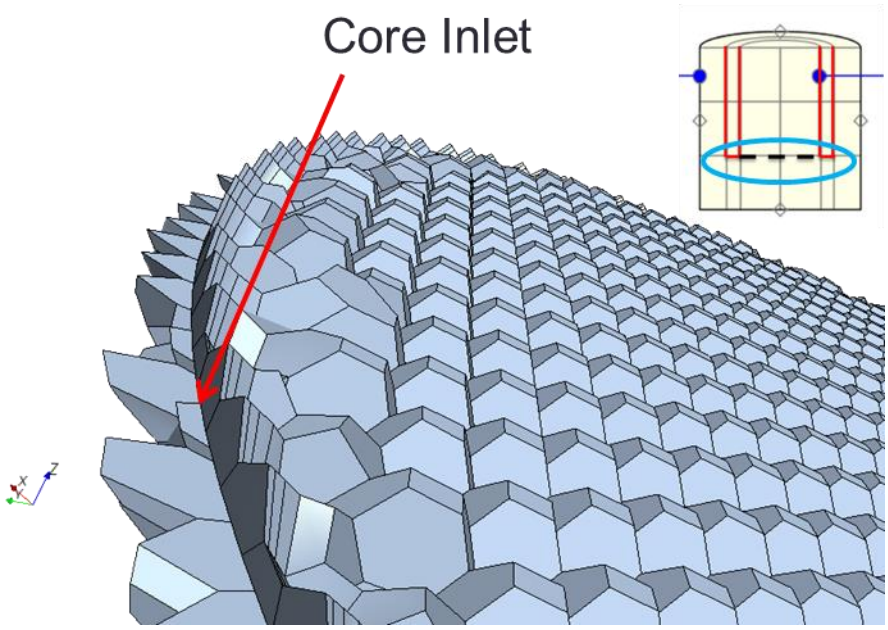

Fig. A-10. CFD and STH meshes at core inlet.

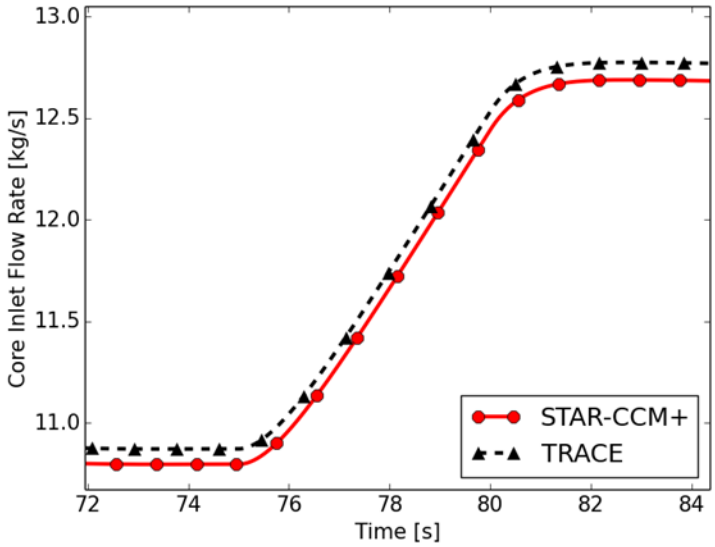

Fig. A-11. Mass flow rates through the core inlet plane as calculated by STAR-CCM+ and TRACE.

Appendix B. Fluid Dynamics and Turbulence Modeling

B-1 Introduction

Although a fluid is truly a system of many particles, the approach to most engineering flows is to treat the fluid as a continuum. This approximation is very accurate, except under special circumstances such as rarefied gases in the upper atmosphere. Under the continuum approximation, field variables such as the three-dimensional velocity $u_i(x_i, t)$ and the pressure $p(x_i, t)$ can be defined pointwise. Additionally, we employ an Eulerian viewpoint under which $u_i(x_i, t)$ provides the flow velocity at a specific location and time, rather than in the Langrangian viewpoint in which $u_i(x_i, t)$ provides the velocity of a specific parcel of fluid. Application of conservation of momentum to an incompressible Newtonian fluid yields the well-known set of Navier-Stokes equations of Eq. B-1:

$$\rho \frac{\partial u_i}{\partial t} + \rho u_i \frac{\partial u_j}{\partial x_i} = \frac{\partial}{\partial x_j}\left[-p\delta_{ij} + \mu\left(\frac{\partial u_i}{\partial x_j} + \frac{\partial u_j}{\partial x_i}\right)\right], \qquad \textit{B-1}$$

where ρ is the fluid density and μ is the dynamic viscosity of the fluid. Conservation of mass then yields Eq. B-2, the continuity equation:

$$\frac{\partial u_i}{\partial x_i} = 0. \qquad \textit{B-2}$$

For isothermal flow, Eqs. B-1 and B-2, together yield a complete system for the 4 dependent variables u_i and p. While the existence and uniqueness of solutions to these equations has not yet been proven, it is widely believed that fluid motion is well described by solutions to the Navier-Stokes equations, a claim supported by much empirical evidence. A particularly vexing aspect of solutions to these equations is the phenomenon of turbulence, which occurs at high values of the Reynolds number ($Re = \rho VD/\mu$, where V and D are characteristic velocity and length scales of the system, respectively). Turbulent flows exhibit variations over very small spatiotemporal scales. The complete simulation of high Reynolds number flow requires extraordinarily fine computational meshes. In fact, direct numerical simulation (DNS) of these equations is only feasible for extremely limited cases. In additional to the mesh requirements, solutions to the Navier-Stokes equation exhibit chaotic behavior in that they display very strong dependence on initial conditions.

One common approach to address turbulence is to model the smaller scales of fluid motion rather than resolve them. Toward this objective, dependent variables are decomposed into means ($\overline{u_i}, \overline{p}$) and fluctuations ($u_i', p'$) in a process called Reynold's averaging:

$$u_i = \overline{u}_i + u_i', \qquad p = \overline{p} + p'. \tag{B-3}$$

The mean values can be conceptualized as temporal averages for flows with stationary statistics, spatial averages for homogenous flows, and ensemble averages for any flows. Applying Eq. B-3 to the Navier-Stokes and continuity equations yields the unsteady Reynolds Averaged Navier-Stokes (URANS or often simply RANS) equations of Eq. B-4:

$$\rho \frac{\partial \overline{u}_i}{\partial t} + \rho \overline{u}_i \frac{\partial \overline{u}_j}{\partial x_i} = \frac{\partial}{\partial x_j}\left[-\overline{p}\delta_{ij} + \mu\left(\frac{\partial \overline{u}_i}{\partial x_j} + \frac{\partial \overline{u}_j}{\partial x_i}\right) - \rho\overline{u_i' u_j'}\right], \tag{B-4}$$

and the averaged continuity equation of Eq. B-5:

$$\frac{\partial \overline{u}_i}{\partial x_i} = 0. \tag{B-5}$$

The URANS equations resemble the Navier-Stokes equations except for the velocity fluctuation covariance tensor $-\rho\overline{u_i' u_j'}$, often referred to as the Reynolds stress tensor. This tensor captures the effects of flow variations on scales smaller than resolution of the computational mesh. The effects of the unresolved flow structures are accounted for through the use of turbulence models. The Reynold's stresses effectively increase viscosity in high turbulence regions, acting to smooth out the mean flow field $\overline{u}_i$. The smoothing benefit comes with the cost of a closure problem: by performing Reynold's averaging, the introduction of $\overline{u_i' u_j'}$ yields 6 additional unknowns (under the constraint $\overline{u_i' u_j'} = \overline{u_j' u_i'}$) without any extra equations. In practice, the closure problem is addressed by the addition of additional equations that constitute turbulence models. A huge number of closure approaches have been documented, ranging from simple to quite complex. In this appendix, we discuss two of the most common approaches, the k-ϵ model and the k-ω model.

B-2 Closure

While many RANS turbulence models are available, the majority of the analysis in this thesis is carried out with the standard k-ϵ model, which applies the turbulent viscosity hypothesis of Eq. B-6 to address the closure problem:

$$-\overline{u_i' u_j'} = 2\nu_T S_{ij} - \frac{2}{3}k\delta_{ij}, \qquad \nu_T = C_\mu \frac{k^2}{\epsilon}, \tag{B-6}$$

where S_{ij} is the strain rate tensor, δ_{ij} is the Kronecker delta, and ν_T is the turbulent viscosity:

$$S_{ij} = \frac{1}{2}\left(\frac{\partial \overline{u}_i}{\partial x_j} + \frac{\partial \overline{u}_j}{\partial x_i}\right). \tag{B-7}$$

The transport equation for the turbulent kinetic energy k is given by Eq. B-8:

$$\frac{\overline{D}k}{\overline{D}t} = \frac{\partial}{\partial x_i}\left[\frac{\nu_T}{\sigma_k}\frac{\partial k}{\partial x_i}\right] - \overline{u_i'u_j'}\frac{\partial \overline{u_i}}{\partial x_j} - \epsilon. \qquad \textit{B-8}$$

The turbulence dissipation rate ϵ is given by Eq. B-9:

$$\frac{\overline{D}\epsilon}{\overline{D}t} = \frac{\partial}{\partial x_i}\left[\frac{\nu_T}{\sigma_\epsilon}\frac{\partial \epsilon}{\partial x_i}\right] - \left[\frac{C_{\epsilon 1}\epsilon}{k}\right]\overline{u_i'u_j'}\frac{\partial \overline{u_i}}{\partial x_j} - \left[\frac{C_{\epsilon 2}\epsilon}{k}\right]\epsilon, \qquad \textit{B-9}$$

where $\frac{\overline{D}}{\overline{D}t} = \frac{\partial}{\partial t} + \overline{u}_i\frac{\partial}{\partial x_i}$ refers to the substantial derivative based on the Reynolds averaged velocity. Like all turbulence model, the k-ϵ model relies on several model coefficients. These coefficients are sometimes tuned so that the model better matches physical mechanisms dependent on the particular conditions of a specific flow. Some standard values are quoted in Eq. B-10 [61] [62]:

$$C_\mu = 0.09, \qquad C_{\epsilon 1} = 1.44, \qquad C_{\epsilon 2} = 1.92, \qquad \sigma_k = 1.0, \qquad \sigma_\epsilon = 1.3. \qquad \textit{B-10}$$

The standard k-ϵ model is a member of a class of models referred to as two-equation models, due to the addition of transport equations for k and ϵ. The k-ϵ model has quadratic and cubic variants in which the prescription of $\overline{u_i'u_j'}$ takes on more sophisticated forms, allowing the tensor to model more complex behavior such as anisotropy and streamline curvature

Another commonly used two-equation model is the k-ω model. The model equation for ω is given in Eq. B-11 [63] [64]:

$$\frac{D\omega}{Dt} = \nabla\cdot\left(\frac{\nu_T}{\sigma_\omega}\nabla\omega\right) + C_{\omega 1}\frac{P\omega}{k} - C_{\omega 2}\omega^2. \qquad \textit{B-11}$$

The value $\omega = \frac{\epsilon}{k}$ is sometimes called the turbulent frequency and, at other times, called the specific dissipation. This model also uses the turbulent viscosity approximation, but instead with the slightly different formulation shown in Eq. B-12:

$$-\overline{u_i'u_j'} = 2\nu_T S_{ij} - \frac{2}{3}\frac{\epsilon}{\omega}\delta_{ij}, \qquad \nu_T = C_\mu\frac{\epsilon}{\omega^2}. \qquad \textit{B-12}$$

Some typical coefficient values are quoted in Eq. B-13 [61]:

$$C_\mu = 0.09, \qquad C_{\omega 1} = 0.44, \qquad C_{\omega 2} = 0.92, \qquad \sigma_k = 2.0, \qquad \sigma_\epsilon = 2.0. \qquad \textit{B-13}$$

Complex rotation and streamline effects can optionally be accounted for with correction factors applied to the turbulent production term [45] [65].

B-3 Near-Wall k-ϵ

This section closely follows the work presented in [66]. The *exact* transport equations for k and ϵ are given in Eq. B-14:

$$\begin{aligned} \frac{Dk}{Dt} &= \tau_{ij}\frac{\partial \overline{u}_i}{\partial x_j} - \epsilon - D + \nu\nabla^2 k, \\ \frac{D\epsilon}{Dt} &= P_\epsilon - \Phi_\epsilon - D_\epsilon + \nu\nabla^2\epsilon. \end{aligned} \qquad \textit{B-14}$$

Specific definitions for each term are given in Eq. B-15:

$$\begin{aligned} D &= \frac{\partial}{\partial x_i}\left(\frac{1}{2}\overline{u_j' u_j' u_i'} + \overline{p' u_i'}\right), \\ D_\epsilon &= 2\nu\frac{\partial}{\partial x_i}\left(\overline{\frac{\partial p'}{\partial x_j}\frac{\partial u_i'}{\partial x_j}}\right) + \nu\frac{\partial}{\partial x_j}\left(\overline{u_j'\frac{\partial u_i'}{\partial x_k}\frac{\partial u_i'}{\partial x_k}}\right), \\ P_\epsilon &= -2\nu\overline{\frac{\partial u_i'}{\partial x_j}\frac{\partial u_k'}{\partial x_j}\frac{\partial \overline{u}_i}{\partial x_k}} - 2\nu\overline{\frac{\partial u_j'}{\partial x_i}\frac{\partial u_j'}{\partial x_k}\frac{\partial \overline{u}_i}{\partial x_k}} - 2\nu\overline{\frac{\partial u_i'}{\partial x_k}\frac{\partial u_i'}{\partial x_j}\frac{\partial u_k'}{\partial x_j}} \\ &\quad + 2\nu u_k'\frac{\partial u_i'}{\partial x_j}\frac{\partial^2 \overline{u}_i}{\partial x_j \partial x_k}, \\ \Phi_\epsilon &= 2\nu^2\overline{\frac{\partial^2 u_i'}{\partial x_j \partial x_k}\frac{\partial^2 u_i'}{\partial x_j \partial x_k}}. \end{aligned} \qquad \textit{B-15}$$

The behavior of these terms near the wall can be better understood with an asymptotic expansion of the velocity fluctuations in terms of distance from the wall, y, as shown in Eq. B-16:

$$\begin{aligned} u' &= a_0 + a_1 y + a_2 y^2 + \cdots, \\ v' &= b_0 + b_1 y + b_2 y^2 + \cdots, \\ w' &= c_0 + c_1 y + c_2 y^2 + \cdots. \end{aligned} \qquad \textit{B-16}$$

The no-slip conditions requires $a_0 = b_0 = c_0 = 0$. Mass conservation leads to Eq. B-17:

$$\frac{\partial u'}{\partial x} = 0 = \frac{\partial v'}{\partial y} = b_1. \qquad \textit{B-17}$$

The asymptotic expansion therefore simplifies to Eq. B-18:

$$\begin{aligned} u' &= a_1 y + a_2 y^2 + \cdots = O(y), \\ v' &= b_2 y^2 + \cdots = O(y^2), \\ w' &= c_1 y + c_2 y^2 + \cdots = O(y). \end{aligned} \qquad \textit{B-18}$$

Applying this result to the relevant terms yields Eq. B-19:

$$k = O(y^2), \quad \epsilon = O(1), \quad \frac{\partial \overline{u}}{\partial y} = O(1),$$
$$\overline{u'^2} = O(y^2), \quad \overline{v'^2} = O(y^4), \quad \overline{w'^2} = O(y^2),$$
$$\overline{u'v'} = O(y^3), \quad P = O(y^3), \quad P_\epsilon = O(y),$$
$$D = O(y), \quad D_\epsilon = O(1), \quad \Phi = O(1),$$
$$\nabla^2 k = O(1), \quad \nabla^2 \epsilon = O(1). \qquad \textit{B-19}$$

Note that in the near wall region $\overline{u'v'} = O(y^3)$ but $\nu_T = C_\mu \frac{k^2}{\epsilon} = O(y^4)$. Thus, in this region, we must introduce a damping function f_u such that the proper asymptotic behavior is possible:

$$\nu_T = C_\mu f_u \frac{k^2}{\epsilon}, \qquad \textit{B-20}$$

with $f_\mu = O\left(\frac{1}{y}\right)$.

It is now of interested to analyze the asymptotic form of model terms in the k-ϵ formulation. The turbulent transport term D is modeled using the gradient diffusion hypothesis as shown in Eq. B-21:

$$D = -\frac{\partial}{\partial x_i}\left(\frac{\nu_T}{\sigma_k}\frac{\partial k}{\partial x_i}\right) = O\left(\frac{1}{y} y^4 y^2 \frac{1}{y}\right) = O(y^4) \neq O(y). \qquad \textit{B-21}$$

This term models *turbulent transport*, and the region of concern is very near the wall ($y^+ \leq 1$) where the flow is essentially viscous. As may be expected, this error is shown to be minimal from DNS simulations. The same is true for D_ϵ.

The production and destruction of dissipation, P_ϵ and Φ_ϵ, however, are not negligible in this region. Consider the latter, which is modeled as follows:

$$\Phi_\epsilon = C_{\epsilon 2} \frac{\epsilon^2}{k} = O\left(\frac{1}{y^2}\right) \neq O(1). \qquad \textit{B-22}$$

Thus in the near wall region, a damping function $f_2 = O(y^2)$ is necessary for this model. Based on this analysis, we notice that two damping functions are necessary in order for the standard k-ϵ model to be asymptotically consistent. While these functions introduce additional modeling efforts, they are not too destructive.

The problem of boundary conditions on ϵ is a significant conern. The condition shown in Eq. B-23 can be derived:

$$\nu \frac{\partial k^2}{\partial y^2} = \epsilon. \qquad \textit{B-23}$$

This requires a second derivative calculation of the turbulent kinetic energy, which introduces considerable stiffness into the solution. Another condition that has been used is given in Eq. B-24, which is more computationally robust:

$$\frac{\partial \epsilon}{\partial y} = 0, \tag{B-24}$$

However, DNS data have shown that this condition can be quite incorrect. In a two-layer wall treatment such as that employed in STAR-CCM+ [45], a one-equation model is solved for k and ϵ is calculated algebraically. For instance, the Wolfstein model prescribes Eq. B-25 for the turbulent dissipation near the wall [67]:

$$\epsilon = \frac{k^{\frac{3}{2}}}{l_\epsilon}, \qquad l_\epsilon = c_l y\left[1 - \exp\left(\frac{Re_y}{A_\epsilon}\right)\right], \qquad A_\epsilon = 2c_l, \qquad c_l = \kappa C_\mu^{-3/4}. \tag{B-25}$$

B-4 Comparison of k-ϵ and k-ω

The boundary condition used for ω at a wall is given by Eq. B-26:

$$\omega = \begin{cases} \dfrac{u^*}{\sqrt{\beta^*}\kappa y}, & high\ y^+, \\ \dfrac{6\nu}{\beta y^2}, & low\ y^+, \\ g\dfrac{6\nu}{\beta y^2} + (1+g)\dfrac{u^*}{\sqrt{\beta^*}\kappa y}, & all\ y^+. \end{cases} \tag{B-26}$$

This is significantly simpler than blending a one equation model with a two equation model, as is used in the k-ϵ model. Indeed, k-ω is widely recognized as having superior near-wall behavior, because of the vast improved nature of the wall boundary conditions. Deriving the k-ω model implied by the k-ϵ model yields Eq. B-27:

$$\frac{D\omega}{Dt} = \nabla\cdot\left(\frac{\nu_T}{\sigma_\epsilon}\nabla\omega\right) + (C_{\epsilon 1}-1)\frac{P\omega}{k} - (C_{\epsilon 2}-1)\omega^2 + C_\mu\left(\frac{1}{\sigma_\epsilon}+\frac{1}{\sigma_k}\right)\frac{1}{\omega}\nabla\omega \cdot \nabla k + C_\mu\left(\frac{1}{\sigma_\epsilon}-\frac{1}{\sigma_k}\right)\left(\nabla^2 k + \frac{1}{k}\nabla k\cdot\nabla k\right). \tag{B-27}$$

Compare with the k-ω model equation of Eq. B-11. In homogenous turbulence (no spatial variation), the two agree exactly with proper tuning of coefficients. However, when spatial gradients exist, the transport equation predicted by the k-ϵ contains extra information in the form of the two terms in Eq. B-28 that aid the k-ϵ model in the prediction of fully turbulent flows away from the wall:

$$C_\mu\left(\frac{1}{\sigma_\epsilon}+\frac{1}{\sigma_k}\right)\frac{1}{\omega}\nabla\omega\cdot\nabla k+C_\mu\left(\frac{1}{\sigma_\epsilon}-\frac{1}{\sigma_k}\right)\left(\nabla^2 k+\frac{1}{k}\nabla k\cdot\nabla k\right). \qquad \textit{B-28}$$

B-5 Conclusions

In this appendix, the k-ϵ and k-ω models were briefly introduced. Both are quite widely used in industrial applications, and no consensus exists as to which model is superior. Based on the analysis presented here, however, it is generally noted that k-ω is capable of superior performance near wall boundaries, due to the more natural boundary conditions on the turbulence frequency. However, the model transport equation used for ω is less complete than the transport equation used for ϵ in regions away from the wall. Attempts to blend the two models have been met with some success. In particular, the shear stress transport (SST) model by Menter [68] has seen wide application.

Appendix C. CFD Meshing Strategy

C-1 Meshing

The decomposition of a macroscopic geometry into a large number of small volumes in a process called meshing is one of the most important considerations in successful CFD practice. Imprudent practices during this stage can result in a very inaccurate or very inefficient simulation. Most commercial CFD packages, including STAR-CCM+, include automatic meshing functionalities. Properly leveraging these assets, a user supplied with a CAD model can efficiently mesh complex geometries. The information in this appendix draws heavily from the STAR-CCM+ user's manual [45].

C-2 Volume Meshers

While several advanced meshers are available in STAR-CCM+, we presently limit ourselves to three of the most-used methods: tetrahedral, trimmer, and polyhedral. Each mesh type is distinguished by the type of cells produced. As will be shown in this appendix, the choice of mesher can have a significant impact of solution accuracy and efficiency. A well-informed CFD practitioner carefully considers the goals of the simulation before selecting a mesh type. A small amount of forethought can greatly streamline the simulation procedure.

C-2.1 Tetrahedral Mesher

Due to the well-developed Delaunay method, a mesh can be built from a complex geometry very efficiently using tetrahedral elements. The tetrahedral mesher is faster and uses less memory than the trimmer and polyhedral meshers. However, tetrahedral meshes often require significantly more elements to achieve the same accuracy as the more advanced mesh structures. This type of mesh is useful for circumstances in which a large number of geometries are to be used, and accuracy is not a high priority, such iterating on the design of a component.

C-2.2 Trimmer Mesher

The trimmer mesher produces a mesh of predominantly hexahedral cells. Near boundaries, cells are trimmed to allow for complex geometries. These trimmed cells are polyhedral cells built by simply "cutting" edges or corners from a hexahedron to allow boundary fitting. In the bulk of a trimmed mesh, the cells are generally orthogonal which eliminates a source of error as well be discussed in §C-3. However, this increase in accuracy can incur a stability penalty in some cases.

C-2.3 Polyhedral Mesher

The polyhedral mesher in a sense produces the most general meshes. In most polyhedral meshes, each cell has an average of 12-14 faces. The freedom provided by such cells shapes allows for relatively simple meshing of complex regions with varied length scales. Polyhedral cells can be

continuously refined, unlike hexahedral cells in the bulk of a trimmed mesh. The polyhedral shape also works to minimize the cell skewness, which can be especially problematic in a tetrahedral mesh.

C-3 Gradient Reconstruction

Discussion in this section borrows heavily from Chapter 11 of [69]. Consider the conservation equation for some quantity ϕ integrated over a control volume (CV):

$$\int_{CV} \frac{\partial}{\partial t}(\rho\phi)dV + \int_{CV} \nabla\cdot(\rho\phi\mathbf{u})dV = \int_{CV} \nabla\cdot(\Gamma\nabla\phi)dV + \int_{CV} S_\phi dV, \qquad C\text{-}1$$

where Γ is a diffusion coefficient. The diffusion term can be written as a sum over the faces of the control volume:

$$\int_{CV} \nabla\cdot(\Gamma\nabla\phi)dV = \int_{\partial CV} \mathbf{n}\cdot(\Gamma\nabla\phi)dS = \sum_{surfaces}\int_{\Delta A_i} \mathbf{n_i}\cdot(\Gamma\nabla\phi)dS$$
$$\approx \sum_{surfaces} \mathbf{n_i}\cdot(\Gamma\nabla\phi)\Delta A_i. \qquad C\text{-}2$$

Consider the two-dimensional meshing schemes of Fig. C-12. When the direction of the line connecting the centroids A and B ($\hat{\zeta}$ in Fig. C-12) is parallel to a vector normal to the plane between the cells ($\hat{n}$ in Fig. C-12), the mesh is called *orthogonal* and it is a simple matter to calculate the sum in Eq. C-2.

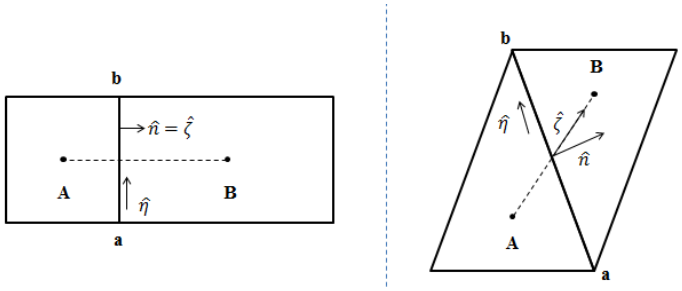

Fig. C-12. Two-dimensional representations of different mesh cells. Left geometry is representative of a hexahedral mesh from a trimmed mesh. Right geometry is representative of a tetrahedral mesh and, to an extent, a polyhedral mesh. The unit vector $\hat{n}$ is perpendicular to the boundary between cells while $\hat{\zeta}$ points from the centroid of cell I to the centroid of cell J.

The flux term can again be broken into a direct gradient term and cross-diffusion term based on Fig. C-12:

$$\mathbf{n_i}\cdot(\Gamma\nabla\phi)\Delta A_i = D_i(\phi_A - \phi_B) + S_{D-cross,i}, \qquad C\text{-}3$$

where the direct diffusion coefficient D_i and the cross-diffusion term $S_{D-cross,i}$ are defined in Eq. C-4:

$$D_i = \frac{\Gamma}{\Delta\zeta}\frac{\mathbf{n_i}\cdot\mathbf{n_i}}{\mathbf{n_i}\cdot\hat{\boldsymbol{\eta}}}\Delta A_i, \qquad S_{D-cross,i} = -\Gamma\frac{\hat{\zeta}\cdot\hat{\eta}}{\hat{n}\cdot\hat{\zeta}}\frac{\phi_b-\phi_a}{\Delta\eta}. \tag{C-4}$$

To evaluate the cross diffusion term, values at cell vertices (ϕ_a, ϕ_b) are required. These values must be interpolated, introducing some error that increases with increasing skewness and aspect ratio. In orthogonal meshes $\hat{\zeta}\cdot\hat{\eta} = 0$ and the cross diffusion terms disappears, removing a source of error.

C-4 Mesh Refinement

One very important aspect of mesh generation is the ability to adjust local cell size to suit the specific needs of simulation. The inability to refine a mesh limits a CFD practitioner to uniformly cell density. In cases of geometries with multiple length scales, efficiency can be improved by refining a mesh where the solution is expected to vary rapidly. In light of this, the performance of the three meshers of §C-2 under refinement is briefly explored.

To illustrate the effect of mesh refinement, the size of the meshing parameter was reduced such that the refined size $S_{refined}$ is related to the base size S_{base} by a factor of R:

$$S_{refined} = R \times S_{base}. \tag{C-5}$$

Results from this exercise are shown in Fig. C-13. In each of the 9 mesh images, the base mesh is on the left and the refined mesh is on the right. Most noteworthy is that for both the tetrahedral and the polyhedral meshes, the refinement happens in a gradual way. With the trimmed mesh, however, the trimmed mesh appears to be refined in steps. Specifically, the trimmed mesh is only refined when one pre-existing cell can be broken into an integer number of cells. In fact, upon inspection it can be observed that the trimmed meshes for $R = 0.7$ and $R = 0.5$ are identical. Based on this consideration, it is observed that polyhedral and tetrahedral meshes are better for geometries with multiple length scales, as they can be more continuously refined to match local cell density requirements efficiently.

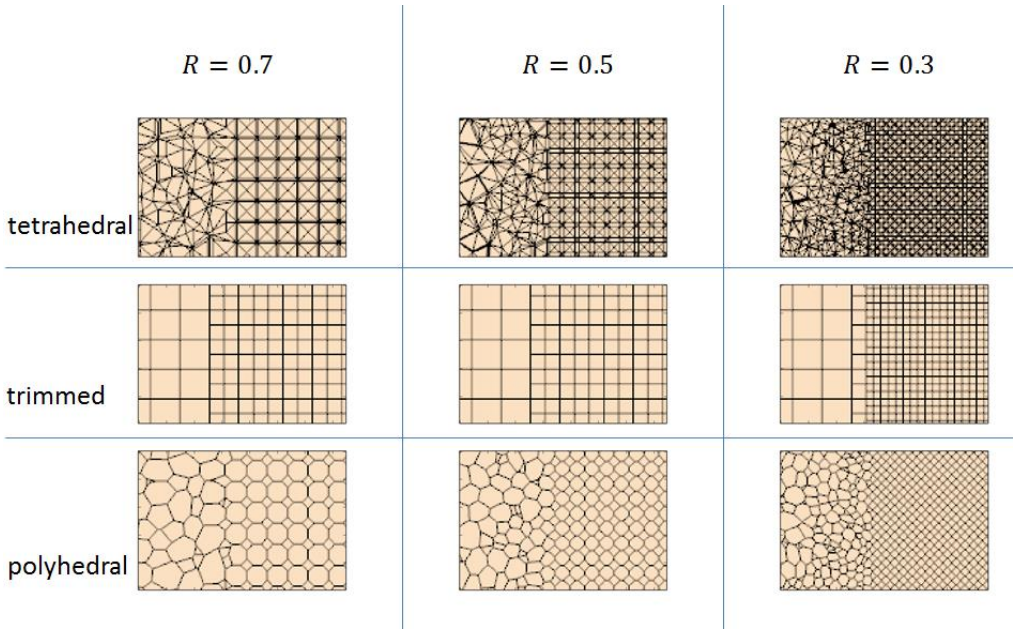

Fig. C-13. Examples of refinement for different mesh types.

C-5 Mesh Comparison

The accuracy of a meshing strategy is of course among the most important considerations. Numerical diffusion, a common cause of inaccuracy in fluid dynamics simulations, occurs when discretization error manifests itself as false viscosity or false diffusion.

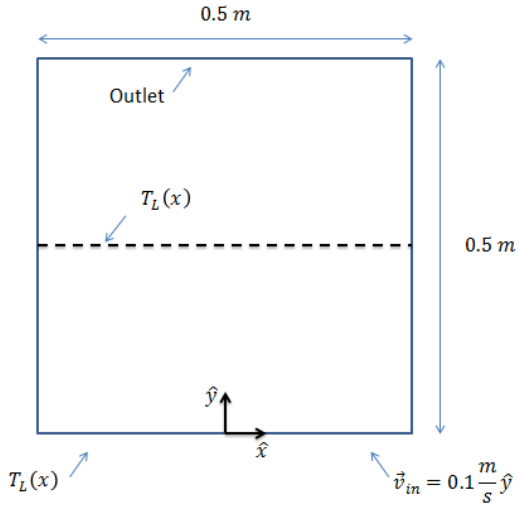

Fig. C-14. Geometry devised to test mesh accuracy.

In order to test the numerical effects of different cell types, the geometry of Fig. C-14 was devised. A constant velocity is imposed at the inlet, while a constant pressure is imposed at the outlet. The two sides are periodic boundaries, while the top and bottom are walls that allow slip. A temperature distribution defined by Eq. C-6 is imposed on the inlet flow:

$$T_{in} = \begin{cases} 300.0\ K, & x < 0, \\ 350.0\ K, & x = 0, \\ 400.0\ K, & x > 0. \end{cases} \qquad \text{C-6}$$

Additionally, the calculated temperature profile along line L is recorded as $T_L(x)$. In order to quantify the amount of temperature diffusion, the coefficient M is defined in Eq. C-7 to measure the departure from the initial shape:

$$M = \frac{\int_L [T_L(x) - T_{in}(x)]dx}{\int_L T_{in}(x)dx}. \qquad \text{C-7}$$

Due to the large differences in temperature in $T_{in}(x)$, conduction will affect the solution and M is not expected to vanish as mesh density increases. Values for this coefficient were calculated for a number of meshes, with results shown in Fig. C-15 along with the times required to calculate those meshes on a desktop computer. While all three mesh types appear to converge to the same value for M, the convergence behavior is quite different. The polyhedral curve appears to approach the true solution significantly faster than the tetrahedral curve. For this geometry, the trimmer mesher produces a purely hexahedral mesh that produces the most accurate results for a given mesh size.

The right of Fig. C-15 clearly shows that tetrahedral meshes are produced much faster than both trimmed (hexahedral in this case) and polyhedral meshes. Indeed, the tetrahedral cells are produced approximately an order of magnitude faster than polyhedral cell. It should be noted that the trimmed mesh is likely to have benefited from parallelepiped geometry more than the other two meshers in terms of run time.

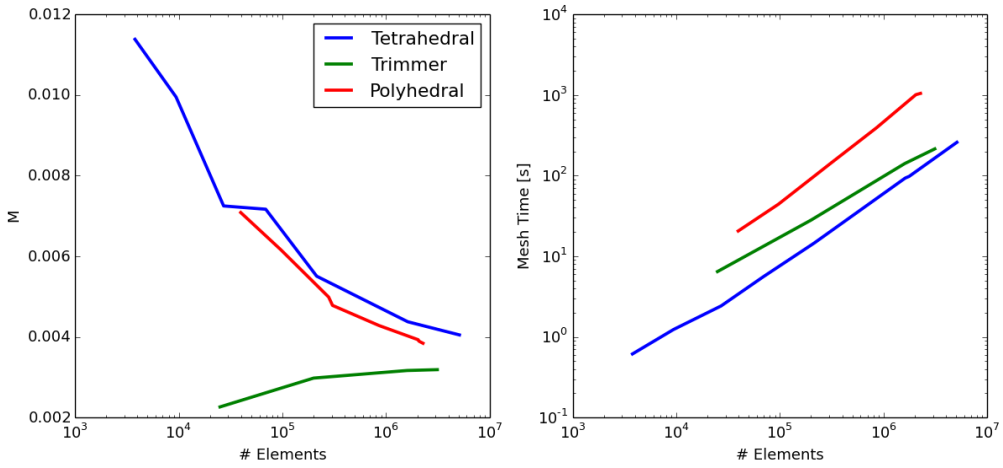

Fig. C-15. (LEFT) Value of mixing coefficient calculated with different meshes. (RIGHT) time required to generate several meshes.

Appendix D. Coupling Implementation

D-1 Design Objective of Coupling

The objectives of the coupling implementations presented in this thesis are based upon practical and efficient application to existing problems. A primary objective was that the source code of TRACE be minimally modified, serving several purposes. First, TRACE is a large code with many interconnected modules and subroutines; keeping modifications few in number and well-organized helps minimize the possibility that the TRACE execution is improperly modified producing unexpected or incorrect results.

Parallel to the first objective is the goal of requiring minimal modification to existing TRACE input decks. Input decks used to simulate large NPP systems are generally quite complex, with many different types of components, many of which are carefully calibrated based on the goals of the simulation. Any modification to these input decks will almost certainly require recalibration and debugging, potentially wasting significant amounts of time. Further, when unmodified input can be used for coupling, a direct comparison can be made between coupled and uncoupled models with confidence that the models are appropriately analogous.

D-1 Data Mapping

Although TRACE and STAR-CCM+ both simulate fluid flow, the codes actually solve different sets of equations on very different computational meshes. Thus, it is necessary to be specific about how data are mapped from one code to another. The general strategy toward data mapping is shown in Fig. C-15. A finely resolved field, in this case pressure or velocity, is first calculated by a CFD code like STAR-CCM+. The field is then reduced to match the order of the STH code, such as TRACE. The reduction is generally carried about by either volume or surface integrals. The data are then compiled by the coupling software Janus. From there, the data is processed to match quantities recognizable by TRACE. After processed values are transferred to TRACE, the STH code calculates a CFD-informed solution. In certain cases, TRACE additionally passes boundary conditions to STAR-CCM+

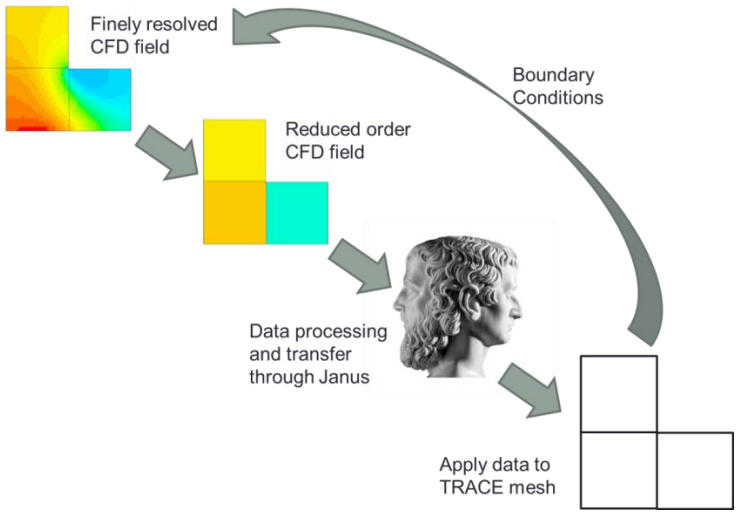

Fig. D-16. Schematic diagram of data mapping approach adopted in this research.

D-2 General Structure

The coupling infrastructure used in this work is implemented in a mixture of Fortran and Java code. While STAR-CCM+ is closed source software, the code is natively equipped with a powerful Java interface that allows for generalized automation. The Java Native Access (JNA) library allows for the use of Fortran libraries in a Java environment [70]. TRACE is then compiled as a subroutine within a shared object library to be called through the JNA interface. TRACE is also modified to include several synchronization points to allow for data transfer throughout the execution of the code.

The execution of a coupled simulation is controlled through a main java driver macro, which launches two additional threads through the Java concurrency functionality: a TRACE thread and a "data management" thread that communicates data between TRACE and STAR-CCM+. A custom library was written that allows for data transfer directly through memory between the Java data types and the Fortran data types. The library includes functionality for translating strings and for accessing specific TRACE data.

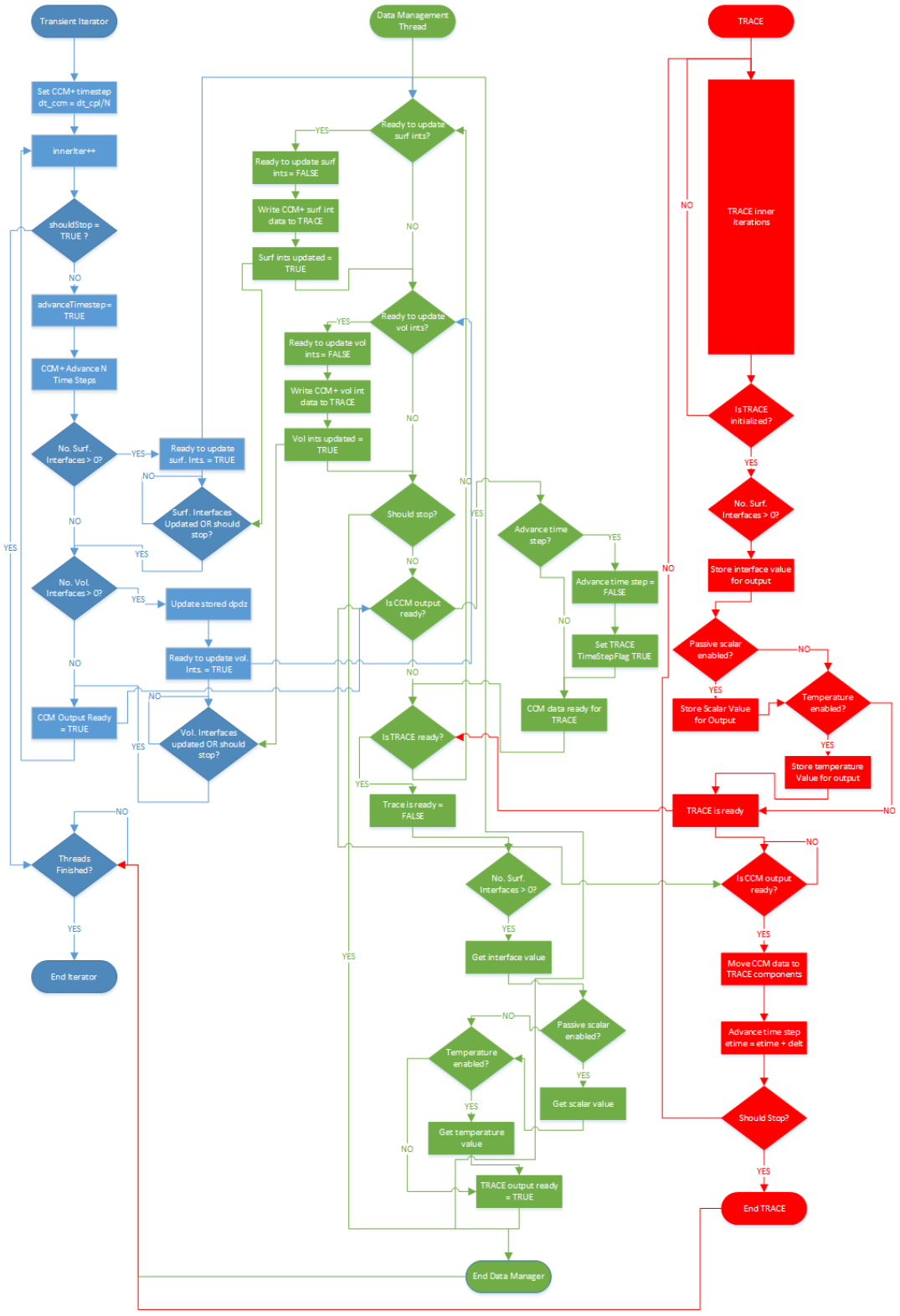

Fig. D-17. General outline of coupling execution. Blue indicates STAR-CCM+, green indicates the data management thread, and red indicates TRACE.

A simplified outline of the coupling execution is shown in Fig. D-17. A coupled simulation is initiated with a single call to STAR-CCM+ with the directive to load and run the Java driver macro. This main thread then spawns a data management thread and a thread which loads the TRACE shared object and executes the system code. Immediately before TRACE actually begins execution, a call is made to a Fortan subroutine that reads the custom coupling input file "interfaces.cpl", which contains information regarding the coupling interfaces, data flow options, debugging options, and transient information. TRACE reads its input normally and passes all relevant information to Java data structures.

D-3 STAR-CCM+ Functionality

STAR-CCM+ is natively equipped with several tools that aid significantly in the reduction of finely resolved CFD solutions to forms more useful for the coarser STH mesh.

The *Reports* functionality of STAR-CCM+ provides a means of evaluating integrals on a finite volume mesh. Volume integrals can be calculated with *Volume Integral Reports,* while surface integrals are calculated with *Surface Integral Reports*. Reports require the user to specify a sub-region or sub-surface over which to calculate the integral, as well as a function to be the integrand. Reports can be manipulated through the Java API.

Evaluating custom functions is made possible through the *User Field Functions*. This tool allows the user to specify a function using generalizable plaintext syntax. Functions are generally a combination of constants and natively available functions, such as pressure or velocity. Operations such as gradient, divergence, and square roots are available.

D-4 Multi-Dimensional Integral Calculations

The multi-dimensional interfacing techniques employed for this work require evaluation of volumetric integrals over sections of the CFD region that correspond with the TRACE cells. The integrations are carried out using existing STAR-CCM+ functionality, coupled with some custom Java data types. In particular, one of the two methods used resulted in significant time savings, warranting the present discussion.

D-4.1 Derived Parts

One native feature of STAR-CCM+ is called "Derived Parts". With this tool, a user can define a sub-region based on a specified criteria. Derived parts defined by coordinate limits are most useful for the purposes of this dissertation. In particular, a TRACE cell is defined in STAR-CCM+ as the set of all elements whose centroids are within the bounds of the relevant cell. Derived parts only allow constraining one variable, and so multiple constraints are needed for each cell. Due to the structure of the TRACE nodalization, some constraints can be used by multiple parts and so it is not necessary to create 3 derived parts for each TRACE cell. The end result is a unique derived part in STAR-CCM+ for each TRACE cell over which integral reports can be defined.

D-4.2 Filter Functions

The use of derived parts can be avoided by instead defining an appropriate filter function and integrating over the entire region. This is accomplished by defining a single user field function $f(\vec{x})$ that is unity inside of a specified region and zero outside:

$$f(\vec{x}) = \begin{cases} 1, x_1 \in [x_{1,min}, x_{1,max}], x_2 \in [x_{2,min}, x_{2,max}], x_3 \in [x_{3,min}, x_{3,max}], \\ 0, \quad otherwise. \end{cases} \qquad \textit{D-1}$$

The limits $x_{i,min}$ and $x_{i,max}$ are also defined as user field functions for a total of 7 functions. Accompanying this is a data structure in Java that contains the limits of each TRACE cell.

During the preparation stage of a coupled simulation, Janus loops through each cell and integrates Eq. D-1 over the STAR-CCM+ region with a Volume Integral Report and stores the resulting volume of each cell for later use. During the course of a coupled calculation, volume averages of fields such as pressure are required. To accomplish this, the relevant variable, such as pressure, is multiplied by the filter function and integrated over the entire domain. Dividing by the cell volume (which is stored in memory) thus provides a volume average, as shown in Eq. D-2:

$$\frac{1}{Vol_i} \iiint_V p(\vec{x}) f_{V_i}(\vec{x}) dV = \frac{1}{Vol_i} \iiint_{V_i} p(\vec{x}) dV = \langle p(\vec{x}) \rangle_{V_i}, \qquad \textit{D-2}$$

where angle brackets with subscript V_i, $\langle \cdot \rangle_{V_i}$, refers to a volume average over the cell defined by V_i.

D-4.3 Comparison

Consider the geometry of Fig. D-18 that was devised to test the efficiency of volume integral calculation in STAR-CCM+. The bulk of the geometry is a $0.5\,m \times 0.5\,m \times 0.5\,m$ cube, along with one inlet and two outlets, all with $0.1\,m \times 0.1\,m$ cross sections. For the sake of testing, each direction is broken into $0.1\,m$ segments, leading to 125 total nodes of dimensions $0.1\,m \times 0.1\,m \times 0.1\,m$. For each of the 125 nodes, the function in Eq. D-3 was evaluated with both the filter and derived part methods. Although this function has units of energy, it is representative of calculations performed in coupled simulations. The value would then be divided by the volume of the cell, which is stored from initial stages of the simulation. The process of using "Volume Integral Reports" rather than "Volume Average Reports" was found to be more efficient in the case that the geometry of each node does not change:

$$f_i = \iiint_{V_i} p(\vec{x}) dV. \qquad \textit{D-3}$$

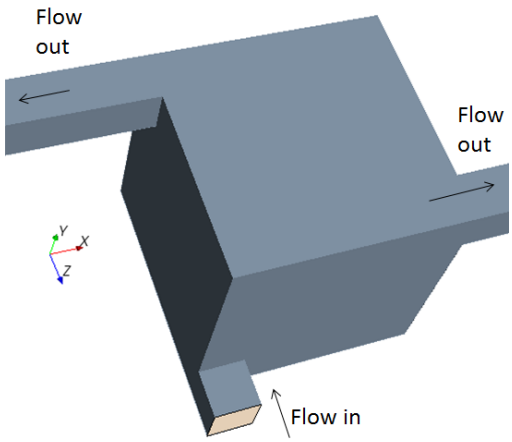

Fig. D-18. Geometry used to test timing of integral calculations.

It was found that the type of mesh had an impact on the efficiency of calculating Eq. D-3, and so exercises were carried out with meshes generated by both polyhedral and trimmer meshers (See §C-2 for description of meshers).

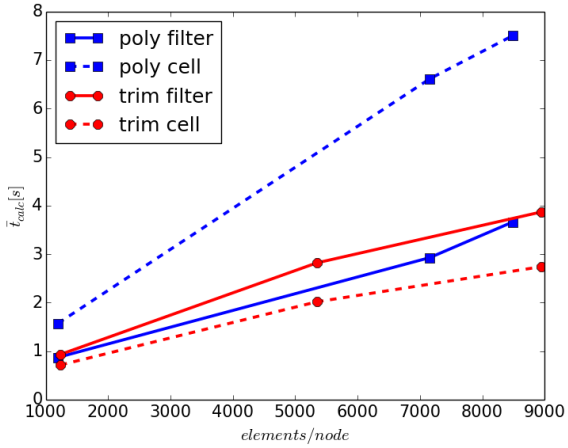

Fig. D-19. Average time taken to perform volume integrals with the cell and filter methods. The trimmer (trim) and polyhedral (poly) meshers were both used. The ordinate axis refers to the approximate number of CFD mesh elements in each node with dimensions $0.1\,m \times 0.1\,m \times 0.1\,m$.

The data in Fig. D-19 were calculated by measuring the time taken to calculate Eq. D-3 for all 125 nodes of the geometry in Fig. D-19. The times are averaged over at least 12 instances to minimized statistical noise. On the ordinate, the number of cells in cube section of the geometry was divided by 125 for an estimate of the number of cells per node. For the trimmed mesh, the time required to calculate the integrals is similar for both calculation methods, with the filter method actually requiring somewhat more time. For the polyhedral mesh, the filter method shows a substantial reduction in required time and is in line with times required for trimmed meshes.

Appendix E. Solution of Fluid Dynamics Equations

E-1 Introduction

The study of incompressible fluid dynamics often begins with the Navier-Stokes equations of Eq. E-1:

$$\rho \frac{\partial \mathbf{v}}{\partial t} + \rho \mathbf{v} \cdot \nabla \mathbf{v} = -\nabla p + \nabla \cdot \mathbf{T}, \qquad E\text{-}1$$

where $\mathbf{v}$ is the flow velocity, ρ is the density, p is the pressure, and $\mathbf{T}$ is the stress tensor. This equation represents the conservation of momentum from an Eulerian viewpoint describing pointwise properties of the flow. The first term from the left ($\rho \frac{\partial \mathbf{v}}{\partial t}$) represents the time rate of change of fluid momentum. The second term on from the left ($\rho \mathbf{v} \cdot \nabla \mathbf{v}$) represents the change in momentum at a point due to flow gradients. Together, the previous two terms represent the material derivative that relates an Eulerian specification to a Lagrangian specification in which the dynamics of a specific parcel of a fluid are described.

The first time to the right of the equality, ($-\nabla p$), accounts for the effects of pressure, or the macroscopic effects of particle collision, on fluid momentum. Finally, the divergence of the stress tensor, ($\nabla \cdot \mathbf{T}$), describes the effects of both normal and shear forces on the fluid that result from viscous effects. The Navier-Stokes equations are usually accompanied by the constraint given by Eq. E-2:

$$\nabla \cdot \mathbf{v} = 0, \qquad E\text{-}2$$

which results from the imposition of mass conservation on the flow.

CFD and STH codes both solve versions of Eqs. E-1 and E-2 to describe fluid flow. However, as discussed often in this dissertation, the scales of the computational meshes of the two approaches are very different. The specific method by which either type of code calculates a flow field is therefore quite different. In this appendix, the solution methods employed by TRACE and STAR-CCM+ are discussed.

E-2 TRACE

TRACE offers two methods of time stepping: a semi-implicit method and a Stability-Enhancing Two-Step (SETS) method. Both methods use the procedure described in §E-2.2, but the SETS method precedes the step by calculating "stabilizer velocities." Additionally, the SETS method solves stabilizer equations for the mass and energy equations after the semi-implicit step. While

both methods are first-order in time and space, the SETS method is more stable and allows the use of larger time steps. Due to the higher complexity of SETS in the TRACE source code, the coupling methods presented in this dissertation are currently only supported for the semi-implicit method.

E-2.1 Discretization

The TRACE discretization is formulated by applying a volume-averaging operator, $\langle\cdot\rangle$, to Eqs. E-1 and E-2. The material in this section closely follows the TRACE User's Manual [16]. In order to simplify the presentation, we only consider incompressible, single-phase, isothermal flow. In reality, TRACE supports two-phase flow and solves an additional heat equation.

The volume-averaged momentum equation is given by:

$$\rho\frac{\partial\langle\mathbf{v}\rangle}{\partial t}+\rho\langle\mathbf{v}\cdot\nabla\mathbf{v}\rangle=-\langle\nabla p\rangle+\langle\nabla\cdot\mathbf{T}\rangle, \qquad E\text{-}3$$

and the volume-averaged mass conservation equation is given by:

$$\langle\nabla\cdot\mathbf{v}\rangle=0. \qquad E\text{-}4$$

At this point, several approximations are made:

- The volume average of a product is assumed to be equation to the product of volume averages.
- Only contributions from the stress tensor, **T**, due to shear at wall surfaces are considered. This assumption precludes TRACE for being able to capture circulation patterns in large open regions. In fact, this is a primary motivator for performing CFD/STH coupling studies.

Under these assumptions, the TRACE momentum equations can be rewritten as:

$$\rho\frac{\partial\langle\mathbf{v}\rangle}{\partial t}+\rho\nabla\cdot\langle\mathbf{v}\rangle\langle\mathbf{v}\rangle=-\nabla\langle p\rangle+\mathbf{f}_{wl}, \qquad E\text{-}5$$

where $\mathbf{f}_{wl}$ is the force per unit volume that the wall boundary exerts on the fluid through friction. The value of this term is calculated with experimental correlations. Specifically, TRACE uses the Churchill friction factor correlation for the Fanning friction factor, f_F, calculated as follows:

$$f_F=2\left[\left(\frac{8}{Re}\right)^{12}+\frac{1}{(a+b)^{\frac{3}{2}}}\right]^{\frac{1}{12}}, \qquad E\text{-}6$$

where

$$a = \left\{ 2.457 \ln \left[\frac{1}{\left(\frac{7}{Re}\right)^{0.9} + 0.27\left(\frac{\epsilon}{D_h}\right)} \right] \right\}^{16}, \qquad \textit{E-7}$$

and

$$b = \left(3.753 \times \frac{10^4}{Re} \right)^{16}. \qquad \textit{E-8}$$

In these equations, Re is the Reynolds number, D_h is the hydraulic diameter, and ϵ is the wall roughness parameter. Replacing $\langle \mathbf{v} \rangle$ with V yields the form of the momentum equation used in TRACE:

$$\frac{V^{n+1}_{\alpha,i+\frac{1}{2},j,k} - V^{n}_{\alpha,i+\frac{1}{2},j,k}}{\Delta t} + (V \cdot \nabla V)_{\alpha,i+\frac{1}{2},j,k} = -\frac{1}{\rho}\frac{p^{n+1}_{i+1,j,k} - p^{n+1}_{i,j,k}}{R_\alpha \Delta\alpha_{i+\frac{1}{2},j,k}} - 2 f_F \frac{R_\alpha \Delta\alpha}{D_h}\left[2V^{n+1}_{\alpha,i+\frac{1}{2},j,k} - V^{n}_{\alpha,i+\frac{1}{2},j,k}\right]\left|V^{n}_{\alpha,i+\frac{1}{2},j,k}\right|, \qquad \textit{E-9}$$

where $V^{n}_{\alpha,i+\frac{1}{2},j,k}$ is the α-component of velocity at the edge between adjacent cells with indices (i,j,k) and $(i+1,j,k)$, Δt is the timestep, $p_{i,j,k}$ is the volume-averaged pressure of cell (i,j,k), ρ is the density, Δt is the timestep, $\Delta\alpha$ is the mesh size in the α direction, and R_α is a length multiplier that is unity for all directions except $\alpha = \theta$ in which R_α is the radius at which the cell centers lie. All three directions are coupled through the convective acceleration terms $V \cdot \nabla V$, as well as through mass conservation, or continuity This formulation is valid for both Cartesian and cylindrical coordinate systems.

TRACE employs a discretization approach for the convective term, $V \cdot \nabla V$, to provide both stability and accuracy. A central difference (relative to edge $j+\frac{1}{2}$) approximation for 1-D flow applied to this term yields:

$$V \cdot \nabla V = V\frac{dV}{dx} = \frac{1}{2}\frac{d(V^2)}{dx} \approx \frac{1}{2}\frac{\left(V^2_{j+1} - V^2_j\right)}{\Delta x_{j+\frac{1}{2}}} = \frac{1}{2}\frac{\left(V_{j+1} + V_j\right)\left(V_{j+1} - V_j\right)}{x_{j+\frac{1}{2}}}. \qquad \textit{E-10}$$

Due to the staggered grid arrangement in TRACE, velocities are actually defined at cell edges and cell-center velocities must be estimated. By assuming constant volumetric flow rates, the cell-center velocities can be related to the cell-edge velocities with the flow areas, A, at these locations:

$$A_{j+1}V_{j+1} = A_{j+\frac{1}{2}}V_{j+\frac{1}{2}} = A_j V_j, \qquad \textit{E-11}$$

and

$$A_j V_j = A_{j-\frac{1}{2}} V_{j-\frac{1}{2}}. \qquad \textit{E-12}$$

Combining these equations therefore yields the discretized expression:

$$V \cdot \nabla V_{j+\frac{1}{2}} = \frac{1}{2} \frac{\left(\frac{A_{j+\frac{1}{2}}}{A_{j+1}} + \frac{A_{j+\frac{1}{2}}}{A_j} \right) V_{j+\frac{1}{2}} \left(\frac{A_{j+\frac{1}{2}} V_{j+\frac{1}{2}}}{A_{j+1}} - \frac{A_{j-\frac{1}{2}} V_{j-\frac{1}{2}}}{A_j} \right)}{x_{j+\frac{1}{2}}}. \qquad \textit{E-13}$$

Eq. E-13 was calculated assuming $V_{j+\frac{1}{2}} \geq 0$, but it is a simple matter to calculated the analogous equation if $V_{j+\frac{1}{2}} < 0$. TRACE therefore using an upwind approach to the convective term in both 1-D and 3-D momentum equations.

E-2.2 Semi-Implicit Solver

The general outline of the TRACE solution procedure is given in Fig. E-1.

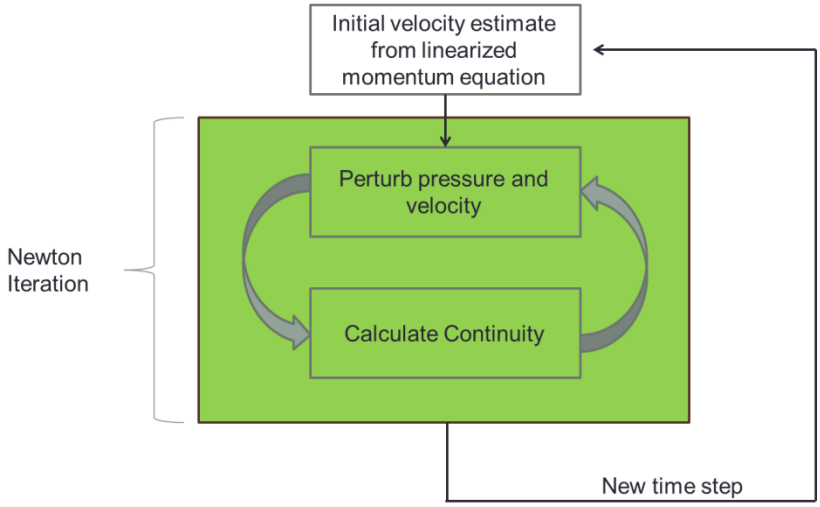

Fig. E-1. Schematic of nonlinear iteration used in the TRACE solution procedure.

TRACE begins a time step by calculating an initial estimate of the new time velocity ($\tilde{V}_\alpha^{n+1,0}$, where the 0 superscript signifies the initial, unadjusted estimate and the tilde represents the intermediate nature of the value) from a version of Eq. E-9 built from previous time step pressures (i.e. replace p^{n+1} with p^n in Eq. E-9). As shown in Eq. E-14, this equation is linear in $\tilde{V}_\alpha^{n+1,0}$ and can be solved directly:

$$\tilde{V}_{\alpha}^{n+1,0}\left[1+2\Delta t K_{\alpha,i+\frac{1}{2},j,k}^{n}\right] = V_{\alpha,i+\frac{1}{2},j,k}^{n} - \Delta t\left[\frac{1}{\rho}\frac{p_{i+1,j,k}^{n}-p_{i,j,k}^{n}}{R_{\alpha}\Delta\alpha_{i+\frac{1}{2},j,k}} - K_{\alpha,i+\frac{1}{2},j,k}^{n} V_{\alpha,i+\frac{1}{2},j,k}^{n}\left|V_{\alpha,i+\frac{1}{2},j,k}^{n}\right|\right]. \quad \textit{E-14}$$

After calculating $\tilde{V}_{\alpha}^{n+1,0}$, the variable given by Eq. E-15 is stored, characterizing the relationship of changes in pressure drop between adjacent cells and the velocity across the edge shared by the adjacent cells:

$$\left.\frac{dV}{d\Delta p}\right|_{j+\frac{1}{2}} = \frac{\Delta t}{\rho R_{\alpha}\Delta\alpha\left[1+\Delta t\left(2K_{j+\frac{1}{2}}^{n}\left|V_{j+\frac{1}{2}}^{n}\right| + \beta\nabla_{j+\frac{1}{2}}V_{j+\frac{1}{2}}^{n}\right)\right]}. \quad \textit{E-15}$$

Eqs. E-14 and E-15 are built from a linearized version of the momentum equation. The fully nonlinear equations of motion are solved with a Newton-Raphson iteration cycle, which can be conceptualized as adjusting the pressure field based on a new velocity estimate, followed by adjusting the velocity field based on the newest pressure field estimate. Specifically, a set of equations is built by perturbing the pressure and velocity variables in the mass and energy conservation equations with the as yet unknown pressure perturbation δp_j^m. The pressure variable is replaced with Eq. E-16:

$$p_j^{n+1,m+1} = p_j^{n+1,m} + \delta p_j^m. \quad \textit{E-16}$$

where j refers to a cell and m refers to the iteration number of the Newton cycle. The velocity perturbation shown in Eq. E-17 is built from the pressure perturbation using Eq. E-15:

$$V_{j+\frac{1}{2}}^{n+1,m+1} = V_{j+\frac{1}{2}}^{n+1,m} + \left.\frac{dV}{d\Delta p}\right|_{j+\frac{1}{2}}\left(\delta p_j^m - \delta p_{j+1}^m\right). \quad \textit{E-17}$$

For incompressible isothermal flow, the linearized mass conservation equation with perturbed values is shown in Eq. E-186-8:

$$\frac{\left.\frac{dV}{d\Delta p}\right|_{j+\frac{1}{2}}\left(\delta p_j^m - \delta p_{j+1}^m\right) - \left.\frac{dV}{d\Delta p}\right|_{j-\frac{1}{2}}\left(\delta p_{j-1}^m - \delta p_j^m\right)}{\Delta x} = \frac{V_{j+\frac{1}{2}}^{n+1,m} - V_{j-\frac{1}{2}}^{n+1,m}}{\Delta x}. \quad \textit{E-18}$$

The 3-D version is built by adding analogous terms for the remaining two directions. Applying the perturbed balance equation to each cell yields a system of expressions to be solved simultaneously for the pressure perturbations δp_j^m, which are used to update the pressure and velocity fields. This cycle continues until convergence, given by ($\lim_{m\to\infty}\tilde{V}_{\alpha}^{n+1,m} = V_{\alpha}^{n+1}$, $\lim_{m\to\infty}\delta p_j^m \to 0$), or a maximum number of iterations is reached.

E-3 STAR-CCM+

CFD codes such as STAR-CCM+ often offer multiple solvers with many options. The solver dominantly used in this dissertation is the "Segregated Flow" solver that solves flow equations in an uncoupled manner. Material in this section is largely based on the STAR-CCM+ user's manual [45]. The coupling between momentum and mass conservation equation is achieved through a predictor-corrector approach. Broadly, the formulation is described as a collocated variable arrangement along with a Rhie-and-Chow-type pressure-velocity coupling combined with a SIMPLE-like algorithm.

STAR-CCM+ discretized flow equations by integrating them over small, but finite volumes as described in Appendix C. In this form, the mass conservation equation is given by:

$$\frac{\partial}{\partial t}\iiint_V \rho dV + \oiint_A \rho \mathbf{v}\cdot\mathbf{da} = \iiint_V S dV, \qquad \textit{E-19}$$

where ρ is the density, $\mathbf{v}$ is the velocity vector, $\mathbf{da}$ is the normal vector for the surface, and S is a source of mass flow. Similarly, the momentum conservation equation is given by:

$$\frac{\partial}{\partial t}\iiint_V \rho \mathbf{v} dV + \oiint_A \rho \mathbf{v}\mathbf{v}\cdot\mathbf{da} = -\iint_A p\mathbf{I}\cdot\mathbf{da} + \iint_A \mathbf{T}\cdot\mathbf{da} + \iiint_V S_b, \qquad \textit{E-20}$$

where p is the pressure, $\mathbf{I}$ is the identity tensor, $\mathbf{T}$ is the viscous stress tensor, and S_b describes body forces, such as gravity.

E-3.1 Discretization

A convective term at a face f is discretized by:

$$[\phi\rho(\mathbf{v}\cdot\mathbf{a})]_f = (\dot{m}\phi)_f, \qquad \textit{E-21}$$

where ϕ_f and $\dot{m}_f$ are the scalar value and mass flow rates at face f, respectively. STAR-CCM+ offers both first- and second- order upwind discretizations of Eq. E-21, both of which are employed in this dissertation. The first-order method is given by:

$$(\dot{m}\phi)_f = \begin{cases} \dot{m}_f\phi_0, & \dot{m}_f \geq 0, \\ \dot{m}_f\phi_1, & \dot{m}_f < 0, \end{cases} \qquad \textit{E-22}$$

where ϕ_0 is the scalar value of cell 0 and ϕ_1 is the scalar value of cell 1. Cells 0 and 1 are defined for each face based on the sign convention of $\dot{m}_f$. The second-order method is given by:

$$(\dot{m}\phi)_f = \begin{cases} \dot{m}_f\left[\phi_0 + \mathbf{s}_0\cdot(\nabla\phi)_{r,0}\right], & \dot{m}_f \geq 0, \\ \dot{m}_f\left[\phi_1 + \mathbf{s}_1\cdot(\nabla\phi)_{r,1}\right], & \dot{m}_f < 0, \end{cases} \qquad \textit{E-23}$$

where $(\nabla\phi)_{r,0}$ and $(\nabla\phi)_{r,1}$ are "reconstruction" gradients in cells 0 and 1, respectively. Also, $\mathbf{s}_0 = \mathbf{x}_f - \mathbf{x}_0$ and $\mathbf{s}_1 = \mathbf{x}_f - \mathbf{x}_1$ are the distances from the centroids of cells 0 and 1, respectively, to the centroid of face f. Reconstruction gradients are briefly discussed in

Appendix C. Multiple methods are used for their calculations, such as the hybrid Gauss/weighted LSQ method or the Green-Gauss method.

The discretization scheme of Eq. E-23 offers improved accuracy over the first-order discretization of Eq. E-22. However, the increased dissipation error of Eq. E-22 can serve to stabilize a solution, as observed in Appendix A.

E-3.2 SIMPLE Algorithm

The Semi-Implicit Method for Pressure-Linked Equations (SIMPLE) algorithm is a very widely-used procedure for fluid flow calculation [71] [72] [73]. The algorithm is iterative and proceeds as follows:

1. Set boundary conditions
2. Compute gradients of velocity and pressure
3. Calculate intermediate velocity field $\mathbf{v}^*$.
4. Compute uncorrected mass fluxes at cell faces $\dot{m}_f^*$ (see §E-3.3)
5. Calculate pressure corrections p'
6. Update the pressure field:

$$p^{n+1} = p^n + \omega p', \tag{E-24}$$

   where ω is an under-relaxation factor used for pressure.
7. Correct face mass fluxes:

$$\dot{m}_f^{n+1} = \dot{m}_f^* + \dot{m}_f'. \tag{E-25}$$

8. Correct cell velocities:

$$\mathbf{v}^{n+1} = \mathbf{v}^* - \frac{V\nabla p'}{\mathbf{a}_p^v}, \tag{E-26}$$

   where $\nabla p'$ is the gradient of the pressure corrections, $\mathbf{a}_p^v$ is the vector of central coefficients for the discretized linear system representing the velocity equation, and V is the cell volume.

E-3.3 Mass Conservation

The discrete continuity equation in STAR-CCM+ is written as follows for each cell:

$$\sum_f \left(\dot{m}_f^* + \dot{m}_f'\right) = 0, \tag{E-27}$$

where the summation is over each face of a cell, $\dot{m}_f^*$ is the "uncorrected" mass flow rate at face f, and $\dot{m}_f'$ is the mass flow correction required to satisfy continuity. For interior faces, the uncorrected mass flow rate is written as shown in Eq. E-28:

$$\dot{m}_f = \rho \left[\mathbf{a} \cdot \left(\frac{\mathbf{v_0^*} + \mathbf{v_1^*}}{2} \right) \right] - \Upsilon_f, \qquad \textit{E-28}$$

where ρ is the density, $\mathbf{a}$ is the area vector of face f, and $\mathbf{v_0^*}$ and $\mathbf{v_1^*}$ are the velocities of the two cells adjacent to face f after the discrete momentum equations have been solved. Υ is the Rhie-and-Chow-type dissipation at face f:

$$\Upsilon_f = \rho \left(\frac{V_0 + V_1}{\overline{a}_0 + \overline{a}_1} \right) \left(\frac{\mathbf{a} \cdot \mathbf{a}}{\mathbf{a} \cdot \mathbf{ds}} \right) \left(p_1^* - p_0^* - \overline{\nabla p_f^*} \cdot \mathbf{ds} \right), \qquad \textit{E-29}$$

where V_0 and V_1 are the volumes of the cells adjacent to face f, $\overline{a}_0$ and $\overline{a}_1$ are the averages of the momentum coefficients for all components of momentum for adjacent cells, and p_1^* and p_0^* are the cell pressure from the previous iteration. $\overline{\nabla p_f^*}$ is the volume-weighted averaged of the cell pressure gradients. $\mathbf{ds}$ is the vector point from the centroid of cell 0 to the centroid of cell 1 and $\mathbf{a}$ is the vector normal to face f pointing from cell 0 to cell 1. The Υ_f dissipation term is useful because it introduces a pressure-velocity link into the mass conservation equations. Formulations without such a link are well-known to fall victim to a so-called "checkerboard instability" in which the continuity equation admits solutions that oscillate unphysically from cell to cell. The staggered grid arrangement of STH codes also serves to dampen this instability.

E-4 Coupled Fluid Solutions

In the previous sections, it is shown that TRACE and STAR-CCM+ seek to model similar phenomena, but with very different approaches. In particular, CFD codes use extremely fine meshes compared to TRACE that allows for more direct model of terms such as the divergence of the stress tensor. In this section, these ideas are combined into a coupled solution. Fig. E-2 shows sample TRACE and STAR-CCM+ meshes for a simple 1-D flow system. Several important observations can be made from this figure:

- There are many more CFD mesh elements than there are STH cells.
- The edges of CFD mesh elements do not align with the STH mesh.
- TRACE uses a staggered grid with pressures defined at cell centers. Velocities and friction factors are defined at cells edges.

As shown in Chapter 4, using a CFD pressure drop to inform an STH friction factor leads the STH code to predict a CFD-like pressure field. CFD-informed friction factors are formulated by calculating the differences in volume-averaged pressure between sub-regions of the CFD mesh corresponding to TRACE cells. The "Reports" functionality described in §D-3 allows for automatic calculation of volume integrals from the CFD solution.

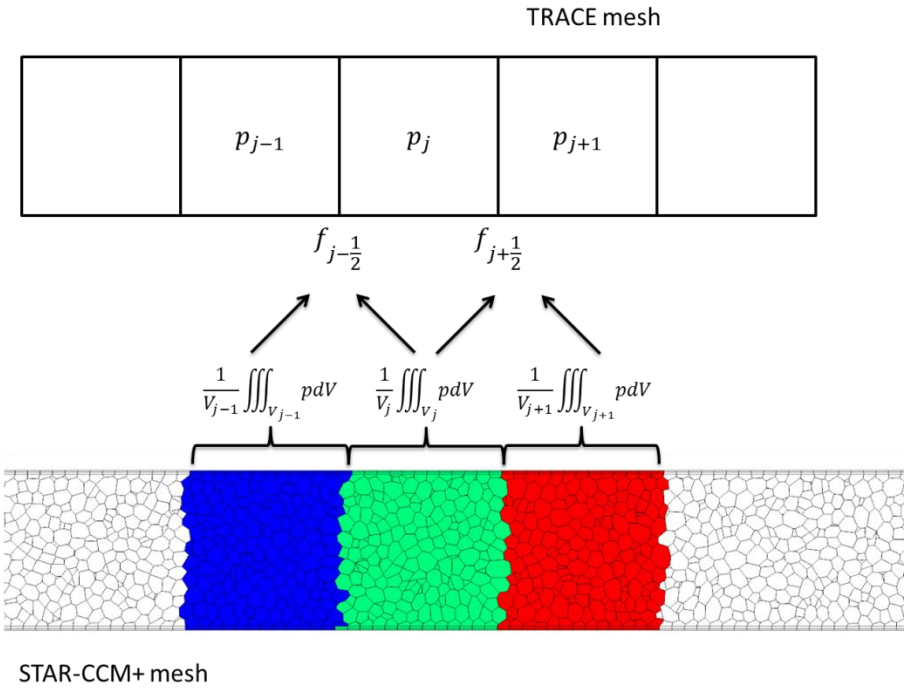

Fig. E-2. Schematic of domain overlapping coupling mechanism showing how data is mapped from a STAR-CCM+ mesh to a TRACE mesh.

For a concrete example recall the case discussed in §4-7.1. The geometry of the coupled simulation, shown in Fig. 4-9, is repeated here for simplicity.

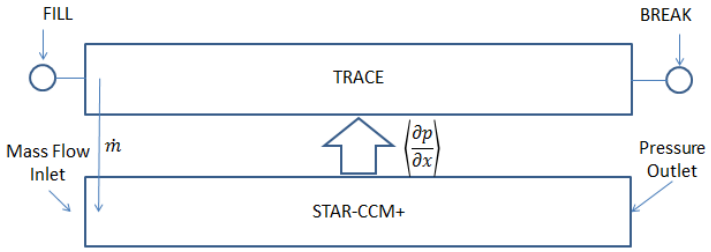

Fig. 4-9. Schematic diagram for domain overlapping coupling setup with imposed mass flow rate.

In this case, the boundary conditions of TRACE dictate the flow. Specifically, the mass flow rate through the pipe is set by a "fill" component to the left of the pipe and the boundary pressure is set by a "break" component to the right of the flow. As indicated in the figure, a mass flow rate, $\dot{m}$, is passed from TRACE to the STAR-CCM+ inlet so that the flow fields are consistent in both codes. Using the TRACE flow rate, STAR-CCM+ calculates volumetric pressure gradient data that is used to construct non-inertial friction factors, as discussed in detail in §4-6. A sample coupled iteration is laid out in Table 4-1:

Table 4-1. Behavior of coupled cases as iteration proceeds.

	TRACE		STAR-CCM+	
Iteration	Δp	$\dot{m}$	Δp	$\dot{m}$
0	$\Delta p_{TRC}(\dot{m}_{TRC,0})$	$\dot{m}_{TRC,0}$	$\Delta p_{CFD}(\dot{m}_{CFD,0})$	$\dot{m}_{CFD,0}$
1	$\Delta p_{CFD}(\dot{m}_{CFD,0})$	$\dot{m}_{TRC,0}$	$\Delta p_{CFD}(\dot{m}_{TRC,0})$	$\dot{m}_{TRC,0}$
2	$\Delta p_{CFD}(\dot{m}_{TRC,0})$	$\dot{m}_{TRC,0}$	$\Delta p_{CFD}(\dot{m}_{TRC,0})$	$\dot{m}_{TRC,0}$

where $\Delta p_{TRC}(\dot{m})$ is the pressure drop across the TRACE component induced by a mass flow rate of $\dot{m}$, $\Delta p_{CFD}(\dot{m})$, is the same quantity for STAR-CCM+, $\dot{m}_{CFD,0}$ is the mass flow initial condition for STAR-CCM+, and $\dot{m}_{TRC,0}$ is the same for TRACE.

In this case, both codes initialize (Iteration 0) with their respective standalone solutions. Specifically, TRACE is initially set with a mass flow rate, $\dot{m}_{TRC,0}$, with which it calculates a TRACE-like pressure drop, $\Delta p_{TRC}(\dot{m}_{TRC,0})$, for the coupled pipe using the method outlined in §E-2.2. STAR-CCM+ is initialized analogously using the solution method outlined in §E-3.2. After initialization, STAR-CCM+ passes the pressure drop $\Delta p_{CFD}(\dot{m}_{CFD,0})$ to TRACE and TRACE passes the mass flow rate $\dot{m}_{TRC,0}$ to STAR-CCM+. After Iteration 1, therefore, both codes have the same inlet mass flow condition of $\dot{m}_{TRC,0}$. However, the pressure drop across the TRACE component is representative of the CFD pressure drop as calculated with the initial mass flow rate for STAR-CCM+, $\Delta p_{CFD}(\dot{m}_{CFD,0})$. After Iteration 1, TRACE again passes the mass flow rate $\dot{m}_{TRC,0}$ to STAR-CCM+, although the CFD code already has this information. More importantly, STAR-CCM+ passes the CFD-like non-inertial friction factors as calculated with $\dot{m}_{TRC,0}$ to TRACE. After iteration 2, both codes have the same mass flow boundary condition and compute the same CFD-like pressure drop and the coupled solution is converged. The boundary condition arrangement of this case simplified the coupled case significantly. In more complex cases, the mass flow rate through the TRACE component will change with iteration. The basic ideas of data transfer remain the same, however.

For a more detailed description of the progression of a coupled simulation for a 3-D configuration, see Fig. E-3. This flow chart summarizes much of the algorithm developed in Chapter 6 with emphasis on the specific process employed by each code including the flow equation solution method.

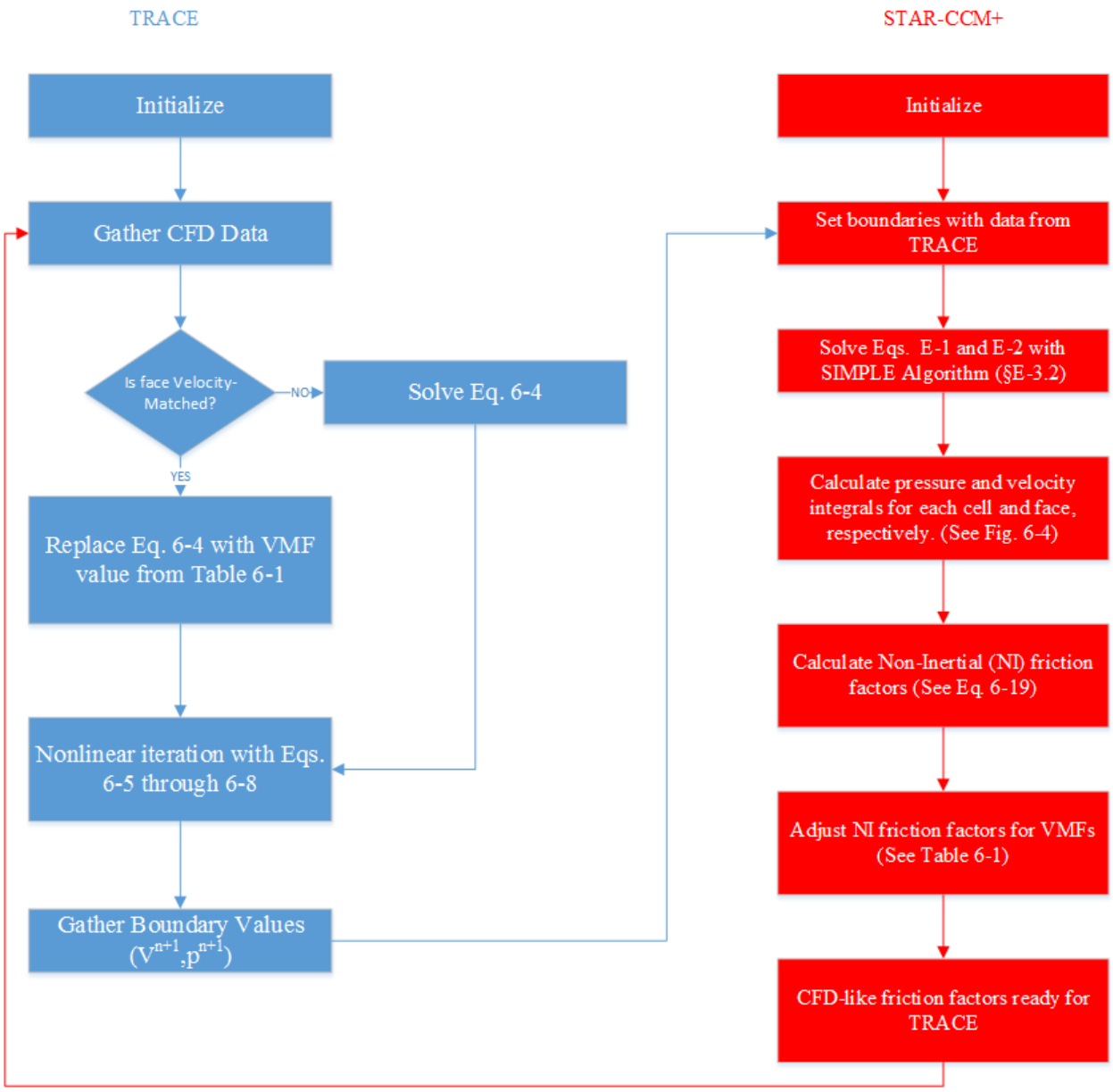

Fig. E-3. Schematic diagram of coupled solution for 3-D geometry.

Bibliography

[1] OECD-NEA, "Technology Roadmap," 2015. [Online]. Available: https://www.oecd-nea.org/pub/techroadmap/techroadmap-2015.pdf. [Accessed 4 February 2015].

[2] United Nations, "United Nations Framework Convention on Climate Change UNFCCC," 12 December 2015. [Online]. Available: https://unfccc.int/resource/docs/2015/cop21/eng/l09r01.pdf. [Accessed 4 April 2016].

[3] World Nuclear Association, "Supply of Uranium," 8 October 2014. [Online]. Available: http://www.world-nuclear.org/info/Nuclear-Fuel-Cycle/Uranium-Resources/Supply-of-Uranium/. [Accessed 5 February 2015].

[4] R. L. Murray, Nuclear Energy: An Introduction to the Concepts, Systems, and Applications of Nuclear Processes (6th Edition), Elsevier, 2009.

[5] Duke Energy, "Form 10-k," 2014.

[6] World Nuclear Association, "Nuclear Power Reactors," January 2015. [Online]. Available: http://www.world-nuclear.org/info/Nuclear-Fuel-Cycle/Power-Reactors/Nuclear-Power-Reactors/. [Accessed 6 February 2015].

[7] B. L. Smith, "Assessment of CFD Codes Used in Nuclear Reactor Safety Simulations," *Nuclear Engineering and Technology,* vol. 42, no. 4, pp. 339-364, 2010.

[8] U.S. DOE and GIF, "A Technology Roadmap for Generation IV Nuclear Energy Systems," 2002.

[9] A. Briard, T. Gomez, P. Sagaut and S. Memari, "Passive scalar decay lays in isotropic turbulence: Prandtl number effects," *Journal of Fluid Mechanics,* vol. 784, pp. 274-303, 2015.

[10] A. Papukchiev, F. Roelofs, A. Shams, G. Lecrivain and W. Ambrosini, "Development and Application of Computational Fluid Dynamics Approaches within the European Project THINS for the Simulation of Next Generation Nuclear Power Systems," *Nuclear Engineering and Design,* Vols. IN-PRESS, 2015.

[11] G. Bandini, M. Polidori, A. Gerschenfeld, D. Pialla, S. Li, W. M. Ma, P. Kudinov, M. Jeltsov, K. Kööp, K. Huber, X. Cheng, C. Bruzzese, A. G. Class, D. P. Prill, A. Papukchiev, C. Geffray, R. Macian-Juan and L. Maas, "Assessment of Systems Codes and their Coupling with CFD Codes in Thermal-Hydraulic Applications to Innovative Reactors,"

Nuclear Engineering and Design, vol. 281, pp. 22-38, 2015.

[12] D. Tenchine, R. Baviere, P. Bazin, F. Ducros, G. Geffraye, D. Kadri, F. Perdu, D. Pialla, B. Rameau and N. Tauveron, "Status of CATHARE code for sodium cooled fast reactors," *Nuclear Engineering and Design,* vol. 245, pp. 140-152, 2012.

[13] U. S. Nuclear Regulatory Commission, "Pressurized Water Reactors," 15 January 2015. [Online]. Available: http://www.nrc.gov/reactors/pwrs.html. [Accessed 9 April 2016].

[14] J. J. Duderstadt and L. J. Hamilton, Nuclear Reactor Analysis, John Wiley & Sons, 1976.

[15] INL, "RELAP5-3D Code Manuals Revision 2.3," Idaho National Lab, Idaho Falls, ID, 2005.

[16] U. S. Nuclear Regulatory Commission, *TRACE V5.0 Theory Manual,* 2010.

[17] G. Lerchl, H. Austregesilo, P. Schöffel, D. von der Cron and F. Weyermann, "ATHLET mod 3.0, Cycle A, User's Manual GRS-p1/Vol1, Rev.6," GRS, Germany, 2012.

[18] J.-J. Jeong, K. S. Ha, B. D. Chung and W. J. Lee, "A Multi-Dimensional Thermal-Hydraulic System Analysis Code, MARS 1.3.1," *Journal of the Korean Nuclear Society,* vol. 31, no. 3, pp. 344-363, 1999.

[19] Los Alamos National Laboratory, *MCNPX User's Manual Version 2.6.0,* D. B. Pelowitz, Ed., 2008.

[20] T. J. Downar, D. A. Barber, R. M. Miller, C. H. Lee, T. Kozlowski, D. Lee, Y. Xu, J. Gan, H. G. Joo, J. Y. Cho and K. Lee, "PARCS: Purdue advanced reactor core simulator," *Proc. Int. Conf. on the New Frontiers of Nuclear Technology: Reactor Physics, Safety and High-Performance Computing,* 2002.

[21] B. Kochunas, B. Collins, D. Jabaay, T. J. Downar and W. R. Martin, "Overview of development and design of MPACT: Michigan parallel characteristics transport code," in *Proceedings of the 2013 International Conference on Mathematics and Computational Methods Applied to Nuclear Science and Engineering - M and C 2013*|, Sun Valley, ID, 2013.

[22] J. D. Anderson Jr., Computational Fluid Dynamics: The Basics with Applications, McGraw-Hill, 1995.

[23] J. H. Jeong and B.-S. Han, "Coolant Flow Field in a Real Geometry of PWR Downcomer and Lower Plenum," *Annals of Nuclear Energy,* vol. 35, pp. 610-619, 2008.

[24] T.-S. Kwon, C.-R. Choi and C.-H. Song, "Three-Dimensional Analysis of Flow Characteristics on the Reactor Vessel Downcomer During the Late Reflood Phase of a Postulated LBLOCA," *Nuclear Engineering and Design,* vol. 226, pp. 255-265, 2003.

[25] T. Höhne, S. Kliem, U. Rohde and F.-P. Weiss, "Boron Dilution Transients During Natural Circulation Flow in PWR-Experiments anad CFD Simulations," *Nuclear Engineering and Design,* vol. 238, pp. 1987-1995, 2008.

[26] H. Tinoco, P. Buchwald and W. Frid, "Numerical Simulation of Boron Injection in a BWR," *Nuclear Engineering and Design,* vol. 240, pp. 221-234, 2010.

[27] G. H. Lee, Y. S. Bang, S. W. Woo and A. J. Cheong, "Comparative study on the effect of reactor internal structure geometry modeling methods on the prediction accuracy for PWR internal flow distribution," *Annals of Nuclear Energy,* vol. 70, pp. 208-215, 2014.

[28] E. Merzari and H. Ninokata, "Proper orthogonal decomposition of the flow in a tight lattice rod-bundle," *Nuclear Engineering and Design,* vol. 241, pp. 4621-4632, 2011.

[29] D. P. Prill and A. G. Class, "Semi-automated proper orthogonal decomposition reduced order model non-linear analysis for future BWR stability," *Annals of Nuclear Energy,* vol. 67, pp. 70-90, 2014.

[30] D. L. Aumiller, E. T. Tomlinson and R. C. Bauer, "A Coupled RELAP5-3D/CFD Methodology with a Proof-of-Principle Calculation," *Nuclear Engineering and Design,* vol. 205, pp. 83-90, 2001.

[31] H. Gibeling and J. Mahaffy, "Benchmarking Simulations with CFD to 1-D Coupling," Penn State University, Applied Research Laboratory, 2002.

[32] N. Anderson, Y. Hassan and R. Schultz, "Analysis of the hot gas flow in the outlet plenum of the very high temperature reactor using coupled RELAP5-3D system code and a CFD code," *Nuclear Engineering and Design,* vol. 238, pp. 274-279, 2008.

[33] D. Bertolotto, A. Manera, S. Frey, H.-M. Prasser and R. Chawla, "Single-phase mixing studies by means of a directly coupled CFD/system-code tool," *Annals of Nuclear Energy,* vol. 36, pp. 310-316, 2009.

[34] A. Papukchiev, G. Lerchl, C. Waata and T. Frank, "Extension of the Simulation Capabilities of the 1D System Code ATHLET by Coupling with the 3D CFD Software Package ANSYS CFX," in *Proc. The 13th International Topical Meeting on Nuclear Reactor Thermal Hydraulics (NURETH-13),* Kanazawa City, Ishikawa Prefecture, Japan.

[35] A. Papukchiev, G. Lerchl, J. Weis, M. Scheuerer and H. Austregesilo, "Development of coupled 1D-3D thermal-hydraulic code for nuclear power plant simulation and its application to a pressurized thermal shock scenario in PWR," in *Proceedings of The 14th International Topical Meeting on Nuclear Reactor Thermalhydraulics, NURETH-14*, Toronto, Ontario, Canada, 2011.

[36] T. Watanabe, Y. Anoda and M. Takano, "System-CFD coupled simulations of flow instability in steam generator U tubes," *Annals of Nuclear Energy,* vol. 70, pp. 141-146, 2014.

[37] W. Li, X. Wu, D. Zhang, G. Su, W. Tian and S. Qiu, "Preliminary study of coupling CFD code FLUENT and system code RELAP5," *Annals of Nuclear Energy,* vol. 73, pp. 96-107, 2014.

[38] T. H. Fanning and J. W. Thomas, "Advances in Coupled Safety Modeling Using Systems Analysis and High-Fidelity Methods," ANL-GENIV-134, 2010.

[39] Argonne National Laboratory, T. H. Fanning, Ed., ANL/NE-12/4, Nuclear Engineering Division, Argonne National Laboratory, 2012.

[40] M. Jeltsov, K. Kööp, P. Kudinov and W. Villanueva, "Development of a Domain Overlapping Coupling Methodology for STH/CFD Analysis of Heavy Liquid Metal Thermal-Hydraulics," in *Proc. The 15th International Topical Meeting on Nuclear Reactor Thermal Hydraulics (NURETH-15)*, Pisa, Italy, 2013.

[41] R. Bavière, N. Tauveron, F. Perdu, E. Garrè and S. Li, "A first system/CFD coupled simulation of a complete nuclear reactor transient using CATHARE2 and TRIO_U. Preliminary validation on the Phénix Reactor Natural Circulation Test," *Nuclear Engineering and Design,* vol. 277, pp. 124-137, 2014.

[42] D. Pialla, D. Tenchine, S. Li, P. Gauthe, A. Vasile, R. Baviere, N. Tauveron, F. Perdu, L. Maas, F. Cocheme, K. Huber and X. Cheng, "Overview of the system alone and system/CFD coupled calculations of the PHENIX Natural Circulation Test within the THINS project," *Nuclear Engineering and Design,* vol. 290, pp. 78-86, 2015.

[43] F. Cadinu and P. Kudinov, "Development of a "Coupling-by-Closure" Approach between CFD and System Thermal-Hydraulic Codes," in *Proc. The 13th International Topical Meeting on Nuclear Reactor Thermal Hydraulics (NURETH-13)*, Kanazawa City, Ishikawa Prefecture, Japan, 2009.

[44] A. Papukchiev, M. Jeltsov, K. Kööp, P. Kudinov and G. Lerchl, "Comparison of different coupling CFD-STH approaches for pre-test analysis of TALL-3D experiment," *Nuclear*

Engineering and Design, vol. 290, pp. 135-143, 2015.

[45] CD-Adapco, *STAR-CCM+ v8.02 Manual,* 2013.

[46] T. L. Bergman, A. S. Lavine, F. P. Incropera and D. P. Dewitt, Fundamentals of Heat and Mass Transfer: Seventh Edition, John Wiley & Sons, Inc., 2011.

[47] K. N. Ivanov, T. M. Beam, A. J. Baratta, A. Irani and N. Trikouros, "Pressurized Water Reactor Main Steam Line Break (MSLB) Benchmark -- Volume I: Final Specifications"," U.S. Nuclear Regulatory Commission, Organization for Economic Cooperation and Development Nuclear Energy Agency, 1999.

[48] U. Grundmann and S. Kliem, "Analyses of the OECD main steam line break benchmark with the DYN3D and ATHLET Codes," *Nuclear Technology,* vol. 142, pp. 146-153, 2003.

[49] T. Kozlowski, R. M. Miller, T. J. Downar, D. A. Barber and H. G. Joo, "Consistent comparison of the codes RELAP5/PARCS and TRAC-M/PARCS for the OECD MSLB coupled code benchmark," *Nuclear Technology,* vol. 146, pp. 15-28, 2004.

[50] H. G. Joo, J.-J. Jeong, B.-O. Cho and W. J. Lee, "Analysis of the OECD main steam line break benchmark problem using the refined cored thermal-hydraulic nodalization feature of the MARS/MASTER code," *Nuclear Technology,* vol. 142, pp. 166-179, 2003.

[51] T. G. Theofanous and E. A. Shabana, "Boron mixing in the lower plenum of a BWR," *Nuclear Engineering and Design,* vol. 126, pp. 245-255, 1991.

[52] CRC, CRC Handbook of Chemistry and Physics 62nd ed., Boca Raton, Florida: The CRC Press, Inc., 1981.

[53] V. Gnielinski, "New Equation for Heat and Mass Transfer in Turbulent Pipe and Channel Flow," *International Chemical Engineering,* vol. 16, pp. 359-368, 1976.

[54] G. K. Filonenko, "Hydraulic Resistance in Pipes," *Teplonergetika,* vol. 1, pp. 40-44, 1965.

[55] D. Bertolotto, *Coupling a System Code with Computational Fluid Dynamics for the Simulation of Complex Coolant Reactivity Effects,* École Polytechnique Fédérale de Lausanne, 2011.

[56] Wolfram Alpha LLC, "Wolfram|Alpha," 2014. [Online]. Available: http://www.wolframalpha.com/input/?i=water+density+at+1.5e7+Pa+550.0K. [Accessed 8 July 2014].

[57] J. Y. Wang, T. J. Chuang and Y. M. Ferng, "CFD Investigating Flow and Heat Transfer Characteristics in a Natural Circulation Loop," *Annals of Nuclear Energy,* vol. 58, pp. 65-71, 2013.

[58] Idaho National Engineering and Environmental Laboratory, "RELAP5-3D Code Manual Volume 1: Code Structure, System Models, and Solution Methods," Idaho Falls, Idaho, 2001.

[59] Y. Yu, E. Merzari, A. Obabko and J. Thomas, "A porous medium model for predicting the duct wall temperature of sodium fast reactor fuel assembly," *Nuclear Engineering and Design,* vol. 295, pp. 48-58, 2015.

[60] Dehbi, A.; Badreddine, H.;, "CFD prediction of mixing in a steam generator mock-up: Comparison between full geometry and porous medium approaches," *Annals of Nuclear Energy,* vol. 58, pp. 178-187, 2013.

[61] S. B. Pope, Turbulent Flows, New York: Cambridge University Press, 2000.

[62] B. E. Launder and B. I. Sharma, "Application of the energy-dissipation model of turbulence to the calculation of flow near a spinning disc," *Lett. Heat Mass Transf.,* vol. 1, pp. 131-138, 1974.

[63] D. C. Wilcox, Turbulence Modeling for CFD (2nd ed.), DCW Industries, 1998.

[64] D. C. Wilcox, "Formulation of the k-ω Turbulence Model Revisited," *AIAA Journal,* vol. 46, no. 11, pp. 2823-2838, 2008.

[65] S. K. Arolla and P. A. Durbin, "Modeling rotation and curvature effects within scalar eddy viscosity model framework," *International Journal of Heat and Fluid Flow,* vol. 39, pp. 78-89, 2013.

[66] C. G. Speziale, R. Abid and E. C. Anderson, "Critical Evaluation of Two-Equation Models for Near-Wall Turbulence," *AIAA Journal,* vol. 30, no. 2, pp. 324-331, 1992.

[67] M. Wolfstein, "The velocity and temperature distribution in one-dimensional flow with turbulence augmentation and pressure gradient," *International Journal of Heat and Mass Transfer,* vol. 12, no. 3, pp. 301-318, 1969.

[68] F. R. Menter, "Two-Equation Eddy-Viscosity Turbulence Models for Engineering Applications," *AIAA Journal,* vol. 32, no. 8, pp. 1598-1605, 1994.

[69] H. K. Versteeg and W. Malalasekera, An Introduction to Computational Fluid Dynamics:

The Finite Volume Method (2nd Edition), Prentice Hall, 2007.

[70] "twall/jna - Github," GitHub, 2015. [Online]. Available: https://github.com/twall/jna. [Accessed 9 February 2015].

[71] S. V. Patankar and D. B. Spalding, "A calculation procedure for heat, mass and momentum transfer in three-dimensional parabolic flows," *International Journal of Heat and Mass Transfer,* vol. 15, no. 10, pp. 1787-1806, 1972.

[72] S. R. Mathur and J. Y. Murthy, "Pressure boundary conditions for incompressible flows using unstructred meshes," *Numerical Heat Transfer, Part B: Fundamentals,* vol. 32, no. 3, pp. 283-298, 1997.

[73] S. R. Mathur and J. Y. Murthy, "Pressure-based method for unstructured meshes," *Numerical Heat Transfer, Part B: Fundamentals,* vol. 31, no. 2, pp. 195-214, 1997.

[74] J. H. Mahaffy, "A Stability-Enhancing Two-Step Method for Fluid Flow Calculations," *Journal of Computational Physics,* vol. 46, pp. 329-341, 1982.

[75] I. K. Park, J. R. Lee, S. W. Lee, H. Y. Yoon and J. J. Jeong, "An Implicit Code Coupling of 1-D System Code and 3-D In-House CFD Code for Multi-Scaled Simulations of Nuclear Reactor Transients," *Annals of Nuclear Energy,* vol. 59, pp. 80-91, 2013.

[76] A. Papukchiev, G. Lerchl, J. Weis, M. Sheuerer and H. Austregesilo, "Development of a Coupled 1D-3D Thermal-Hydraulic Code for Nuclear Power Plant Simulation and its Application to a Pressurized Thermal Shock Scenario in PWR," in *Proc. The 14th International Topical Meeting on Nuclear Reactor Thermalhydraulics, NURETH-14,* Toronto, Ontario, Canada, 2011.

[77] J. Mahaffy, "Best Practice Guidelines for the Use of CFD in Nuclear Reactor Safety Applications," NEA/CSNI/R, 2007.

[78] R. Hu, J. W. Thomas, E. Munkhzul and T. H. Fanning, "Coupled System and CFD Code Simulation of Thermal Stratification in SFR Protected Loss-Of-Flow Transients," in *Proceedings of ICAPP 2014,* Charlotte, NC, USA, 2014.

[79] A. Palazzi, M. J. Bluck and S. Lo, "A Coupled RELAP5-3D/STAR-CCM+ Simulation for the Calculation of Friction Factor in Pipes," in *Proceedings of ICAPP 2014,* Charlotte, NC, USA, 2014.

[80] T. H. Fanning and J. W. Thomas, "Integration of CFD into Systems Analysis Codes for Modeling Thermal Stratification During SFR Transients," in *Proc. The 14th International*

Topical meeting on Nuclear Reactor Thermalhydraulics, NURETH-14, Toronto, Ontario, Canada, 2011.

[81] E. W. Weisstein, "Cylindrical Coordinates," MathWorld--A Wolfram Web Resource, [Online]. Available: http://mathworld.wolfram.com/CylindricalCoordinates.html. [Accessed 23 March 2015].

[82] X. J. Liu and X. Cheng, "Sub-Channel/System Coupled Code Development and its Application to SCWR-FQT Loop," *Nuclear Engineering and Design*, vol. 285, pp. 39-47, 2015.

[83] J.-J. Jeong, W. J. Lee and B. D. Chung, "Simulation of a Main Steam Line Break Accident Using a Coupling "System Thermal-Hydraulics,Three-Dimensional Reactor Kinetics, and Hot Channel Analysis" Code," *Annals of Nuclear Energy*, vol. 33, pp. 820-828, 2006.

[84] D. L. Aumiller, E. T. Tomlinson and W. L. Weaver, "An Integrated RELAP5-3d and Multiphase CFD Code System Utilizing a Semi-Implicit Coupling Technique," *Nuclear Engineering and Design*, vol. 216, pp. 77-87, 2002.

[85] W. L. Weaver, E. T. Tomlinson and D. L. Aumiller, "A generic semi-implicit coupling methodology for use in RELAP5-3D," *Neuclear Engineering and Design*, vol. 211, pp. 13-26, 2002.

[86] S. Yang, X. Chen, D. Wu and P. Yan, "Dynamic analysis of the pump system based on MOC-CFD coupled method," *Annals of Nuclear Energy*, vol. 78, pp. 60-69, 2015.

[87] J. Galindo, A. Tiseira, P. Fajardo and R. Navarro, "Coupling methodology of 1D finite difference and 3D finite volume CFD codes based on the Method of Characteristics," *Mathematical and Computer Modeling*, vol. 54, pp. 1738-1746, 2011.

[88] Z. Chen, X.-N. Chen, A. Rineiski, P. Zhao and H. Chen, "Coupling a CFD code with neutron kinetics and pin thermal models for nuclear reactor safety analyses," *Annals of Nuclear Energy*, vol. 83, pp. 41-49, 2015.

[89] D. Ramajo, S. Corzo, N. Schiliuk and N. Nigro, "3D modeling of the primary circuit in the reactor pressure vessel of a PHWR," *Nuclear Engineering and Design*, vol. 265, pp. 356-365, 2013.

[90] S. Corzo, D. Ramajo and N. Nigro, "1/3D modeling of the core coolant circuit of a PHWR nuclear power plant," *Annals of Nuclear Energy*, vol. 83, pp. 386-397, 2015.

[91] D. Pialla, D. Tenchine, S. Li, P. Gauthe, A. Vasile, R. Baviere, N. Tauveron, F. Perdu, L.

Maas, F. Cocheme, K. Huber and X. Cheng, "Overview of the system alone and system/CFD coupled calculations of the PHENIX Natural Circulation Test within the THINGS project," *Nuclear Engineering and Design*, vol. ARTICLE IN PRESS, 2015.

[92] F. Perdu and S. Vandroux, "System/CFD Coupling For Reactor Transient Analysis. An Application To The Gas Fast Reactor With CATHARE And TRIO_U," in *Proceedings of ICAPP '08*, Anaheim, CA, USA, 2008.

[93] A. P. Kuprat, S. Kabilan, J. P. Carson, R. A. Corley and D. R. Einstein, "A bidirectional coupling procedure applie to multiscale respiratory modeling," *Journal of Computational Physics*, vol. 244, pp. 148-167, 2013.

[94] F. Nobile, "Coupling strategies for the numerical simulation of blood flow in deformable arteries by 3D and 1D models," *Mathematical and Computer Modelling*, vol. 49, pp. 2152-2160, 2009.

[95] G. Lerchl and H. Austregesilo, "ATHLET mod 2.1 Cycle A, User's Manual GRS-p1/Vol1, Rev.4," GRS, Germany, 2006.